

UNIVERSITY OF SÃO PAULO  
SÃO CARLOS SCHOOL OF ENGINEERING

RAQUEL RICIATI DO COUTO VILELA

**Luminescent host-guest systems based on coordination compounds:  
Synthesis, characterization, and applications**

São Carlos  
2023

RAQUEL RICIATI DO COUTO VILELA

**Luminescent host-guest systems based on coordination compounds:  
Synthesis, characterization, and applications**

Revised Version

Thesis presented to the São Carlos School of Engineering, University of São Paulo, as requirement to obtain the title of Doctor in Sciences - Postgraduate Program in Materials Science and Engineering.

Concentration area: Characterization, Development and Application of Materials

Advisor: Prof<sup>a</sup>. Dr<sup>a</sup>. Andréa Simone Stucchi de Camargo Alvarez Bernardez

São Carlos

2023

I AUTHORIZE TOTAL OR PARTIAL REPRODUCTION OF THIS WORK BY ANY CONVENTIONAL OR ELECTRONIC MEANS, FOR RESEARCH PURPOSES, SO LONG AS THE SOURCE IS CITED.

Catalog card prepared by Patron Service at "Prof. Dr. Sergio Rodrigues Fontes Library" at EESC/USP

V6951 Vilela, Raquel Riciati do Couto  
Luminescent host-guest systems based on coordination compounds: synthesis, characterization, and applications / Raquel Riciati do Couto Vilela; advisor Andréa Simone Stucchi de Camargo Alvarez Bernardez. -- São Carlos, 2023.

Doctoral (Thesis) - Graduate Program in Materials Science and Engineering and Concentration area in Characterization, Development and Application of Materials. -- São Carlos School of Engineering, at University of São Paulo, 2023.

1. Ir(III) complex. 2. Host-guest materials. 3. Sol-gel process. 4. Photophysics. I. Título.

## FOLHA DE JULGAMENTO

Candidata: Bacharela **RAQUEL RICIATI DO COUTO VILELA.**

Título da tese: "Sistemas hóspede-hospedeiros luminescentes baseados em compostos de coordenação: síntese, caracterização e aplicações".

Data da defesa: 06/10/2022.

### **Comissão Julgadora**

### **Resultado**

Profa. Associada **Andréa Simone Stucchi de Camargo Alvarez Bernardes**  
**(Orientadora)**

(Instituto de Física de São Carlos/IFSC-USP)

Aprovado

Prof. Dr. **Sergio Antonio Marques de Lima**

(Universidade Estadual Paulista "Júlio de Mesquita Filho"/UNESP - Presidente Prudente)

Aprovado

Prof. Dr. **Thiago Branquinho de Queiroz**

(Universidade Federal do ABC/UFABC)

Aprovada

Prof. Dr. **Fabio Simões de Vicente**

(Universidade Estadual Paulista "Júlio de Mesquita Filho"/UNESP - Rio Claro)

Aprovada

Prof. Associado **Ubirajara Pereira Rodrigues Filho**

(Instituto de Química de São Carlos/IQSC-USP)

Aprovada

Coordenador do Programa de Pós-Graduação em Engenharia de Materiais:

Prof. Associado **Rafael Salomão**

Presidente da Comissão de Pós-Graduação:

Prof. Titular **Murilo Araujo Romero**

*To my parents, who made me the person I am.  
To my brother and sister, for their love and support during this journey.*

## ACKNOWLEDGEMENTS

First of all, I would like to thank my parents, Marta and Mauro, and my siblings Marina and Leonardo, for the support at all stages of my life. Thank you for always being by my side and for being the biggest encouragers of my achievements. This thesis is also yours.

I thank Matheus who, in so many ways, made this journey lighter for me. Thank you for the support, understanding and caring you always dedicate to me, without which I cannot imagine what the last few years would have been like.

I would like to thank my advisor Prof. Andréa de Camargo for the opportunity to perform this work. Thank you for accepting me in LEMAF and for providing all the means to make the development of this project possible. Above all, thank you for the personal and professional growth that working with you over these years has brought me.

Part of the work in this thesis would not have been possible without the help and guidance of Dr. Kassio Zanoni. Thank you for introducing me to the amazing world of coordination compounds, for always being there and willing to share your knowledge, for the words of encouragement that were needed in some curves of this way, but more than that, thank you for being such a good friend.

During these years in São Carlos, I had the opportunity to work and live with several people. Among them, I dedicate a special thanks to the best lab/roommate I could ever have, Marylyn. Thank you for sharing the days with me, for the support during difficult times, and for everything we have been through together. From homework to happy hours, you made this chapter of my life a wonderful experience. I also thank my friends Thiago and Walter, for the friendship that extends beyond LEMAF. The journey to a doctorate came with its highs and lows, and I am glad to have people like you by my side.

I thank everyone of the Laboratory of Spectroscopy of Functional Materials (LEMAF), especially Prof. Marcos de Oliveira Júnior and Prof. Hellmut Eckert, for all their contribution to the development of this work and for the fruitful discussions.

I would like to thank Prof. Cristian Strassert from the University of Münster, Germany, where I had the privilege of doing a 6-month internship during my PhD. Thank you for sharing your knowledge of Pt(II) complexes with me, and for the chance to learn and grow in this field.

Finally, I thank the University of São Paulo (USP), the São Carlos School of Engineering (EESC), and the São Carlos Institute of Physics (IFSC) for the opportunity to carry out this doctorate. Additionally, I would like to thank all the funding agencies that supported

this research (FAPESP, CNPq and CAPES), and all the people who somehow contributed to the realization of this work, teachers, technicians, employees, and colleagues.

This study was financed in part by the Coordenação de Aperfeiçoamento de Pessoal de Nível Superior – Brasil (CAPES) – Grant Finance Code 001.

“Seja você quem for, seja qual for a posição social que você tenha na vida, a mais alta ou a mais baixa, tenha sempre como meta muita força, muita determinação e sempre faça tudo com muito amor e com muita fé em Deus, que um dia você chega lá. De alguma maneira você chega lá.” Ayrton Senna



## ABSTRACT

VILELA, R. R. C. **Luminescent host-guest systems based on coordination compounds: Synthesis, characterization, and applications.** 2023. 146 p. Thesis (Doctor) – São Carlos School of Engineering, University of São Paulo, São Carlos, 2022.

Host-guest materials are under fast development and constitute an attractive research topic on account of the versatility and wide range of applications they serve. In many of these applications, the photoactivity of coordination compounds embedded in a solid matrix is exploited. Besides attaining application versatility (as opposed to their study in solution), the appropriate dispersion or binding of these molecular species in solid matrices offers the possibility of protecting them from vibronic coupling with solvent molecules, preventing self-quenching processes, increasing their photostability and biocompatibility. This doctoral work was dedicated to the synthesis and investigation of the photophysical properties of Ir(III) complexes, in solid state and solution, as well as the design of applications based on their derived host-guest materials, which were obtained via sol-gel methodology. Three different approaches were explored: i) Synthesis of highly luminescent hybrid organosilicate materials based on the immobilization of the complex  $[\text{Ir}(\text{Fppy})_2(\text{dmb})]^+$  in the GPTS:TEOS matrix; ii) Preparation of MCM-41-type mesoporous nanoparticles doped with amphiphilic  $[\text{Ir}(\text{NC})_2(\text{dnbp})]^+$  complexes via templated synthesis and iii) Surface modification of MCM-41 nanoparticles and incorporation of Ir(III) complexes of the series  $[\text{Ir}(\text{NC})_2(\text{dmb})]^+$  for applications in photodynamic therapy. The characterizations of the synthesized complexes, as well as of the materials derived from them, were carried out by conventional techniques such as X-ray diffraction, microscopy (TEM and confocal fluorescence microscopy), FTIR, Raman, dynamic light scattering (DLS), as well as optical (UV-VIS, PL and PLE) and nuclear magnetic resonance (NMR) spectroscopic techniques. Altogether, the experimental strategies used in this work stands as an advance in the design of photo-functional materials with promising applications in optical sensors, luminescent devices and photodynamic therapy.

**Key words:** Ir(III) complex, host-guest materials, sol-gel process, photophysics.

## RESUMO

VILELA, R. R. C. **Sistemas hóspedes-hospedeiros luminescentes baseados em compostos de coordenação: Síntese, caracterização e aplicações.** 2023. 146 p. Tese (Doutorado) – Escola de Engenharia de São Carlos, Universidade de São Paulo, São Carlos, 2022.

Os materiais hóspedes-hospedeiros estão em rápido desenvolvimento e constituem um tópico de pesquisa bastante atrativo devido à versatilidade e ampla gama de aplicações que oferecem. Em muitas dessas aplicações, a fotoatividade de compostos de coordenação é explorada quando carregado em uma matriz sólida. Além de conferir versatilidade à aplicação em estado sólido, a dispersão ou ligação adequada dessas espécies moleculares (geralmente estudadas em solução) em estruturas sólidas rígidas oferece a possibilidade de protegê-las do acoplamento vibrônico com moléculas de solvente, previne processos de autosupressão da luminescência, aumenta suas fotoestabilidade e biocompatibilidade. Este projeto de doutorado foi dedicado à síntese e caracterização das propriedades fotofísicas de complexos de Ir(III) e ao planejamento de suas aplicações, introduzindo-os em diferentes matrizes hospedeiras obtidas pelo processo sol-gel. Para tanto, três abordagens foram exploradas: i) Síntese de materiais organossilicatos para a produção de materiais monolíticos altamente luminescentes, a partir da imobilização do complexo  $[\text{Ir}(\text{Fppy})_2(\text{dmb})]^+$  na matriz GPTS:TEOS, ii) Preparação de nanopartículas mesoporosas do tipo MCM-41 dopadas com complexos anfífilicos  $[\text{Ir}(\text{NC})_2(\text{dnbp})]^+$  via síntese modelada. e iii) Funcionalização da superfície de nanopartículas de MCM-41 e incorporação de complexos de Ir(III) da série  $[\text{Ir}(\text{NC})_2(\text{dmb})]^+$  para aplicações em terapia fotodinâmica. As caracterizações dos complexos sintetizados, bem como dos materiais deles derivados, foram realizadas por técnicas convencionais como difração de raios X, microscopia (de transmissão, TEM, e de fluorescência confocal), FT-IR, Raman, espalhamento dinâmico de luz (DLS), bem como técnicas espectroscópicas ópticas (UV-VIS, PL e PLE) e de ressonância magnética nuclear (RMN). Em conjunto, as estratégias experimentais utilizadas no trabalho representam um avanço no projeto de materiais fotofuncionais com grande promessa para aplicações em sensores ópticos, dispositivos luminescentes, bem como em terapia fotodinâmica.

**Palavras-chave:** Complexo de Ir(III), materiais hóspedes-hospedeiros, processo sol-gel, fotofísica.

## LIST OF FIGURES

<b>1. Introduction</b> .....	<b>21</b>
<b>Figure 1.</b> Preparation scheme of some products obtained by the sol-gel process [39].....	<b>25</b>
<b>Figure 2.</b> (Upper part) Examples of surfactants. (Lower part) Schematic representation of micellar aggregates of a surfactant: a) spherical; b) cylindrical; c) reverse; d) laminar micelles [48].....	<b>28</b>
<b>Figure 3.</b> Schematic model of the templating mechanism in the formation of MSNs: a) micelle formation; b) organization of the micelles into aggregates; c) TEOS addition and hydrolysis and condensation reactions; d) silica growth around the surfactant template; e) surfactant removal (i.e. calcination or extraction) [48].....	<b>29</b>
<b>Figure 4.</b> Structures of mesoporous M41S materials: a) MCM-41 (2D hexagonal), b) MCM-48 (cubic), and c) MCM-50 (lamellar) [50] .....	<b>29</b>
<b>Figure 5.</b> Jablonski-Perrin diagram illustrating photophysical processes [62].....	<b>33</b>
<b>Figure 6.</b> Simplified orbital-molecular diagram in a coordination environment. M stands for metal and L stands for ligand [62].....	<b>35</b>
<b>Figure 7.</b> a) Separation of <i>d</i> orbitals, in an octahedral ligand field; b) orbital description of the MC, MLCT and LC transitions, where S is a substituent group capable of exerting electron withdrawal or release effects (resulting in the stabilization or destabilization, respectively, of the energy level of the filled <i>d</i> and $\pi$ orbitals); c) electronic transitions involving MC, MLCT and LC excited states; MC levels are generally non-emissive [64].....	<b>37</b>
<b>Figure 8.</b> a) Generic structure of an Ir(III) complex where two bidentate ligands C <sup>N</sup> coordinate to Ir(III) through N and C atoms, and a third bidentate ligand binds to Ir(III) by N atoms; b) Modulation of the $\Delta E$ energy between the HOMO and LUMO states through the addition of electron donor and acceptor groups to the N <sup>N</sup> and C <sup>N</sup> ligands; c) Example of possible emission colors to be obtained through molecular engineering exemplified in b) [11].....	<b>38</b>

**3. Structural and photophysical characterization of highly luminescent organosilicate xerogel doped with Ir(III) complex.....48**

**Figure 1.** Chemical structures of the silica precursors used in this work and the investigated  $[\text{Ir}(\text{Fppy})_2(\text{dmb})]^+$  complex .....51

**Figure 2.** FTIR spectra of GPTS:TEOS and GPTS:TEOS:FIrDmb. Attributions of the bands are given, see main text for more details.....55

**Figure 3.** Raman spectra of GPTS:TEOS and GPTS:TEOS:FIrDmb. Attributions of the vibrational bands are given, see main text for more details.....56

**Figure 4.**  $^{29}\text{Si}$  MAS NMR spectra for GPTS:TEOS and GPTS:TEOS:FIrDmb xerogels (black curves). Spectral deconvolutions into Gaussian functions are also shown (blue curves are Gaussian components and red curves are the total deconvoluted spectra). Attributions of the lines to  $\text{T}^n$  and  $\text{Q}^n$  species are also given, see main text for more details.....57

**Figure 5.**  $^{13}\text{C}\{^1\text{H}\}$  CPMAS NMR spectra for GPTS:TEOS and GPTS:TEOS:FIrDmb xerogels and  $^{13}\text{C}$  liquid NMR spectrum for the pure GPTS compound. In (a) the full spectra are displayed, while in (b) the region from 57 to 79 ppm is shown in detail. Peak attributions are given as numbers corresponding to the C atom labeling shown for the GPTS compound. Letters a to f in (b) corresponds to attributions for the possible products of the GPTS epoxy ring opening reactions (see Figure S4 in Supporting Information).....59

**Figure 6.** (a)  $^1\text{H}$  NMR spectra obtained at 60 kHz MAS for GPTS:TEOS and GPTS:TEOS:FIrDmb xerogels. Peak attributions correspond to the chemical shifts expected for the protons bounded to carbons of the GPTS moiety (see C labeling in Figure 5). (b) Double-CP  $^1\text{H}$ - $^{29}\text{Si}$ - $^1\text{H}$  ( $^1\text{H}\{^{29}\text{Si}\}$ ) and  $^1\text{H}$ - $^{13}\text{C}$ - $^1\text{H}$  ( $^1\text{H}\{^{13}\text{C}\}$ ) spectra for the GPTS:TEOS:FIrDmb sample, obtained at 60 kHz MAS. The  $^1\text{H}$  MAS spectrum is also displayed in (b) for comparison.....61

**Figure 7.** Bi-dimensional double-CP HETCOR  $^1\text{H}$ - $^{13}\text{C}$ - $^1\text{H}$  (a) and  $^1\text{H}$ - $^{29}\text{Si}$ - $^1\text{H}$  (b) spectra for the sample GPTS:TEOS:FIrDmb, obtained with 60 kHz MAS and  $^1\text{H}$  detection. Numbers in (a) correspond to assignments to the GPTS moiety (see C labels in Figure 5).....63

**Figure 8.** Thermal degradation (TG) profile (a) and differential scanning calorimetry (DSC) thermograms (b) of GPTS:TEOS and GPTS:TEOS:FIrDmb xerogels.....64

**Figure 9.** Absorption (a) and emission spectra (b) of undoped GPTS:TEOS xerogel at 298 K ( $\lambda_{exc} = 370$  nm).....64

**Figure 10.** Absorption spectrum of free FIrDmb complex in acetonitrile at 298 K.....65

**Figure 11.** Emission spectra (a) of free Ir(III) complexes (FIrDmb) and the GPTS:TEOS-doped matrix in the sol phase and the monolithic material (b) at 298 K ( $\lambda_{exc} = 370$  nm).....67

**Figure 12.** Emission decay for GPTS:TEOS:FIrDmb monolithic materials with different complex concentrations. The prepared samples present no change in the emission lifetime....67

#### **4. Photophysical properties of Ir(III) complexes immobilized in MCM-41 via templated synthesis.....74**

**Chart 1.** Chemical structures of the investigated  $[\text{Ir}(\text{C}^{\wedge}\text{N})_2(\text{dnbp})]^+$  complexes.....77

**Figure 1.** Absorption spectra of  $[\text{Ir}(\text{C}^{\wedge}\text{N})_2(\text{dnbp})]^+$  complexes in methanol at 298 K. The inset shows a zoomed view of the 420 - 570 nm spectral range.....78

**Figure 2.** Emission spectra of  $[\text{Ir}(\text{C}^{\wedge}\text{N})_2(\text{dnbp})]^+$  complexes in  $\text{N}_2$ -saturated methanol at 298 K ( $\lambda_{exc} = 370$  nm).....79

**Figure 3.** Sol-gel encapsulation of  $[\text{Ir}(\text{C}^{\wedge}\text{N})_2(\text{dnbp})]^+$  complexes inside MCM-41 mesopores.....81

**Figure 4.** XRD patterns of the developed complex@MCM-41 nanoparticles (non-calcined).....81

**Figure 5.** TEM images of complex@MCM-41 nanoparticles.....82

**Figure 6.**  $^{19}\text{F}$  MAS NMR spectra at 25 kHz for (A) pure FIrDnbp complex, (B) FIrDnbp@MCM-41, and (C) physical mixture containing FIrDnbp (1 mg) diluted in blank MCM-41 (98 mg). Dashed lines mark  $\delta = -107.5$  ppm (black - - -) and  $\delta = -122.8$  ppm (red · · ·). Spinning side-bands are marked with asterisks. To improve visualization of features the spectrum (A) was divided by 30. All spectra were normalized by mass and number of scans.....83

**Figure 7.** (A) Photographs and (B) spectra of the emission of  $[\text{Ir}(\text{C}^{\wedge}\text{N})_2(\text{dnbp})]^+$  complexes encapsulated in MCM-41 nanoparticles under  $\text{N}_2$  atmosphere at 298 K ( $\lambda_{\text{exc}} = 360$  nm).....84

**Figure 8.** (A) Normalized emission decay (inset: log scale) and (B) time-resolved emission spectra of  $[\text{Ir}(\text{C}^{\wedge}\text{N})_2(\text{dnbp})]^+$  complexes encapsulated in MCM-41. The grey arrows in (A) indicate the time points in which time-resolved spectra in (B) were obtained (laser  $\lambda_{\text{exc}} = 370$  nm).....87

**Figure 9.** The decrease in quantum yield ( $\phi/\phi_0$ ) as a function of  $\text{O}_2$  saturation for  $[\text{Ir}(\text{C}^{\wedge}\text{N})_2(\text{dnbp})]^+$  complexes in methanol (straight lines) or encapsulated in MCM-41 (broken lines).....87

**Figure 10.** Emission spectra ( $\lambda_{\text{exc}} = 365$  nm) of  $\text{FIrDnbp@MCM-41}:\text{pqiIrDnbp@MCM-41}$  mixtures in different m/m proportions: 1:0, 5:1, 1:1 and 0:1. The inset shows a color diagram with the respective CIE coordinates. The definition for Lines a and b is presented in the main text.....89

## **5. Mesoporous silica nanoparticles incorporated with Ir(III) complexes: From photophysics to photodynamic therapy.....98**

**Chart 1.** Chemical structures of the  $[\text{Ir}(\text{NC})_2(\text{dmb})]^+$  complexes.....101

**Figure 1.** Emission spectra of Ir(III) complexes (Ir1– Ir3) as water-soluble chloride ( $\text{Cl}^-$ ) at 298 K ( $\lambda_{\text{exc}} = 365$  nm).....103

**Figure 2.** Schematic illustration of the MCM41-COOH obtained by post-synthetic route, incorporated with Ir(III) complexes.....105

**Figure 3.** a) XRD patterns of unmodified MCM41-OH nanoparticles and those incorporated with Ir(III) complexes; and b) TEM images of MCM41-COOH nanoparticles.....106

**Figure 4.** Emission spectra of MCM41-COOH nanoparticles incorporated with Ir(III) complexes dispersed in  $\text{H}_2\text{O}$  ( $1 \text{ mg mL}^{-1}$ , approximately  $0.6 \times 10^{-5} \text{ mol mL}^{-1}$  of complex) at 298 K ( $\lambda_{\text{exc}} = 365$  nm).....107

**Figure 5.** In vitro studies of MCM41-COOH and complex@MCM41-COOH nanoparticles for cancer therapy. Cell viability of (A) Hepa-RG and (B) Hep-G2 cells after 24 h of incubation in

the dark; cell viability of Hep-G2 cell line after 24 h of incubation and irradiated for (C) 10 min ( $24 \text{ J.cm}^{-2}$ ) and (D) 20 min ( $48 \text{ J.cm}^{-2}$ ) using a 405 nm LED biotable. All experiments assessed by MTT. Statistical analysis was performed by two-way ANOVA with Tukey's comparison. The measurements are represented by average  $\pm$  standard error, \* $p < 0.05$ , \*\* $p < 0.01$ , \*\*\* $p < 0.001$  and \*\*\*\*  $p\text{-value} < 0.0001$ ).....110

**Figure 6.** Confocal microscopy of the cellular uptake behavior of complex@MCM41-COOH in Hep-G2 cell line. Green and red florescence, nanoparticles; blue florescence, nuclei stained with Hoechst 33258 (DAPI). Scale bars represent  $20 \mu\text{m}$ .....111

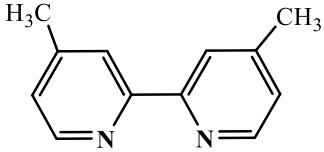
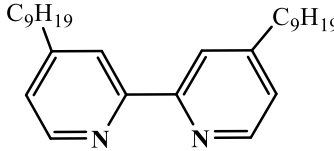
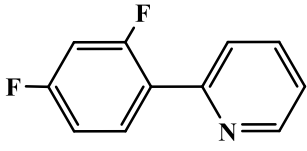
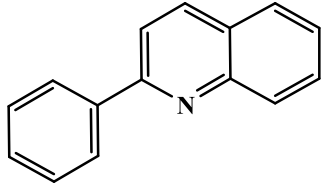
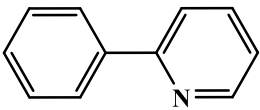
## LIST OF TABLES

<b>3. Structural and photophysical characterization of highly luminescent organosilicate xerogel doped with Ir(III) complex.....</b>	<b>48</b>
<b>Table 1.</b> $^{29}\text{Si}$ NMR Parameters, chemical shift ( $^{29}\text{Si}-\delta$ ) and percentage area (I), obtained from deconvolutions of the spectra in Figure 4.....	<b>58</b>
<b>Table 2.</b> $^{13}\text{C}$ and $^1\text{H}$ chemical shifts for the various species identified in this work. Numbers 1-6 are related to the carbon labeling of the GPTS moiety, given in Figure 5. Letters a-f are related with the various products of the GPTS epoxy ring opening reaction (see Figure S4 in Supporting Information). Proton chemical shifts correspond to the correlations observed in $^1\text{H}\{^{29}\text{Si}\}$ and $^1\text{H}\{^{13}\text{C}\}$ HETCOR spectra.....	<b>60</b>
<b>Table 3.</b> Photophysical parameters of investigated samples at 298 K.....	<b>66</b>
<b>4. Photophysical properties of Ir(III) complexes immobilized in MCM-41 via templated synthesis.....</b>	<b>74</b>
<b>Table 1.</b> Emission properties of $[\text{Ir}(\text{C}^{\wedge}\text{N})_2(\text{dnbp})]^+$ complexes in degassed methanol at 298 K.....	<b>78</b>
<b>Table 2.</b> Mesopore parameters of the developed complex@MCM-41 nanoparticles (calcined at 500 °C).....	<b>83</b>
<b>Table 3.</b> Photophysical parameters of $[\text{Ir}(\text{C}^{\wedge}\text{N})_2(\text{dnbp})]^+$ complexes encapsulated in MCM-41 nanoparticles at 298 K.....	<b>85</b>
<b>5. Mesoporous silica nanoparticles incorporated with Ir(III) complexes: From photophysics to photodynamic therapy.....</b>	<b>98</b>

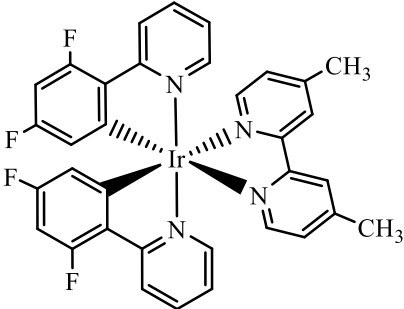
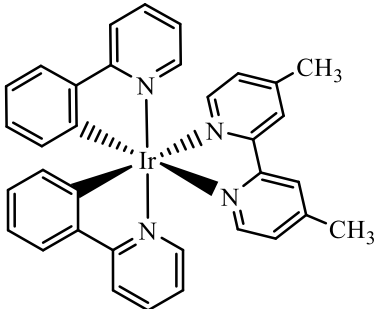
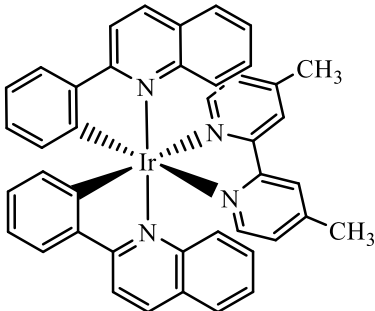
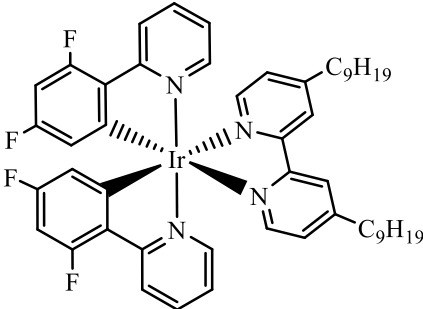


<b>Table 1.</b> Photophysical parameters of Ir(III) complexes in aqueous solution ( $\sim 10^{-5}$ mol mL <sup>-1</sup> ) at 298 K.....	103
<b>Table 2.</b> Photophysical parameters of the nanoparticles incorporated with Ir(III) complexes dispersed in H <sub>2</sub> O at 298 K.....	107
<b>Table 3.</b> Encapsulation yield of Ir complexes inside MCM41-COOH.....	113

## LIST OF LIGANDS

Ligand	Abbreviation	Structure
4,4'-dimethyl-2,2'-bipyridine	dmb	
4,4'-dinonyl-2,2'-bipyridine	dnbp	
2-(2,4-difluorophenyl)pyridine	Fppy	
2-phenylquinoline	pqi	
2-phenylpyridine	ppy	

## LIST OF COMPLEXES

Complex	Abbreviation	Structure
$[\text{Ir}(\text{Fppy})_2(\text{dmb})]^+$	FIrDmb	
$[\text{Ir}(\text{ppy})_2(\text{dmb})]^+$	HIrDmb	
$[\text{Ir}(\text{pqi})_2(\text{dmb})]^+$	pqiIrDmb	
$[\text{Ir}(\text{Fppy})_2(\text{dnbp})]^+$	FIrDnbp	

Complex	Abbreviation	Structure
$[\text{Ir}(\text{ppy})_2(\text{dnbp})]^+$	HIrDnbp	
$[\text{Ir}(\text{pqi})_2(\text{dnbp})]^+$	pqiIrDnbp	

## CONTENTS

<b>1. Introduction.....</b>	<b>21</b>
1.1.General introduction.....	21
1.2.Sol-gel processing of materials.....	23
1.3.Photophysics of coordination compounds.....	32
1.4.Outline of the thesis.....	39
References.....	41
<b>2. Objectives.....</b>	<b>47</b>
<b>3. Structural and photophysical characterization of highly luminescent organosilicate xerogel doped with Ir(III) complex.....</b>	<b>48</b>
<b>4. Photophysical properties of Ir(III) complexes immobilized in MCM-41 via templated synthesis.....</b>	<b>74</b>
<b>5. Mesoporous silica nanoparticles incorporated with Ir(III) complexes: From photophysics to photodynamic therapy.....</b>	<b>98</b>
<b>6. Conclusions.....</b>	<b>119</b>
<b>Appendix.....</b>	<b>121</b>
Supporting information of: Structural and photophysical characterization of highly luminescent organosilicate xerogel doped with Ir(III) complex.....	121
Supporting information of: Photophysical properties of Ir(III) complexes immobilized in MCM-41 via templated synthesis.....	124
Supporting information of: Mesoporous silica nanoparticles incorporated with Ir(III) complexes: From photophysics to photodynamic therapy.....	139

## 1. Introduction

### 1.1. General introduction

Photoluminescence is a fascinating phenomenon that has a huge impact on our daily life. Many important applications are based on this principle, such as diagnostic imaging, bioanalytics, photocatalysis, solar conversion in photovoltaics, and optoelectronics [1–5]. The emerging demands for versatile and more efficient photoluminescent materials have encouraged generations of scientists to develop different types of luminophores, and the difficulties involved in this process have led to the development of numerous supramolecular architectures. Among them, we can highlight the host-guest systems that constitute the study focus of this thesis.

Host-guest materials can be defined as systems composed of two or more chemical species that preserve their structural relationships when held together [6]. Generally, “hosts” are larger assemblies of molecules that are able to accommodate smaller species as “guests”. The interactions between them result in new supramolecular architectures, usually with optical, luminescent, electrical, and catalytic properties superior to or inexistent in their individual counterparts. One issue of particular interest in this area, for example, is the possibility of embedding luminescent species into normally non-emissive materials, leading to new optical systems that preserve both the guest’s photophysical characteristics and the host’s mechanical, thermal and morphological properties. The resulting materials present better processability than the individual luminescent component, hence becoming interesting not only at the fundamental level, but also for different practical applications. In this regard, understanding the relationship between the structure and the properties of both components, as well as the nature of the interface between them, allows more efficient photoluminescent systems to be designed [7].

Considering the key role of the photophysics properties of transition metal complexes (TMCs) in many technological and biological applications, the incorporation of such complexes as guests into solid host matrices presents a formidable challenge to the materials scientists. This class of compounds is distinct from pure organic luminophores due to their characteristic long emission lifetime ( $\tau$ ), significant absorption–emission Stokes shift, and strategic excited states properties that can be modulated by the appropriate choice of the metal ion and ligands. Indeed, as a consequence of the strong spin-orbit coupling (SOC) exerted by the heavy metal atom, intersystem crossing (ISC) processes lead to the population of energetically low-lying otherwise forbidden triplet excited states and, therefore, beyond the fluorescence transition ( $S_1 \rightarrow S_0$ ), radiative decay from the excited triplet state ( $T_1 \rightarrow S_0$ , phosphorescence) is also

allowed [8]. Despite the formally spin-forbidden nature of the triplet emission, its combination with the allowed singlet emission can lead to quantum yields of up to 100%. For these reasons, these complexes make up one of the most versatile and promising classes of phosphorescent emitters in recent decades and have attracted considerable attention for applications in light-emitting devices and panels [2,9–11], in photo-oxidation, photodynamic therapy [12–15], in addition to photocatalysts for hydrogen and oxygen generation [16–18], and in chemical and biological sensors [19–22].

In particular, these applications have focused on a few crucial 2<sup>nd</sup> and 3<sup>rd</sup> row transition metals, especially those of Iridium. Ir(III) complexes exhibit a range of desirable electronic properties, which are unique in terms of reactivity, photochemistry, photophysics, and redox behavior [11,23]. Generally, they exhibit intense emission arising from a metal-to-ligand charge transfer (MLCT) excited state, in an adjustable color range (from blue to red). In the particular case of Ir(III) complexes, their high SOC constant stands out (the highest among transition elements), which allows these compounds to be one of the most efficient class of phosphorescent emitters, exhibiting high quantum emission yields (up to ~ 100%) and relatively low excited state lifetimes (usually hundreds of nanoseconds) which are desirable characteristics for luminescent devices [11,24,25]. Although these luminescent centers have extremely attractive optical properties, their excited state properties are significantly affected by the environment, including vibronic coupling with solvent molecules, as well as the presence of <sup>3</sup>O<sub>2</sub> and other dynamic or static quenchers, making them often unsuitable for direct applications in luminescent devices. Furthermore, when it comes to bioanalytical applications, the intrinsic high cytotoxicity exhibited by most Ir(III) complexes can reduce their range of application as this could adversely affect cellular viability [22,26]. Therefore, the host-guest approach has been a widely used strategy to simultaneously minimize such interactions and enhance their luminescence properties, as besides protecting them from external influences, the rigid environment can suppress roto-vibration-mediated non-radiative deactivation pathways [27].

In the search for appropriate hosts for highly luminescent organometallic emitters, a variety of matrices has been explored such as conjugated polymer nanoparticles, nanoclays, silica-based materials, metal-organic frameworks (MOFs), among many others [6,22,25,27–30]. Within this list, luminescent silica-based materials have been widely studied over the last decade. The chemical inertness, and optical transparency in the UV-VIS region of silica make it an excellent substrate for the incorporation of coordination chromophores. In addition, the materials can be easily processed as particles, films, or monoliths, in the form of amorphous or

crystalline, bulky and porous samples, usually based on sol–gel reactions [7]. In the sol-gel process, liquid precursors such as silicon alkoxides are mixed and transformed into silica via hydrolytic polycondensation reactions. The flexible solution chemistry and the ability to prepare solid matrices with no need for heating means that sol-gel is compatible with organic and thermally sensitive doping agents, giving rise to hybrid materials in which the host–guest interaction can be tailored.

Traditionally, the most common approaches for incorporating molecular species into silica hosts consist of: i) non-covalent uptake, mainly by impregnation of the solid host with a solution containing the guest molecule; ii) covalent grafting, towards functionalization and chemical reaction between the guest and the silicate precursors, and iii) the templated synthesis of the solid material in the presence of the guest chromophore [6,31,32]. The potential of these approaches relies on exploiting the synergy between the intrinsic characteristics of sol–gel derived hosts (highly controlled purity, versatile shaping and patterning, excellent optical quality, encapsulation of large amounts of isolated emitting centers protected by the host) and the luminescence features of the complexes. Promising applications may be envisioned, such as in light-emitting devices, active coatings, and bio-medical actuators and sensors, opening up exciting directions in materials science and related technologies.

For over ten years, the development of modern host-guest materials based on the loading of luminescent guest complexes into versatile, inorganic or hybrid host matrices has been a major part of the research agenda of the Laboratory of Spectroscopy of Functional Materials (LEMAF) at the University of São Paulo in Brazil. Our group has been working on the design, synthesis, characterization, and structure-property correlations of such materials by association of photoluminescence, NMR and EPR spectroscopies. The systems explored so far are sol-gel derived mesoporous silicates, alumino- and organosilicates, as well as the nanoclays laponite and bentonite, loaded with Eu(III)-, Cu(I)- and Ir(III)-complexes, Rh6G dye, CdTe quantum dots, and photosensitizers as phthalocyanines. Pursuing our interest in the preparation of these promising materials, this work reports an exploratory research on the photophysical properties of different cationic emissive Ir(III) complexes and the design of their applications by introducing them into different solid host matrices prepared by sol-gel process. In the sequence, general concepts that support the understanding of the work are presented.

## **1.2. Sol-gel processing of materials**

In a strict sense, the sol–gel methodology allows the synthesis of an oxide network via inorganic polymerization from salts or alkoxides of the desired metal/non-metal in solution



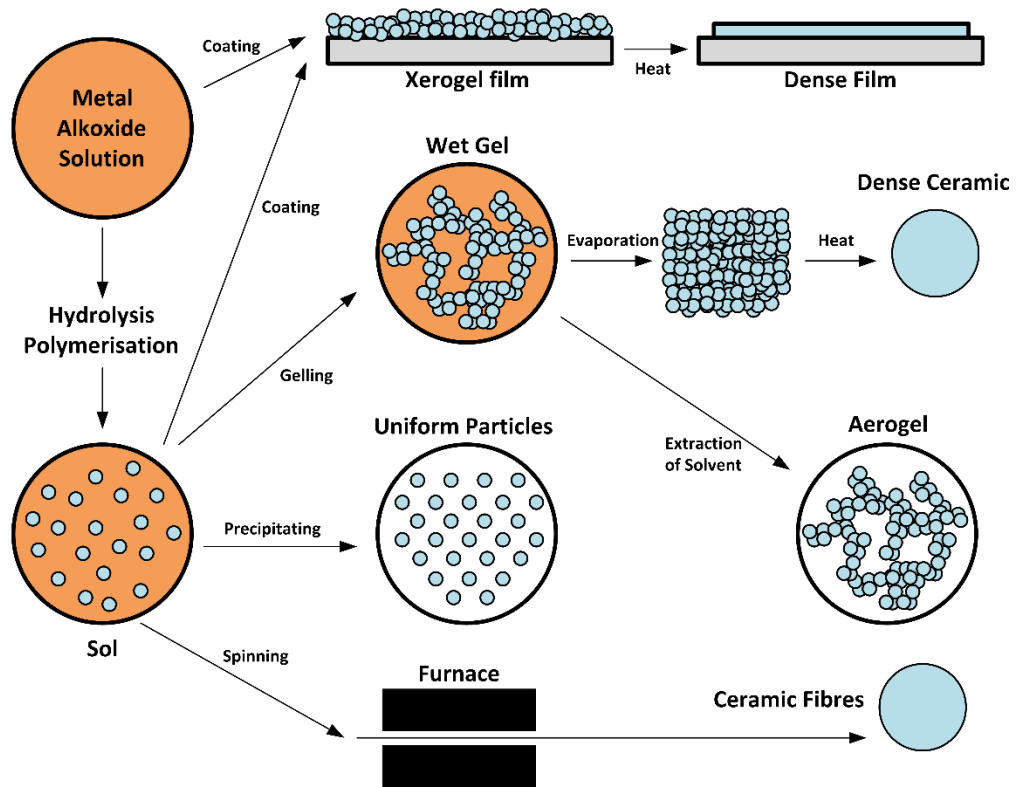
[33–36]. This term is also often extended to refer to the preparation of inorganic oxides through “wet chemistry”. By creating reactive M-OH groups, which are able to form M-O-M bonds, the molecular precursor in solution transforms into a colloidal suspension called sol (“solids on liquids”). Initially, the produced oxide particles have colloidal dimensions between 1 and 100 nm and over time they begin to aggregate or interconnect, giving rise to a rigid network. This process, known as gelation, gives rise to the “gel”, which defines a rigid structure of colloidal particles (colloidal gel) or polymeric chains (polymeric gel) that immobilizes the liquid phase in its interstices [37].

For many applications the residual liquid is removed, and depending on the strategy chosen the gel can be converted into: i) xerogel (from the Greek xero = dry), when drying takes place by evaporating the liquid phase at ambient pressure; ii) aerogel (from the Greek aero = air), obtained by supercritical extraction of the liquid phase or drying at ambient pressure after treatment with a surface modifying agent; iii) cryogel (from the Greek cryo = cold), when the liquid phase of the gel is frozen and extracted by vacuum sublimation [38].

The versatility of processing after the formation of the sol allows the preparation of materials with different morphologies. Figure 1 presents a scheme of some products obtained via the sol-gel process. Through this methodology, ultra-fine and uniform ceramic powders can be formed by the precipitation of the sol. Thin films can be produced by the spin-coating or dip-coating techniques. When the sol is cast onto a mold, a wet gel will form. By drying and heat treatment, the gel is converted into dense ceramic or glass materials. If the liquid in the wet gel is removed, a highly porous and low-density material is obtained. In addition, if the viscosity of a sol is adjusted into a suitable viscosity range, ceramic fibers can also be drawn.

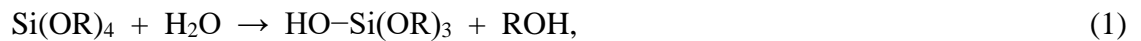
The sol may be produced from various organic or inorganic precursors in non-aqueous or aqueous solutions, but the most widely used precursors are metal alkoxides of formula  $M(OR)_n$ , where  $M = Al, Sn, Ce, Ti, Hf, Zr, Si$ , etc., and  $R$  is an alkyl group. Among the various compositions explored in sol-gel synthesis, silicon-containing materials are certainly the most studied systems, in which the employment of alkoxysilanes plays an important role. Since in this work the sol-gel methodology was employed for the synthesis of amorphous silica, we will focus on the synthesis procedure of this class of materials.

**Figure 1.** Preparation scheme of some products obtained by the sol-gel process [39].



### *The sol-gel process of silicon alkoxides*

The sol-gel process involving silicon alkoxides can be described in three reaction steps. The first is called hydrolysis, where the hydroxyl radical of the water bonds directly to the metal. Depending on the amount of water, the catalyst, the temperature, the form of homogenization, the pH of the solution, among other factors, the hydrolysis reaction can occur until it is fully completed. The reaction below shows only one silicon metal alkoxide radical being hydrolyzed.



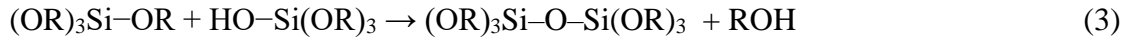
where R represents the alkyl radical, and ROH represents the alcohol (Methanol, Ethanol, Propanol, and others).

The hydrolysis reaction is complete when all OR groups are replaced by OH, as follows:

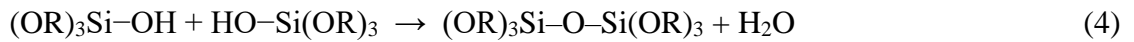


Two other reactions occur with the appearance of hydrolyzed molecules, which can trigger two condensation processes involving the silanol groups (Si–OH) with the production of siloxane (Si–O–Si) and the release of water or alcohol.

Condensation reaction with alcohol production:

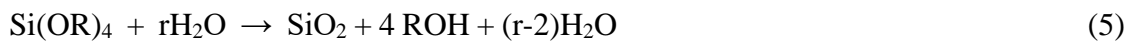


Condensation reaction with water production:



The release of water in the condensation reaction allows the hydrolysis process to continue, so an initial molar ratio  $r = [\text{H}_2\text{O}]/[\text{Si}] = 2$  would theoretically be sufficient to complete the overall hydrolysis and polycondensation reaction (equation 5), yielding as end products only silica and alcohol. However, even with excess water ( $r > 2$ ) the hydrolysis and polycondensation reactions may not be completed, mainly due to the steric effects and the reverse reactions that would be restoring the Si–OR bonds of the alkoxides [33,40].

Global reaction of hydrolysis and polycondensation:



As silicon alkoxides have low reactivity, acidic or basic catalysts are added to the process to increase the reaction rate. The catalysts have a major impact on the final structure of the derived network. For example, under acid catalysis conditions, condensation occurs preferentially between silanol groups located in monomers or at the end of polymer chains. This leads to the formation of gels composed of interlaced linear polymeric chains, which, after drying, form a dense matrix with low pore volume and transparent. Under basic conditions on the other hand, the condensation occurs preferentially between highly branched oligomers, which leads to the formation of particulate gels that, after drying, produce materials with high porosity and an opaque appearance [33,40,41].

#### *Organically Modified Silicates (ORMOSILs)*

Sol-gel synthesis also allows the combination of organic and inorganic components in a single matrix, leading to Organic-Inorganic Hybrid Materials, commonly called OIHM. These

materials are homogeneous, due to the mixture of components at the molecular level and combine the thermal and chemical stability of ceramic materials with the processability and flexibility of organic compounds and polymers. In general, the desired characteristics are not found in a single constituent and the proper combination of the components leads to the formation of multifunctional materials that have complementary properties.

Due to the central role played by the hybrid interface, its nature has been used to categorize these materials into two distinct classes [42]. While in Class I materials, organic and inorganic components additively exchange weak bonds (hydrogen, Van der Waals, or electrostatic bonds), in Class II the two phases are totally or partly linked together through strong chemical bonds (covalent or ionic-covalent bonds).

When silicon oxide is responsible for the inorganic contribution, the material is called ORMOSIL (Organically Modified Silicate). In ORMOSILs, it is also possible to incorporate metallic ions, organic dyes, quantum dots or even coordination compounds, making them excellent inert, hydrophobic or hydrophilic matrices with linear or non-linear optical properties, high transparency, and high mechanical resistance, which are easily prepared as nanoparticles, coating, fibers, or bulk solids, depending on the desired technological application.

In the ORMOSILs picture based mainly in the silica as inorganic phase, we can distinguish three types after the classification of Mackenzie [43]:

- Type A (entrapped organics): In general, the organic species, initially mixed in the sol-gel solution, is retained in the matrix after condensation of the silicate network. There is no connection between the organic and inorganic moieties.

- Type B (impregnated organics): In this case, a porous gel has its pores impregnated with the organic species of interest. The connection between the organic and inorganic parts is made through secondary bonds, which avoid phase separation.

- Type C (chemically bonded organics-inorganics): The organic and inorganic phases of the material are chemically linked by covalent bonds. The stronger nature of this bond improves the mechanical properties of these hybrids. In this case, the inorganic precursor contains a chemically bonded organic group via a non-hydrolyzable covalent Si–C bond [44].

Although initially the term ORMOSIL was referred to types A, B and C, nowadays it is commonly used only for the C type. In these materials, tetraethoxysilane (TEOS) is the most frequently used silica monomer due to its property of easily converting into silicon dioxide at low temperatures. However, owing to the fast reaction rate and severe shrinkage during the drying process, the gels invariably fracture because of their brittle nature [43]. Therefore, it is generally difficult to obtain flexible and crack-free bulks, consequently resulting in materials

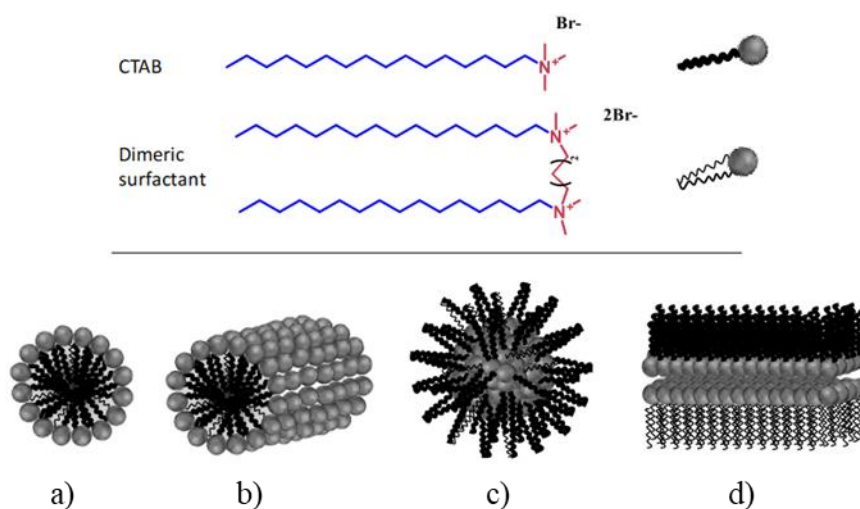
with poor optical properties [45,46]. Processing hybrid monomer(s) into a three-dimensional, crosslinked structure leads to a material in which the silica domains are strictly interconnected with the polymeric network [47]. The bulky organic compounds incorporated in glasses fill the pores between the inorganic oxide chains causing higher mobility during gelation and weaker contraction during drying [45,46]. This creates an opportunity to obtain monolithic materials with modulated properties such as thermal and chemical stability, refractive index, optical transparency, and toughness. It is also possible to tune the wettability of the final material by a judicious choice of the ratio of hydrophilic to hydrophobic sol-gel precursor monomers [44].

Lastly, ORMOSILs types A, B, and C can further be mixed. Together, they offer a very wide spectrum of chemistry, structures, and applications. They constitute a new family of exciting materials with new scientific challenges and technical possibilities.

#### *Engineering the porosity and surface chemistry of silica-based materials*

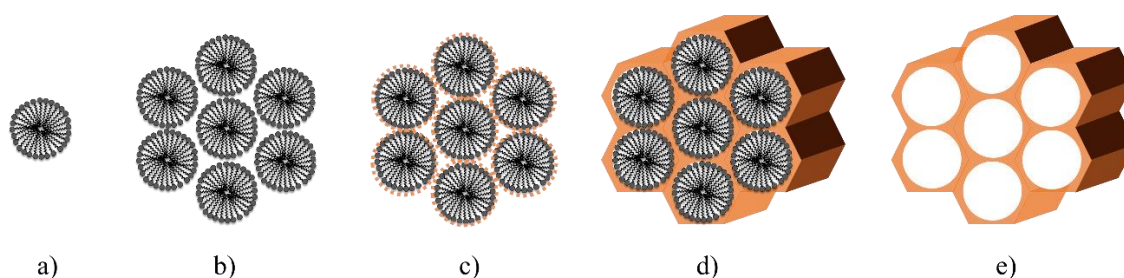
When the interests are focused on obtaining ordered mesoporous silica nanoparticles (MSNs), the role of surfactants is crucial [48]. These surfactants are amphiphilic molecules, generally formed by a hydrophilic head (charged group, such as a quaternary amine for example) and a hydrophobic tail (alkyl chain). Depending on their nature, concentration, temperature, and the polarity of the water-based solvent in which the molecules are dispersed, the surfactant molecules assemble, as to stabilize their hydrophobic tails, in the form of micelles with different geometries (Figure 2), giving rise to supramolecular structures.

**Figure 2.** (Upper part) Examples of surfactants. (Lower part) Schematic representation of micellar aggregates of a surfactant: a) spherical; b) cylindrical; c) reverse; d) laminar micelles [48].



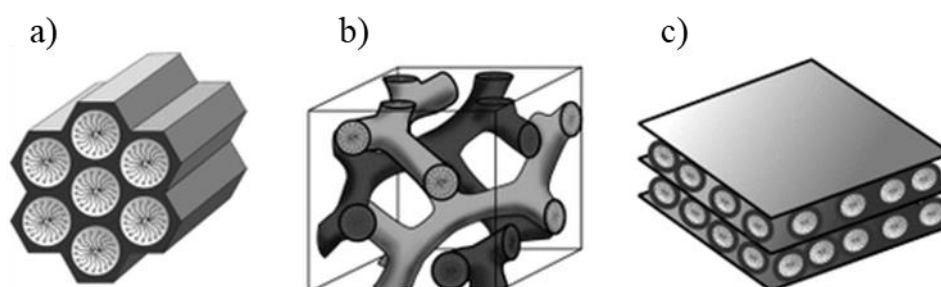
When incorporated into the sol-gel reaction medium, these molecules are able to act as structure-directing agents (SDAs) around which the silica precursors can condense (Figure 3). The mesoporous materials are obtained by subsequent removal of the surfactant molecules, usually by calcination of the solid or by its extraction with different solvents.

**Figure 3.** Schematic model of the templating mechanism in the formation of MSNs: a) micelle formation; b) organization of the micelles into aggregates; c) TEOS addition and hydrolysis and condensation reactions; d) silica growth around the surfactant template; e) surfactant removal (i.e. calcination or extraction) [48].



Among all the types of MSNs reported in the literature, the family of periodic mesoporous ones known as M41S can be regarded as one of the most studied. The term M41S is used to generalize the various types of MCM (Mobil Composition of Matter) synthesized under basic conditions in the presence of the silica source and alkylammonium surfactants, mainly the cetyltrimethylammonium bromide (CTAB) [49]. The most well-known representatives of this class include the solids MCM-41 (with a hexagonal arrangement of the mesopores, space group  $P6mm$ ), MCM-48 (with a cubic arrangement of the mesopores, space group  $Ia3d$ ), and MCM-50 (with a lamellar structure, space group  $P2$ ) (Figure 4) [50].

**Figure 4.** Structures of mesoporous M41S materials: a) MCM-41 (2D hexagonal), b) MCM-48 (cubic), and c) MCM-50 (lamellar) [50].



The MCM-41 is the most popular of the M41S materials because the other members of this family are thermally unstable or difficult to obtain [51,52]. In particular, MCM-41 have found uses in a variety of applications such as adsorption, chromatography, catalysis, chemical sensors, and drug delivery systems in the biomedical field owing to the unique mesoporous structure with channel-like pores packed in a hexagonal fashion, usually presenting very large surface areas ( $800\text{--}1400\text{ m}^2\text{ g}^{-1}$ ), with pore diameters around 20 to 50 Å [51]. Introducing organic groups in the readily accessible pores of MCM-41 provide a way of manipulating the chemical and physical properties of these materials, without compromising the basic geometry and mechanical strength. In this regard, silica is a good matrix material due to its flexible chemistry, which allows surface modification with different types of functional groups.

The most popular way of covalently functionalizing is by grafting the nanoparticles post synthesis with organotrialkoxysilanes. This reaction is performed on surfactant-removed MSN in nonpolar anhydrous solvents to avoid a reaction of the organosilanes with anything but the silica material [53]. In this process, silanol groups (Si-OH) at the surface act as anchoring points when treated with a functionalized siloxane bearing the desired group. Covalent bonds with amino, epoxy, isocyanate or thiol groups are most often formed when matrix is obtained with (3-aminopropyl)triethoxysilane (APTS), (3-glycidyloxypropyl)trimethoxysilane (GPTS), 3-isocyanatopropyltriethoxysilane (ICPTS) or (3-mercaptopropyl)trimethoxysilane (MPTS). Importantly, the original structure of the mesoporous support is maintained after grafting [54].

Alternatively, mesoporous silica nanoparticles can also be functionalized following the so-called co-condensation method. This functionalization method is fundamentally based on the sol-gel process, in which the simultaneous condensation of corresponding silica and organosilica precursors takes place in the presence of structure-directing agents, leading to materials with organic residues anchored covalently to the pore walls and incorporated directly into the mesoporous silica framework [50,54].

Each of these approaches has unique advantages and drawbacks. For example, the stability of MCM-41 prepared by the co-condensation method can be affected by the presence of structural defects in the silicate matrix, originating from the organosilane inside the walls of the nanoparticle. This limits the concentration of functional groups on the surface, as the higher their concentration in the sol-gel reaction media, the more unstable the structure becomes [52]. On the other hand, the final structure of the nanoparticles functionalized through the post-synthetic method remains orderly and the resulting material has high hydrothermal stability where functional groups can be chosen according to predetermined goals. Although this method

often results in an uneven distribution of these groups, depending on the synthesis conditions, it has been considered the most promising route [51].

#### *Luminescent guest species in sol-gel host matrices*

As described in the previous sections, the flexible solution chemistry, and the ability to prepare solid matrices with no heating means that sol-gel is compatible with thermally sensitive doping agents. One issue of particular interest is the possibility of using sol-gel procedures for trapping into solid materials photoactive molecules that display interesting (luminescent) properties when in solution. Once entrapped in the host matrix, the resulting compounds expand the range of physical and chemical properties that define their practical value, hence rendering them suitable for a wide spectrum of applications.

Traditionally, molecular species are incorporated into silica hosts by means of doping or adsorption or grafting onto the pre-formed silica network, which are also performed *in-situ* or by post-synthesis treatments [31]. *In-situ* doping is the most straightforward method, as it basically consists of introducing the active species into the sol-gel reaction medium. After the gelation, the guest species becomes entrapped within the solid host matrix, which is responsible for promoting molecular dispersion and imparting further functionalities on the final material. This process has been widely used for the preparation of hybrid monolithic materials with high mass doping of different chromophores, but it can also be modified for the preparation of films [55]. These host-guest materials have emerged as one of the best alternatives for organic light emitting diodes (OLEDs), high performance optical limiting materials, active waveguides, and solid-state dye lasers [47,56–58]. An alternative *in-situ* approach involves the co-condensation of properly functionalized luminescent compounds with terminal trialkoxysilane groups and the silica precursor (TEOS) during the sol-gel process. Thus, in the final material, the dye derivative is not only homogeneously incorporated into the silica network, but also becomes part of its structure. Despite being a very interesting approach, it requires sufficient chemical groups towards functionalization and chemical reaction between the emitter center and the silicate precursors. This concept might enhance considerably the difficulty of the compound preparation.

As for the development of MCM-41 nanoparticles, a promising approach for *in situ* encapsulation consists in the co-assembly of CTAB micelles with a luminescent guest in a simple procedure that can lead to high levels of guest emitters within the silica mesopores [25,59,60]. Remarkably, the O<sub>2</sub>'s diffusion inside the mesopores is hampered, substantially preventing emission quenching processes in the case of triplet emitters, for example. These



results demonstrate the feasibility of incorporating complexes in silica for the development of more stable light-emitting devices, even in O<sub>2</sub>-rich environments [25]. However, such systems cannot be used in bioanalytical applications, since CTAB remains inside the pores and is cytotoxic in the cellular environment.

Otherwise, post-synthesis treatments are realized in solution by wet impregnation or grafting the active species onto pre-functionalized mesoporous silica networks, after surfactant has been removed [30–32,61]. In general, luminescent species are introduced inside the pore structure of MCM-41 by its passive diffusion into the mesoporous channels and physical entrapment through van der Waals interaction,  $\pi$ -stacking, electrostatic attractions, or hydrogen bonding. Covalent binding is an interesting alternative when leaching problems must be completely excluded, although it requires more laborious chemical processing steps. In this approach, the internal surface of the mesopores is grafted and functionalized with a coordinating ligand and the emissive complex of interest can be assembled inside the pores in a stepwise reaction known as “ship-in-a-bottle” [6,30]. In summary, the wet impregnation approach has been widely employed for the development of O<sub>2</sub>-sensitive optical MCM-41 materials, and the immobilization of photosensitizers for applications in photodynamic therapy (PDT) due its high in vivo biocompatibility.

### **1.3. Photophysics of coordination compounds**

The photophysics of luminescent molecular systems represents one of the main current topics in molecular physical chemistry. Knowledge of the properties of excited electronic states has allowed the development of technological areas of vital importance, such as renewable energies, medicine, fluorescent sensors, among many others.

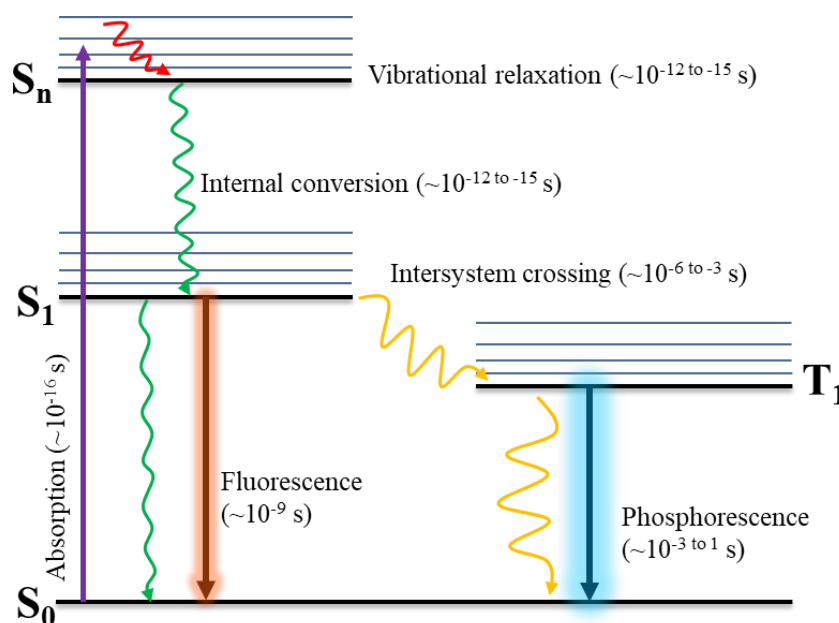
Transition metal complexes, which are the most common coordination compounds, has an electronic structure in which ligands and metals can contribute to the formation of occupied and unoccupied states. Various processes, radiative or non-radiative, can lead to electron transitions. The following discussion summarizes some of these processes.

#### *General molecular photophysics upon excitation*

The photophysical process begins with the absorption of a photon by the molecule and results in the transition of an electron from the ground state to an excited state of the same multiplicity. From this more energetic excited state, the electron can return to a less energetic excited state or to the ground state, dissipating the energy acquired in the absorption through different pathways.

The processes that occur between the absorption and emission of light are generally illustrated by the Jablonski diagram, represented in Figure 5 for species with a singlet ground state ( $S_0$ ). In the diagram exemplified in the figure, the states described by the letter “S” are singlet states, in which the electrons have anti-parallel spins, and those described by the letter “T” are triplets, in which the electrons have parallel spins. Transitions between states are represented as vertical lines to illustrate the instantaneous nature of light [62].

**Figure 5.** Jablonski-Perrin diagram illustrating photophysical processes [62].



In general, the electron rapidly decays to the lower-energy vibrational state of the excited electronic state it occupies, this process being known as vibrational relaxation. Nonradiative relaxations to lower energy electronic states with the same multiplicity are known as internal conversion (IC). Another possibility of non-radiative decay occurs between excited states with different multiplicities, called intersystem crossings (ISC), for example from the singlet state  $S_1$  to the triplet state  $T_1$ . As this requires a change in spin multiplicity, this process is forbidden in traditional organic compounds, but it can occur when heavy atoms are part of the molecular structure, such as in compounds of second and third transition metal series. These elements generally have a strong spin-orbit coupling (SOC) that relaxes the selection rules for singlet-triplet and triplet-singlet transitions.

The return of the molecule to the ground state can occur radiatively or not, through transitions in which there can also be changes in spin orientation. Radiative processes can be classified as fluorescence or phosphorescence. Fluorescence occurs from the excited state that

has the same spin multiplicity as the ground state; whereas phosphorescence occurs from an excited state of different multiplicity than the ground state and therefore is subject to null or low probability for compounds with low SOC. For heavy metal complexes such as those of iridium, the efficiency of the ISC from singlet to triplet excited states is so high that, in general, no fluorescence is observed from these materials. Owing to the triplet contribution in the excited state, this leads to slower emission and consequently elongates the emission lifetimes.

The rate with which each process occurs is represented by the corresponding rate constants ( $k$ ) for the different deactivation pathways the molecule can take. Depending on the physical and chemical nature of the excited species, the environment, and experimental conditions (temperature, solvent, concentration, and atmosphere), different deactivation pathways such as fluorescence, phosphorescence or non-radiative transitions are favored [62].

#### *Emission quantum yield and lifetime*

Non-radiative decay pathways compete with luminescence, potentially reducing the quantum yield of photoluminescence of the emitting species due to deactivation that occurs by vibrational (thermal) rather than radiative dissipation. The quantum yield, defined as the ratio between the number of photons emitted and the number of photons absorbed, is related to the radiative ( $k_r$ ) and non-radiative ( $k_{nr}$ ) rates by Equation 6 [62]:

$$\phi_0 = \frac{n \text{ emitted photons}}{n \text{ absorbed photons}} = \frac{k_r}{k_r + k_{nr}} \quad (6)$$

The excited electronic state lifetime is the time required for the population to decay to  $1/e$  ( $= 0.3678$ ) of its initial value. The lifetime of the excited states can then be written as the inverse of the sum of the radiative and non-radiative decay rates, as shown in Equation 7:

$$\tau_0 = \frac{1}{k_r + k_{nr}} \quad (7)$$

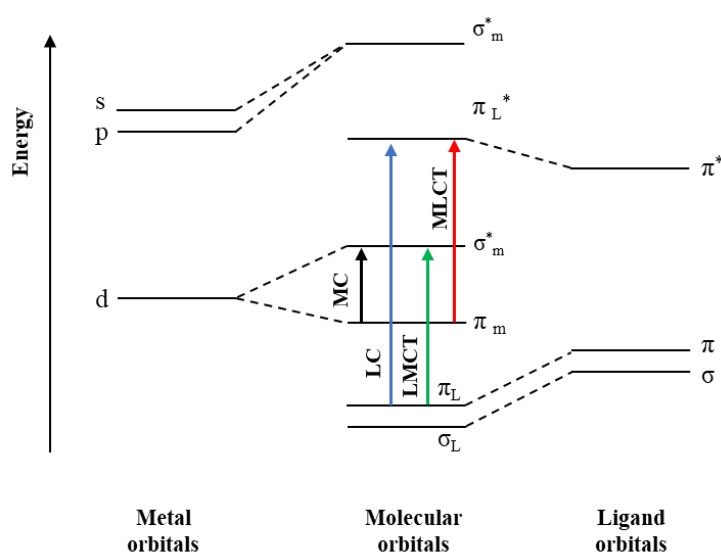
Combining equations 6 and 7, it is possible to obtain a direct relationship between the lifetime of the excited state and the emission quantum yield, as follows:

$$\phi_0 = k_r \tau_0 \quad (8)$$

### Electronic excited states in transition-metal complexes

As far as transition-metal complexes are concerned, the presence of the metal atom induces admixing of the metal  $d$  orbitals with the counterparts located on the conjugated ligands possessing  $\pi$ -character. Therefore, photoexcitation of such compounds can involve diverse electronic transitions that are determined by the nature of molecular orbitals (MOs). In this sense, four main excited states are possible (Figure 6):  $d-d$ ,  $d-\pi^*$ ,  $\pi-\pi^*$ , and  $\pi-d$  [62].

**Figure 6.** Simplified orbital-molecular diagram in a coordination environment. M stands for metal and L stands for ligand [62].



- i)  $d-d$  transition states - these are generated via metal-centered (MC) transitions. This type of excited state arises from transitions in which only the metal filled, and unoccupied  $d$  orbitals participate.
- ii)  $\pi-\pi^*$  transition states - these are generated via ligand-centered (LC) transitions. They are formed as a result of an electron transfer between  $\pi$  bonding or non-bonding orbital and higher anti-bonding  $\pi^*$  orbitals within the ligands. If the orbitals are located in different ligands, the excitation is accompanied by inter-ligand or ligand-to-ligand charge transfer (ILCT or LLCT).
- iii)  $\pi-d$  transition states - these are generated via ligand-to-metal charge transfer (LMCT) transitions. Electrons are excited from a ligand  $\pi$  orbital to an orbital that is primarily metal based.

- iv)  $d-\pi^*$  transition states - these are generated via metal-to-ligand charge transfer (MLCT) transitions. These transitions involve mainly the excitation from a metal centered  $d$  electron to a ligand  $\pi^*$  orbital.

The relative energetic position of the mentioned states is crucial in defining the resulting photophysical properties of organometallic complexes. They can be tuned to a good extent by judicious choice of the ligands system and the central metallic atom.

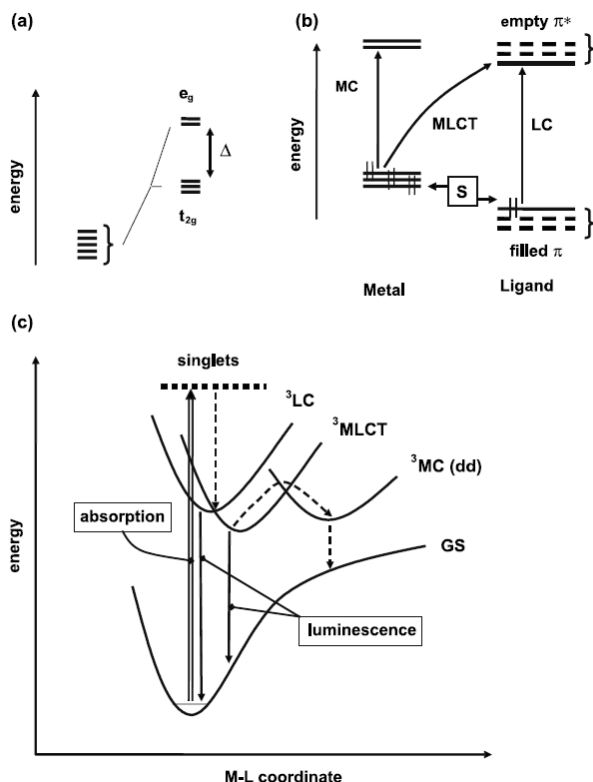
### *Ir(III) complexes*

Out of all classes of luminescent emitters, phosphorescent Ir(III) complexes have attracted particular interest due to a number of advantageous properties such as high photo-, chemical- and thermal stability, potential for unitary phosphorescent quantum yield, relatively short phosphorescent lifetimes, color tuning from the deep-blue to the near-infrared region of the electromagnetic spectrum through ligand structure modification and a large cross-section for exciton formation [14]. For these reasons, new materials based on Ir(III) complexes have attracted considerable attention in many technological applications, ranging from emitting devices, photocatalytic and sensing, to biological labeling agents [63].

Ir(III) is a transition metal with  $5d^6$  configuration and which coordinates with its ligands in a (pseudo-) octahedral symmetry [64]. The electronic properties of their complexes share several characteristics with those of other well-known  $d^6$  octahedral complexes, such as Fe(II), Ru(II), Os(II) and Re(I) [64].

When transition metal ions are inserted into an octahedral ligand field, the  $d$  orbitals unfold into three degenerate  $t_{2g}$  orbitals and two degenerate  $e_g$  orbitals (Figure 7a) and the energy difference between these two levels ( $\Delta$ ) depends on: i) the oxidation state from the metallic center (the higher the oxidation state, the higher  $\Delta$ ); ii) the spatial extent of  $d$  orbitals (it is smaller for  $3d$  metals and progressively increases with  $4d$  and  $5d$  metals); and iii) the field strength exerted by the ligands [11,64]. If the energy  $\Delta$  is large enough, the electron configuration of the metallic center will be of low spin ( $t_{2g}^6e_g^0$ ), as in the case of Ir(III) complexes. Thus, the ground state multiplicity of Ir(III) compounds will always be singlet, as there are no unpaired electrons, while the excited states are singlet or triplet.

**Figure 7.** a) Separation of  $d$  orbitals, in an octahedral ligand field; b) orbital description of the MC, MLCT and LC transitions, where S is a substituent group capable of exerting electron withdrawal or release effects (resulting in the stabilization or destabilization, respectively, of the energy level of the filled  $d$  and  $\pi$  orbitals); c) electronic transitions involving MC, MLCT and LC excited states; MC levels are generally non-emissive [64].

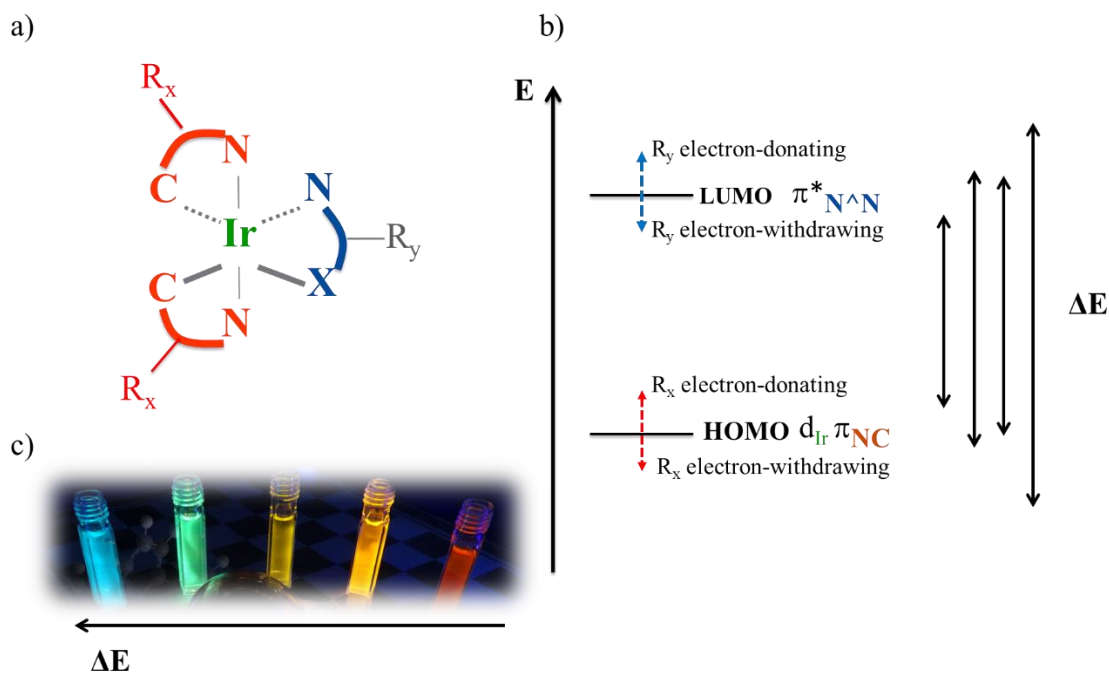


In addition to the already mentioned strong SOC exhibited within Ir(III) complexes (estimated  $\xi_{\text{Ir}} = 4430 \text{ cm}^{-1}$  [65]), the efficient photoluminescence displayed by these complexes is also due to their high ligand-field splitting energy of the  $d$ -orbitals which is increased by the commonly used high field cyclometallating ligands. This approach results in a large energy gap between the  $d$ - $d$  orbitals of cyclometallated Ir(III) complexes, decreasing the rate of non-radiative MC transitions [11,64]. Thus, the emitting state is the lowest-energy triplet ( $T_1$ ), which normally arises from mixed triplet levels, due to the contributions of  $^3\text{MLCT}$  and  $^3\text{LC}$  states, or a mixture between the two (a direct result of SOC responsible for mixing the excited states with similar energies as well as creating new mixed states). The MLCT or LC character will depend on the energy of the ligand's  $\pi/\pi^*$  orbitals. Therefore, a judicious selection and/or design of the cyclometallated ligand can adjust both the identity of the emitting state and the color of the emission [6,11,64].

The adjustment of the color and character of the excited state is achieved through molecular engineering. Emitters in different colors can be obtained, for example, by associating phenylpyridine ligands and their derivatives (which bind to Ir(III) by C and N atoms, hence also called

C<sup>^</sup>N ligands) with bipyridine/phenanthroline ligands and its derivatives (which bind to Ir(III) by two N atoms, therefore also called N<sup>^</sup>N ligands) (Figure 8). The C<sup>^</sup>N ligand, due to its anionic character, has much of the electron density of the highest occupied molecular orbital (HOMO), while the neutral ligand, N<sup>^</sup>N, which has the lower energy antibonding orbital ( $\pi^*$ ), contains the electron density of the lowest unoccupied molecular orbital (LUMO) [64]. To shift the emission to shorter wavelengths (thus emission in the blue), it is necessary to increase the energy gap between the HOMO and the LUMO. This can be accomplished by inserting electron-withdrawing “R” substituent groups into the C<sup>^</sup>N ligands that participate in HOMO. For example, fluorine can be added to these ligands as an electron-withdrawing group, in order to stabilize the HOMO and obtain an emitting complex at higher energies (in the blue). The same effect can be achieved by adding electron-donating “R” groups to the N<sup>^</sup>N ligands that participate in the LUMO. Conversely, electron donating groups on C<sup>^</sup>N ligands or electron withdrawing groups on N<sup>^</sup>N ligands lead to red emission.

**Figure 8.** a) Generic structure of an Ir(III) complex where two bidentate ligands C<sup>^</sup>N coordinate to Ir(III) through N and C atoms, and a third bidentate ligand binds to Ir(III) by N atoms; b) Modulation of the  $\Delta E$  energy between the HOMO and LUMO states through the addition of electron donor and acceptor groups to the N<sup>^</sup>N and C<sup>^</sup>N ligands; c) Example of possible emission colors to be obtained through molecular engineering exemplified in b) [11].



Some photophysical characteristics help to identify the nature of the excited state (whether MLCT or LC), such as: (i) the profile of the phosphorescence spectrum, which is structured in vibronic modes for  $^3\text{LC}$  emissions and widened and unstructured for  $^3\text{MLCT}$  emissions; and (ii) the rigidochromic effect, based on the fact that CT states are shifted to higher energies (blue shift) when their degrees of freedom are restricted in rigid media, while LC levels are not affected. Furthermore, the transition from the ground state to the MLCT excited state, in general, involves a change in the dipole moment of the complex, which makes the absorption and emission bands of this nature sensitive to polarity.

The main phenomena that can negatively affect the quantum yield of emission of these compounds are molecular aggregation and deactivation of the excited state due to interaction with oxygen molecules (via Dexter energy transfer). Both phenomena are due to energy transfer processes and require contact between the luminescent and the suppressor species. For example, the presence of molecular oxygen drastically reduces the lifetime and quantum efficiency of the complexes upon formation of triplet radical species. If, on one hand, this fact constitutes a disadvantage for the application in lighting devices, for instance, the ability to generate different reactive oxygen species (ROS), especially  $^1\text{O}_2$ , allows the use of these complexes as efficient photosensitizers (PSs) in photodynamic therapy and as  $\text{O}_2$  sensors. Therefore, the versatility of Ir(III) complexes combined with their unique properties is what has motivated the development of this project. To disperse the molecules of the complex, different host-guest approaches were used. This strategy aims to attenuate the diffusion of molecular oxygen in the environment of the complex and to control the luminescence self-quenching effects. It was also evaluated whether encapsulation in MCM-41 can prevent  $\text{O}_2$  from reaching the complexes inside the micelles, thus decreasing the suppression effects. Another feature investigated was the possible decrease in the cytotoxicity of the encapsulated complexes for applications in PDT and intracellular theranostic.

#### **1.4. Outline of the thesis**

Based on these premises, this doctorate project was focused on the design, synthesis and characterization, from a structural and photophysical point of view, systems consisting of hybrid host matrices - obtained by the sol-gel methodology, incorporated with Ir(III) complexes of the series  $[\text{Ir}(\text{Xppy})_2(\text{Rbpy})]^+$  (ppy = 2-phenylpyridine, bpy = 2,2'-bipyridine, X = F, H or phenyl, R = methyl or dinonyl) synthesized in collaboration with Dr. K.P.S. Zanoni (former LEMAF postdoc). The results obtained are described in this thesis through a collection of



articles that were published and submitted during the development of the project, which are divided into the following three main parts:

- i. **Synthesis of hybrid organosilicate materials for the production of highly luminescent materials.** The hybrid materials were obtained from the immobilization of the complex  $[\text{Ir}(\text{Fppy})_2(\text{dmb})]^+$  in the GPTS:TEOS host matrix. The study of the photophysical properties of these materials was carried out in solutions, in the sol, and in their final xerogel forms. In addition, a detailed structural study using the solid-state NMR technique was carried out in collaboration with Prof. Marcos de Oliveira Jr. (IFSC/USP). Discussions about the structural and photophysical characterization of the hybrid organic-inorganic matrix doped with Ir(III) complexes resulted in an article in the Journal of Sol-Gel Science and Technology titled “Structural and photophysical characterization of highly luminescent organosilicate xerogel doped with Ir(III) complex.” DOI: 10.1007/s10971-021-05593-z.
- ii. **Preparation of MCM-41-type mesoporous nanoparticles with  $[\text{Ir}(\text{NC})_2(\text{dnbp})]^+$  complexes.** These materials were developed via a simple, one-step preparation route by incorporating the amphiphilic complexes into CTAB micelles. In the MCM-41 materials, the restricted diffusion of  $^3\text{O}_2$  into the mesopores remarkably prevents the Ir(III) complexes’ emission quenching even in pure  $\text{O}_2$  atmosphere. The energy transfer between MCM-41 optical solids is weakened as compared to Ir(III) complexes in solutions, a remarkable characteristic that may be exploited for designing white-light emitting systems. These results were published in collaboration with a former postdoctoral fellow of our group, Dr. Kassio P. S. Zanoni in the journal Inorganic Chemistry, which was titled “Photophysical Properties of Ir(III) Complexes Immobilized in MCM-41 via Templated Synthesis”. DOI: 10.1021/acs.inorgchem.8b03633.
- iii. **Incorporation of Ir(III) complexes in MCM-41 mesoporous materials for applications in photodynamic therapy.** It is also a viable strategy to eliminate the cytotoxicity of Ir(III) complexes and it represents a further advancement in the design of multifunctional nanoplatfoms including imaging, delivery and therapy. These materials have been evaluated via structural characterization, encapsulation efficiency and study of photophysical properties. In addition, cell toxicity tests and photodynamic

studies in cancer cell lines were evaluated in collaboration with postdoctoral student Dr. Bianca Estevão, supervised by Professor Valtencir Zucolotto (GNano-IFSC/USP). A manuscript with the results obtained was published in the scientific journal *Photodiagnosis and Photodynamic Therapy*, titled “Mesoporous silica nanoparticles incorporated with Ir(III) complexes: From photophysics to photodynamic therapy”. DOI: 10.1016/j.pdpdt.2022.103052

## References

- [1] C. Ulbricht, B. Beyer, C. Friebe, A. Winter, U.S. Schubert, Recent developments in the application of phosphorescent Iridium(III) complex systems, *Adv. Mater.* 21 (2009) 4418–4441.
- [2] J.C. Deaton, F.N. Castellano, Archetypal Iridium(III) Compounds for Optoelectronic and Photonic Applications, in: *Iridium(III) Optoelectron. Photonics Appl.*, 2017: pp. 1–69.
- [3] A.M. Ibarra-Ruiz, D.C. Rodríguez Burbano, J.A. Capobianco, Photoluminescent nanoplatforms in biomedical applications, *Adv. Phys. X.* 1 (2016) 194–225.
- [4] E. Baranoff, J.H. Yum, M. Graetzel, M.K. Nazeeruddin, Cyclometallated iridium complexes for conversion of light into electricity and electricity into light, *J. Organomet. Chem.* 694 (2009) 2661–2670.
- [5] L. Wondraczek, E. Tyystjärvi, J. Méndez-Ramos, F.A. Müller, Q. Zhang, Shifting the Sun: Solar Spectral Conversion and Extrinsic Sensitization in Natural and Artificial Photosynthesis, *Adv. Sci.* 2 (2015) 1–13.
- [6] K.P.S. Zanoni, L.P. Ravaro, A.S.S. De Camargo, Host-guest luminescent materials based on highly emissive species loaded into versatile sol-gel hosts, *Dalt. Trans.* 47 (2018) 12813–12826.
- [7] C. Ezquerro, A.E. Sepu, E. Serrano, J.R. Berenguer, E. Lalinde, Organometallic phosphors as building blocks in sol-gel chemistry: luminescent organometallo- silica materials, *J. Mater. Chem. C.* 5 (2017) 9721–9732.
- [8] M. Mauro, A. Aliprandi, D. Septiadi, N.S. Kehr, L. De Cola, When self-assembly meets biology: Luminescent platinum complexes for imaging applications, *Chem. Soc. Rev.* 43 (2014) 4144–4166.
- [9] R.D. Costa, E. Ortí, H.J. Bolink, F. Monti, G. Accorsi, N. Armaroli, Luminescent ionic transition-metal complexes for light-emitting electrochemical cells, *Angew. Chemie - Int. Ed.* 51 (2012) 8178–8211.
- [10] K.P.S. Zanoni, N.Y. Murakami Iha, Sky-blue OLED through PVK:[Ir(Fppy)<sub>2</sub>(Mepic)]

- active layer, *Synth. Met.* 222 (2016) 393–396.
- [11] K.P.S. Zanoni, R.L. Coppo, R.C. Amaral, N.Y. Murakami Iha, Ir(III) complexes designed for light-emitting devices: Beyond the luminescence color array, *Dalt. Trans.* 44 (2015) 14559–14573.
- [12] S.P.Y. Li, C.T.S. Lau, M.W. Louie, Y.W. Lam, S.H. Cheng, K.K.W. Lo, Mitochondria-targeting cyclometalated Iridium(III)-PEG complexes with tunable photodynamic activity, *Biomaterials.* 34 (2013) 7519–7532.
- [13] D.L. Ma, C. Wu, W. Tang, A.R. Gupta, F.W. Lee, G. Li, C.H. Leung, Recent advances in Iridium(III) complex-assisted nanomaterials for biological applications, *J. Mater. Chem. B.* 6 (2018) 537–544.
- [14] Y. You, S.Y. Park, Phosphorescent Iridium(III) complexes: Toward high phosphorescence quantum efficiency through ligand control, *J. Chem. Soc. Dalt. Trans.* 9226 (2008) 1267–1282.
- [15] K.K.-S. Tso, K.K.-W. Lo, Strategic Applications of Luminescent Iridium(III) Complexes as Biomolecular Probes, Cellular Imaging Reagents, and Photodynamic Therapeutics, in: *Iridium(III) Optoelectron. Photonics Appl.*, 2017: pp. 415–477.
- [16] J.J. Concepcion, J.W. Jurss, M.K. Brennaman, P.G. Hoertz, A.O.T. Patrocinio, N.Y. Murakami Iha, J.L. Templeton, T.J. Meyer, Making oxygen with ruthenium complexes, *Acc. Chem. Res.* 42 (2009) 1954–1965.
- [17] J.I. Goldsmith, W.R. Hudson, M.S. Lowry, T.H. Anderson, S. Bernhard, Discovery and high-throughput screening of heteroleptic iridium complexes for photoinduced hydrogen production, *J. Am. Chem. Soc.* 127 (2005) 7502–7510.
- [18] J.H. Alstrum-Acevedo, M.K. Brennaman, T.J. Meyer, Chemical approaches to artificial photosynthesis, *Inorg. Chem.* 44 (2005) 6802–6827.
- [19] K.K.W. Lo, C.K. Chung, N. Zhu, Nucleic acid intercalators and avidin probes derived from luminescent cyclometalated Iridium(III)-dipyridoquinoxaline and -dipyridophenazine complexes, *Chem. - A Eur. J.* 12 (2006) 1500–1512.
- [20] M.E. Köse, B.F. Carroll, K.S. Schanze, Preparation and spectroscopic properties of multiluminophore luminescent oxygen and temperature sensor films, *Langmuir.* 21 (2005) 9121–9129.
- [21] L.H. Fischer, S.M. Borisov, M. Schaeferling, I. Klimant, O.S. Wolfbeis, Dual sensing of pO<sub>2</sub> and temperature using a water-based and sprayable fluorescent paint, *Analyst.* 135 (2010) 1224–1229.
- [22] M.C. Grüner, K.P.S. Zanoni, C.F. Borgognoni, C.C. Melo, V. Zucolotto, A.S.S. De

- Camargo, Reaching Biocompatibility with Nanoclays: Eliminating the Cytotoxicity of Ir(III) Complexes, *ACS Appl. Mater. Interfaces*. 10 (2018) 26830–26834.
- [23] K.P.S. Zanoni, A. Ito, N.Y. Murakami Iha, Molecular-engineered [Ir(Fppy)<sub>2</sub>(Mepic)] towards efficient blue-emission, *New J. Chem.* 39 (2015) 6367–6376.
- [24] K.P.S. Zanoni, A. Ito, M. Grüner, N.Y. Murakami Iha, A.S.S. De Camargo, Photophysical dynamics of the efficient emission and photosensitization of [Ir(Pqi)<sub>2</sub>(NN)]<sup>+</sup> complexes, *Dalt. Trans.* 47 (2018) 1179–1188.
- [25] A.S.S. Zanoni, K. P.S. Vilela, R. R. C., Silva, D. A. I., Murakami Iha, N. Y., Eckert, H., de Camargo, Photophysical Properties of Ir(III) Complexes Immobilized in MCM-41 via Templated Synthesis, *Inorg. Chem.* 28 (2019) 4962–4971.
- [26] F.S.M. Canisares, A.M.G. Mutti, E.F. Santana, V.C. Oliveira, D.G.S.M. Cavalcante, A.E. Job, A.M. Pires, S.A.M. Lima, Red-emitting heteroleptic Iridium(III) complexes: photophysical and cell labeling study, *Photochem. Photobiol. Sci.* 21 (2022) 1077–1090.
- [27] I. Maisuls, C. Wang, M.E. Gutierrez Suburu, S. Wilde, C.G. Daniliuc, D. Brünink, N.L. Doltsinis, S. Ostendorp, G. Wilde, J. Kösters, U. Resch-Genger, C.A. Strassert, Ligand-controlled and nanoconfinement-boosted luminescence employing Pt(II) and Pd(II) complexes: From color-tunable aggregation-enhanced dual emitters towards self-referenced oxygen reporters, *Chem. Sci.* 12 (2021) 3270–3281.
- [28] S.C. Gangadharappa, I.P. Salto, S. Niemann, V. Bachtin, F.C. Herrmann, C.A. Strassert, Intermolecular Interactions and Self-Assembly in Pt(II) Complex–Nanoclay Hybrids as Luminescent Reporters for Spectrally Resolved PLIM, *J. Phys. Chem. C.* (2021) 5739–5747.
- [29] Y. Zhang, H. Fu, S. Chen, B. Liu, W. Sun, H. Gao, Construction of an Iridium(III)-complex-loaded MOF nanoplatfom mediated with a dual-responsive polycationic polymer for photodynamic therapy and cell imaging, *Chem. Commun.* 56 (2020) 762–765.
- [30] M. Ilibi, T.B. De Queiroz, J. Ren, L. De Cola, A.S.S. De Camargo, H. Eckert, Luminescent hybrid materials based on covalent attachment of Eu(III)-tris(bipyridinedicarboxylate) in the mesoporous silica host MCM-41, *Dalt. Trans.* 43 (2014) 8318–8330.
- [31] B. Lebeau, P. Innocenzi, Hybrid materials for optics and photonics, *Chem. Soc. Rev.* 40 (2011) 886–906.
- [32] A. Auger, J. Samuel, O. Poncelet, O. Raccurt, A comparative study of non-covalent encapsulation methods for organic dyes into silica nanoparticles, *Nanoscale Res. Lett.* 6

- (2011) 1–12.
- [33] G.W.S. C. Jeffrey Brinker, *Sol-Gel Science: The Physics and Chemistry of Sol-Gel Processing*, First Edit, Academic Press, Inc., 1990.
- [34] L.C. Klein, *Sol-Gel technology for thin films, fibers, preforms, electronics, and specialty shapes*, First Edit, Noyes Publications, 1988.
- [35] S. Sakka, *Handbook of Sol-Gel Science and Technology- Processing Characterization and Applications*, First Edit, Kluwer Academic Publishers, 2005.
- [36] N.D. La Rosa-Fox, L. Esquivias, M. Piñero, *Handbook of Organic-Inorganic Hybrid Materials and Nanocomposites*, First Edit, American Scientific Publishers, 2003.
- [37] R.S. Hiratsuka, C.V. Santilli, S.H. Pulcinelli, O processo sol-gel: uma visão físico-química - Revisão, *Quim. Nova.* 18 (1995) 171–180.
- [38] C.M. Awano, *Preparação e caracterização de sílicas mesoporosas*, Dissertação (Mestrado), Instituto de Geociências e Ciências Exatas, Universidade Estadual Paulista, 2012.
- [39] P. Innocenzi, Understanding sol–gel transition through a picture. A short tutorial, *J. Sol-Gel Sci. Technol.* 94 (2020) 544–550.
- [40] C.J. Brinker, Hydrolysis and condensation of silicates: Effects on structure, *J. Non. Cryst. Solids.* 100 (1988) 31–50.
- [41] M. Buckley, A. M., & Greenblatt, The Sol-Gel Preparation of Silica Gels, *J. Chem. Educ.* 71 (1994) 599.
- [42] C. Sanchez, P. Belleville, M. Popall, L. Nicole, Applications of advanced hybrid organic–inorganic nanomaterials: from laboratory to market, *Chem. Soc. Rev.* 40 (2011) 696–753.
- [43] J.D. Mackenzie, Structures and properties of ormosils, *J. Sol-Gel Sci. Technol.* 2 (1994) 81–86.
- [44] M. Barczak, C. Mcdonagh, D. Wencel, Micro- and nanostructured sol-gel-based materials for optical chemical sensing (2005 – 2015), *Microchim. Acta.* 183 (2016) 2085–2109.
- [45] D.R. Vollet, L.A. Barreiro, C.M. Awano, D. Vicente, M. Yoshida, D.A. Donatti, Rod-like particles growing in sol–gel processing of 1:1 molar mixtures of 3-glycidoxypropyltrimethoxysilane and tetraethoxysilane research papers, *J. Appl. Crystallogr.* 50 (2017) 489–497.
- [46] C.M. Awano, F.S. De Vicente, D.A. Donatti, D.R. Vollet, Structure and growth kinetics of 3-glycidoxypropyltrimethoxysilane-derived organic/silica hybrids at different

- temperatures, *J. Phys. Chem. C*. 116 (2012) 24274–24280.
- [47] R.R.C. Vilela, K.P.S. Zanoni, M. de Oliveira, F.S. de Vicente, A.S.S. de Camargo, Structural and photophysical characterization of highly luminescent organosilicate xerogel doped with Ir(III) complex, *J. Sol-Gel Sci. Technol.* (2021).
- [48] C.E. Parmo, Diseño y aplicaciones de materiales híbridos fotoactivos, Tesis (Doctoral), Facultad de Ciencia y Tecnología, Universidad de La Rioja, 2019.
- [49] S. ho Hong, Y. Choi, Mesoporous silica-based nanoplatfoms for the delivery of photodynamic therapy agents, *J. Pharm. Investig.* 48 (2018) 3–17.
- [50] F. Hoffmann, M. Cornelius, J. Morell, M. Fröba, Silica-based mesoporous organic-inorganic hybrid materials, *Angew. Chemie - Int. Ed.* 45 (2006) 3216–3251.
- [51] F. Habeche, M. Hachemaoui, A. Mokhtar, K. Chikh, F. Benali, A. Mekki, F. Zaoui, Z. Cherifi, B. Boukoussa, Recent Advances on the Preparation and Catalytic Applications of Metal Complexes Supported-Mesoporous Silica MCM-41 (Review), *J. Inorg. Organomet. Polym. Mater.* 30 (2020) 4245–4268.
- [52] J.A.S. Costa, R.A. de Jesus, D.O. Santos, J.F. Mano, L.P.C. Romão, C.M. Paranhos, Recent progresses in the adsorption of organic, inorganic, and gas compounds by MCM-41-based mesoporous materials, *Microporous Mesoporous Mater.* 291 (2020) 109698.
- [53] B.G. Trewyn, I.I. Slowing, S. Giri, H.T. Chen, V.S.Y. Lin, Synthesis and functionalization of a mesoporous silica nanoparticle based on the sol-gel process and applications in controlled release, *Acc. Chem. Res.* 40 (2007) 846–853.
- [54] G. Martínez-Edo, A. Balmori, I. Pontón, A.M. Del Rio, D. Sánchez-García, Functionalized ordered mesoporous silicas (MCM-41): Synthesis and applications in catalysis, *Catalysts*. 8 (2018).
- [55] F.S. de Vicente, P. Freddi, A.J.G. Otuka, C.R. Mendonça, H.F. Brito, L.A.O. Nunes, D.R. Vollet, D.A. Donatti, Photoluminescence tuning and energy transfer process from Tb<sup>3+</sup> to Eu<sup>3+</sup> in GPTMS/TEOS-derived organic/silica hybrid films, *J. Lumin.* 197 (2018) 370–375.
- [56] L.M.G. Abegão, D.S. Manoel, A.J.G. Otuka, P.H.D. Ferreira, D.R. Vollet, D.A. Donatti, L. De Boni, C.R. Mendona, F.S. De Vicente, J.J. Rodrigues, M.A.R.C. Alencar, Random laser emission from a Rhodamine B-doped GPTS/TEOS-derived organic/silica monolithic xerogel, *Laser Phys. Lett.* 14 (2017) 0–6.
- [57] P.H.D. Ferreira, A.J.G. Otuka, E.C. Barbano, D.S. Manoel, F.S. De Vicente, D.R. Vollet, D.A. Donatti, L. Misoguti, C.R. Mendonça, Femtosecond laser fabrication of waveguides in Rhodamine B-doped GPTS/TEOS-derived organic/silica monolithic

- xerogel, *Opt. Mater. (Amst)*. 47 (2015) 310–314.
- [58] D. Chateau, F. Chaput, C. Lopes, M. Lindgren, C. Brännlund, J.O. Hgren, N. Djourelou, P. Nedelec, C. Desroches, B. Eliasson, T. Kindahl, F. Lerouge, C. Andraud, S. Parola, Silica Hybrid Sol – Gel Materials with Unusually High Concentration of Pt–Organic Molecular Guests: Studies of Luminescence and Nonlinear Absorption of Light, 4 (2012) 2369–2377.
- [59] Y. Atoini, E.A. Prasetyanto, P. Chen, S. Silvestrini, J. Harrowfield, L. De Cola, Luminescence of Amphiphilic Pt<sup>II</sup> Complexes Controlled by Confinement, *Chem. - A Eur. J.* 24 (2018) 12054–12060.
- [60] M. De Barros, J.M. Fernandez-hernandez, B. De Queiroz, H. Eckert, D. Cola, A. Simone, S. De Camargo, Iridium(III)–surfactant complex immobilized in mesoporous silica via templated synthesis: a new route to optical materials, (2011) 8829–8834.
- [61] T.B. De Queiroz, M.B.S. Botelho, M. Ferna, H. Eckert, R.Q. Albuquerque, A.S.S. De Camargo, New Luminescent Host – Guest System Based on an Iridiu (III) Complex: Design , Synthesis , and Theoretical – Experimental Spectroscopic Characterization, 117 (2013) 2966–2975.
- [62] J.R. Lakowicz, Principles of fluorescence spectroscopy, Third Edit, Springer, 2006.
- [63] K. Kalyanasundaram, M. Grätzel, Applications of functionalized transition metal complexes in photonic and optoelectronic devices, *Commun. Chem. Rev.* 177 (1998) 347–414.
- [64] L. Flamigni, A. Barbieri, C. Sabatini, B. Ventura, F. Barigelletti, Photochemistry and Photophysics of Coordination Compounds: Iridium, in: *Top. Curr. Chem.*, 2007: pp. 143–203.
- [65] S.A. Moore, D.L. Davies, M.M. Karim, J.K. Nagle, M.O. Wolf, B.O. Patrick, Photophysical behaviour of cyclometalated Iridium(III) complexes with phosphino(terthiophene) ligands, *Dalt. Trans.* 42 (2013) 12354–12363.

## 2. Objectives

From the above introduction, the general objectives of this project were to present new perspectives for optical applications of luminescent host-guest materials based on coordination compounds, and it took place from the immobilization of Ir(III) complexes in different solid matrices. This initiative has progressed towards the search for emitters in different colors, using the concept of molecular engineering to adjust the photophysical properties and to control molecular interactions with the hosts. From this perspective, the specific objectives of the project were:

- i. Synthesis of different heteroleptic Ir(III) complexes, aiming to obtain emission with high quantum yields and in varied colors.
- ii. Photophysical characterization of the luminescent properties of the synthesized complexes and the suppression of emission by  $^3\text{O}_2$  in solution.
- iii. Preparation of silica-based hybrid materials, via sol-gel process, incorporated with the synthesized Ir(III) complexes, in the form of monoliths and MCM-41 mesoporous particulate materials.
- iv. Photophysical characterization and analysis of luminescence suppression by  $^3\text{O}_2$  of solid-state samples.
- v. Determination of the quantum yield of  $^1\text{O}_2$  production for both, complexes in fluid solutions and encapsulated in MCM-41 nanoparticles.
- vi. Evaluate cell the cytotoxicity of the developed nanoparticles in cellular medium aiming applications in PDT.



### 3. Structural and photophysical characterization of highly luminescent organosilicate xerogel doped with Ir(III) complex

Journal of Sol-Gel Science and Technology (2022) 102:236–248  
<https://doi.org/10.1007/s10971-021-05593-z>

ORIGINAL PAPER: SOL-GEL AND HYBRID MATERIALS FOR OPTICAL,  
 PHOTONIC AND OPTOELECTRONIC APPLICATIONS



## Structural and photophysical characterization of highly luminescent organosilicate xerogel doped with Ir(III) complex

Raquel R. C. Vilela<sup>1</sup> · Kassio P. S. Zanoni<sup>1,2</sup> · Marcos de Oliveira Jr.<sup>1</sup> · Fábio S. de Vicente<sup>3</sup> ·  
 Andrea S. S. de Camargo<sup>1</sup>

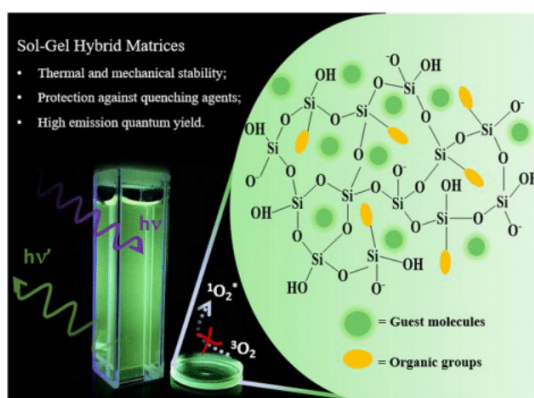
Received: 31 March 2021 / Accepted: 6 July 2021 / Published online: 14 August 2021

© The Author(s), under exclusive licence to Springer Science+Business Media, LLC, part of Springer Nature 2021

#### Abstract

In the search for appropriate host matrices for highly luminescent molecular guest species, an organo-silica monolithic xerogel prepared by the hydrolysis and co-condensation reactions of 3-glycidoxypropyltrimethoxysilane (GPTS) and tetraethylorthosilicate (TEOS) is proposed. Such alkoxides allowed the development of hybrid silica monoliths with a cross-linked three-dimensional structure, in which the silica domains are strictly interconnected with the polymeric network. Highly luminescent monoliths were prepared from the immobilization of a blue-green emissive Ir(III) phosphor in the host matrix, with improved luminescent properties attributed to the greater rigidity of the medium and less diffusion of oxygen within the matrix. The structure of the hybrid material was elucidated by high-resolution solid-state NMR, confirming that the final structure of the developed silica matrix is very similar for both Ir(III)-doped and undoped xerogels. Altogether, the experimental strategy used in this work stands as an advance in the design of photo-functional materials with substantial potential for optical and photonic applications.

#### Graphical Abstract



**Supplementary information** The online version contains supplementary material available at <https://doi.org/10.1007/s10971-021-05593-z>.

- ✉ Raquel R. C. Vilela  
 raquelvilela@usp.br
- ✉ Andrea S. S. de Camargo  
 andreasc@ifsc.usp.br

<sup>2</sup> Instituto de Ciencia Molecular (ICMol), Universidad de Valencia, 46980 Paterna Valencia, Spain

<sup>3</sup> Department of Physics, Institute of Geosciences and Exact Sciences, Sao Paulo State University (UNESP), Rio Claro, SP 13506-900, Brazil

<sup>1</sup> São Carlos Institute of Physics, University of São Paulo, PO Box 369, São Carlos, SP 13560-970, Brazil

## Abstract

In the search for appropriate host matrices for highly luminescent molecular guest species, an organo-silica monolithic xerogel prepared by the hydrolysis and co-condensation reactions of 3-glycidoxypropyltrimethoxysilane (GPTS) and tetraethylorthosilicate (TEOS) is proposed. Such alkoxides allowed the development of hybrid silica monoliths with a cross-linked three-dimensional structure, in which the silica domains are strictly interconnected with the polymeric network. Highly luminescent monoliths were prepared from the immobilization of a blue-green emissive Ir(III) phosphor in the host matrix, with improved luminescent properties attributed to the greater rigidity of the medium and less diffusion of oxygen within the matrix. The structure of the hybrid material was elucidated by high-resolution solid-state NMR, confirming that the final structure of the developed silica matrix is very similar for both Ir(III)-doped and undoped xerogels. Altogether, the experimental strategy used in this work stands as an advance in the design of photo-functional materials with substantial potential for optical and photonic applications.

**Keywords:** Sol-gel; Hybrid host matrices; Host-guest optical materials; Ir(III) complexes; Solid-state NMR; Photophysics.

## Introduction

Silica-based materials prepared by sol-gel process present unique physical and chemical properties, such as high thermal stability, mechanical resistance, low chemical reactivity, and high transparency in the UV-VIS region. This is a multifunctional class of materials that has been extensively employed in many industrial, environmental and biomedical applications [1–4]. By using mixtures of tetralkoxysilane and organically functionalized trialkoxysilane precursors in the sol-gel processing, it is possible to obtain hybrid materials called Organically Modified Silicates (ORMOSILs) [5]. A key advantage of such systems is the combination of the most favorable properties of their individual organic and inorganic components in a single-phase material, which allows overcoming limitations of each individual counterpart [6, 7]. In addition, the sol-gel process starts from a liquid mixture, facilitating the incorporation of doping compounds, such as metal ions, organic dyes, quantum dots and organometallic complexes. After the gelation, the guest species become entrapped within the solid host matrix, giving rise to a material with refined conformation and micro structural control in compositions that would be impracticable via solid-state reactions [8, 9]. In this sense, sol-gel chemistry

offers numerous possibilities for the synthesis of materials for specific applications, among them optical and luminescent.

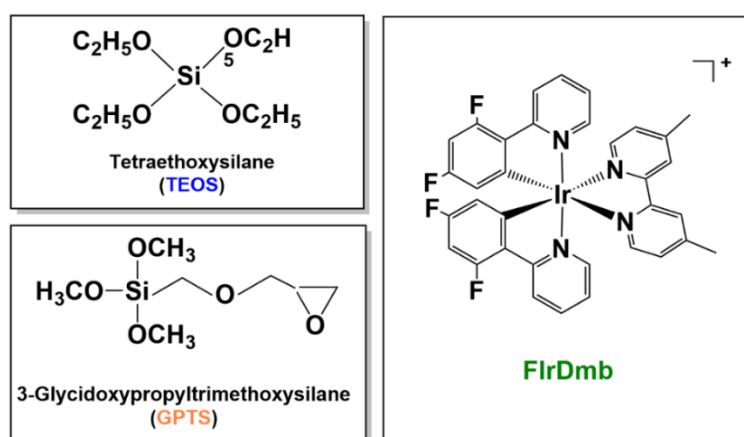
Hybrid monolithic xerogels obtained through co-condensation reactions of mixed 3-Glycidoxypropyltrimethoxysilane (GPTS) and Tetraethoxysilane (TEOS) are promising host matrices for the development of highly efficient optical materials. The large shrinkage associated with the gelation process and shattering of gelled samples during drying of purely inorganic matrix is avoided due to the presence of the epoxy group at the end of the glycidoxypropyl chain of the GPTS precursor [10, 11]. The organically functionalized trialkoxysilane acts as an important coupling agent to strengthen the interaction between organic and silica domains, allowing to properly conjugate guest molecules inside while retaining their photophysical properties. Therefore, this hybrid system is promising for different applications such as optical amplifiers, optical waveguides, light-emitting devices and sensors. For example, it has been demonstrated that the thermo-optical properties of CdSe/ZnS core-shell quantum dots (QDs) embedded in a GPTS:TEOS matrix have been improved, exhibiting higher quantum emission efficiency when compared to CdSe/ZnS QDs suspended in toluene [12]. Also, the fabrication of waveguides inside a dye doped-GPTS:TEOS bulk material via femtosecond laser micro-fabrication has been reported [13], while their potential as a random laser host was investigated [14]. The GPTS:TEOS-derived hybrid has also proven to be an excellent matrix to host  $\text{Eu}^{3+}$  and  $\text{Tb}^{3+}$  organic complexes, yielding thin films with outstanding fine-tunable optical properties, making those materials very promising for luminescent applications [15].

Concerning the many hybrid materials that may be produced for optical purposes, special attention has been given to those incorporated with transition metal complexes, as they offer highly efficient phosphorescence at room temperature [16, 17]. Ir(III) complexes are among the most interesting ones due to the wide range of versatile structures and photophysical features [18–20]. In this particular case, the intense spin-orbit coupling (SOC) of iridium results in mixed character excited states, both in spin and electronic nature, which allows these compounds to exhibit high quantum emission yields (up to ~100% in deaerated conditions) and relatively low excited state lifetimes (usually hundreds of nanoseconds) rising from the emitting states containing a high degree of triplet character [18, 20–23]. Some of the challenges faced for successful applications of the Ir(III) complexes are the need for increased stability in solid matrices and prevention of the rapid processes of suppression of the triplet emission caused by exposure to  $\text{O}_2$  [8, 24]. Several approaches have been used to encapsulate the complexes guest molecules in solid host matrices, a strategy that allows not only to isolate the complexes from

undesired interactions with their neighboring molecules but also to provide a stable environment where leakage must be avoided (for biological applications, for example) [8, 24, 25]. In addition, such immobilization does not affect the thermal and mechanical stability of the material, which attains the necessary strength for applications in luminescent solid-state devices.

The development of the applications of such photoactive host-guest systems requires a good understanding of the molecular structure of the hybrid matrices and the conditions that it imposes on the optical properties of the dopant. Therefore, the goal of the present study was to study the incorporation of Ir(III) complex into a GPTS:TEOS-derived monolithic xerogel from a structural and photophysical standpoint. More specifically, we have investigated the properties of a pure GPTS:TEOS matrix in comparison with those of a sample doped with the complex  $[\text{Ir}(\text{Fppy})_2(\text{dmb})]^+$  (Fppy = 2-(2,4-difluorophenyl) pyridine; and dmb = 4,4'-dimethyl-2,2'-bipyridine) due to its remarkable photophysical properties, such as spectral shape, lifetime, and nature of the emissive state, which are highly sensitive to the surrounding environment. Figure 1 presents the chemical structures of the silica precursors and the complex. We have conducted a structural description of the different parts of the organic-inorganic material and their mutual interaction, using a set of multinuclear high-resolution solid-state NMR techniques. The final state of the organic functionalities was studied by  $^{13}\text{C}$  NMR, while  $^{29}\text{Si}$  NMR gives insight about the condensation state of the siloxane matrix. On the other hand,  $^1\text{H}$  experiments at very fast Magic Angle Spinning (MAS) speeds of up to 60 kHz reveal details about the hydrogen species present in the sample. Finally, double resonance  $^1\text{H}$ - $^{29}\text{Si}$  and  $^1\text{H}$ - $^{13}\text{C}$  gives structural insight about the interaction between different components of the material, which was supported by vibrational analysis.

**Figure 1.** Chemical structures of the silica precursors used in this work and the investigated  $[\text{Ir}(\text{Fppy})_2(\text{dmb})]^+$  complex.



## Experimental

### *Materials and synthesis methodology*

All chemicals and solvents employed in the syntheses were purchased from Sigma-Aldrich or Synth and used without further purification. The complex  $[\text{Ir}(\text{Fppy})_2(\text{dmb})]^+$  was synthesized as described in previous contributions of the group [19, 26] and used as available.

The synthesis of the GPTS:TEOS-derived organosilicate hybrid material was done through the sol-gel process as previously described by Ferreira *et al* [13]. In a typical preparation, the matrix solution is obtained via hydrolysis of the Tetraethylortosilicate (TEOS) and 3-Glycidoxypropyltrimethoxysilane (GPTS), in mutual solvent (ethanol), under acidic conditions and in reflux. Therefore, a solution of 6.6 ml of ethanol, 61 ml of GPTS and 62 ml of TEOS was prepared in an Erlenmeyer flask, connected to a condenser. The solution was kept under mechanical stirring for 30 minutes at 80 °C for homogenization. After cooling to room temperature, 21 ml of  $\text{HNO}_3$  (0.6 M) was added dropwise to promote hydrolysis. This mixture was kept under the same reflux conditions at 80 °C for 4 hours. The matrix solution obtained by this process is a viscous and translucent liquid that is stable against gelation (if stored at room temperature) for months. The sol is composed of primary organic/silica particles dispersed in the solvent.

In the following step, the GPTS:TEOS monolithic xerogels were prepared by dividing a known volume of the sol added with acetonitrile (4:1 volume ratio) into sealed flasks. These vials were left in an oven at 40 °C for four weeks. Using this procedure, the sol underwent gelation, loss of solvents by evaporation and densification, reaching the end of a four-week period in the form of a monolithic xerogel with about 10 mm-diameter and 3 mm-thickness. The solid materials obtained by this methodology are optically clear, present no porosity when measured by  $\text{N}_2$  physisorption analysis [14] and exhibited a flat and nearly polished surface, which is highly suitable for general optical and spectroscopic studies.

The highly luminescent hybrid monoliths xerogels doped with Ir(III) complex (which will be called GPTS:TEOS:FIrDmb) were prepared from the immobilization of the complex molecules in the host matrix by adding a solution of the complex in acetonitrile, to the sol stage. The ratio of sol to acetonitrile used was also 4:1, and the mass of the complexes was adjusted so that the final concentration of the doped solution was  $1 \text{ mmol.L}^{-1}$ . After that, the mixtures were filled and followed the same procedure described above. The intense and homogeneous color of the GPTS:TEOS:FIrDmb xerogels, achieved after solvent evaporation, confirms the efficient dispersion of Ir(III) complexes within the organic/silica hybrid network. Finally, the

density of the monolithic xerogels was measured through Archimedes Principle, allowing an estimation of the complex concentration in the solid sample as 3.18 mmol.L<sup>-1</sup>.

#### *Characterization techniques*

Thermogravimetric analysis (TGA) was carried out using a Perkin Elmer Pyris 1 TGA Thermogravimetric Analyzer, under a nitrogen atmosphere with a continuous flux of 20.0 mL.min<sup>-1</sup>. The weight change patterns were recorded over a temperature range from 25 to 800 °C, at heating rate of 10 °C min<sup>-1</sup>. Differential scanning calorimetry (DSC) was performed with the NETZSCH DSC 200 PC instrument by heating the sample in a sealed aluminium pan, under nitrogen atmosphere. The instrument was ramped at 10 °C.min<sup>-1</sup> from 25 to 550 °C.

Fourier Transformed Infrared Spectroscopy (FTIR) measurements were performed at room temperature using a Thermo Nicolet Nexus 470 spectrometer. Prior to measurements, the samples were diluted in KBr using an agate mortar and pressed under high pressures to produce IR transparent pastille discs. A HORIBA LabRAM HR800 Evolution spectrometer was used to measure the Raman spectra, using a 532 nm diode laser with ~20 mW power on the sample. The spectra were taken using a 50x visible objective, a 100mm pinhole, and 1800 gr/mm grating.

The electronic absorption spectra were recorded on a Perkin Elmer Lambda 1050 UV/Vis/NIR spectrometer. Steady-state and time-resolved emission spectra were recorded using a Horiba Fluorolog time-correlated single photon-counting. A xenon lamp ( $\lambda_{\text{exc}} = 370$  nm) or a Horiba Delta Diode ( $\lambda_{\text{exc}} = 370$  nm, frequency = 20 kHz) were employed as excitation sources for steady-state or time-resolved measurements, respectively. Absolute emission quantum yields ( $\phi_0$ ) were measured using a BaSO<sub>4</sub> coated integrating sphere, model Horiba Quanta- $\phi$  following data treatment reported in previous contributions [19, 24, 25].

<sup>13</sup>C and <sup>1</sup>H solid-state NMR spectra were measured on a Bruker Avance Neo spectrometer operating at 14.1 T (600 MHz for <sup>1</sup>H Larmor frequency) equipped with a Bruker HX 1.3 mm probe. Before the NMR measurements, the samples were powdered and heat treated at 80 °C for 12 h to eliminate water molecules adsorbed on the surface of the material. <sup>1</sup>H MAS spectra were obtained at MAS frequency of 60 kHz using the EASY (Elimination of Artifacts in NMR Spectroscopy) pulse sequence [27] for suppression of the probe background signal. The excitation was performed with  $\pi/2$  pulse of 1.0  $\mu$ s. The recycle delay for the first scan in the sequence was set to 2 s, long enough to ensure full spin-lattice (T<sub>1</sub>) relaxation, and the delay for the second scan was set to 0.1 s. <sup>13</sup>C{<sup>1</sup>H} cross-polarization magic angle spinning (CPMAS) spectra were recorded at 60 kHz spinning rate using a contact time of 2.0 ms, and a typical

repetition delay of 2 s, respectively. The spectra were acquired with TPPM [28] proton decoupling during the data acquisition.  $^{13}\text{C}$  and  $^1\text{H}$  chemical shifts are reported relative to tetramethylsilane (TMS) using  $\alpha$ -glycine as secondary reference,  $^{13}\text{C}-\delta_{(\text{C}=\text{O})} = 176.5$  ppm and  $^1\text{H}-\delta_{(\text{NH}_3)} = 8.5$  ppm [29, 30].

$^1\text{H}-^{29}\text{Si}-^1\text{H}$  and  $^1\text{H}-^{13}\text{C}-^1\text{H}$  double cross polarization (double-CP) experiments were performed on the Bruker equipment described above. The experiments were performed using the pulse sequence described by Baccile *et al* [31], where polarization is first transferred from  $^1\text{H}$  to X spin (in our case X is  $^{13}\text{C}$  or  $^{29}\text{Si}$ ) followed by a second polarization transfer from X to nearby protons and  $^1\text{H}$  detection. The first contact pulse was optimized to maximize X polarization and was fixed at 3 ms and 2 ms for  $^{13}\text{C}$  and  $^{29}\text{Si}$  respectively. The second pulse was fixed at 500  $\mu\text{s}$  to select  $^1\text{H}$  species in the local environment of X species. After the first CP transfer, the residual  $^1\text{H}$  magnetization is saturated by 6  $\pi/2$  pulses nested in a time-decreasing loop starting with 20 ms interpulse delay [31]. During  $^1\text{H}$  saturation X nucleus magnetization is stored at +z direction [31]. Typical  $\pi/2$  pulse lengths were adjusted to 1.15 and 2  $\mu\text{s}$  for  $^1\text{H}$  and X nuclear species respectively. Spinning speed was 60 kHz to achieve improved resolution for  $^1\text{H}$  signals and up to 8000 and 2000 scans were accumulated for  $^{13}\text{C}$  and  $^{29}\text{Si}$  respectively. Polarization transfer was achieved by applying adiabatic tangentially ramped pulses [32] on  $^1\text{H}$  channel ( $\nu_{\text{rf}} = 80 \pm 20$  kHz) and squared pulses on X channel ( $\nu_{\text{rf}} = 140$  kHz). No decoupling was necessary during  $^1\text{H}$  acquisition.

Indirectly detected 2D  $^1\text{H}-^{13}\text{C}$  and  $^1\text{H}-^{29}\text{Si}$  heteronuclear correlation (HETCOR) spectra were acquired with the double-CP sequence described above, except that after the first polarization transfer the X magnetization is allowed to evolve during time  $t_1$ , while  $^1\text{H}$  decoupling was achieved by a single 2  $\mu\text{s}$  long  $\pi$  pulse applied in the middle of the  $t_1$  period, as described by Wiench *et al* [33].

$^{29}\text{Si}$  solid state NMR spectra were acquired on an Agilent DD2 spectrometer operating at 5.64 T (240 MHz for  $^1\text{H}$  Larmor frequency) equipped with a triple-channel 7.5 mm probe. The spectra were measured using a single  $\pi/2$  pulse of 5  $\mu\text{s}$  length, spin rate of 5.0 kHz, recycle delay of 400 s for up to 400 scans.  $^{29}\text{Si}$  chemical shifts were referenced using kaolinite as a secondary standard (-91.5 ppm relative to tetramethylsilane) [34].

## Results and discussion

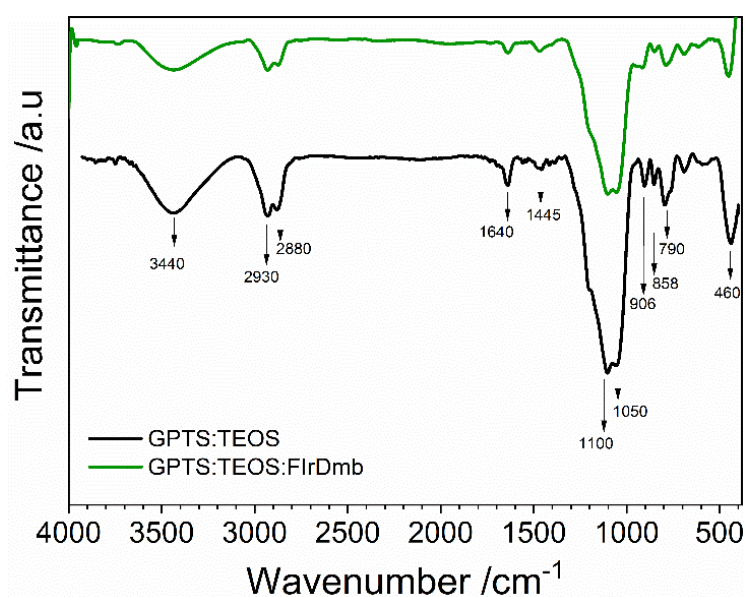
### *Structural and thermal characterization*

As seen in FTIR spectra for GPTS:TEOS monolithic xerogels, Figure 2, the presence of typical bands between  $4000\text{ cm}^{-1}$  and  $450\text{ cm}^{-1}$  brings evidence of the formation of the hybrid

network [35]. The main peaks, visible in both spectra, centered at  $1100\text{ cm}^{-1}$  and  $1050\text{ cm}^{-1}$ , correspond to stretching vibrations of the siloxane bonds (Si–O–Si). The large linewidth of the band suggests that a large cross-linked of randomly oriented species is forming the inorganic framework [36]. In addition, the presence of less pronounced bands at  $790\text{ cm}^{-1}$  and  $460\text{ cm}^{-1}$ , also ascribed to (Si–O–Si) vibration modes, suggests that the samples are mainly composed of silica network, as also confirmed by  $^{29}\text{Si}$  NMR results described below [37]. Furthermore, the presence of the characteristic peaks corresponding to the GPTS precursor gives information about the polymeric phase content in the final hybrids. For both GPTS:TEOS and GPTS:TEOS:FIrDmb samples, the bending modes at  $906\text{ cm}^{-1}$  and  $858\text{ cm}^{-1}$  attributed to the epoxy ring vibrations confirm that the functional group is still embedded in the matrix, while the bands at  $2930\text{ cm}^{-1}$  and  $2880\text{ cm}^{-1}$  correspond to the stretching of  $-\text{CH}_2$  groups from GPTS alkyl chain and the band at  $1445\text{ cm}^{-1}$  corresponds to the  $\text{CH}_2$  scissoring of glycidoxy groups [38–40]. Additionally, a broad peak characteristic of the hydroxyl groups is observed around  $3440\text{ cm}^{-1}$ , which is associated with Si–OH groups and/or adsorbed water molecules on the surface of the solid. Finally, the band at  $1640\text{ cm}^{-1}$  is also related to the presence of water.

Comparing the spectra of doped GPTS:TEOS:FIrDmb sample with the GPTS:TEOS pristine material, no significant changes in the energy of the peaks are observed, which indicates that the incorporation of Ir(III) complex (the FTIR of the complex is shown in Figure S1 in Supporting Information) did not affect the structural and chemical integrity of the host matrix, as also suggested by the solid state NMR results described below.

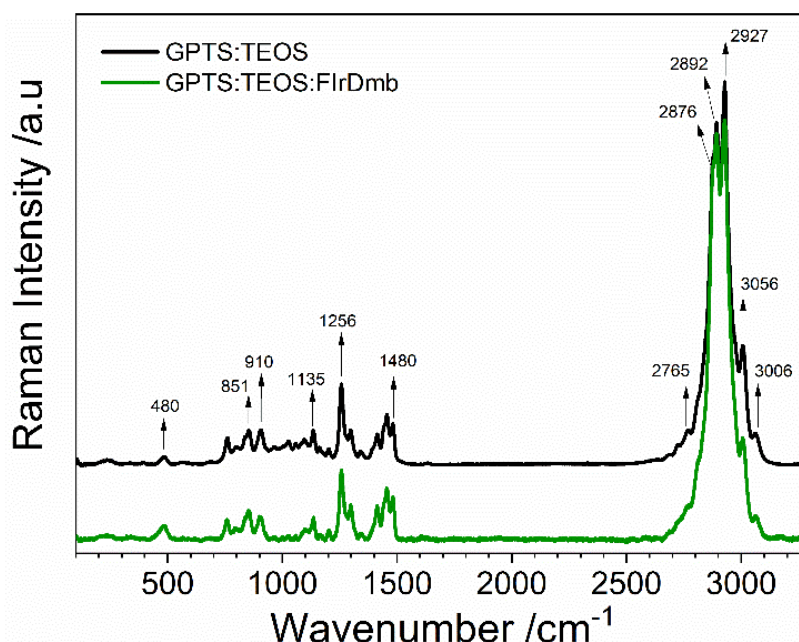
**Figure 2.** FTIR spectra of GPTS:TEOS and GPTS:TEOS:FIrDmb. Attributions of the bands are given, see main text for more details.





Raman spectra, Figure 3, were also recorded as complementary data. Both GPTS and TEOS precursors exhibit a strong frequency shift signal between  $600\text{ cm}^{-1}$  and  $650\text{ cm}^{-1}$ , originated from oscillations of alkoxy groups connected with silicon atoms: at  $650\text{ cm}^{-1}$  with four groups ( $-\text{OC}_2\text{H}_5$ ) and at  $610\text{ cm}^{-1}$  and  $640\text{ cm}^{-1}$  due to symmetric stretching vibrations  $\nu_s(\text{Si}(\text{OCH}_3)_3)$ . The disappearance of these peaks for the GPTS:TEOS xerogels indicates a high degree of hydrolysis of the methoxy and ethoxy groups after the synthetic procedure, while the  $480\text{ cm}^{-1}$  peak attributed to Si–O–Si bending confirms the inorganic network formation [5, 40–43]. Most importantly, the Raman spectroscopy also evidences the maintenance of organic groups in the final hybrids. The vibrational modes identified at  $1256\text{ cm}^{-1}$ ,  $910\text{ cm}^{-1}$  and at  $851\text{ cm}^{-1}$  are characteristic for epoxy ring vibrations, and the two bands at  $3006\text{ cm}^{-1}$  and  $3056\text{ cm}^{-1}$  are assigned to  $\text{CH}_2$  and  $\text{CH}$  stretching modes connected to epoxy groups. The four vibrational bands observed at  $2927\text{ cm}^{-1}$ ,  $2891\text{ cm}^{-1}$ ,  $2876\text{ cm}^{-1}$  and  $2765\text{ cm}^{-1}$  are assigned as  $\text{CH}_2$  group vibrations of GPTS alkyl chain, as well the modes in the regions at about  $1300\text{ cm}^{-1}$  and around  $1480\text{ cm}^{-1}$ . The maintenance of the glycidoxy group is proved by weak Raman bands in the region of  $1135\text{ cm}^{-1}$  [5, 40–42].

**Figure 3.** Raman spectra of GPTS:TEOS and GPTS:TEOS:FirDmb. Attributions of the vibrational bands are given, see main text for more details.



In order to elucidate the structure of the different parts of the organic-inorganic material and their mutual interaction, high-resolution solid-state NMR was employed. Figure 4 shows  $^{29}\text{Si}$  MAS NMR spectra of GPTS:TEOS and GPTS:TEOS:FirDmb samples. The  $^{29}\text{Si}$  spectra

exhibit signals corresponding to  $T^n$  and  $Q^n$  species. The notation  $T^n$  represents silicon species covalently attached to carbon and sharing  $n$  ( $n = 0, 1, 2, 3$ ) oxygen atoms with other Si units [ $-\text{CSi}(\text{OR})_{3-n}(\text{OSi})_n$ , with  $R = \text{H}$  or  $\text{CH}_2$ ] [44]. The notation  $Q^n$  represents pure  $\text{SiO}_4$  units sharing  $n$  ( $n = 0, 1, 2, 3, 4$ ) oxygen atoms with other Si units [ $\text{Si}(\text{OR})_{4-n}(\text{OSi})_n$ , with  $R = \text{H}$  or  $\text{CH}_2$ ]. The  $^{29}\text{Si}$  spectra could be deconvoluted into five Gaussian curves, which are centered around -52, -58, -65, -101 and -110 ppm, corresponding respectively to  $T^1$ ,  $T^2$ ,  $T^3$ ,  $Q^3$  and  $Q^4$  species (see Table 1). As described in the experimental section, the  $^{29}\text{Si}$  spectra were acquired in a quantitative fashion. Therefore, the area under each deconvoluted curve is proportional to the relative concentration of the corresponding Si structural unit. The percentage values are shown in Table 1. Both samples show very similar composition, confirming that the incorporation of FlrDmb complex does not affect the structure of the siloxane matrix (as already indicated by FTIR results). The samples show a very high degree of condensation (i.e. high Si–O–Si connectivity), with around 72 to 74% of fully condensate  $T^3/Q^4$  Si units.

**Figure 4.**  $^{29}\text{Si}$  MAS NMR spectra for GPTS:TEOS and GPTS:TEOS:FlrDmb xerogels (black curves). Spectral deconvolutions into Gaussian functions are also shown (blue curves are Gaussian components and red curves are the total deconvoluted spectra). Attributions of the lines to  $T^n$  and  $Q^n$  species are also given, see main text for more details.

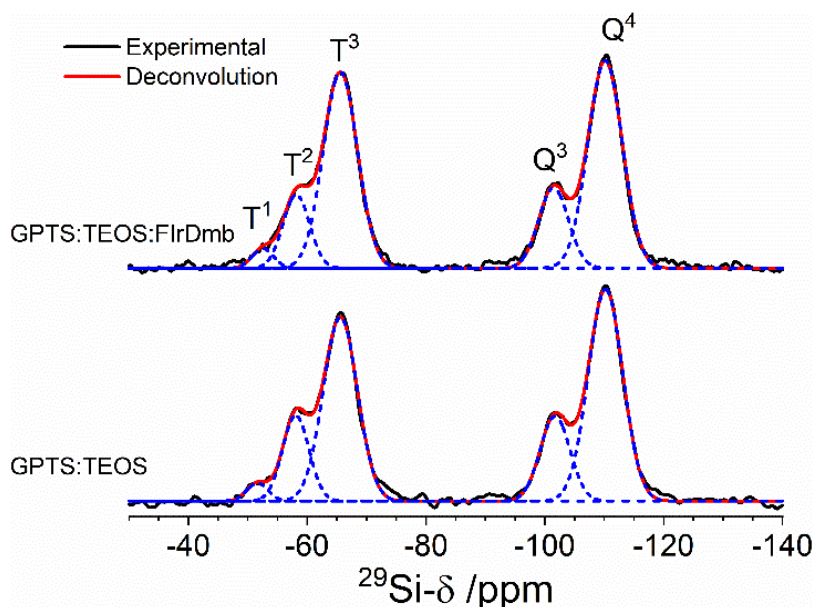
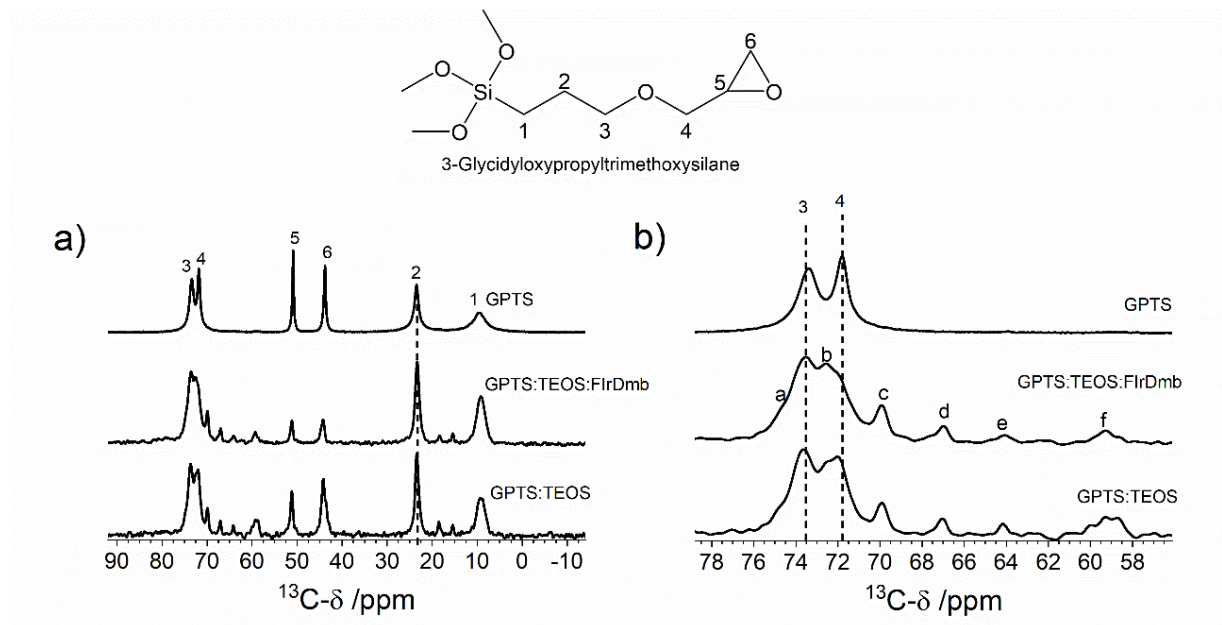


**Table 1.**  $^{29}\text{Si}$  NMR Parameters, chemical shift ( $^{29}\text{Si}$ - $\delta$ ) and percentage area (I), obtained from deconvolutions of the spectra in Figure 4.

Si unit	GPTS:TEOS		GPTS:TEOS:FIrDmb	
	$^{29}\text{Si}$ - $\delta$ ( $\pm 1$ ppm)	I ( $\pm 1$ %)	$^{29}\text{Si}$ - $\delta$ ( $\pm 0.1$ ppm)	I ( $\pm 1$ %)
T <sup>1</sup>	-52	2	-53	2
T <sup>2</sup>	-58	12	-58	11
T <sup>3</sup>	-66	33	-66	36
Q <sup>3</sup>	-102	14	-101	13
Q <sup>4</sup>	-110	39	-110	38

Figure 5a shows  $^{13}\text{C}\{^1\text{H}\}$  CPMAS NMR spectra for the undoped (GPTS:TEOS) and doped (GPTS:TEOS:FIrDmb) xerogels. For comparison, the spectrum of pure GPTS is also shown and the corresponding peak assignments are given [45, 46]. Table 2 summarizes all  $^{13}\text{C}$  signal assignments. For both xerogels the  $^{13}\text{C}\{^1\text{H}\}$  CPMAS spectra exhibit all lines expected for the GPTS moieties, indicating that, to some extent, the GPTS structure is preserved after the sol-gel synthesis, as already indicated by FTIR results (see Figure 2 and related text). For the doped sample, the peaks around 44 and 55 ppm, which correspond to the epoxy ring (C6 and C5 respectively), show slightly smaller relative intensities than the observed for the undoped xerogel. Factors that can influence the peak intensities in a CPMAS experiment include (i) relative concentration of observed species and (ii) cross-polarization dynamic (iii) efficiency of the polarization transfer mechanism. From  $^1\text{H}$  MAS results described below (Figure 6) we conclude that the fraction of unreacted epoxy groups in both samples is of the same order.  $^{13}\text{C}\{^1\text{H}\}$  CPMAS experiments with variable contact time show very similar dynamic to the polarization transfer mechanism (see Figure S2 in Supporting Information). Therefore, the difference in signal intensity observed for the epoxy groups in both samples is most probably related to inefficient polarization transfer due to the interaction between the GPTS functionalities and the FIrDmb complex. Unfortunately, due to low concentration, NMR signals corresponding to FIrDmb moieties could not be resolved in the  $^{13}\text{C}$  NMR spectrum of GPTS:TEOS:FIrDmb sample. Nevertheless, the  $^{19}\text{F}$  spectrum for sample GPTS:TEOS:FIrDmb shows a signal centered around -107 ppm (see Figure S3 in Supporting Information), which corresponds to FIrDmb moieties incorporated in the sample [24].

**Figure 5.**  $^{13}\text{C}\{^1\text{H}\}$  CPMAS NMR spectra for GPTS:TEOS and GPTS:TEOS:FirDmb xerogels and  $^{13}\text{C}$  liquid NMR spectrum for the pure GPTS compound. In (a) the full spectra are displayed, while in (b) the region from 57 to 79 ppm is shown in detail. Peak attributions are given as numbers corresponding to the C atom labeling shown for the GPTS compound. Letters a to f in (b) corresponds to attributions for the possible products of the GPTS epoxy ring opening reactions (see Figure S4 in Supporting Information).



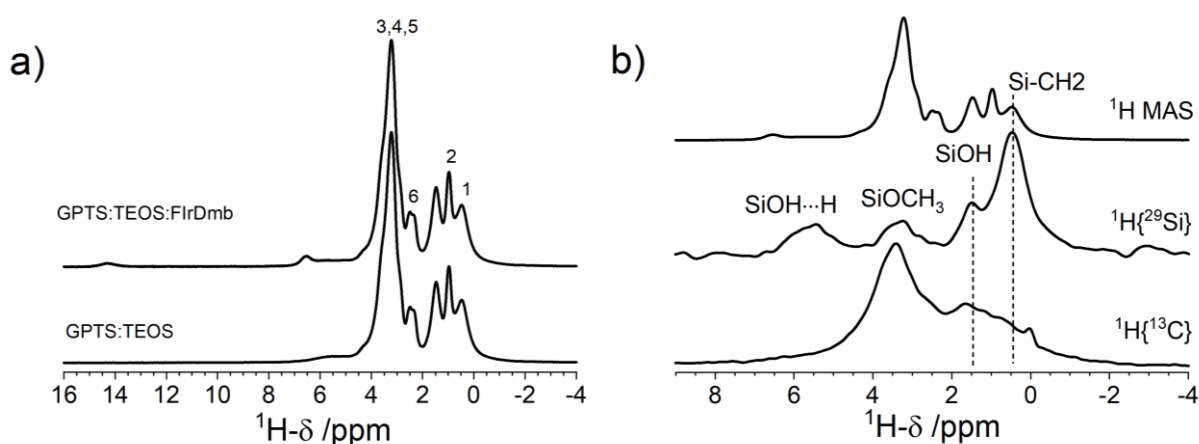
Besides the  $^{13}\text{C}$  peaks attributed to GPTS moieties, the  $^{13}\text{C}\{^1\text{H}\}$  NMR spectra also exhibits peaks around 74 (shoulder), 72 (shoulder), 70, 67, 64, 59 ppm (**a**, **b**, **c**, **d**, **e**, **f** respectively, as detailed in Figure 5b). These peaks are all assigned to products resulting from reactions of the GPTS epoxy group during the sol-gel synthesis (the possible reactions are shown in Figure S4 in Supporting Information). The signal **f** is assigned to  $-\text{OCH}_3$  in methyl ether groups formed from the reaction of open epoxy groups methyl alcohol, which by its turn is present as a product of the hydrolysis of methoxy groups (see Figure S4 in Supporting Information) [47]. This signal at 59 ppm can also be assigned to methoxysilyl groups from non-hydrolyzed methoxy silane species, as demonstrated by  $^1\text{H}-^{29}\text{Si}$  HETCOR results described below. The signals around 64 and 70 ppm (**e**, **c**) are assigned to diol groups as a result of the hydrolysis of epoxy groups [45, 47]. The signal **d**, around 67 ppm, can be assigned to dioxane groups resulting from the reaction of two diol groups [47]. Finally, the shoulders around 74 and 72 ppm (**a**, **b**) are attributed to oligo- and/or poly-ethylene oxide species formed from a ring-opening reaction of the epoxy groups followed by polymerization reaction [47]. The small peaks at 15 and 18 ppm can be assigned to aliphatic impurities, respectively from residual ethanol [48] and diethyl ether [49] molecules physisorbed on the siloxane matrix.

**Table 2.**  $^{13}\text{C}$  and  $^1\text{H}$  chemical shifts for the various species identified in this work. Numbers 1-6 are related to the carbon labeling of the GPTS moiety, given in Figure 5. Letters a-f are related with the various products of the GPTS epoxy ring opening reaction (see Figure S4 in Supporting Information). Proton chemical shifts correspond to the correlations observed in  $^1\text{H}\{^{29}\text{Si}\}$  and  $^1\text{H}\{^{13}\text{C}\}$  HETCOR spectra.

Assignment	$^{13}\text{C}$ - $\delta$ ( $\pm 1$ ppm)	$^1\text{H}$ - $\delta$ ( $\pm 0.2$ ppm)
1 (SiCH <sub>2</sub> )	10 [45, 46]	0.5
2 (Aliphatic)	23 [45, 46]	1.6
3 (OCH <sub>2</sub> )	74 [45, 46]	3.4
4 (OCH <sub>2</sub> )	72 [45, 46]	3.4
5 (CH in epoxy ring)	51 [45, 46]	3.0
6 (CH <sub>2</sub> in epoxy ring)	44 [45, 46]	2.6
a / b (CH <sub>2</sub> in oligo- or poly-ethylene )	74 / 72 [47]	-
c (CH in diol)	70 [47]	-
d (CH <sub>2</sub> in dioxane)	67 [47]	3.4
e (CH <sub>2</sub> in diol)	64 [47]	-
f (CH <sub>3</sub> in methyl ether)	59 [47]	3.3
SiOCH <sub>3</sub>	-	3.3
SiOH	-	1.5 [50]
SiOH $\cdots$ H	-	5.7 [50]

Figure 6a shows solid state  $^1\text{H}$  MAS NMR spectra for both xerogels, GPTS:TEOS and GPTS:TEOS:FirDmb. Double-CP  $^1\text{H}$ - $^{29}\text{Si}$ - $^1\text{H}$  and  $^1\text{H}$ - $^{13}\text{C}$ - $^1\text{H}$  experiments were also performed to help in the elucidation of  $^1\text{H}$  chemical shifts. The double-CP spectra of sample GPTS:TEOS:FirDmb are shown in Figure 6b. In this experiment polarization is first transferred from  $^1\text{H}$  to X species ( $\text{X} = ^{29}\text{Si}$  or  $^{13}\text{C}$ ) through Hartmann-Hahn cross-polarization, then  $^1\text{H}$  magnetization is saturated before a second polarization transfer occurs, now from X to  $^1\text{H}$ , with subsequent  $^1\text{H}$  observation [31]. Only those  $^1\text{H}$  in close proximity (dipolar coupled) to  $^{29}\text{Si}$  or  $^{13}\text{C}$  are polarized, resulting in filtered  $^1\text{H}$  spectra.

**Figure 6.** (a)  $^1\text{H}$  NMR spectra obtained at 60 kHz MAS for GPTS:TEOS and GPTS:TEOS:FirDmb xerogels. Peak attributions correspond to the chemical shifts expected for the protons bounded to carbons of the GPTS moiety (see C labeling in Figure 5). (b) Double-CP  $^1\text{H}$ - $^{29}\text{Si}$ - $^1\text{H}$  ( $^1\text{H}\{^{29}\text{Si}\}$ ) and  $^1\text{H}$ - $^{13}\text{C}$ - $^1\text{H}$  ( $^1\text{H}\{^{13}\text{C}\}$ ) spectra for the GPTS:TEOS:FirDmb sample, obtained at 60 kHz MAS. The  $^1\text{H}$  MAS spectrum is also displayed in (b) for comparison.

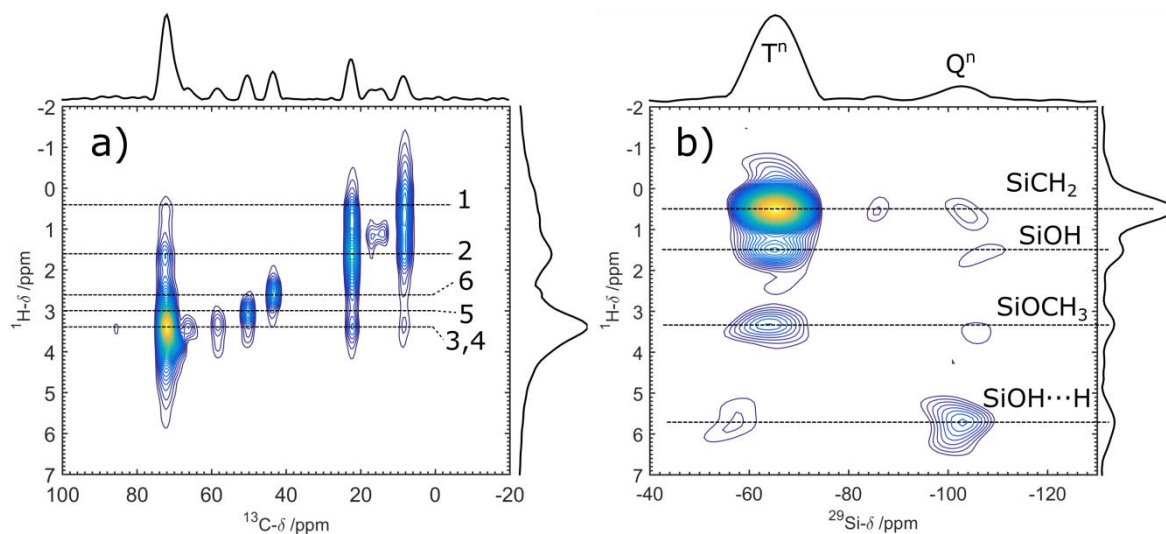


In Figure 6a the peaks corresponding to hydrogen bonded to carbons 1, 2 and 6 of the GPTS molecules are clearly resolved in the  $^1\text{H}$  MAS spectra, respectively around 0.5, 0.98 and 2.4/2.5 ppm [47]. On the other hand, many signals overlaps in the chemical shift range 3 – 4 ppm, corresponding to the summed contribution from (i) hydrogen species in  $-\text{OCH}_2$  groups, i.e., hydrogen bounded to carbon atoms 3, 4 ( $-\text{CH}_2\text{O}-$ ) and 5 from GPTS [47]; (ii) hydrogen from  $\text{CH}_3$  groups in residual methanol or methoxy groups [47]; (iii) hydrogen in the products of the epoxy opening reaction, such as methyl ether (**f**), dioxane (**d**) and diol (**c,e**) groups [47] and (iv) small water clusters adsorbed on the siloxane network [50]. The broad shoulder around 4.2 ppm can also be attributed to water clusters adsorbed in the material [50]. The  $^1\text{H}\{^{13}\text{C}\}$  double-CP spectrum is composed of multiple overlapping signals, limiting the interpretation (better insight is given by HETCOR experiments described below). On the other hand, the  $^1\text{H}\{^{29}\text{Si}\}$  double-CP spectrum in Figure 6b exhibits well resolved peaks at 5.5, 3.4, 1.5, and 0.5 ppm. The broad signal at 5.5 ppm, also present in  $^1\text{H}$  MAS spectrum (Figure 6a), corresponds to hydrogen in silanol groups participating in hydrogen bonds with either  $\text{H}_2\text{O}$  or other neighboring silanol ( $\text{SiOH}\cdots\text{H}$ ) [50]. The signal at 3.4 ppm corresponds to methyl hydrogens in  $\text{OCH}_3$  from non-hydrolyzed silane species. HETCOR results shown below indicate that these non-hydrolyzed species are only present for GPTS moieties, i.e. TEOS is completely hydrolyzed during the synthesis. The efficient cross-polarization observed for these  $\text{CH}_3$  species indicate

low mobility, probably due to hydrogen bonds with silanol or H<sub>2</sub>O species. The signal at 1.5 ppm is attributed to SiOH species and/or water molecules hydrogen bounded to silanol (H<sub>2</sub>O⋯HO) [50]. Finally, peaks around 6.5 and 14 ppm are only observed for the <sup>1</sup>H MAS NMR spectrum of sample GPTS:TEOS:FIRdmb (Figure 6a), which leads to the conclusion that these resonances are related to the presence of the FIRdmb complex. Attributions to the peak around 6.6 ppm are still uncertain. The peak around 14 ppm is assigned to acidic protons in strong hydrogen bonds. Since these acidic protons are observed only for the doped xerogels, we can conclude that this signal is associated with the interaction between organic groups in FIRdmb and either hydroxyl groups from the organic-inorganic matrix or (ii) water molecules [51].

Further insight about the hydrogen species present in the studied xerogels can be obtained by means of <sup>1</sup>H-<sup>13</sup>C and <sup>1</sup>H-<sup>29</sup>Si heteronuclear correlation (HETCOR) experiments. Figure 7 shows 2D HETCOR spectra obtained with very fast MAS spinning rate (60 kHz) and <sup>1</sup>H detection, using the Double-CP <sup>1</sup>H-X-<sup>1</sup>H described in the experimental section, with X = <sup>13</sup>C (Figure 7a) or <sup>29</sup>Si (Figure 7b). In the <sup>13</sup>C{<sup>1</sup>H} HETCOR spectrum chemical shifts for all <sup>1</sup>H species belonging to GPTS moieties can be identified, the chemical shift values are given in Table 2. The <sup>13</sup>C{<sup>1</sup>H} HETCOR spectrum also confirms the attributions given for carbon species **d** and **f** attributed respectively to dioxane and methyl ether groups. Both species show cross peaks with <sup>1</sup>H resonating around 3.3 to 3.8 ppm, which is in the chemical shift range expected for OCH<sub>2</sub> and OCH<sub>3</sub> species. The carbon impurities resonating around 15 and 18 ppm show cross peaks with <sup>1</sup>H at 1.1 ppm, confirming the attribution of these signals to aliphatic impurities. The <sup>29</sup>Si{<sup>1</sup>H} HETCOR spectrum in Figure 7b exhibit all <sup>29</sup>Si-<sup>1</sup>H cross peaks corresponding to SiCH<sub>2</sub>, SiOH, SiOCH<sub>3</sub> and SiOH⋯H groups, in agreement with the peak assignments given above. More interestingly, the SiOCH<sub>3</sub> groups show correlation only with T<sup>n</sup> groups, indicating that the hydrolysis of GPTS is not complete. On the other hand, the absence of this cross peak for Q<sup>n</sup> groups indicates complete hydrolysis of TEOS. Finally, different silanol groups are observed for T<sup>n</sup> and Q<sup>n</sup> species. For T<sup>n</sup> the majority of silanol groups are isolated, while for Q<sup>n</sup> they are hydrogen bounded to H<sub>2</sub>O or other neighboring silanol groups. A weak correlation is observed between Q<sup>n</sup> and SiCH<sub>2</sub> species, indicating spatial proximity between Q<sup>n</sup> and T<sup>n</sup> groups, as expected for homogeneously distributed species.

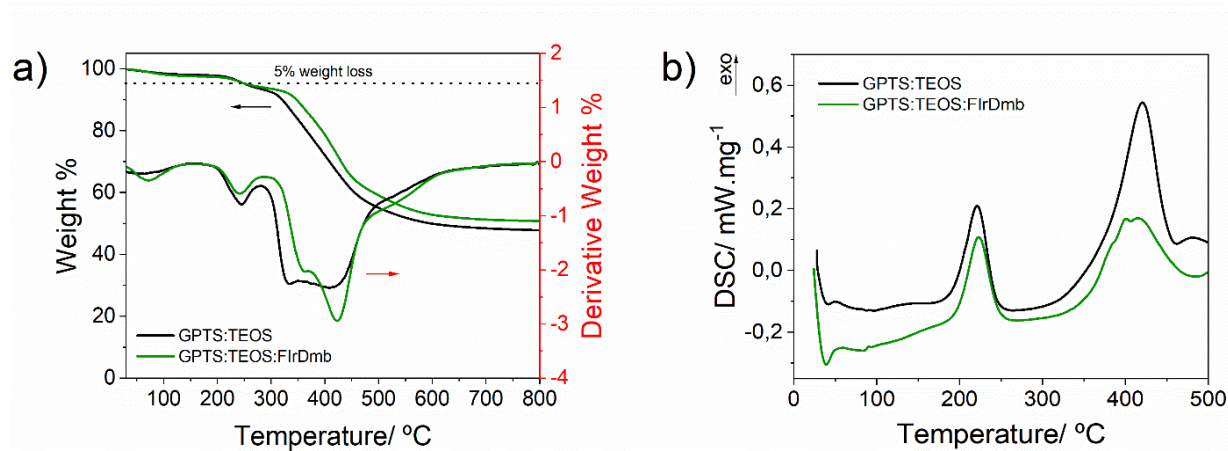
**Figure 7.** Bi-dimensional double-CP HETCOR  $^1\text{H}$ - $^{13}\text{C}$ - $^1\text{H}$  (a) and  $^1\text{H}$ - $^{29}\text{Si}$ - $^1\text{H}$  (b) spectra for the sample GPTS:TEOS:FirDmb, obtained with 60 kHz MAS and  $^1\text{H}$  detection. Numbers in (a) correspond to assignments to the GPTS moiety (see C labels in Figure 5).



Finally, we studied the thermal properties of the synthesized hybrid xerogels. The thermal degradation (TG) profile of the pure GPTS:TEOS monolithic xerogel, Figure 8a, displays two distinct regions of weight loss, accompanied by exothermic events with onset temperatures near  $T_1 = 180\text{ }^\circ\text{C}$  and  $T_2 = 300\text{ }^\circ\text{C}$ , Figure 8b. The first event, which corresponds to a weight loss of about 5% over the temperature interval  $200\text{--}280\text{ }^\circ\text{C}$  is assigned to the polymerization of the epoxy group, with some contribution of the degradation due to the unreacted methoxy groups in the grafted GPTS precursor. This is followed by the main event of degradation ( $T_2$ ) with an onset temperature of  $300\text{ }^\circ\text{C}$ , which corresponds to a weight loss of about 50% over the temperature interval  $300\text{--}600\text{ }^\circ\text{C}$ . This event is assigned to the decomposition of the organic residue bound to the  $\text{T}^3$  units of the ORMOSIL, which is completed near  $600\text{ }^\circ\text{C}$ . On the other hand, the thermal degradation profile for the doped xerogels presents a slight shift towards high temperatures. Near  $400\text{ }^\circ\text{C}$  the data observed for the GPTS:TEOS:FirDmb sample reveal some additional contribution from the decomposition of the ligands bound to the incorporated Ir(III) complex.



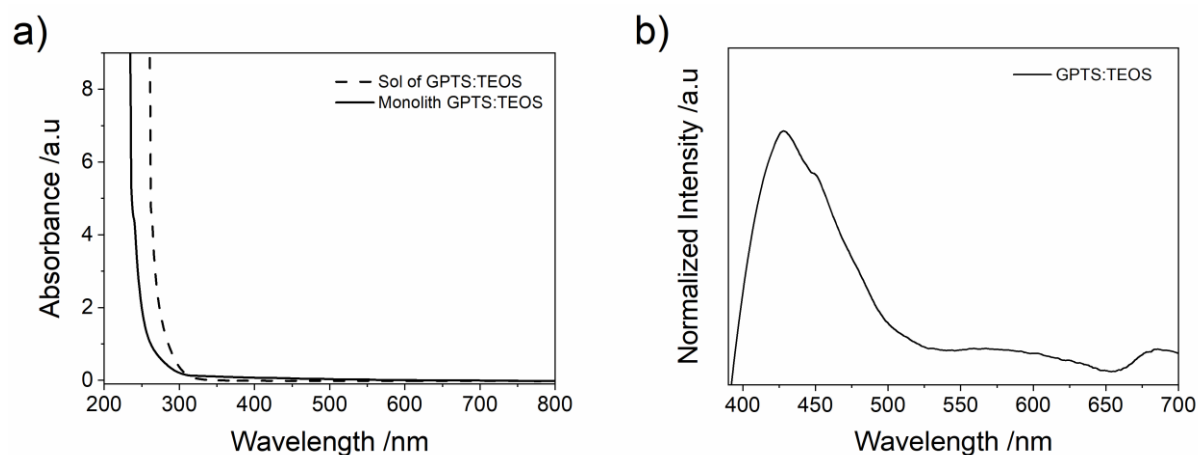
**Figure 8.** Thermal degradation (TG) profile (a) and differential scanning calorimetry (DSC) thermograms (b) of GPTS:TEOS and GPTS:TEOS:FirDmb xerogels.



### *Photophysical characterization*

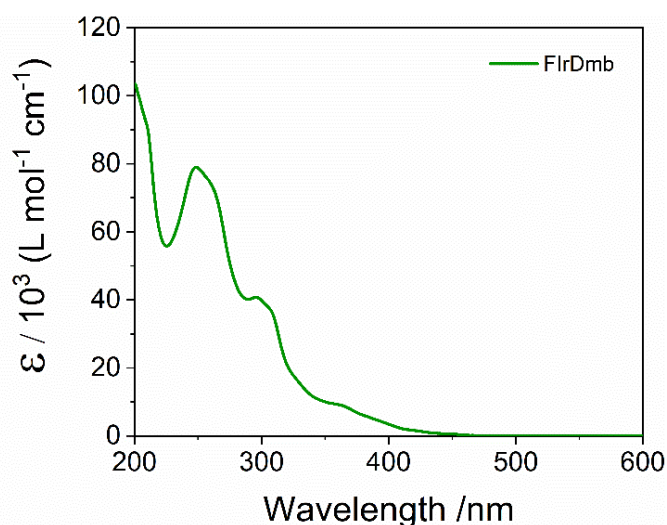
Figure 9 shows the absorption (a) and emission (b) spectra of undoped GPTS:TEOS xerogels. The hybrid matrix in the sol stage showed a wide transmission range from near infrared to ultraviolet around 330 nm, while for the solid hybrid samples this range is wider (up to 300 nm) due to the evaporation of organic solvents during the sol gelation and xerogel densification. Despite the low absorption of the matrices for wavelengths greater than 300 nm, when excited at 370 nm (wavelength used to excite the Ir(III) complex) they have a wide emission band ranging from 400 to 700 nm. However, this emission is not very intense and does not appear in the emission spectrum of the samples after the insertion of luminescent species, probably due to energy transfer from the matrix to the Ir(III) guest [52].

**Figure 9.** Absorption (a) and emission spectra (b) of undoped GPTS:TEOS xerogel at 298 K ( $\lambda_{\text{exc}} = 370$  nm).



The absorption spectrum of the investigated Ir(III) complex readily soluble in acetonitrile, Figure 10, exhibits high energy bands (230 - 350 nm) mostly ascribed to the singlet ligand-centered ( $^1\text{LC}$ ) transitions from  $\pi$  to  $\pi^*$  orbitals in both of the NC and dmb ligands, and relatively less intense absorptions in the low energy regions ( $\lambda > 325$  nm), which are an overlap of mixed character transitions in spin (singlet and triplet) and in electronic nature, as a direct consequence of the strong SOC effect exerted by the iridium core ( $\xi_{\text{Ir}} = 4430 \text{ cm}^{-1}$ ) [53]. In addition, a weak band referring to the direct population of the lowest triplet excited state  $T_1$  (assumed to be a metal-to-ligand-charge-transfer state, ascribed as  $^3\text{MLCT}$ ) can be observed from 450 to 550 nm, whose deactivation results in intense phosphorescence, with emission lifetime ( $\tau_0$ ) in the microsecond range and the emission quantum yields ( $\phi_0$ ) quite high (Table 3), typical of Ir(III) emitters. Such remarkable photophysical properties were thoroughly addressed in previous publications [20, 26].

**Figure 10.** Absorption spectrum of free FIrDmb complex in acetonitrile at 298 K.



The absorption of the FIrDmb complex incorporated in the GPTS:TEOS monolithic xerogel at high energy bands (Figure S5 in Supporting Information) is obscured due to the high concentration of the complex in the matrix ( $3.18 \text{ mmol.L}^{-1}$ ) and the intense absorption of the hybrid matrix in UV region. Although these effects make interpretation of the absorption spectrum complicated, the excitation spectrum emphasizes that the low-energy bands in the region from 300 to 500 nm are largely preserved in the solid material (see Figure S5 in Supporting Information).

**Table 3.** Photophysical parameters of investigated samples at 298 K.

Sample	$\lambda_{\text{max}}/$ nm <sup>a</sup>	$\phi_0 / \%$	$\tau /$ $\mu\text{s}$	$k_r /$ $10^5 \text{ s}^{-1}$	$k_{nr} /$ $10^5 \text{ s}^{-1}$
<b>FIrDmb in acetonitrile</b>	522	$96^b \pm 10$	$0.66 \pm 0.03^d$	$15 \pm 2$	$0.6 \pm 0.01$
<b>GPTS:TEOS:FIrDmb - Sol</b>	522	$63^b \pm 6$	$1.06 \pm 0.01^d$	$5.9 \pm 0.6$	$3.5 \pm 0.3$
<b>GPTS:TEOS:FIrDmb - Xerogel</b>	508	$86^c \pm 9$	$1.20 \pm 0.03^e$	$7.2 \pm 0.7$	$1.1 \pm 0.1$

<sup>a</sup>Emission maxima ( $\lambda_{\text{exc}} = 370 \text{ nm}$ ); <sup>b</sup>Absolute emission quantum yield, measured in an integrating sphere in  $\text{N}_2$ -saturated solution; <sup>c</sup>Absolute emission quantum yield, measured in an integrating sphere in air; <sup>d</sup>Emission lifetime in  $\text{N}_2$ -saturated solution; <sup>e</sup>Average emission lifetime of solid sample in air.

The phosphorescence properties of the Ir(III) complex, however, are strongly altered after gelation and densification of the GPTS:TEOS matrix. The emission spectrum of the free FIrDmb complex in both acetonitrile or GPTS:TEOS sol is broad and non-structured (Figure 11), which is a characteristic feature of a  $T_1$  state with predominant MLCT character (ascribed to the  ${}^3\text{MLCT}_{\text{Ir}(\text{NC}) \rightarrow \text{dmb}}$  state). In comparison, the emission of the GPTS:TEOS:FIrDmb xerogel showed a blue shift ( $\sim 15 \text{ nm}$ ), Figure 9, characteristic of the rigidochromism observed only for transitions with high dipole moment (i.e, charge transfer transitions, such as MLCT). The dipole reorientation of the solvent/medium molecules in response to the new dipole configuration of the MLCT states, which occurs promptly in fluid solutions, is restrained in rigid media, destabilizing the MLCT state energy. Therefore, the observation of a strong rigidochromism for the emission of GPTS:TEOS:FIrDmb evidences even more that the nature of  $T_1$  state of the complex in fluid solution is mostly  ${}^3\text{MLCT}_{\text{Ir}(\text{NC}) \rightarrow \text{dmb}}$  [20, 26].

In addition, an increase in the lifetime of the  $T_1$  excited state was observed in the solid GPTS:TEOS:FIrDmb even in the presence of oxygen, Table 3. In order to investigate the luminescence quenching mechanisms, such as self-quenching due to the proximity between the molecules of the complexes in the most concentrated medium, xerogels with different concentrations of the Ir(III) complex were prepared and present no change in the emission lifetime (Figure 12). Thus, there are strong evidences that even the high concentrated samples does not present a significant extent of Ir(III) complex aggregation, approaching a homogeneous molecular dispersion. The rigidification of the surrounding environment of the complex also leads to an increase in the radiative decay, which would result in quite high  $\phi_0$

values. The improvements in luminescent properties observed after confinement can be attributed to the low diffusion of molecular oxygen within the matrix and the greater rigidity of the complex, which destabilizes charge transfer states, decreasing the probability of nonradiative vibrational deactivations.

**Figure 11.** Emission spectra (a) of free Ir(III) complexes (FIrDmb) and the GPTS:TEOS-doped matrix in the sol phase and the monolithic material (b) at 298 K ( $\lambda_{exc}=370$  nm).

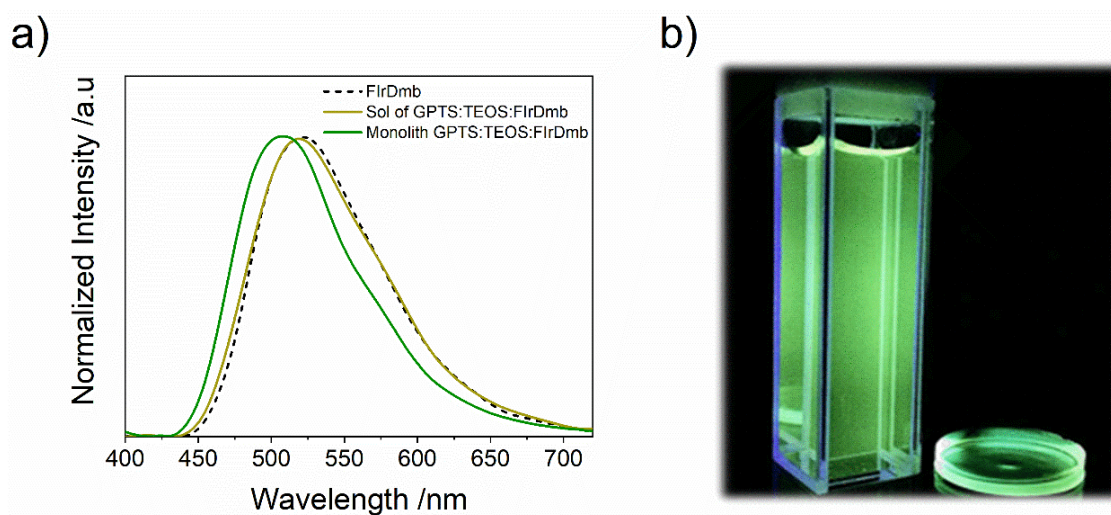
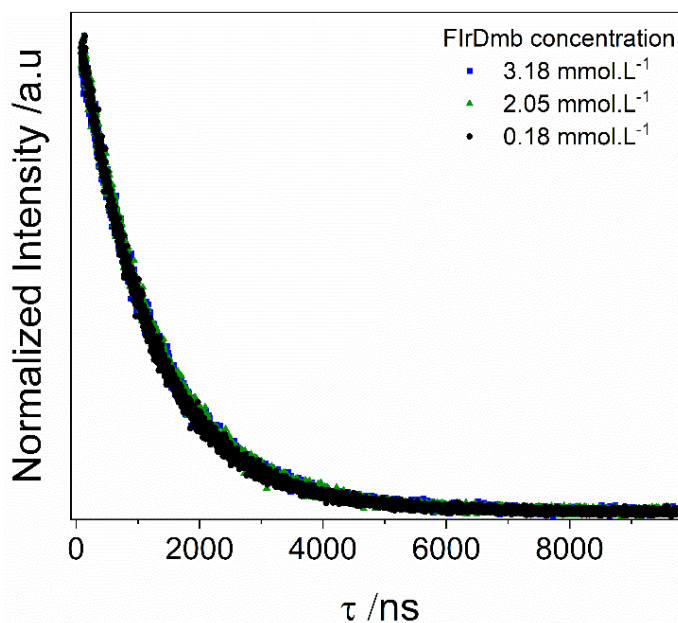


**Figure 12.** Emission decay for GPTS:TEOS:FIrDmb monolithic materials with different complex concentrations. The prepared samples present no change in the emission lifetime.



## Conclusions

GPTS:TEOS-derived organosilicate hybrid material prepared via hydrolysis and polycondensation of the GPTS and TEOS precursors were successfully developed. Due to the high concentration of the epoxy groups of the GPTS precursor in the matrix, the resulting monoliths were free from cracks and showed very good optical quality. Furthermore, their easy and relatively low cost preparation, with high mechanical strength and UV-vis transparency, characterize them as excellent hosts for highly luminescent guest species such as the Ir-complex applied in this work.

Altogether, solid state NMR results show a high degree of condensation for the siloxane matrix, with about 72% to 74% of fully condensate Si units. The results show that the hydrolysis of TEOS is complete, while for GPTS there are still residual terminal SiOCH<sub>3</sub> groups. Isolated silanol groups are observed to T<sup>1</sup> and T<sup>2</sup> units, while for Q<sup>3</sup> units the silanol groups are hydrogen bounded to H<sub>2</sub>O or other SiOH groups. The epoxy ring of GPTS is partially preserved after the synthesis, while a small fraction reacts to form diol, dioxane, methyl ether and oligo- and/or poly-ethylene oxide species. Efficient <sup>1</sup>H-<sup>29</sup>Si cross-polarization transfer for SiOCH<sub>3</sub> species indicates restricted mobility for the terminal CH<sub>3</sub> groups, probably due to the interaction with water molecules or with groups from the siloxane matrix.

The presence of the FIrDmb complex is demonstrated by <sup>19</sup>F and <sup>1</sup>H NMR experiments. The <sup>1</sup>H MAS NMR spectrum show a resonance at very low field (14 ppm) which is observed only for the doped xerogel, indicating that the FIrDmb complex is interacting with the organic-inorganic structure through strong hydrogen bonds. The highly luminescent hybrid monolith xerogels doped with [Ir(Fppy)<sub>2</sub>(dmb)]<sup>+</sup> preserves the photophysics of the complex, hence showing compatibility with the matrix. The results from solid state NMR evidence that the final structure of the organically modified silica matrix is very similar for both, doped and undoped xerogels. The improvements in the luminescent properties such as higher absolute quantum yield and excited state lifetime values can be attributed to the rigidity effect around the complex and the lower diffusion of O<sub>2</sub> in the matrix.

## References

- [1] M. Pagliaro, *Silica-Based Materials for Advanced Chemical Applications*, The Royal Society of Chemistry, 2009.
- [2] R. Ciriminna, A. Fidalgo, V. Pandarus, F. Béland, L.M. Ilharco, M. Pagliaro, The sol-gel route to advanced silica-based materials and recent applications, *Chem. Rev.* 113 (2013) 6592–6620.

- [3] H. Schmidt, Considerations about the sol-gel process: From the classical sol-gel route to advanced chemical nanotechnologies, *J. Sol-Gel Sci. Technol.* 40 (2006) 115–130.
- [4] C. Sanchez, P. Belleville, M. Popall, L. Nicole, Applications of advanced hybrid organic–inorganic nanomaterials: from laboratory to market, *Chem. Soc. Rev.* 40 (2011) 696–753.
- [5] D. Wencel, M. Barczak, P. Borowski, C. McDonagh, The development and characterisation of novel hybrid sol-gel-derived films for optical pH sensing, *J. Mater. Chem.* 22 (2012) 11720–11729.
- [6] G. Schottner, Hybrid sol-gel-derived polymers: Applications of multifunctional materials, *Chem. Mater.* 13 (2001) 3422–3435.
- [7] M. Barczak, C. McDonagh, D. Wencel, Micro- and nanostructured sol-gel-based materials for optical chemical sensing (2005 – 2015), *Microchim. Acta.* 183 (2016) 2085–2109.
- [8] K.P.S. Zanoni, L.P. Ravaro, A.S.S. De Camargo, Host-guest luminescent materials based on highly emissive species loaded into versatile sol-gel hosts, *Dalt. Trans.* 47 (2018) 12813–12826.
- [9] A. Lukowiak, W. Streck, Sensing abilities of materials prepared by sol-gel technology, *J. Sol-Gel Sci. Technol.* 50 (2009) 201–215.
- [10] C.M. Awano, F.S. De Vicente, D.A. Donatti, D.R. Vollet, Structure and growth kinetics of 3-glycidoxypropyltrimethoxysilane-derived organic/silica hybrids at different temperatures, *J. Phys. Chem. C.* 116 (2012) 24274–24280.
- [11] D.R. Vollet, L.A. Barreiro, C.M. Awano, D. Vicente, M. Yoshida, D.A. Donatti, Rod-like particles growing in sol–gel processing of 1:1 molar mixtures of 3-glycidoxypropyltrimethoxysilane and tetraethoxysilane research papers, *J. Appl. Crystallogr.* 50 (2017) 489–497.
- [12] L.D.S. Alencar, V. Pilla, A.A. Andrade, D.A. Donatti, D.R. Vollet, F.S. De Vicente, High fluorescence quantum efficiency of CdSe/ZnS quantum dots embedded in GPTS/TEOS-derived organic/silica hybrid colloids, *Chem. Phys. Lett.* 599 (2014) 63–67.
- [13] P.H.D. Ferreira, A.J.G. Otuka, E.C. Barbano, D.S. Manoel, F.S. De Vicente, D.R. Vollet, D.A. Donatti, L. Misoguti, C.R. Mendonça, Femtosecond laser fabrication of waveguides in Rhodamine B-doped GPTS/TEOS-derived organic/silica monolithic xerogel, *Opt. Mater. (Amst).* 47 (2015) 310–314.

- [14] L.M.G. Abegão, D.S. Manoel, A.J.G. Otuka, P.H.D. Ferreira, D.R. Vollet, D.A. Donatti, L. De Boni, C.R. Mendona, F.S. De Vicente, J.J. Rodrigues, M.A.R.C. Alencar, Random laser emission from a Rhodamine B-doped GPTS/TEOS-derived organic/silica monolithic xerogel, *Laser Phys. Lett.* 14 (2017) 0–6.
- [15] F.S. de Vicente, P. Freddi, A.J.G. Otuka, C.R. Mendonça, H.F. Brito, L.A.O. Nunes, D.R. Vollet, D.A. Donatti, Photoluminescence tuning and energy transfer process from  $Tb^{3+}$  to  $Eu^{3+}$  in GPTMS/TEOS-derived organic/silica hybrid films, *J. Lumin.* 197 (2018) 370–375.
- [16] R.C. Evans, P. Douglas, C.J. Winscom, Coordination complexes exhibiting room-temperature phosphorescence: Evaluation of their suitability as triplet emitters in organic light emitting diodes, *Coord. Chem. Rev.* 250 (2006) 2093–2126.
- [17] K. Kalyanasundaram, M. Grätzel, Applications of functionalized transition metal complexes in photonic and optoelectronic devices, *Commun. Chem. Rev.* 177 (1998) 347–414.
- [18] Y. You, S.Y. Park, Phosphorescent Iridium(III) complexes: Toward high phosphorescence quantum efficiency through ligand control, *J. Chem. Soc. Dalt. Trans.* 9226 (2008) 1267–1282.
- [19] K.P.S. Zanoni, A. Ito, M. Grüner, N.Y. Murakami Iha, A.S.S. De Camargo, Photophysical dynamics of the efficient emission and photosensitization of  $[Ir(Pqi)_2(NN)]^+$  complexes, *Dalt. Trans.* 47 (2018) 1179–1188.
- [20] K.P.S. Zanoni, R.L. Coppo, R.C. Amaral, N.Y. Murakami Iha, Ir(III) complexes designed for light-emitting devices: Beyond the luminescence color array, *Dalt. Trans.* 44 (2015) 14559–14573.
- [21] A.R.G. Smith, P.L. Burn, B.J. Powell, Spin-orbit coupling in phosphorescent Iridium(III) complexes, *ChemPhysChem.* 12 (2011) 2429–2438.
- [22] L. Flamigni, A. Barbieri, C. Sabatini, B. Ventura, F. Barigelletti, Photochemistry and Photophysics of Coordination Compounds: Iridium, in: *Top. Curr. Chem.*, 2007: pp. 143–203.
- [23] T.H. and T.F. H. Yersin, A. F. Rausch, R. Czerwieniec, Charge-Transfer Excited States in Phosphorescent Organo-Transition Metal Compounds: A Difficult Case for Time Dependent Density Functional Theory?, *Coord. Chem. Rev.* 255 (2011) 2622–2652.
- [24] K.P.S. Zanoni, R.R.C. Vilela, I.D.A. Silva, N.Y. Murakami Iha, H. Eckert, A.S.S. De Camargo, Photophysical Properties of Ir(III) Complexes Immobilized in MCM-41 via Templated Synthesis, *Inorg. Chem.* 58 (2019) 4962–4971.

- [25] M.C. Grüner, K.P.S. Zanoni, C.F. Borgognoni, C.C. Melo, V. Zucolotto, A.S.S. De Camargo, Reaching Biocompatibility with Nanoclays: Eliminating the Cytotoxicity of Ir(III) Complexes, *ACS Appl. Mater. Interfaces*. 10 (2018) 26830–26834.
- [26] K.P.S. Zanoni, B.K. Kariyazaki, A. Ito, M.K. Brennaman, T.J. Meyer, N.Y. Murakami Iha, Blue-green Iridium(III) emitter and comprehensive photophysical elucidation of heteroleptic cyclometalated Iridium(III) complexes, *Inorg. Chem.* 53 (2014) 4089–4099.
- [27] C. Jaeger, F. Hemmann, EASY: A simple tool for simultaneously removing background, deadtime and acoustic ringing in quantitative NMR spectroscopy - Part I: Basic principle and applications, *Solid State Nucl. Magn. Reson.* 57–58 (2014) 22–28.
- [28] A.E. Bennett, C.M. Rienstra, M. Auger, K. V. Lakshmi, R.G. Griffin, Heteronuclear decoupling in rotating solids, *J. Chem. Phys.* 103 (1995) 6951–6958.
- [29] H. Kimura, K. Nakamura, A. Eguchi, H. Sugisawa, K. Deguchi, K. Ebisawa, E.I. Suzuki, A. Shoji, Structural study of  $\alpha$ -amino-acid crystals by  $^1\text{H}$  CRAMPS NMR spectroscopy, *J. Mol. Struct.* 447 (1998) 247–255.
- [30] M.J. Potrzebowski, P. Tekely, Y. Dusauroy, Comment to  $^{13}\text{C}$ -NMR studies of  $\alpha$  and  $\gamma$  polymorphs of glycine, *Solid State Nucl. Magn. Reson.* 11 (1998) 253–257.
- [31] N. Baccile, G. Laurent, C. Bonhomme, P. Innocenzi, F. Babonneau, Solid-state NMR characterization of the surfactant-silica interface in templated silicas: Acidic versus basic conditions, *Chem. Mater.* 19 (2007) 1343–1354.
- [32] S.C. Christiansen, N. Hedin, J.D. Epping, M.T. Janicke, Y. Del Amo, M. Demarest, M. Brzezinski, B.F. Chmelka, Sensitivity considerations in polarization transfer and filtering using dipole-dipole couplings: Implications for biomineral systems, *Solid State Nucl. Magn. Reson.* 29 (2006) 170–182.
- [33] J.W. Wiench, C.E. Bronnimann, V. S-Y Lin, M. Pruski, *Chemical Shift Correlation NMR Spectroscopy with Indirect Detection in Fast Rotating Solids: Studies of Organically Functionalized Mesoporous Silicas*, (2007).
- [34] D. Massiot, P. Dion, J.F. Alcover, F. Bergaya,  $^{27}\text{Al}$  and  $^{29}\text{Si}$  MAS NMR Study of Kaolinite Thermal Decomposition by Controlled Rate Thermal Analysis, *J. Am. Ceram. Soc.* 78 (1995) 2940–2944.
- [35] P.J. Launer, Infrared analysis of organosilicon compounds: spectra-structure correlations, in: B. Arkles, G.L. Larson (Eds.), *Silicon Compd. Silanes Silicones*, 3rd edition, Gelest Inc., Morrisville PA, 2013: pp. 175–178.



- [36] I.R. Fontinha, M.M. Salta, M.L. Zheludkevich, M.G.S. Ferreira, EIS Study of Amine Cured Epoxy-silica-zirconia Sol-gel Coatings for Corrosion Protection of the Aluminium Alloy EN AW 6063, *Port. Electrochim. Acta.* 31 (2013) 307–319.
- [37] Z. Chan, L. Ai'mei, Z. Xiao, F. Miao, H. Juan, Z. Hongbing, Microstructures and properties of ORMOSIL comprising methyl, vinyl, and  $\gamma$ -glycidoxypropyl-substituted silica. *Opt Mater (Amst)* 29 (2007) 1543–1547.
- [38] K.M. Aujara, B.W. Chieng, N.A. Ibrahim, N. Zainuddin, C.T. Ratnam, Gamma-irradiation induced functionalization of graphene oxide with organosilanes, *Int. J. Mol. Sci.* 20 (2019).
- [39] D.K. Shukla, S. V. Kasisomayajula, V. Parameswaran, Epoxy composites using functionalized alumina platelets as reinforcements, *Compos. Sci. Technol.* 68 (2008) 3055–3063.
- [40] I.M. Šapić, L. Bistričić, V. Volovšek, V. Dananić, K. Furić, DFT study of molecular structure and vibrations of 3-glycidoxypropyltrimethoxysilane, *Spectrochim. Acta - Part A Mol. Biomol. Spectrosc.* 72 (2009) 833–840.
- [41] I.M. Šapić, L. Bistričić, V. Volovšek, V. Dananić, Vibrational analysis of 3-glycidoxypropyltrimethoxysilane polymer, *Macromol. Symp.* 339 (2014) 122–129.
- [42] U. Posset, M. Lankers, W. Kiefer, H. Steins, G. Schottner, Polarized raman spectra from some sol-gel precursors and micro-raman study of one selected copolymer, *Appl. Spectrosc.* 47 (1993) 1600–1603.
- [43] B. Riegel, S. Blittersdorf, W. Kiefer, S. Hofacker, M. Müller, G. Schottner, Kinetic investigations of hydrolysis and condensation of the glycidoxypropyltrimethoxysilane/aminopropyltriethoxysilane system by means of FT-Raman spectroscopy I, *J. Non. Cryst. Solids.* 226 (1998) 76–84.
- [44] G. Engelhardt, D. Michel, *High Resolution Solid State NMR of Silicates and Zeolites*, John Wiley & Sons, Ltd, New York, USA, 1987.
- [45] M. Templin, U. Wiesner, H.W. Spiess, Multinuclear solid-state-NMR studies of hybrid organic-inorganic materials, *Adv. Mater.* 9 (1997) 814–817.
- [46] F. de Buyl, A. Kretschmer, Understanding hydrolysis and condensation kinetics of  $\gamma$ -glycidoxypropyltrimethoxysilane, *J. Adhes.* 84 (2008) 125–142.
- [47] P. Innocenzi, C. Figus, T. Kidchob, M. Valentini, B. Alonso, M. Takahashi, Sol-gel reactions of 3-glycidoxypropyltrimethoxysilane in a highly basic aqueous solution, *Dalt. Trans.* (2009) 9146–9152.

- [48] N.R. Babij, E.O. McCusker, G.T. Whiteker, B. Canturk, N. Choy, L.C. Creemer, C.V.D. Amicis, N.M. Hewlett, P.L. Johnson, J.A. Knobelsdorf, F. Li, B.A. Lorsbach, B.M. Nugent, S.J. Ryan, M.R. Smith, Q. Yang, NMR Chemical Shifts of Trace Impurities: Industrially Preferred Solvents Used in Process and Green Chemistry, *Org. Process Res. Dev.* 20 (2016) 661–667.
- [49] H.E. Gottlieb, V. Kotlyar, A. Nudelman, NMR Chemical Shifts of Common Laboratory Solvents as Trace Impurities, 1997.
- [50] G. Buntkowsky, H. Breitzke, A. Adamczyk, F. Roelofs, T. Emmler, E. Gedat, B. Grünberg, Y. Xu, H.-H. Limbach, I. Shenderovich, A. Vyalikh, G. Findenegg, Structural and dynamical properties of guest molecules confined in mesoporous silica materials revealed by NMR, *Phys. Chem. Chem. Phys.* 9 (2007) 4843.
- [51] V. Marin, E. Holder, R. Hoogenboom, E. Tekin, U.S. Schubert, Light-emitting Iridium(III) and Ruthenium(II) polypyridyl complexes containing quadruple hydrogen-bonding moieties, (2006).
- [52] K.P.S. Zaroni, N.Y. Murakami Iha, Sky-blue OLED through PVK:[Ir(Fppy)<sub>2</sub>(Mepic)] active layer, *Synth. Met.* 222 (2016) 393–396.
- [53] S.A. Moore, D.L. Davies, M.M. Karim, J.K. Nagle, M.O. Wolf, B.O. Patrick, Photophysical behaviour of cyclometalated Iridium(III) complexes with phosphino(terthiophene) ligands, *Dalt. Trans.* 42 (2013) 12354–12363.

## 4. Photophysical properties of Ir(III) complexes immobilized in MCM-41 via templated synthesis

## Photophysical Properties of Ir(III) Complexes Immobilized in MCM-41 via Templated Synthesis

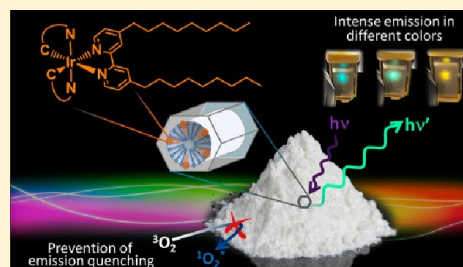
Kassio P. S. Zaroni,<sup>\*,†,‡,⊕</sup> Raquel R. C. Vilela,<sup>†</sup> Igor D. A. Silva,<sup>†</sup> Neyde Y. Murakami Iha,<sup>‡,⊕</sup> Hellmut Eckert,<sup>†,⊕</sup> and Andrea S. S. de Camargo<sup>\*,†</sup>

<sup>†</sup>Laboratório de Espectroscopia de Materiais Funcionais, Instituto de Física de São Carlos, Universidade de São Paulo, 13566-590 São Carlos, São Paulo, Brazil

<sup>‡</sup>Laboratório de Fotoquímica e Conversão de Energia, Departamento de Química Fundamental, Instituto de Química, Universidade de São Paulo, 05508-900 São Paulo, São Paulo, Brazil

### Supporting Information

**ABSTRACT:** In the search for understanding and improving the luminescence of optical materials based on Ir(III) complexes, three  $[\text{Ir}(\text{C}^{\wedge}\text{N})_2(\text{dnbp})]^+$  (dnbp = 4,4'-dinonyl-2,2'-bipyridine) emitters were immobilized in MCM-41 mesoporous nanoparticles. By taking advantage of the amphiphilic nature of  $[\text{Ir}(\text{C}^{\wedge}\text{N})_2(\text{dnbp})]^+$ , the complexes were mixed with an appropriate surfactant and the resulting micelles served as templates for the synthesis of mesoporous silica host materials in a one-step sol-gel route. The MCM-encapsulated  $[\text{Ir}(\text{C}^{\wedge}\text{N})_2(\text{dnbp})]^+$  complexes present intense emissions with prominent rigidochromic spectral changes that are substantially less affected by  $\text{O}_2$  as compared to methanolic solutions, with a thousand-fold decrease in quenching rate constants. These photophysical results points to a possible suitability of Ir(III)-complex-MCM-41 host-guest systems for possible future optoelectronic devices, rigidity optical sensors, or biological markers in different colors.



### INTRODUCTION

New materials based on heteroleptic Ir(III) complexes have attracted considerable attention in the fields of light-emitting devices and panels, sensing, organelle-targeting, photo-oxidation, controlled DNA damage, photodynamic therapy, and theranostics due to their unique and strategic photophysical features.<sup>1–20</sup> In general, these complexes exhibit high emission quantum yields (as high as ~100%), relatively short excited state lifetimes (0.1–2.5  $\mu\text{s}$ ), emission colors (over a wide range from blue to red) tunable by molecular engineering, high sensitivity to quenching by triplet oxygen, and very effective singlet oxygen photosensitization.<sup>3,8,9,11,21–29</sup> Also, their photophysical properties, such as spectral shape, lifetime, and nature of the emissive state, are highly sensitive to the surrounding environment.<sup>3,30</sup> Some of the challenges for successful applications of Ir(III)-phosphors are enhancing their stability in solid host structures and preventing rapid energy transfer processes between high- and low-energy emitters, such as the emission quenching caused by exposure to molecular oxygen.

The dispersion of these complexes within inorganic porous solid host materials can potentially enhance their photostability as compared to solutions.<sup>30</sup> Particularly, mesoporous silica hosts have been widely employed for the encapsulation of large guest molecules, with applications in optical materials and

photodynamic therapy.<sup>2,30–42</sup> Many approaches have been demonstrated for the development of silica-based host-guest materials, usually by coassembly of gel-forming solutions containing the molecule of interest and an appropriate silica precursor. For example, this method has been successfully used to prepare new optical materials by incorporating iridium- and ruthenium-based luminescent surfactant complexes into mesoporous silica.<sup>36,43</sup>

Herein we describe the encapsulation and photophysical behavior of three amphiphilic Ir(III) complexes of the  $[\text{Ir}(\text{C}^{\wedge}\text{N})_2(\text{dnbp})]^+$  series (dnbp = 4,4'-dinonyl-2,2'-bipyridine) inside MCM-41 host-guest systems. Derived from highly emissive  $[\text{Ir}(\text{C}^{\wedge}\text{N})_2(\text{dmb})]^+$  parent complexes (dmb = 4,4'-dimethyl-2,2'-bipyridine), the  $[\text{Ir}(\text{C}^{\wedge}\text{N})_2(\text{dnbp})]^+$  compounds combine the photophysical properties of the parent complexes with the ability to produce micelles. The precursor ligands are commercially available, and the chemical structures of the final complexes are relatively simple, allowing syntheses through straightforward chemical reactions. To represent the  $[\text{Ir}(\text{C}^{\wedge}\text{N})_2(\text{dnbp})]^+$  series, complexes  $[\text{Ir}(\text{Fppy})_2(\text{dnbp})]\text{Cl}$ ,  $[\text{Ir}(\text{ppy})_2(\text{dnbp})]\text{Cl}$ , and  $[\text{Ir}(\text{pqi})_2(\text{dnbp})]\text{Cl}$  (Fppy = 2-(2,4-difluorophenyl)pyridinate; ppy = 2-phenylpyridinate; pqi = 2-

Received: December 28, 2018

Published: April 1, 2019

## Abstract

In the search for understanding and improving the luminescence of optical materials based on Ir(III) complexes, three  $[\text{Ir}(\text{C}^{\wedge}\text{N})_2(\text{dnbp})]^+$  ( $\text{dnbp}$  = 4,4'-dinonyl-2,2'-bipyridine) emitters were immobilized in MCM-41 mesoporous nanoparticles. By taking advantage of the amphiphilic nature of  $[\text{Ir}(\text{C}^{\wedge}\text{N})_2(\text{dnbp})]^+$ , the complexes were mixed with an appropriate surfactant and the resulting micelles served as templates for the synthesis of mesoporous silica host materials in a one-step sol-gel route. The MCM-encapsulated  $[\text{Ir}(\text{C}^{\wedge}\text{N})_2(\text{dnbp})]^+$  complexes present intense emissions with prominent rigidochromic spectral changes that are substantially less affected by  $\text{O}_2$  as compared to methanolic solutions, with a thousand-fold decrease in quenching rate constants. These photophysical results points to a possible suitability of Ir(III)-complex–MCM-41 host–guest systems for possible future optoelectronic devices, rigidity optical sensors, or biological markers in different colors.

**Keywords:** Ir(III) complex; MCM-41; Optical materials; Emission quenching; Photophysics.

## Introduction

New materials based on heteroleptic Ir(III) complexes have attracted considerable attention in the fields of light-emitting devices and panels, sensing, organelle-targeting, photo-oxidation, controlled DNA damage, photodynamic therapy and theranostics due to their unique and strategic photophysical features [1–20]. In general, these complexes exhibit high emission quantum yields (as high as ~100%), relatively short excited state lifetimes (0.1–2.5  $\mu\text{s}$ ), wide range of emission colors (from blue to red) tunable by molecular engineering, high sensitivity to quenching by triplet oxygen and very effective singlet oxygen photosensitization [3, 8, 9, 11, 21–29]. Also, their photophysical properties – such as spectral shape, lifetime and nature of the emissive state – are highly sensitive to the surrounding environment [3, 30]. Some of the challenges for successful applications of Ir(III)-phosphors are enhancing their stability in solid host structures and preventing rapid energy transfer processes between high- and low-energy emitters, such as the emission quenching caused by exposure to molecular oxygen.

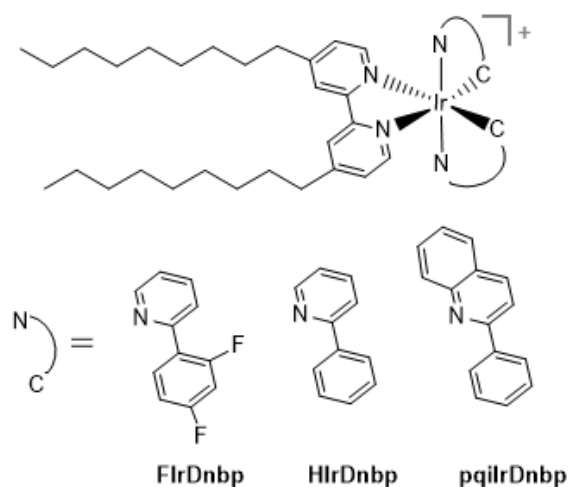
The dispersion of these complexes within inorganic porous solid host materials can potentially enhance their photostability as compared to solutions [30]. Particularly, mesoporous silica hosts have been widely employed for the encapsulation of large guest molecules, with applications in optical materials and photodynamic therapy [2, 30–42]. Many approaches have been demonstrated for the development of silica-based host–guest materials, usually by co-assembly of gel-forming solutions containing the molecule of interest and an appropriate silica

precursor. For example, this method has been successfully used to prepare new optical materials by incorporating iridium- and ruthenium-based luminescent surfactant complexes into mesoporous silica [36, 43].

Herein we describe the encapsulation and photophysical behavior of three amphiphilic Ir(III) complexes of the  $[\text{Ir}(\text{C}^{\wedge}\text{N})_2(\text{dnbp})]^+$  series ( $\text{dnbp} = 4,4'$ -dinonyl-2,2'-bipyridine) inside MCM-41 host-guest systems. Derived from highly-emissive  $[\text{Ir}(\text{C}^{\wedge}\text{N})_2(\text{dmb})]^+$  parent complexes ( $\text{dmb} = 4,4'$ -dimethyl-2,2'-bipyridine), the  $[\text{Ir}(\text{C}^{\wedge}\text{N})_2(\text{dnbp})]^+$  compounds combine the photophysical properties of the parent complexes with the ability to produce micelles. The precursor ligands are commercially available and the chemical structures of the final complexes are relatively simple, allowing syntheses through straightforward chemical reactions. To represent the  $[\text{Ir}(\text{C}^{\wedge}\text{N})_2(\text{dnbp})]^+$  series, complexes  $[\text{Ir}(\text{Fppy})_2(\text{dnbp})]\text{Cl}$ ,  $[\text{Ir}(\text{ppy})_2(\text{dnbp})]\text{Cl}$  and  $[\text{Ir}(\text{pqi})_2(\text{dnbp})]\text{Cl}$  ( $\text{Fppy} = 2$ -(2,4-difluorophenyl)pyridinate;  $\text{ppy} = 2$ -phenylpyridinate;  $\text{pqi} = 2$ -phenylquinolate), respectively, named FIrDnbp, HIrDnbp and pqiIrDnbp, Chart 1, were synthesized aiming at a variation of emission colors, which could be achieved by changing the nature of the cyclometalated  $\text{C}^{\wedge}\text{N}$  ligands. Micelles containing the amphiphilic Ir(III) complexes were encapsulated (while serving as pore templates) within the MCM-41 matrix, exhibiting emission in assorted colors.

This work expands previous photophysical studies of Ir(III)-complex-MCM-41 host-guest systems by exploring new insights into rigidochromism and the excited state nature as well as quantifying competitive energy transfer and emission quenching processes in the matrix via quenching constant calculations, time-resolved emission spectra and analyzes of emission properties of sample mixtures. The synthesis, characterization, and application of pqiIrDnbp is reported for the first time. This is also the first work to apply FIrDnbp and HIrDnbp complexes in silica mesopores and to characterize the photophysical properties of these host-guest materials. Previous studies were limited to solutions and in thin films towards applications as labeling agents, polymerization photoinitiator and active molecular emitters located within the interlayer space of clay compounds and in other light-emitting devices [44–52].

**Chart 1.** Chemical structures of the investigated  $[\text{Ir}(\text{C}^{\wedge}\text{N})_2(\text{dnbp})]^+$  complexes.



## Results and discussion

### *Synthesis of the Complexes*

The investigated  $[\text{Ir}(\text{C}^{\wedge}\text{N})_2(\text{dnbp})]^+$  series have two bidentate  $\text{C}^{\wedge}\text{N}$  ligands disposed in a *trans*-N,N configuration. Before coordination, the phenyl moiety of the  $\text{C}^{\wedge}\text{N}$  ligands disposes of a proton from the ortho position to the pyridyl ring. The negatively charged C and the pyridyl's N atoms both coordinate strongly to Ir(III) in a 5-membered metallocycle. The third ligand to coordinate to Ir(III) is *dnbp*, a bidentate electrically-neutral diimine carrying nonyl chains. Thus, the  $[\text{Ir}(\text{C}^{\wedge}\text{N})_2(\text{dnbp})]^+$  complexes are amphiphilic, with a polar moiety in the charged (+1) metal center and two long apolar chains in the *dnbp* ligand.

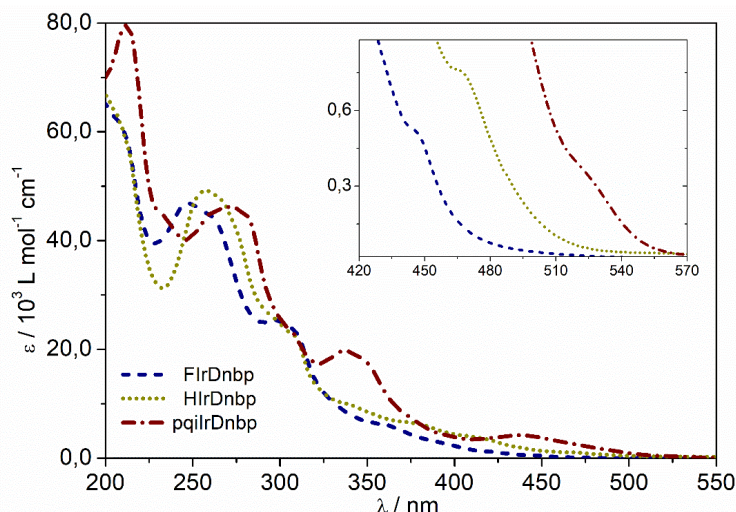
The *trans*-N,N prevalence as the sole isomer is a characteristic of the Nonoyama synthesis procedure [3, 44, 53, 54] as proven by  $^1\text{H}$  NMR (Figures S1-3 in the Supporting Information). The spectra indicate the sole presence of the *trans*-N,N isomer ( $\text{C}_2$  symmetry), in which the  $\text{C}_2$  axis bisects the *dnbp* ligand and the two  $\text{C}^{\wedge}\text{N}$  ligands are equivalent. Additional characterization by mass spectrometry and FT-IR spectroscopy are summarized in the Supporting Information.

### *Photophysics of $[\text{Ir}(\text{C}^{\wedge}\text{N})_2(\text{dnbp})]^+$ in methanol*

At 298 K, the absorption spectra of  $[\text{Ir}(\text{C}^{\wedge}\text{N})_2(\text{dnbp})]^+$  methanolic solutions, Figure 1, exhibit intense bands in the UV ascribed to singlet ligand-centered ( $^1\text{LC}$ ,  $\pi \rightarrow \pi^*$ ) transitions in the  $\text{C}^{\wedge}\text{N}$  and/or *NN* ligands, which overlaps with much less intense  $d(t_{2g}) \rightarrow d(e_g)$  transitions. Less intense absorptions in the visible are assigned to overlapping metal-to-ligand charge

transfer (MLCT,  $d(t_{2g}) \rightarrow \pi^*$ ) and ligand-to-ligand charge transfer bands (LLCT,  $\pi \rightarrow \pi^*$  from a ligand A to another ligand B) and LC excited states [3, 21, 24, 25, 30].

**Figure 1.** Absorption spectra of  $[\text{Ir}(\text{C}^{\wedge}\text{N})_2(\text{dnbp})]^+$  complexes in methanol at 298 K. The inset shows a zoomed view of the 420 - 570 nm spectral range.



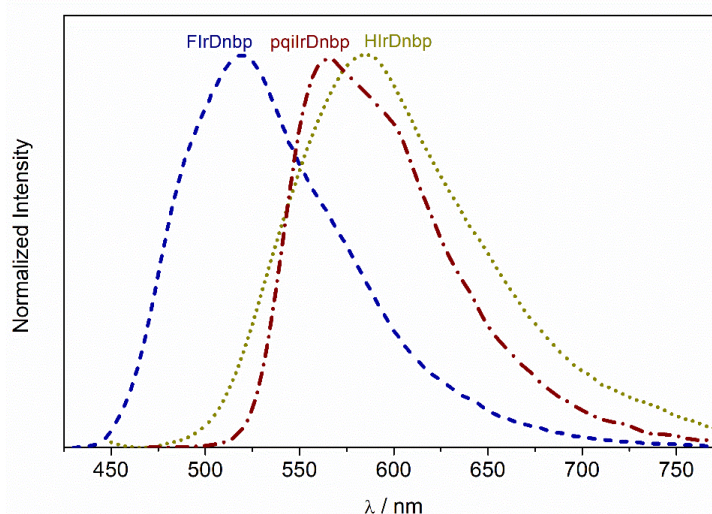
Due to the strong spin-orbit coupling (SOC) exerted by the Ir(III) core, the overlapped excited states in the visible present high degrees of SOC-induced mixing, both in spin and in electronic character [3, 26, 27]. For example, their low-intensity shoulder in the 420-570 nm region, inset in Figure 1, is indicative of a direct absorption into their lowest-lying triplet excited state ( $T_1$ ), which normally should be spin-forbidden [3, 26, 27]. The strong SOC also facilitates rapid population of  $T_1$  after excitation at any wavelength. For the investigated complexes, deactivation processes from  $T_1$  occur mainly by intersystem crossing, leading to intense phosphorescence, Figure 2, with emission properties summarized in Table 1.

**Table 1.** Emission properties of  $[\text{Ir}(\text{C}^{\wedge}\text{N})_2(\text{dnbp})]^+$  complexes in degassed methanol at 298 K.

Compound	$\lambda_{max} /$ nm <sup>a</sup>	$\phi / \%$ <sup>b</sup>			$\tau_0 /$ $\mu\text{s}$ <sup>c</sup>	$k_r /$ $10^5 \text{ s}^{-1}$ <sup>d</sup>	$k_{nr} /$ $10^6 \text{ s}^{-1}$ <sup>d</sup>	$P_{O_2}^{T_1}$ <sup>e</sup>	$k_q /$ $10^9 \text{ L mol}^{-1} \text{ s}^{-1}$ <sup>f</sup>
		N <sub>2</sub> - saturated ( $\phi_0$ )	Air- equilibrated	O <sub>2</sub> - saturated					
<b>FIrDnbp</b>	519	89 ± 3	9.0	2.2	1.1	8.1	0.10	0.97	3.5
<b>HIrDnbp</b>	585	25 ± 1	3.4	1.3	0.6	4	1	0.94	3
<b>pqiIrDnbp</b>	564	71 ± 2	8.3	2.5	2.3	3.1	0.13	0.96	1.2

<sup>a</sup> Wavelength at the emission maximum; <sup>b</sup> Absolute emission quantum yield, measured using an integrating sphere; <sup>c</sup> emission lifetime in N<sub>2</sub>-saturated solution; <sup>d</sup> radiative and nonradiative decay rate constants in N<sub>2</sub> saturated solution; <sup>e</sup> Fraction of  $T_1$  states quenched by <sup>3</sup>O<sub>2</sub> in O<sub>2</sub>-saturated solutions; <sup>f</sup> Quenching rate constant. See data treatment in the Experimental Section in the Supporting Information.

**Figure 2.** Emission spectra of  $[\text{Ir}(\text{C}^{\wedge}\text{N})_2(\text{dnbp})]^+$  complexes in  $\text{N}_2$ -saturated methanol at 298 K ( $\lambda_{\text{exc}} = 370$  nm).



Analyses of emission quantum yields ( $\phi$ ) and emission lifetimes ( $\tau$ ) reveal intense microsecond-lived luminescence, typical of Ir(III) emitters. The photophysical properties exhibited herein are in agreement with previously published results for the complex series [44–46, 49, 50, 52]; They are also very similar to the ones observed for their  $[\text{Ir}(\text{C}^{\wedge}\text{N})_2(\text{dmb})]^+$  parent complexes in acetonitrile at 298 K [21, 23] because both series share the same  $\pi$  and  $\pi^*$  orbitals, with differences arising exclusively from the  $\sigma$  apolar groups (methyl or nonyl). Thus, the electronic structures differ solely in the energies required for the  $\sigma \rightarrow \sigma^*$ ,  $\sigma \rightarrow \pi^*$  or  $\pi \rightarrow \sigma^*$  transitions, which are much higher than for the  $\pi \rightarrow \pi^*$  transitions.

FIrDnbp and HIrDnbp exhibit a broad emission band, a characteristic feature of  $T_1$  states with a major MLCT character, while the emission band for pqiIrDnbp is relatively narrow, resolved in vibronic modes, which is a characteristic feature for LC emissions. Based on TD-DFT calculations for  $[\text{Ir}(\text{Fppy})_2(\text{dmb})]^+$  [21] the FIrDnbp emissive  $T_1$  state is better ascribed to a SOC-induced hybrid  ${}^3\text{MLCT}_{\text{Ir}(\text{Fppy}) \rightarrow \text{dnbp}}/\text{LC}_{\text{dnbp}}$  state, in which the  ${}^3\text{MLCT}_{\text{Ir}(\text{Fppy}) \rightarrow \text{dnbp}}$  counterpart exerts a higher contribution. On the other hand, HIrDnbp presents a pure  ${}^3\text{MLCT}_{\text{Ir}(\text{ppy}) \rightarrow \text{dnbp}}$   $T_1$  state, as demonstrated by DFT calculations previously reported for this complex [45, 46] or even for the parent complex  $[\text{Ir}(\text{ppy})_2(\text{dmb})]^+$  [21]. Finally, based on TD-DFT investigations for  $[\text{Ir}(\text{pqi})_2(\text{dmb})]^+$  [23], the  $T_1$  state for pqiIrDnbp has a hybrid  ${}^3\text{LC}/\text{MLCT}_{\text{Ir}(\text{pqi}) \rightarrow \text{pqi}}$  nature, with stronger influences from the  $\text{LC}_{\text{pqi}}$  counterpart due to a small  $\pi_{\text{pqi}} - \pi^*_{\text{pqi}}$  energy gap.



*Emission quenching of [Ir(C^N)<sub>2</sub>(dnbp)]<sup>+</sup> in methanol*

In methanol, the investigated complexes undergo rapid quenching by molecular triplet oxygen (<sup>3</sup>O<sub>2</sub>), a characteristic drawback of long-lived triplet emitters [23, 55–58]. The quenching of the complex's T<sub>1</sub> by <sup>3</sup>O<sub>2</sub> can sensitize singlet oxygen (<sup>1</sup>O<sub>2</sub><sup>\*</sup>) [59, 60], whose deactivation through a characteristic narrow phosphorescence around 1270 nm cannot be observed by the naked eye. As a consequence, the emission intensity of the investigated complexes drastically decreases in air-equilibrated methanol solutions ([<sup>3</sup>O<sub>2</sub>] = 2.5 × 10<sup>-3</sup> mol L<sup>-1</sup>), with quantum yield losses of ~89%. The fraction of T<sub>1</sub> states quenched by <sup>3</sup>O<sub>2</sub> (P<sub>O<sub>2</sub></sub><sup>T<sub>1</sub></sup>) in O<sub>2</sub>-saturated solutions ([<sup>3</sup>O<sub>2</sub>] = 10.5 × 10<sup>-3</sup> mol L<sup>-1</sup>) is even higher, approximately 95%, Table 1.

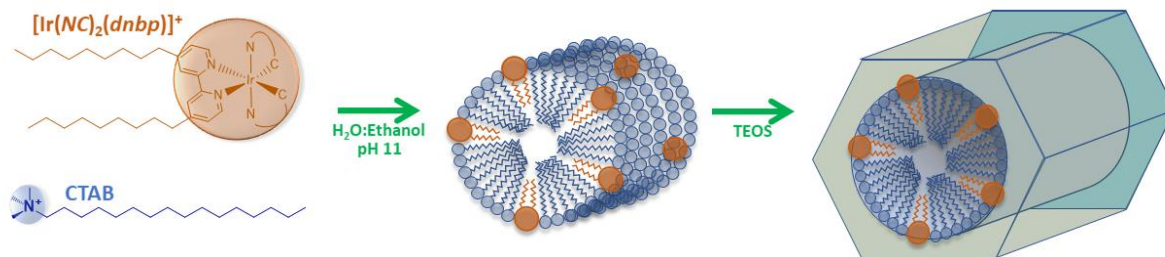
The quenching rate constants (*k<sub>q</sub>*) obtained from Stern–Volmer plots (Figures S4–S7 in the Supporting Information) are summarized in Table 1. The magnitude of their *k<sub>q</sub>* (1.2–3.5 × 10<sup>9</sup> L mol<sup>-1</sup> s<sup>-1</sup>) is similar to the ones observed for other Ru(II), Os(II) and Ir(III) phosphors [1, 7, 23, 61].

*Encapsulation of [Ir(C^N)<sub>2</sub>(dnbp)]<sup>+</sup> in MCM-41*

When added to ethanolic solutions containing hexadecyltrimethylammonium bromide (CTAB) at pH 11 (see the experimental section), the long nonyl groups of the *dnbp* ligand allow the incorporation of the complexes in the CTAB's micelles, as depicted in Figure 3. Subsequent addition of tetraethylorthosilicate (TEOS) – a well-known silica precursor – leads to the sol–gel formation of silica nanoparticles with well-ordered mesopores in a hexagonal crystal lattice templated by the CTAB:complex micelles. To facilitate the discussion, the encapsulated samples are named complex@MCM-41.

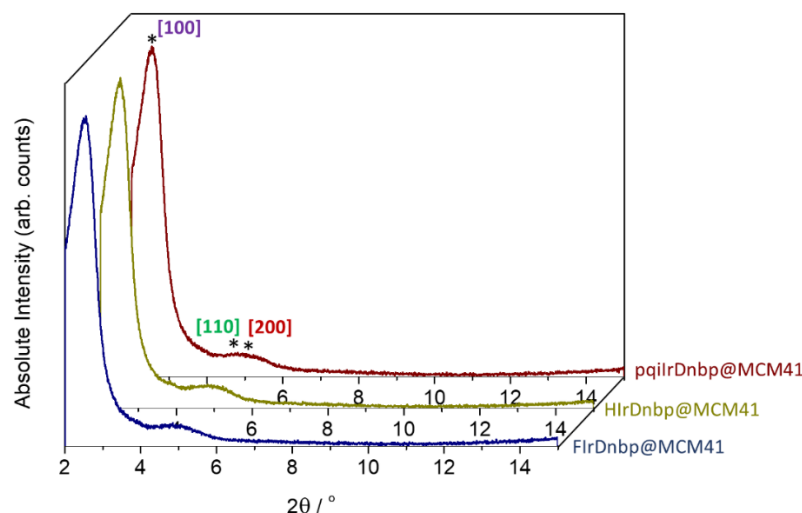
We note that: i) ethanolic/aqueous solutions of complexes without CTAB are not able to form stable micelles, hence a silica prepared using the complexes alone would not result in the desired MCM-41 morphology; ii) the CTAB:complex encapsulation approach ensures a high levels of Ir(III) emitter retention, higher than obtained by surface modification or grafting [30, 38]; iii) washing the as synthesized complex@MCM-41 samples with ethanol for four consecutive times ensures complete removal of excess templates not encapsulated; iv) additional successive washings with ethanol does not remove the retained CTAB:complex, as proven by clear UV-Vis spectra of the solutions; v) CTAB does not affect the photophysical properties of the investigated guest complexes.

**Figure 3.** Sol-gel encapsulation of  $[\text{Ir}(\text{C}^{\wedge}\text{N})_2(\text{dnbp})]^+$  complexes inside MCM-41 mesopores.



The X ray diffraction patterns of the as-prepared nanoparticles (non-calcined), Figure 4, are similar and independent of the nature of the encapsulated complex, presenting diffraction peaks around  $2.5^\circ$ ,  $4.7^\circ$  and  $5.2^\circ$ , assigned to [100], [110] and [200] plane directions, respectively [62]. These results are typical of hexagonal MCM-41 silica, space group  $P6mm$  [63]. Comparison with the XRD pattern of a blank sample of MCM-41 (Figure S8 in the Supporting Information) confirms that the introduction of the Ir(III) complexes into the CTAB micelles does not affect the structural integrity of the host. Two further diffraction peaks characteristic of MCM-41 nanoparticles, [210] and [300], could not be observed in our materials.

**Figure 4.** XRD patterns of the developed complex@MCM-41 nanoparticles (non-calcined).

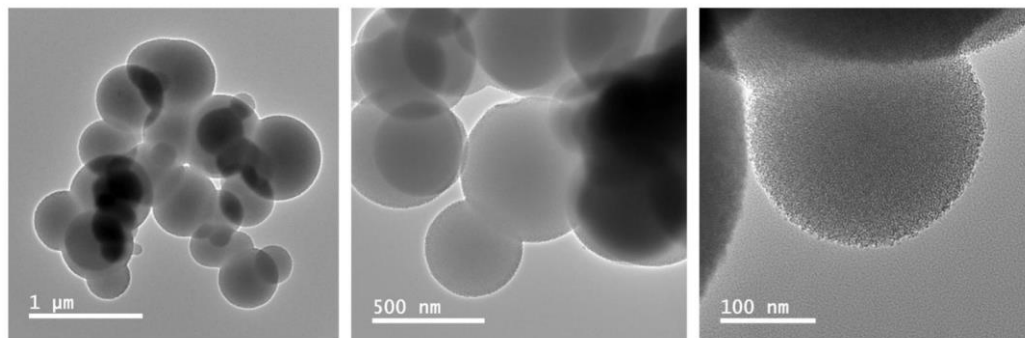


The  $d$ -spacings ( $d_{[hkl]}$ ) for the observed [100], [110] and [200] plane directions are 35 Å, 19 Å and 17 Å, respectively, as calculated by Bragg's law. The average lattice constant ( $a_0$ ) for the so-obtained hexagonal MCM-41 is 40.8 Å.

Transmission electron microscopy (TEM) data in Figure 5 reveal that the produced silica nanoparticles are spherical (average diameter =  $0.51 \pm 0.15 \mu\text{m}$ ) and highly porous.

Unfortunately, the equipment resolution was too low to allow observation of the hexagonal ordering of the tubular mesopores.

**Figure 5.** TEM images of complex@MCM-41 nanoparticles.



The N<sub>2</sub> sorption isotherms for the developed nanoparticles (samples were calcined at 500 °C for this experiment) present a type IV isotherm without hysteresis at any relative pressures (Figure S9 in the Supporting Information), typical for MCM-41 silica bearing very small mesopores [64]. The pore volumes ( $V_t$ ), surface areas ( $S_{BET}$ ) and pore sizes ( $W_{KJS}$ ) of the three samples (summarized in Table 2) are analogous to those of a blank sample produced with no complexes inside the CTAB micelles (keeping in mind that the systematic errors involved in pore analyses of reversible type IV isotherms are relatively high and that the BET equation has been developed for solids having uniformly distributed cylindrical pores). These results confirm that insertion of Ir(III) complexes does not change the final structure of the host. Due to their very-high porosity, the prepared samples, including the blank, present large  $S_{BET}$  ( $\sim 1,6 \times 10^3 \text{ m}^2 \text{ g}^{-1}$ ). Their average  $W_{KJS}$  ( $\sim 29 \text{ \AA}$ ) are consistent with their small lattice constants. The average thickness of the silica structure between two mesopores (i.e.  $d_{[100]} - W_{KJS}$ ) can be estimated as  $\sim 6 \text{ \AA}$ .

<sup>19</sup>F MAS NMR was employed to quantify the amount of encapsulated FIrDnbp complex remaining in the pores following template removal. For this purpose, four physical mixtures of both pure FIrDnbp complex and MCM-41 powders were prepared (see Experimental section for details) and their 25.0 kHz MAS NMR spectra were obtained. Figure 6 shows the spectra found for (a) pure solid FIrDnbp complex, (b) FIrDnbp@MCM-41, and (c) the physical mixture containing 1 mg of FIrDnbp powder diluted in 98 mg of blank MCM-41 (non-calcined) as a representative of all four physical mixtures. For pure FIrDnbp complex, a peak is observed around  $\delta = -107.5 \text{ ppm}$  vs.  $\text{CFCl}_3$ , while for FIrDnbp@MCM-41, the signal is found at  $\delta = -122.8 \text{ ppm}$  as a result of the change in the local environment of the <sup>19</sup>F nuclei after encapsulation

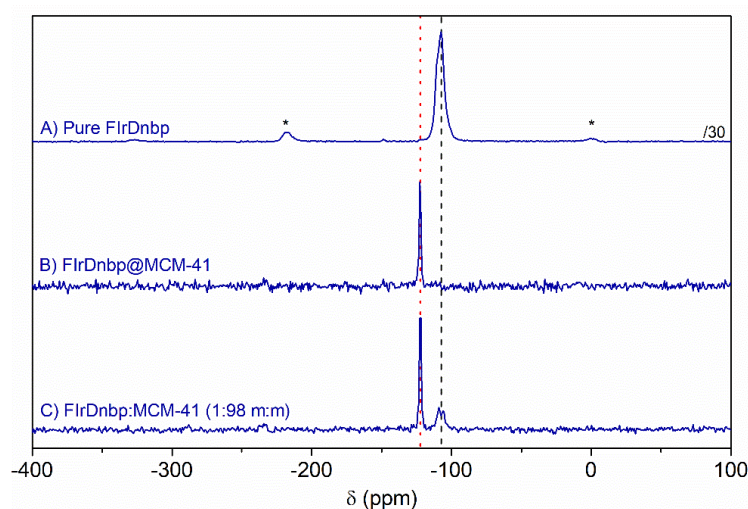
into the MCM-41 pores. For spectra of the physical mixtures, both features are spotted, which indicate that merely grinding the powders in a mortar is also able to insert some FIrDnbp inside MCM-41 mesopores; evidently, however, complexes inserted by such a simple process are easily washable away.

**Table 2.** Mesopore parameters of the developed complex@MCM-41 nanoparticles (calcined at 500 °C).

Sample	$V_t / 10^{-6} \text{ m}^3 \text{ g}^{-1}$ <sup>a</sup>	$S_{\text{BET}} / 10^3 \text{ m}^2 \text{ g}^{-1}$ <sup>b</sup>	$W_{\text{KJS}} / \text{nm}$ <sup>c</sup>
<b>FIrDnbp@MCM-41</b>	0.72	1.6	2.7
<b>HIrDnbp@MCM-41</b>	0.84	1.7	2.9
<b>pqiIrDnbp@MCM-41</b>	0.80	1.7	2.9
<b>MCM-41 (blank)</b>	0.85	1.6	3.0

<sup>a</sup> Pore volume; <sup>b</sup> Superficial area; <sup>c</sup> Pore size determined at the maximum of the pore size distributions, calculated by the KJS method [65].

**Figure 6.** <sup>19</sup>F MAS NMR spectra at 25 kHz for (A) pure FIrDnbp complex, (B) FIrDnbp@MCM-41, and (C) physical mixture containing FIrDnbp (1 mg) diluted in blank MCM-41 (98 mg). Dashed lines mark  $\delta = -107.5$  ppm (black - - -) and  $\delta = -122.8$  ppm (red · · ·). Spinning side-bands are marked with asterisks. To improve visualization of features the spectrum (A) was divided by 30. All spectra were normalized by mass and number of scans.

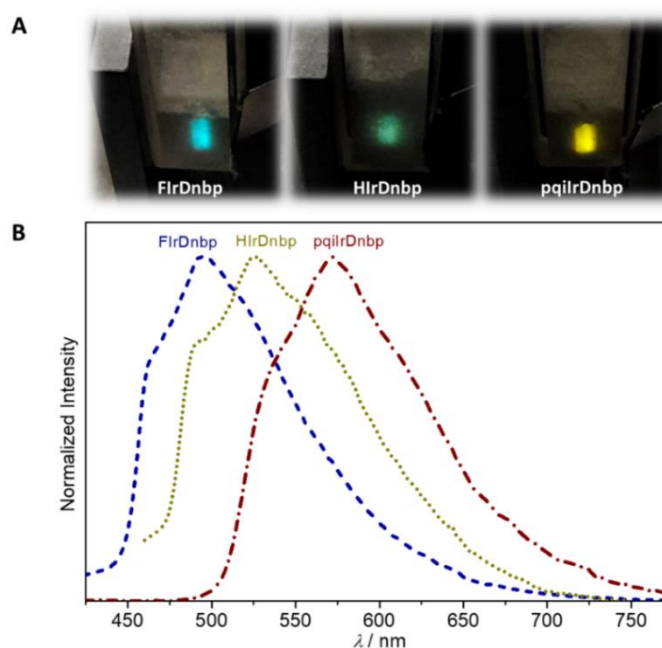


The total areas of the NMR spectra for the physical mixtures were obtained by peak integration and compared (in Figure S10 in the Supporting Information) to the total area of the spectrum from FIrDnbp@MCM-41, normalized by sample mass and number of scans. With this procedure, we found that the real FIrDnbp:MCM-41 ratio is near 1 mg:98 mg (or 1 mol:1.6 kmol) in the final sample, a result that can be extrapolated to the other two complex@MCM-41 as well, since the sizes of the complexes are approximately similar.

*Photophysical properties of complex@MCM-41*

Irradiation of the developed complexes@MCM-41 at 298 K (xenon lamp,  $\lambda_{\text{exc}} = 365$  nm, 1 nm bandwidth, 400 nm long pass filter) results in intense emission in a wide color array, Figure 7A, with properties summarized in Table 3. The emission originates exclusively from the radiative deactivation of the complex's  $T_1$  and thus depends on the nature of the complex, with the spectra shown in Figure 7B. The contribution of the silica host's emission in the near UV and blue is negligible. Worth noting, the emission intensity was constant even after three additional washes with ethanol (the same solvent used in the encapsulation process), indicating zero (or very low) leakage. Thus, the chromophores that remain incorporated after the initial four washing cycles following the synthesis remain completely trapped inside the bulky MCM-41 mesopores.

**Figure 7.** (A) Photographs and (B) spectra of the emission of  $[\text{Ir}(\text{C}^{\wedge}\text{N})_2(\text{dnbp})]^+$  complexes encapsulated in MCM-41 nanoparticles under  $\text{N}_2$  atmosphere at 298 K ( $\lambda_{\text{exc}} = 360$  nm).



The complex@MCM-41 nanoparticles present medium-high quantum yields ( $\phi$ ), Table 3, with similar magnitudes to e.g. anthracene crystals, a standard emissive crystalline material [66, 67]. The values are lower than in solution, however such a comparison is not straightforward. In opposite to the translucent solvent, the intense scattering of the internal silica walls stands as an internal filter to the emitted light and additionally imposes a barrier to the excitation light to reach the encapsulated complexes. In this regard, the terms in Eq. S11 (in the

supporting information) are too sensitive, because they will strongly depend on the amount and positioning of the samples, hence the errors are high.

**Table 3.** Photophysical parameters of  $[\text{Ir}(\text{C}^{\wedge}\text{N})_2(\text{dnbp})]^+$  complexes encapsulated in MCM-41 nanoparticles at 298 K.

Sample	$\lambda_{\text{max}} /$ nm <sup>a</sup>	$\phi / \%$ <sup>b</sup>			$\varpi$ <sup>c</sup>				$P_{\text{O}_2}^{\text{T}_1}$ <sup>d</sup>	$k_q /$ 10 <sup>6</sup> L mol <sup>-1</sup> s <sup>-1</sup> e
		N <sub>2</sub> ( $\phi_0$ )	Air	O <sub>2</sub>	$\tau_1 / \mu\text{s}$	$A_1$	$\tau_2 / \mu\text{s}$	$A_2$		
<b>FIrDnbp@MCM-41</b>	494	30	22	18	0.4±0.1	0.49	1.9±0.1	0.56	0.39	7.6
<b>HIrDnbp@MCM-41</b>	528	20	18	14	0.5±0.1	0.65	2.2±0.1	0.42	0.30	4.4
<b>pqiIrDnbp@MCM-41</b>	570	25	17	12	1.0±0.1	0.64	3.5±0.2	0.38	0.53	7.2

<sup>a</sup> Wavelength at the emission maximum; <sup>b</sup> Absolute emission quantum yield, measured using an integrating sphere; <sup>c</sup> Fraction of T<sub>1</sub> states quenched by <sup>3</sup>O<sub>2</sub> in O<sub>2</sub> atmosphere; <sup>d</sup> Quenching rate constant calculated using  $\tau_2$  in the Stern-Volmer equation. See data treatment in the Experimental Section of the Supporting Information.

The emission spectra of FIrDnbp and HIrDnbp in rigid MCM-41 are blueshifted in comparison to their luminescence in fluid methanolic solutions ( $\Delta\lambda_{\text{max}} > 25$  nm). This is ascribed to the rigidochromic effect [3, 68–71] that destabilizes MLCT states (with high dipole moments) in rigid media, but does not affect LC transitions (with practically zero dipole moments). Additionally, the vibronic structure of the emission profile for FIrDnbp and HIrDnbp is better resolved in the rigid silica matrix than in fluid methanol.

For comparison, FIrDnbp and HIrDnbp were also dispersed in transparent PMMA films, which are rigid matrices more commonly used to explore the rigidochromism of <sup>3</sup>MLCT emitters. As exhibited in Figure S11 in the Supporting Information, the emission profiles in PMMA films resemble those in MCM-41, with similar blueshifted  $\lambda_{\text{max}}$  (490 nm for FIrDnbp and 526 nm for HIrDnbp) and analogous vibronic progressions. Therefore, FIrDnbp and HIrDnbp experience similar degrees of immobilization either in MCM-41 and in PMMA matrices. Still, the resolved vibronic progressions are more easily observed in the transparent PMMA than in the strongly scattering MCM-41 matrix.

In both rigid matrices, the individual vibronic bands present lower full width at half maximum than in fluid solution, indicating that their T<sub>1</sub> excited state can be populated at the cost of a lower solvent reorganization energy [72]. Such an observation is symptomatic of a higher content of an LC character in the T<sub>1</sub> excited state [21–23]. Therefore, the emissive T<sub>1</sub> state for FIrDnbp and HIrDnbp in rigid MCM-41 and PMMA is probably ascribed to a mixed <sup>3</sup>LC<sub>dnbp</sub>/MLCT<sub>Ir(C<sup>^</sup>N)→dnbp</sub> excited state with a stronger influence from <sup>3</sup>LC.

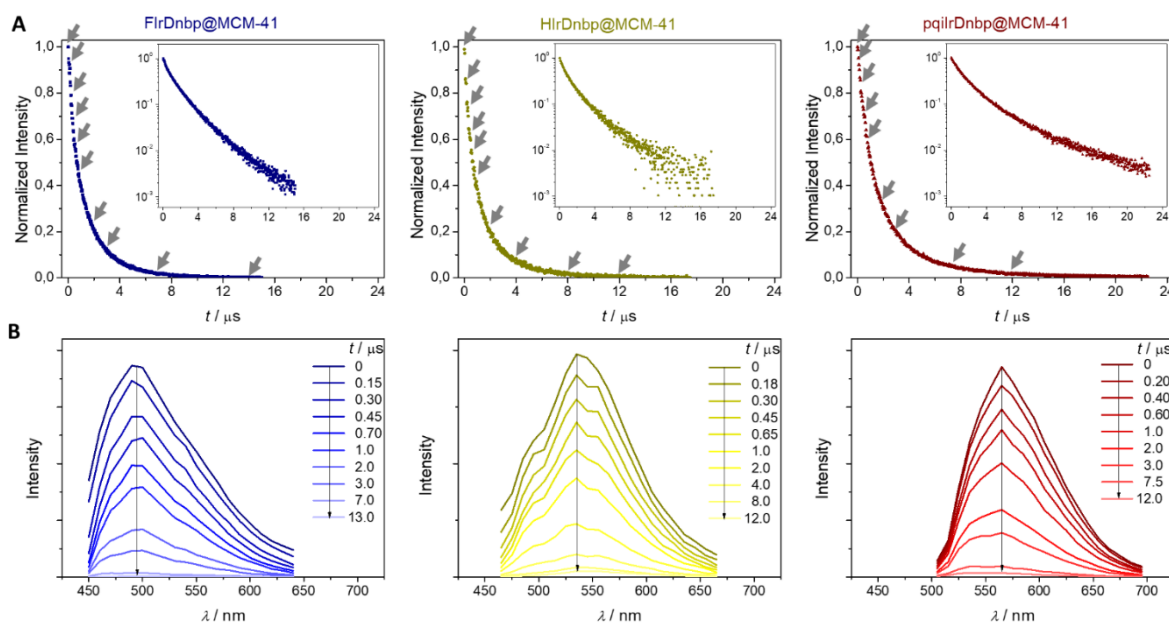
Thus, a rigidochromic-induced inversion of excited-state energies takes place when changing from fluid methanol (majorly  ${}^3\text{MLCT}_{\text{Ir}(\text{C}^{\wedge}\text{N})\rightarrow\text{dnbp}}$ ) to rigid MCM-41 silica or PMMA film (dominantly  ${}^3\text{LC}_{\text{dnbp}}$ ). Similar state inversions and vibronic progressions were also observed for  $[\text{Ir}(\text{Fppy})_2(\text{dmb})]^+$  after rigidochromism in rigid polyethylene glycol films and frozen nitrile solutions [21].

On the other hand, the emission of  $\text{pqIrDnbp}$  presents analogous energy and spectral profiles both in MCM-41 and in methanolic solution. The emission of the complex also matches in PMMA film (Figure S11 in the Supporting Information). The non-rigidochromic emission of this complex is centered at the  $\text{pqi}$  ligand, from a lowest-lying  ${}^3\text{LC}_{\text{pqi}}$  state, independently of the rigidity, due to the small  $\pi_{\text{pqi}}\rightarrow\pi^*_{\text{pqi}}$  energy gap.

The emissive  $\text{T}_1$  state is longer-lived in MCM-41 mesopores than in fluid solutions due to the rigidification of the system. Their emission decays in  $\text{N}_2$  atmosphere are composed of several exponential components, Figure 8. Nevertheless, time-resolved emission spectra in Figure 8 reveal no differences in spectral profiles and emission energies when passing from faster to slower regimes; in fact, the time-resolved spectra resemble the photo-stationary ones at any time delays after laser flashes. Based on these observations, faster exponential components are more-likely ascribed to the emissive deactivation of Ir(III) complexes confined in smaller mesopores, with adverse intermolecular  $\pi$ -stackings between adjacent Ir(III) emitters, while slower exponential components are assigned to a less-restricted encapsulation of Ir(III) guests in larger mesopores. For a quantitative estimation, a simplified double-exponential fit, Equation 1, was used, where  $\tau_1$  and  $\tau_2$  represent the average emission lifetimes of Ir(III) complexes in smaller and larger mesopores, respectively, and  $A_1$  and  $A_2$  are their respective average amplitudes. The obtained values are summarized in Table 3.

$$y = A_1 e^{(-t/\tau_1)} + A_2 e^{(-t/\tau_2)} \quad (1)$$

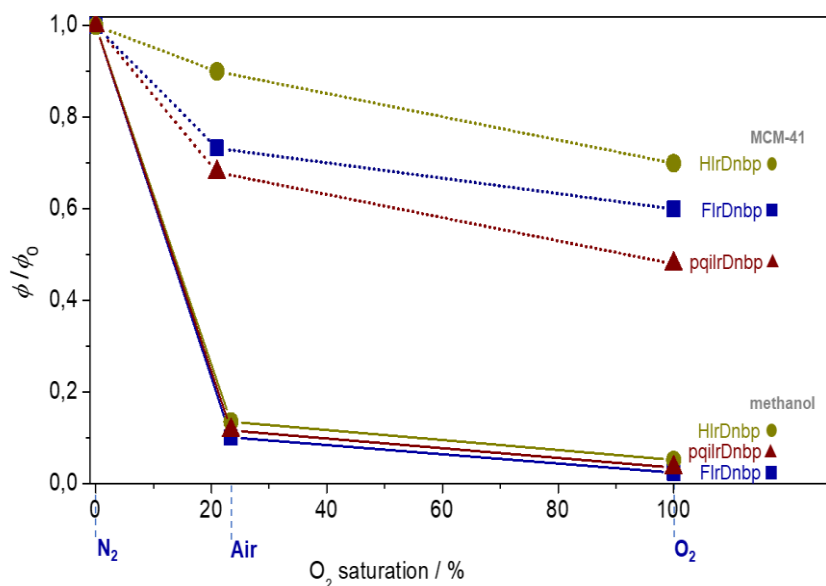
**Figure 8.** (A) Normalized emission decay (inset: log scale) and (B) time-resolved emission spectra of  $[\text{Ir}(\text{C}^{\wedge}\text{N})_2(\text{dnbp})]^+$  complexes encapsulated in MCM-41. The grey arrows in (A) indicate the time points in which time-resolved spectra in (B) were obtained (laser  $\lambda_{\text{exc}} = 370 \text{ nm}$ ).



#### *Prevention of emission quenching in complex@MCM-41*

Luminescence quenching studies of the encapsulated complexes were carried out in  $\text{N}_2$ , air and  $\text{O}_2$  atmospheres leading to the variations in  $\phi$  summarized in Table 3 and compared to methanol solutions in Figure 9.

**Figure 9.** The decrease in quantum yield ( $\phi/\phi_0$ ) as a function of  $\text{O}_2$  saturation for  $[\text{Ir}(\text{C}^{\wedge}\text{N})_2(\text{dnbp})]^+$  complexes in methanol (straight lines) or encapsulated in MCM-41 (broken lines).





The quenching of the complex's  $T_1$  by  $^3O_2$  is dramatically reduced in the MCM-41 matrices, with losses in quantum yield of only 10–32% in air ( $P_{O_2} = 0.21$  atm;  $[^3O_2] = 9.4 \times 10^{-3}$  mol L $^{-1}$ ) and 30–53% in  $O_2$  atmosphere ( $P_{O_2} \approx 1$  atm;  $[^3O_2] \approx 44.6 \times 10^{-3}$  mol L $^{-1}$ ), Table 3. The  $k_q$  magnitudes in MCM-41 nanoparticles are a thousand-fold lower ( $10^6$  L mol $^{-1}$  s $^{-1}$ , Table 3) than in methanol ( $10^9$  L mol $^{-1}$  s $^{-1}$ , Table 1). If one considers that the  $O_2$  concentrations are higher in the MCM experiments than in the methanol experiments, then the comparison is even more favorable for the encapsulated samples. Additionally, the quenching phenomenon slightly deviates from the linear Stern-Volmer relationship, with fitted- $R^2$  around  $\sim 0.8$  (Figures S5-S7 and S12 in the Supporting Information). These facts indicate that the  $O_2$  diffusion inside the MCM-41 mesopores is restricted either by the silica wall themselves or by the larger CTAB molecules also confined inside the mesopores. Such a restricted environment prevents the dynamic collision between the Ir(III) phosphors and oxygen inside the nanoparticle's bulk, and the small amount of oxygen able to reach the complexes might undergo a heterogeneous quenching reaction. In this sense, prevention of emission quenching is also observed when the Ir(III) complexes are immobilized in rigid PMMA films, with losses in  $\phi_0$  of only 22% in  $O_2$  atmosphere (Figures S13-S15 in the Supporting Information). Therefore, a slower emission quenching is inherent of solid host matrices.

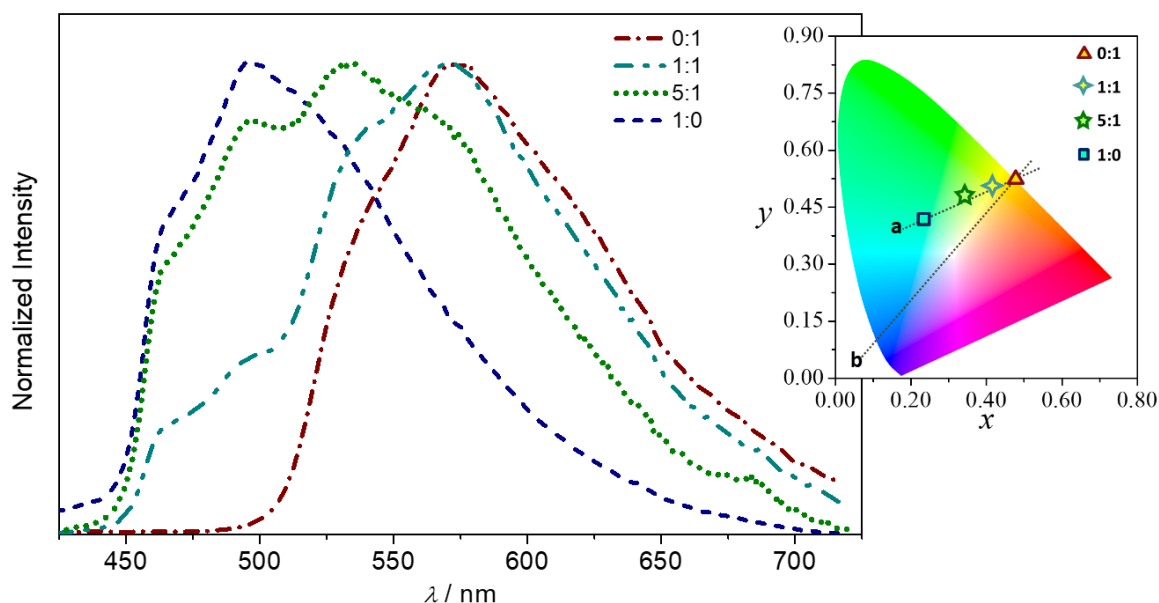
#### *Dual complex@MCM-41 systems and CIE coordinates*

The FIrDnbp@MCM-41 and pqiIrDnbp@MCM-41 optical materials were mixed in different m/m proportions (1:1 and 5:1) and the emission spectra of these mixtures are exhibited in Figure 10.

The emission spectra of the mixtures are a sum in different ratios of the individual spectra. The individual contributions of both FIrDnbp@MCM-41 and pqiIrDnbp@MCM-41 can be estimated by the  $I_{495\text{ nm}}/I_{570\text{ nm}}$  intensity ratio. In the 1:1 mixture,  $I_{495\text{ nm}}/I_{570\text{ nm}}$  is  $\sim 0.35$  and an equal contribution of both counterparts, with  $I_{495\text{ nm}}/I_{570\text{ nm}} \sim 1.0$ , is reached only when 5 mass equivalents of FIrDnbp@MCM-41 are added to 1 mass equivalent of pqiIrDnbp@MCM-41. The fact that  $I_{495\text{ nm}}/I_{570\text{ nm}}$  is not linear to the increase in the FIrDnbp content indicates energy transfer from the blue-emissive material to the orange one. Nevertheless, such an energy transfer process in the MCM-41 matrix is much weaker than the commonly fast energy transfer in solutions, for which irradiation of any mixture leads solely to the observation of pqiIrDnbp's spectrum, without FIrDnbp's contributions. For further comparisons, a PMMA film was also doped with a 5:1 FIrDnbp:pqiIrDnbp mixture, and its emission spectrum (Figure S16 in the

Supporting Information) is dominated by the emission of pqiIrDnbp, with a much lower contribution of FIrDnbp (i.e.  $I_{495\text{ nm}}/I_{570\text{ nm}} \approx 0.20$ ). Therefore, the energy transfer between phosphors is also less effective in MCM-41 than in PMMA films.

**Figure 10.** Emission spectra ( $\lambda_{\text{exc}} = 365\text{ nm}$ ) of FIrDnbp@MCM-41:pqiIrDnbp@MCM-41 mixtures in different m/m proportions: 1:0, 5:1, 1:1 and 0:1. The inset shows a color diagram with the respective CIE coordinates. The definition for Lines a and b is presented in the main text.



The probability of a Dexter energy transfer is predicted to decrease exponentially with distance, being also diffusional and concentration dependent [72]. In this sense, the less probable energy transfer between MCM-41 optical materials is an obvious consequence of the large separation between the immobilized Ir(III) phosphors. On the contrary, in methanol solutions (or even in PMMA films), the total complex concentration is higher while the diffusion is quicker (to a lower degree in PMMA) with a greater chance of collision between phosphors, leading to higher energy transfer probabilities in these media.

The less effective energy transfer in MCM-41 can be strategically exploited through a judicious material engineering for the pursuit of white-light emitting systems. As demonstrated by line *a* in the inset of Figure 10, the CIE color coordinates for the emission of the investigated complex@MCM-41 mixtures lie on a direct line connecting the CIE coordinates of pure FIrDnbp@MCM-41 and pqiIrDnbp@MCM-41. By a similar approach, white-light systems can be engineered by employing two complex@MCM-41 samples whose connecting line crosses the “pure white” region at the center of the diagram (around  $x = 0.33$ ;  $y = 0.33$ ) [3]. For example,

pqiIrDnbp@MCM-41 can be paired (through line **b**, Figure 10) to a designable blue-emissive MCM-41 material lying within the blue CIE region ( $x < 0.20$ ;  $y < 0.20$ ), e.g.  $[\text{Ir}(\text{PhFppz})_2(\text{dhdbp})]^+@MCM-41$  [40], to produce white light.

## Conclusions

The three synthesized  $[\text{Ir}(C^N)_2(\text{dnbp})]^+$  complexes exhibit intense emission in methanolic solutions, although the intensity can be drastically decreased in the presence of  $\text{O}_2$ . Host-guest MCM-41- $[\text{Ir}(C^N)_2(\text{dnbp})]^+$  optical materials were developed in a simple, one-step preparation route by incorporation of the amphiphilic complexes in CTAB micelles, which act as templates for the highly organized mesopores of MCM-41 silica. For FIrDnbp and HIrDnbp, the rigidochromic effect leads to dramatic changes in the emission characteristics from fluid solutions to rigid silica. In the MCM-41 materials, the restricted diffusion of  $^3\text{O}_2$  into the mesopores remarkably prevents the  $T_1$ 's emission quenching even in pure  $\text{O}_2$  atmosphere. Finally, the energy transfer between MCM-41 optical solids is weakened as compared to Ir(III) complexes in solutions, a remarkable characteristic that may be exploited for designing white-light emitting systems. These are important perspectives for the development of more-stable and more-efficient light-emitting systems (e.g. optoelectronic devices, optical rigidity sensors and biological markers) in assorted colors, even in  $\text{O}_2$ -rich environments.

## Experimental procedures

Detailed syntheses of the complexes as well as their immobilization in PMMA and general characterization procedures ( $^1\text{H}$  NMR, mass and FTIR spectra) are described in the Supporting Information file.

### *General procedure for the synthesis of $[\text{Ir}(C^N)_2(\text{dnbp})]\text{Cl}$*

In a general synthesis, iridium chloride hydrate (1 eq., Sigma Aldrich) was dissolved with a  $C^N$  ligand (2 eq., Sigma Aldrich) in a 5/3 (v/v) solution of 2-ethoxyethanol/water (8 mL) and heated at reflux with stirring for 24 h. After cooling to room temperature, greenish-yellow powders of  $[\text{Ir}(C^N)_2(\mu\text{-Cl})]_2$  precursors were collected by filtration and employed in the following steps without further purification. The *dnbp* ligand (2 eq., Dyesol) was mixed to the  $[\text{Ir}(C^N)_2(\mu\text{-Cl})]_2$  precursors (1 eq.) in 2-ethoxyethanol and heated at reflux with stirring for 18 to 20 h to produce the  $[\text{Ir}(C^N)_2(\text{dnbp})]\text{Cl}$  complexes. Upon cooling, the resultant solutions were roto-evaporated then the resultant oils redissolved in 70/1 (v/v) solutions of dichloromethane/methanol (5 mL). The final products were purified through column

chromatography using a silica gel (200-400 mesh Sigma-Aldrich) stationary phase and dichloromethane/methanol eluent solutions with increasing extents of methanol over time. Finally, the solvent was roto-evaporated to isolate pure  $[\text{Ir}(\text{C}^{\wedge}\text{N})_2(\text{dnbp})]\text{Cl}$  as yellowish powders which were dried under vacuum.

*Encapsulation of  $[\text{Ir}(\text{C}^{\wedge}\text{N})_2(\text{dnbp})]\text{Cl}$  complexes in MCM-41*

CTAB (1.50 g) and  $[\text{Ir}(\text{C}^{\wedge}\text{N})_2(\text{dnbp})]\text{Cl}$  (15 mg) were added to 74 mL of a 2/3 (v/v) solution of water/ethanol. The pH was adjusted to 11 by addition of approx. 2.5 mL of NaOH. Subsequently 2.92 mL of tetraethylorthosilicate were added under magnetic stirring. Initially, the stirring rate was fixed at 550 RPM for 5 h, then decreased to 300 RPM for 10 h. The produced thin powder is mainly white with a subtle yellow tone and was filtrated, washed four times with ethanol and subsequently dried under vacuum to obtain between 1.25–1.40 g of the product. To avoid decomposition of the complexes inside the mesopores, these so-obtained MCM-41 nanoparticles were not calcined (except for TEM and  $\text{N}_2$  isotherms, as specified).

**References**

- [1] P.I. Djurovich, D. Murphy, M.E. Thompson, B. Hernandez, R. Gao, P.L. Hunt, M. Selke, Cyclometalated Iridium and Platinum complexes as singlet oxygen photosensitizers: quantum yields, quenching rates and correlation with electronic structures, *Dalt. Trans.* (2007) 3763–3770.
- [2] C.-H. Yang, S. Yang, C. Hsu, Solution-processable phosphorescent to organic light-emitting diodes based on chromophoric amphiphile/silica nanocomposite, *Nanotechnology*. 20 (2009) 315601.
- [3] K.P.S. Zaroni, R.L. Coppo, R.C. Amaral, N.Y. Murakami Iha, Ir(III) complexes designed for light-emitting devices: Beyond the luminescence color array, *Dalt. Trans.* 44 (2015) 14559–14573.
- [4] J.S. Nam, M.G. Kang, J. Kang, S.Y. Park, S.J.C. Lee, H.T. Kim, J.K. Seo, O.H. Kwon, M.H. Lim, H.W. Rhee, T.H. Kwon, Endoplasmic Reticulum-Localized Iridium(III) Complexes as Efficient Photodynamic Therapy Agents via Protein Modifications, *J. Am. Chem. Soc.* 138 (2016) 10968–10977.
- [5] X. Jiang, J. Peng, J. Wang, X. Guo, D. Zhao, Y. Ma, Iridium-Based High-Sensitivity Oxygen Sensors and Photosensitizers with Ultralong Triplet Lifetimes, *ACS Appl. Mater. Interfaces*. 8 (2016) 3591–3600.

- [6] L. Guo, H. Peng, R. Shen, J. Ping, F. You, Y. Wang, M. Song, Q. Zhen, Iridium-Based Dual-Functional Nanoparticles for Far-Red Imaging and Photodynamic Therapy, *Nano Biomed Eng.* 9 (2017) 1–8.
- [7] M.C. Grüner, K.P.S. Zanoni, C.F. Borgognoni, C.C. Melo, V. Zucolotto, A.S.S. De Camargo, Reaching Biocompatibility with Nanoclays: Eliminating the Cytotoxicity of Ir(III) Complexes, *ACS Appl. Mater. Interfaces.* 10 (2018) 26830–26834.
- [8] J. Torres, M.C. Carrión, J. Leal, F.A. Jalón, J. V. Cuevas, A.M. Rodríguez, G. Castañeda, B.R. Manzano, Cationic Bis(cyclometalated) Ir(III) Complexes with Pyridine–Carbene Ligands. Photophysical Properties and Photocatalytic Hydrogen Production from Water, *Inorg. Chem.* 57 (2018) 970–984.
- [9] L.-P. Li, H.-L. Peng, L.-Q. Wei, B.-H. Ye, Diastereoselective Photooxidation and Reduction of Chiral Iridium(III) Complexes, *Inorg. Chem.* 58 (2019) 785–793.
- [10] B.-H. Wu, M.-J. Huang, C.-C. Lai, C.-H. Cheng, I.-C. Chen, Isomerization Reaction of mer- to fac-Tris(2-phenylpyridinato-N,C2') Iridium(III) Monitored by Using Surface-Enhanced Raman Spectroscopy, *Inorg. Chem.* 57 (2018) 4448–4455.
- [11] R. Bevernaegie, L. Marcélis, B. Laramée-Milette, J. De Winter, K. Robeyns, P. Gerbaux, G.S. Hanan, B. Elias, Trifluoromethyl-Substituted Iridium(III) Complexes: From Photophysics to Photooxidation of a Biological Target, *Inorg. Chem.* 57 (2018) 1356–1367.
- [12] C. Zhang, M. Liu, S. Liu, H. Yang, Q. Zhao, Z. Liu, W. He, Phosphorescence Lifetime Imaging of Labile Zn<sup>2+</sup> in Mitochondria via a Phosphorescent Iridium(III) Complex, *Inorg. Chem.* 57 (2018) 10625–10632.
- [13] E. Baranoff, J.-H. Yum, M. Graetzel, M.K. Nazeeruddin, Cyclometallated iridium complexes for conversion of light into electricity and electricity into light, *J. Organomet. Chem.* 694 (2009) 2661–2670.
- [14] S. Takizawa, R. Aboshi, S. Murata, Photooxidation of 1,5-dihydroxynaphthalene with iridium complexes as singlet oxygen sensitizers, *Photochem. Photobiol. Sci.* 10 (2011) 895–903.
- [15] D.-L. Ma, V.P.-Y. Ma, D.S.-H. Chan, K.-H. Leung, H.-Z. He, C.-H. Leung, Recent advances in luminescent heavy metal complexes for sensing, *Coord. Chem. Rev.* 256 (2012) 3087–3113.
- [16] K.K.-W. Lo, A.W.-T. Choi, W.H.-T. Law, Applications of luminescent inorganic and organometallic transition metal complexes as biomolecular and cellular probes., *Dalt. Trans.* 41 (2012) 6021–6047.

- [17] S.P.Y. Li, C.T.S. Lau, M.W. Louie, Y.W. Lam, S.H. Cheng, K.K.W. Lo, Mitochondria-targeting cyclometalated Iridium(III)-PEG complexes with tunable photodynamic activity, *Biomaterials*. 34 (2013) 7519–7532.
- [18] Y. You, S. Cho, W. Nam, Cyclometalated Iridium(III) complexes for phosphorescence sensing of biological metal ions, *Inorg. Chem.* 53 (2014) 1804–1815.
- [19] D. Ashen-Garry, M. Selke, Singlet oxygen generation by cyclometalated complexes and applications, *Photochem. Photobiol.* 90 (2014) 257–274.
- [20] S.B. Meier, D. Tordera, A. Pertegás, C. Roldán-Carmona, E. Ortí, H.J. Bolink, Light-emitting electrochemical cells: recent progress and future prospects, *Mater. Today*. 17 (2014) 217–223.
- [21] K.P.S. Zanoni, B.K. Kariyazaki, A. Ito, M.K. Brennaman, T.J. Meyer, N.Y. Murakami Iha, Blue-green Iridium(III) emitter and comprehensive photophysical elucidation of heteroleptic cyclometalated Iridium(III) complexes, *Inorg. Chem.* 53 (2014) 4089–4099.
- [22] K.P.S. Zanoni, A. Ito, N.Y. Murakami Iha, Molecular Engineered  $[\text{Ir}(\text{Fppy})_2(\text{Mepic})]$  Towards Efficient Blue Emission, *New J. Chem.* 39 (2015) 6367–6376.
- [23] K.P.S. Zanoni, A. Ito, M. Grüner, N.Y. Murakami Iha, A.S.S. de Camargo, Photophysical dynamics of the efficient emission and photosensitization of  $[\text{Ir}(\text{pqi})_2(\text{NN})]^+$  complexes, *Dalt. Trans.* 47 (2018) 1179–1188.
- [24] L. Flamigni, A. Barbieri, C. Sabatini, B. Ventura, F. Barigelletti, Photochemistry and Photophysics of Coordination Compounds: Iridium, in: *Top. Curr. Chem.*, 2007: pp. 143–203.
- [25] Y. You, S.Y. Park, Phosphorescent Iridium(III) complexes: toward high phosphorescence quantum efficiency through ligand control, *Dalt. Trans.* (2009) 1267–1282.
- [26] A.R.G. Smith, P.L. Burn, B.J. Powell, Spin-orbit coupling in phosphorescent Iridium(III) complexes, *ChemPhysChem*. 12 (2011) 2429–2438.
- [27] H. Yersin, A.F. Rausch, R. Czerwieniec, T. Hofbeck, T. Fischer, The triplet state of organo-transition metal compounds. Triplet harvesting and singlet harvesting for efficient OLEDs, *Coord. Chem. Rev.* 255 (2011) 2622–2652.
- [28] Y. You, W. Nam, Photofunctional triplet excited states of cyclometalated Ir(III) complexes: beyond electroluminescence., *Chem. Soc. Rev.* 41 (2012) 7061–7084.
- [29] B. Minaev, G. Baryshnikov, H. Agren, Principles of phosphorescent organic light emitting devices., *Phys. Chem. Chem. Phys.* 16 (2014) 1719–1758.

- [30] K.P.S. Zanoni, L.P. Ravaro, A.S.S. De Camargo, Host-guest luminescent materials based on highly emissive species loaded into versatile sol-gel hosts, *Dalt. Trans.* 47 (2018) 12813–12826.
- [31] B. Martins Estevão, I. Miletto, L. Marchese, E. Gianotti, Optimized Rhodamine B labeled mesoporous silica nanoparticles as fluorescent scaffolds for the immobilization of photosensitizers: a theranostic platform for optical imaging and photodynamic therapy, *Phys. Chem. Chem. Phys.* 18 (2016) 9042–9052.
- [32] N. Alarcos, B. Cohen, M. Ziółek, A. Douhal, Photochemistry and Photophysics in Silica-Based Materials: Ultrafast and Single Molecule Spectroscopy Observation, *Chem. Rev.* 117 (2017) 13639–13720.
- [33] M. Rizzi, S. Tonello, B.M. Estevão, E. Gianotti, L. Marchese, F. Renò, Verteporfin based silica nanoparticle for in vitro selective inhibition of human highly invasive melanoma cell proliferation, *J. Photochem. Photobiol. B Biol.* 167 (2017) 1–6.
- [34] L. Donato, Y. Atoini, E.A. Prasetyanto, P. Chen, C. Rosticher, C. Bizzarri, K. Rissanen, L. De Cola, Selective Encapsulation and Enhancement of the Emission Properties of a Luminescent Cu(I) Complex in Mesoporous Silica, *Helv. Chim. Acta.* 101 (2018) e1700273.
- [35] D. Aiello, A.M. Talarico, F. Teocoli, E.I. Szerb, I. Aiello, F. Testa, M. Ghedini, Self-incorporation of a luminescent neutral Iridium(III) complex in different mesoporous micelle-templated silicas, *New J. Chem.* 35 (2011) 141–148.
- [36] M. de Barros e Silva Botelho, J.M. Fernandez-Hernandez, T.B. de Queiroz, H. Eckert, L. De Cola, A.S.S. de Camargo, Iridium(III)–surfactant complex immobilized in mesoporous silica via templated synthesis: a new route to optical materials, *J. Mater. Chem.* 21 (2011) 8829.
- [37] D.J. Lewis, V. Dore, N.J. Rogers, T.K. Mole, G.B. Nash, P. Angeli, Z. Pikramenou, Silica Nanoparticles for Micro-Particle Imaging Velocimetry: Fluorosurfactant Improves Nanoparticle Stability and Brightness of Immobilized Iridium(III) Complexes, *Langmuir.* 29 (2013) 14701–14708.
- [38] M. Ilibi, T.B. de Queiroz, J. Ren, L. De Cola, A.S.S. de Camargo, H. Eckert, Luminescent hybrid materials based on covalent attachment of Eu(III)-tris(bipyridinedicarboxylate) in the mesoporous silica host MCM-41, *Dalt. Trans.* 43 (2014) 8318.

- [39] E. Gianotti, B. Martins Estevão, F. Cucinotta, N. Hioka, M. Rizzi, F. Renò, L. Marchese, An efficient rose bengal based nanoplatform for photodynamic therapy, *Chem. - A Eur. J.* 20 (2014) 10921–10925.
- [40] Y. Qu, L. Feng, B. Liu, C. Tong, C. Lü, A facile strategy for synthesis of nearly white light emitting mesoporous silica nanoparticles, *Colloids Surfaces A Physicochem. Eng. Asp.* 441 (2014) 565–571.
- [41] J. Wang, W. Dou, A.M. Kirillov, W. Liu, C. Xu, R. Fang, L. Yang, Hybrid materials based on novel 2D lanthanide coordination polymers covalently bonded to amine-modified SBA-15 and MCM-41: assembly, characterization, structural features, thermal and luminescence properties, *Dalt. Trans.* 45 (2016) 18610–18621.
- [42] E. Gianotti, B.M. Estevão, I. Miletto, S. Tonello, F. Renò, L. Marchese, Verteporfin based silica nanoplatform for photodynamic therapy, *ChemistrySelect.* 1 (2016) 127–131.
- [43] K.E. Amos, N.J. Brooks, N.C. King, S. Xie, J. Canales-Vázquez, M.J. Danks, H.B. Jervis, W. Zhou, J.M. Seddon, D.W. Bruce, A systematic study of the formation of mesostructured silica using surfactant ruthenium complexes in high- and low-concentration regimes, *J. Mater. Chem.* 18 (2008) 5282.
- [44] F. Neve, M. La Deda, A. Crispini, A. Bellusci, F. Puntoriero, S. Campagna, Cationic Cyclometalated Iridium Luminophores: Photophysical, Redox, and Structural Characterization, *Organometallics.* 23 (2004) 5856–5863.
- [45] F. Dumur, D. Bertin, C.R. Mayer, A. Guerlin, G. Wantz, G. Nasr, E. Dumas, F. Miomandre, G. Clavier, D. Gigmes, Design of blue or yellow emitting devices controlled by the deposition process of a cationic Iridium(III) complex, *Synth. Met.* 161 (2011) 1934–1939.
- [46] F. Dumur, G. Nasr, G. Wantz, C.R. Mayer, E. Dumas, A. Guerlin, F. Miomandre, G. Clavier, D. Bertin, D. Gigmes, Cationic iridium complex for the design of soft salt-based phosphorescent OLEDs and color-tunable light-emitting electrochemical cells, *Org. Electron.* 12 (2011) 1683–1694.
- [47] K. Morimoto, T. Nakae, K. Ohara, K. Tamura, S. Nagaoka, H. Sato, Dual emitting Langmuir–Blodgett films of cationic iridium complexes and montmorillonite clay for oxygen sensing, *New J. Chem.* 36 (2012) 2467.
- [48] H. Sato, M. Ochi, M. Kato, K. Tamura, A. Yamagishi, Energy transfer in hybrid Langmuir–Blodgett films of iridium complexes and synthetic saponite: dependence of transfer efficiency on the interlayer distance, *New J. Chem.* 38 (2014) 5715–5720.



- [49] H. Sato, K. Tamura, K. Ohara, S. Nagaoka, Multi-emitting properties of hybrid Langmuir–Blodgett films of amphiphilic Iridium complexes and the exfoliated nanosheets of saponite clay, *New J. Chem.* 38 (2014) 132–139.
- [50] A. Mechler, B.D. Stringer, M.S.H. Mubin, E.H. Doeven, N.W. Phillips, J. Rudd-Schmidt, C.F. Hogan, Labeling phospholipid membranes with lipid mimetic luminescent metal complexes, *Biochim. Biophys. Acta - Biomembr.* 1838 (2014) 2939–2946.
- [51] T.-S. Kang, Z. Mao, C.-T. Ng, M. Wang, W. Wang, C. Wang, S.M.-Y. Lee, Y. Wang, C.-H. Leung, D.-L. Ma, Identification of an Iridium(III)-Based Inhibitor of Tumor Necrosis Factor- $\alpha$ , *J. Med. Chem.* 59 (2016) 4026–4031.
- [52] M.-A. Tehfe, M. Lepeltier, F. Dumur, D. Gigmes, J.-P. Fouassier, J. Lalevée, Structural Effects in the Iridium Complex Series: Photoredox Catalysis and Photoinitiation of Polymerization Reactions under Visible Lights, *Macromol. Chem. Phys.* 218 (2017) 1700192.
- [53] M. Nonoyama, Benzo[h]quinolin-10-yl-N Iridium(III) Complexes, *Bull. Chem. Soc. Jpn.* 47 (1974) 767–768.
- [54] C. Ulbricht, B. Beyer, C. Friebe, A. Winter, U.S. Schubert, Recent developments in the application of phosphorescent Iridium(III) complex systems, *Adv. Mater.* 21 (2009) 4418–4441.
- [55] M.C. DeRosa, R.J. Crutchley, Photosensitized singlet oxygen and its applications, *Coord. Chem. Rev.* 233–234 (2002) 351–371.
- [56] C. Schweitzer, R. Schmidt, Physical Mechanisms of Generation and Deactivation of Singlet Oxygen, *Chem. Rev.* 103 (2003) 1685–1758.
- [57] A. Ruggi, F.W.B. van Leeuwen, A.H. Velders, Interaction of dioxygen with the electronic excited state of Ir(III) and Ru(II) complexes: Principles and biomedical applications, *Coord. Chem. Rev.* 255 (2011) 2542–2554.
- [58] L.D. Ramos, H.M. da Cruz, K.P. Morelli Frin, Photophysical properties of Rhenium(I) complexes and photosensitized generation of singlet oxygen, *Photochem. Photobiol. Sci.* 16 (2017) 459–466.
- [59] M. Bregnhøj, M. Westberg, B.F. Minaev, P.R. Ogilby, Singlet Oxygen Photophysics in Liquid Solvents: Converging on a Unified Picture, *Acc. Chem. Res.* 50 (2017) 1920–1927.
- [60] B.F. Minaev, Spin-orbit coupling mechanism of singlet oxygen A1Dg quenching by solvent vibrations, *Chem. Phys.* 483–484 (2017) 84–95.

- [61] A.A. Abdel-Shafi, D.R. Worrall, A.Y. Ershov, Photosensitized generation of singlet oxygen from Ruthenium(II) and Osmium(II) bipyridyl complexes, *Dalt. Trans.* (2004) 30–36.
- [62] F. Raji, M. Pakizeh, Study of Hg(II) species removal from aqueous solution using hybrid ZnCl<sub>2</sub>-MCM-41 adsorbent, *Appl. Surf. Sci.* 282 (2013) 415–424.
- [63] J.S. Beck, J.C. Vartuli, W.J. Roth, M.E. Leonowicz, C.T. Kresge, K.D. Schmitt, C.T.W. Chu, D.H. Olson, E.W. Sheppard, S.B. McCullen, J.B. Higgins, J.L. Schlenker, A New Family of Mesoporous Molecular Sieves Prepared with Liquid Crystal Templates, *J. Am. Chem. Soc.* 114 (1992) 10834–10843.
- [64] B. Martins Estevão, F. Cucinotta, N. Hioka, M. Cossi, M. Argeri, G. Paul, L. Marchese, E. Gianotti, Rose Bengal incorporated in mesostructured silica nanoparticles: structural characterization, theoretical modeling and singlet oxygen delivery, *Phys. Chem. Chem. Phys.* 17 (2015) 26804–26812.
- [65] A.A.S. Gonçalves, M.J.F. Costa, L. Zhang, F. Ciesielczyk, M. Jaroniec, One-Pot Synthesis of MeAl<sub>2</sub>O<sub>4</sub> (Me = Ni, Co, or Cu) Supported on  $\gamma$ -Al<sub>2</sub>O<sub>3</sub> with Ultralarge Mesopores: Enhancing Interfacial Defects in  $\gamma$ -Al<sub>2</sub>O<sub>3</sub> To Facilitate the Formation of Spinel Structures at Lower Temperatures, *Chem. Mater.* 30 (2018) 436–446.
- [66] R. Katoh, K. Suzuki, A. Furube, M. Kotani, K. Tokumaru, Fluorescence Quantum Yield of Aromatic Hydrocarbon Crystals, *J. Phys. Chem. C.* 113 (2009) 2961–2965.
- [67] H. Ishida, S. Tobita, Y. Hasegawa, R. Katoh, K. Nozaki, Recent advances in instrumentation for absolute emission quantum yield measurements, *Coord. Chem. Rev.* 254 (2010) 2449–2458.
- [68] A.J. Lees, Luminescence properties of organometallic complexes, *Chem. Rev.* 87 (1987) 711–743.
- [69] P. Chen, T.J. Meyer, Medium Effects on Charge Transfer in Metal Complexes, *Chem. Rev.* 98 (1998) 1439–1478.
- [70] A.J. Lees, The Luminescence Rigidochromic Effect Exhibited by Organometallic Complexes: Rationale and Applications, *Comments Inorg. Chem.* 17 (1995) 319–346.
- [71] M. Xue, J.I. Zink, Probing the Microenvironment in the Confined Pores of Mesoporous Silica Nanoparticles, *J. Phys. Chem. Lett.* 5 (2014) 839–842.
- [72] A. Ito, T.J. Meyer, The Golden Rule. Application for fun and profit in electron transfer, energy transfer, and excited-state decay, *Phys. Chem. Chem. Phys.* 14 (2012) 13731–13745.

## 5. Mesoporous silica nanoparticles incorporated with Ir(III) complexes: From photophysics to photodynamic therapy

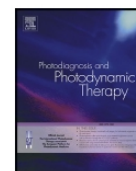
Photodiagnosis and Photodynamic Therapy 40 (2022) 103052



Contents lists available at ScienceDirect

### Photodiagnosis and Photodynamic Therapy

journal homepage: [www.elsevier.com/locate/pdpdt](http://www.elsevier.com/locate/pdpdt)



## Mesoporous silica nanoparticles incorporated with Ir(III) complexes: From photophysics to photodynamic therapy

Bianca M. Estevão<sup>a,1,\*</sup>, Raquel R.C. Vilela<sup>b,1,\*</sup>, Isabella P. Geremias<sup>a</sup>, Kassio P.S. Zanoni<sup>b,c</sup>,  
Andrea S.S. de Camargo<sup>b</sup>, Valtencir Zucolotto<sup>a</sup>

<sup>a</sup> Nanomedicine and Nanotoxicology Group, São Carlos Institute of Physics, University of São Paulo, São Carlos, SP 13566-590, Brazil

<sup>b</sup> Laboratory of Spectroscopy of Functional Materials, São Carlos Institute of Physics, University of São Paulo, São Carlos, SP 13566-590, Brazil

<sup>c</sup> Molecular Optoelectronic Devices, Instituto de Ciencia Molecular (ICMol), University of Valencia, Catedrático J. Beltrán 2, Paterna, Valencia 46980, Spain

#### ARTICLE INFO

##### Keywords:

Mesoporous silica nanoparticles  
Ir(III) complexes  
PDT  
Liver cancer  
Photophysics  
Photodynamic Therapy

#### ABSTRACT

Organically modified mesoporous silica nanoparticles (MSNs) containing Ir complexes (Ir1, Ir2 and Ir3) were successfully synthesized. These Ir-entrapped MCM41-COOH nanoparticles have shown relevant photophysical characteristics including high efficiency in the photoproduction and delivery of singlet oxygen ( $^1\text{O}_2$ ), which is particularly promising for photodynamic therapy (PDT) applications. *In vitro* tests have evidenced that complex@MCM41-COOH are able to reduce cell proliferation after 10 min of blue-light irradiation in Hep-G2 liver cancer cells.

### 1. Introduction

Since the first report of a luminescent transition metal complex,  $[\text{Ru}(\text{bpy})_3]^{2+}$ , in 1959 [1], this class of compounds has emerged as one of the main protagonists in many technological applications, ranging from emitting devices, photocatalytic and sensing, to biological labeling agents [2]. In particular, heteroleptic Ir(III) complexes, featuring  $d^6$  electronic configuration, are among the most promising triplet emitters due to their unique photophysical features arising from intense spin-orbit coupling (SOC) induced by the heavy Ir metal, and structural/electronic interactions with ligands through strong Ir–C bonds [3,4]. As a result, these complexes can exhibit intense luminescence at room temperature with high emission quantum yields ( $\sim 100\%$ ), relatively long phosphorescence lifetimes ( $\mu\text{s}$ ), tunable luminescence in a wide spectral range (from blue to red) and significant Stokes shifts (often  $> 200$  nm), which avoids self-quenching processes [5–8]. It has already been demonstrated that Ir(III) complexes can be conveniently applied to light-harvesting and emitting devices, phosphorescent sensors, biological probes, photocatalysts for  $\text{CO}_2$  and water reduction, etc [5,9–16]. If, on one hand, Ir(III) complexes' excited states are effectively quenched by molecular oxygen, which constitutes a disadvantage for the application in lighting devices, for instance, the ability to generate different reactive oxygen species (ROS), especially singlet oxygen ( $^1\text{O}_2$ ), allows

the use of these complexes as efficient photosensitizers (PS) in photodynamic therapy (PDT) [7,17–20].

PDT is an emerging treatment for a variety of oncological, cardiovascular, dermatological, and ophthalmic diseases, which is based on the generation of  $^1\text{O}_2$  and/or ROS by a PS under irradiation with specific wavelength [21,22]. Based on the  $^1\text{O}_2$  generation and action as a cytotoxic agent responsible for irreversible damage of the treated tissues, PDT has become promising for cancer therapy, due to its minimal invasiveness, specific space-time selectivity and the fact that it does not induce resistance like traditional chemotherapy. Regardless of the potential benefits, the PDT success is governed by different factors, such as the efficiency of the PS delivery, targeting ability, and  $^1\text{O}_2$  generation quantum yield [22–24]. Although the most studied PS are organic dye molecules (e.g., porphyrins and cyanines), many of these compounds suffer from non-specific targeting and poor water solubility, which compromises the PDT efficacy [17,24,25]. Additionally, organic agents are susceptible to photobleaching and can decompose upon prolonged light exposure. Therefore, considerable efforts have been devoted to the use of Ir(III) complexes as substitute PS as besides meeting essential requirements for this purpose, they even offer advantages. Their highly sensitive excited states properties toward the surrounding environment, high photostability, and distinctive intracellular localization are just a few examples [17,20,26]. Many effective strategies have been

\* Corresponding authors.

E-mail addresses: [estevaobm@usp.br](mailto:estevaobm@usp.br) (B.M. Estevão), [raquelvilela@usp.br](mailto:raquelvilela@usp.br) (R.R.C. Vilela).

<sup>1</sup> These authors contributed equally to this work.

<https://doi.org/10.1016/j.pdpdt.2022.103052>

Received 25 May 2022; Received in revised form 26 July 2022; Accepted 2 August 2022

Available online 5 August 2022

1572-1000/© 2022 Elsevier B.V. All rights reserved.

## Abstract

Organically modified mesoporous silica nanoparticles (MSNs) containing Ir complexes (Ir1, Ir2 and Ir3) were successfully synthesized. These Ir-entrapped MCM41-COOH nanoparticles have shown relevant photophysical characteristics including high efficiency in the photoproduction and delivery of singlet oxygen ( $^1\text{O}_2$ ), which is particularly promising for photodynamic therapy (PDT) applications. *In vitro* tests have evidenced that complex@MCM41-COOH are able to reduce cell proliferation after 10 min of blue-light irradiation in Hep-G2 liver cancer cells.

**Keywords:** Mesoporous silica nanoparticles, Ir(III) complexes, PDT, liver cancer, photophysics

## Introduction

Since the first report of a luminescent transition metal complex,  $[\text{Ru}(\text{bpy})_3]^{2+}$ , in 1959 [1], this class of compounds has emerged as one of the main protagonists in many technological applications, ranging from emitting devices, photocatalytic and sensing, to biological labeling agents [2]. In particular, heteroleptic Ir(III) complexes, featuring  $d^6$  electronic configuration, are among the most promising triplet emitters due to their unique photophysical features arising from intense spin-orbit coupling (SOC) induced by the heavy Ir metal, and structural/electronic interactions with ligands through strong Ir–C bonds [3, 4]. As a result, these complexes can exhibit intense luminescence at room temperature with high emission quantum yields ( $\sim 100\%$ ), relatively long phosphorescence lifetimes ( $\mu\text{s}$ ), tunable luminescence in a wide spectral range (from blue to red) and significant Stokes shifts (often  $> 200$  nm), which avoids self-quenching processes [5–8]. It has already been demonstrated that Ir(III) complexes can be conveniently applied to light-harvesting and emitting devices, phosphorescent sensors, biological probes, photocatalysts for  $\text{CO}_2$  and water reduction, etc [5, 9–16]. If, on one hand, Ir(III) complexes' excited states are effectively quenched by molecular oxygen, which constitutes a disadvantage for the application in lighting devices, for instance, the ability to generate different reactive oxygen species (ROS), especially singlet oxygen ( $^1\text{O}_2$ ), allows the use of these complexes as efficient photosensitizers (PS) in photodynamic therapy (PDT) [7, 17–20].

PDT is an emerging treatment for a variety of oncological, cardiovascular, dermatological, and ophthalmic diseases, which is based on the generation of  $^1\text{O}_2$  and/or ROS by a PS under irradiation with specific wavelength [21, 22]. Based on the  $^1\text{O}_2$  generation and action as a cytotoxic agent responsible for irreversible damage of the treated tissues, PDT has

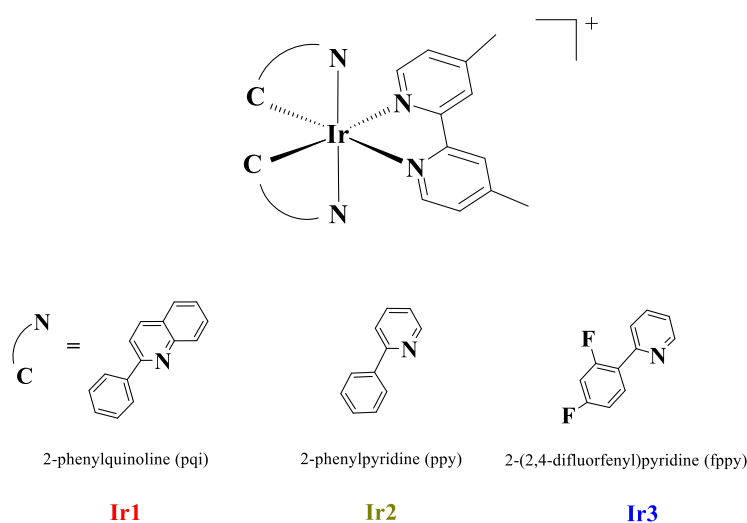
become promising for cancer therapy, due to its minimal invasiveness, specific space-time selectivity and the fact that it does not induce resistance like traditional chemotherapy. Regardless of the potential benefits, the PDT success is governed by different factors, such as the efficiency of the PS delivery, targeting ability, and  $^1\text{O}_2$  generation quantum yield [22, 24]. Although the most studied PS are organic dye molecules (e.g., porphyrins and cyanines), many of these compounds suffer from non-specific targeting and poor water solubility, which compromises the PDT efficacy [17, 24, 25]. Additionally, organic agents are susceptible to photobleaching and can decompose upon prolonged light exposure. Therefore, considerable efforts have been devoted to the use of Ir(III) complexes as substitute PS as besides meeting essential requirements for this purpose, they even offer advantages. Their highly sensitive excited states properties toward the surrounding environment, high photostability, and distinctive intracellular localization are just a few examples [17, 20, 26]. Many effective strategies have been developed to fabricate different nanoparticles incorporated with these complexes for improved PDT, and some encouraging results can be found. In particular, we highlight the work of Sun et al., who developed a conjugated polymer-Ir(III) complex matrix based on the glycopolymers polygalactose (PGal) for the photodynamic treatment of HepG2 cells and tumors [27], with excellent water stability, efficient energy transfer from the PPF backbone to Ir(III) complex, and low dark toxicity, which inhibited the growth of HepG2 tumors when illuminated due to the production of singlet oxygen from the Ir(III) complex. Another example is the hyperbranched phosphorescent conjugated polymer dots filled with Ir(III) developed by Feng and co-workers [28] for hypoxia imaging and highly efficient image-guided PDT. As confirmed by real-time luminescence imaging and MTT assays of light-induced apoptosis and death of HepG2 cells, the cell viability decreased quite fast upon increasing the dose of polymer dots and exposure time, confirming the highly efficient PDT of Ir-based HPC/PSMA dots.

Nevertheless, for biomedical applications, the high intrinsic dark-cytotoxicity exhibited by Ir(III) complexes is still a limiting factor and demands the development of nanocarriers that are capable of granting them biocompatibility [17, 29, 30]. Among various encapsulating and delivering vehicles for PS, mesoporous silica nanoparticles (MSNs) have attracted interest due to their tunable size, shape and pore diameter, large surface area, facile topologically functionalization that can be fine-tuned for a specific application, and adequate cell uptake. The well know MSNs show high in vivo biocompatibility and have been widely employed as carriers for PS in PDT [21, 31–36]. In general, silica nanoparticles are degraded to orthosilicic acid ( $\text{Si}(\text{OH})_4$ ), which is used by the human organism in the formation of proteins that support

the skin, nails and hair [37]. Furthermore, the surface of MSNs can be easily modified to improve dispersion, increase blood circulation time, control possible interactions with biological environment, in addition to enable greater yield in the drug encapsulation inside pores, when compared to polymeric lipid nanoparticles and liposomes [38].

We anticipate that combining the specific chemical and physical properties of MSNs and Ir(III) PSs allows developing new hybrid materials that minimize unfavorable interference from the complexes in cellular processes, while inducing efficient ROS generation under proper light irradiation. In this study we report a surface modification of MCM-41-like MSN, leading to acid-functionalized mesoporous channels that properly conjugate to Ir(III) complex molecules. Three different Ir(III) complexes (Chart 1) of the  $[\text{Ir}(\text{NC})_2(\text{dmb})]^+$  series (NC = 2-phenylquinoline, 2-phenylpyridine or 2-(2,4-difluorophenyl) pyridine; and dmb = 4,4'-dimethyl-2,2'-bipyridine) were employed and their photophysical properties and photosensitizing capabilities were characterized in aqueous solution. Complex@MCM41-COOH hybrid systems were then prepared by encapsulating these complexes in the mesopores of the functionalized MCM-41 nanoparticles to access their encapsulation efficiency and  $^1\text{O}_2$  release by structural, morphological and photophysical characterization. Finally, the cell uptake and photosensitization efficacy of the complex@MCM41-COOH hybrids were investigated to verify their potential as multifunctional nanoplatforms for cancer theranostic *in vitro*, including imaging and therapy. To the best of our knowledge, our work is the first to report Ir(III) complexes supported into mesoporous silica nanoparticles for therapeutic properties, although the literature on general silica-based materials with different PSs is abundant.

**Chart 1.** Chemical structures of the  $[\text{Ir}(\text{NC})_2(\text{dmb})]^+$  complexes.



## Results and discussion

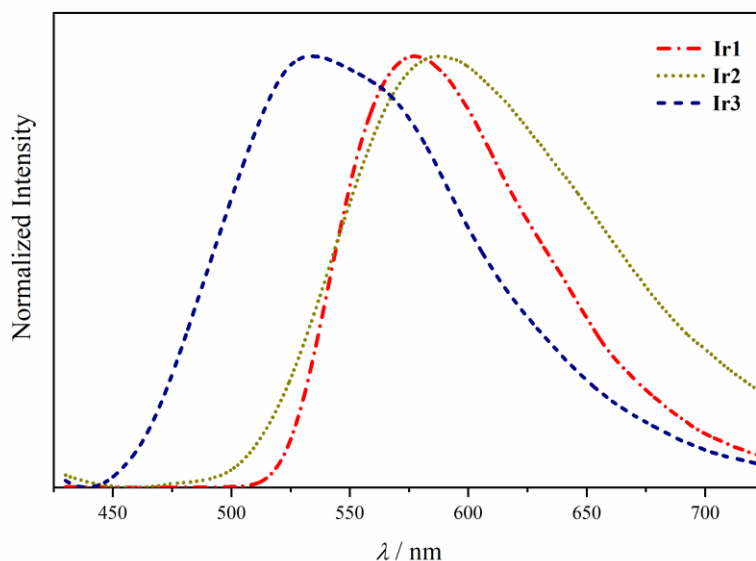
### *Photophysical properties of [Ir(NC)<sub>2</sub>(dmb)]<sup>+</sup> in aqueous solution*

For the photophysical investigation in H<sub>2</sub>O, the water-soluble chloride (Cl<sup>-</sup>) salts of the cationic Ir(III) complexes (Chart 1) were prepared. The photophysical properties are very similar to those of the hexafluorophosphate (PF<sub>6</sub><sup>-</sup>) salts in acetonitrile, as addressed in depth in preceding publications [4, 39].

On the absorption spectra of complexes **Ir1**, **Ir2** and **Ir3** measured in aqueous solutions, at 298 K (Figure SII), the relatively less intense absorption below 325 nm corresponds to an overlap of mixed character transitions, both in spin (singlet and triplet) and in electronic nature [40], as a direct consequence of the strong SOC effect exerted by the iridium core (estimated  $\xi_{\text{Ir}} = 4430 \text{ cm}^{-1}$ ) [6]. For example, bands from 320 to 440 nm are mainly assigned to an overlap of metal-to-ligand-charge-transfer (MLCT – from d(e<sub>g</sub>) orbital to a  $\pi^*$  orbital in one of the ligands), ligand-to-ligand-charge-transfer (LLCT – from  $\pi$  to  $\pi^*$  orbitals within different NC and dmb ligands) and LC transitions [5]. Additionally, the SOC effect allows the mixing between singlet and triplet states, which increases the chances of a direct population of the lowest triplet excited state (known as T<sub>1</sub>, assumed to be mixed <sup>3</sup>MLCT/LC) from the singlet ground state [5, 9, 40], which can be observed as a weak band around 450 - 550 nm.

The excitation of these complexes leads to instant formation of predominantly-singlet excited states, from which the strong SOC enables rapid population of T<sub>1</sub> by internal conversions (IC) and intersystem crossings (ISC) [5, 41]. The deactivation from T<sub>1</sub> of complexes **Ir1** – **Ir3** results in intense phosphorescence, Figure 1, with relatively short emission lifetimes ( $\tau_0$ , in the order of hundreds of nanoseconds) and quite high emission quantum yields ( $\phi_0$ ), Table 1, as typically observed for other Ir(III) emitters [5].

The emission spectrum of complexes **Ir2** and **Ir3** is broad (FWHM = 120-130 nm) and non-structured, which is a typical feature of a T<sub>1</sub> state with predominant MLCT character (ascribed to the <sup>3</sup>MLCT<sub>Ir(NC)→dmb</sub> state). On the other hand, the emission of complex **Ir1** is narrower (FWHM = 95 nm) and resolved in weak vibronic modes, as it is typical for an emission with greater LC influences (attributed to the <sup>3</sup>LC<sub>pqi → pqi</sub>). These qualitative trends are in agreement with the results of TD-DFT calculations previously published for this complex series in acetonitrile [4, 39].

**Figure 1.** Emission spectra of Ir(III) complexes (Ir1– Ir3) as water-soluble chloride (Cl<sup>-</sup>) at 298 K ( $\lambda_{\text{exc}} = 365$  nm).**Table 1.** Photophysical parameters of Ir(III) complexes in aqueous solution ( $\sim 10^{-5}$  mol mL<sup>-1</sup>) at 298 K.

Sample	$\lambda_{\text{max}}$ (FWHM)/ nm <sup>a</sup>	$\phi / \%$ <sup>b</sup>			$\tau_0 /$ $\mu\text{s}$ <sup>c</sup>	$k_q /$ $10^9 \text{ L mol}^{-1} \text{ s}^{-1}$ <sup>d</sup>	$\Phi_{\Delta} / \%$ <sup>e</sup>
		N <sub>2</sub> - saturated ( $\phi$ )	Air- equilibrated	O <sub>2</sub> - saturated			
<b>Ir1</b>	575 (96)	67	32	5	2.4	4.1	47 ± 3
<b>Ir2</b>	582 (130)	7	3	2	0.47	4.6	53 ± 2
<b>Ir3</b>	535 (120)	77	47	14	1.0	3.6	47 ± 3

<sup>a</sup> Emission maximum and full-width at half maximum; <sup>b</sup> Absolute emission quantum yield, measured using an integrating sphere; <sup>c</sup> Emission lifetime in N<sub>2</sub>-saturated solution; <sup>d</sup> Estimated quenching rate constant; <sup>e</sup> Singlet oxygen quantum yield measured in air-equilibrated CD<sub>3</sub>CN solution against complex Ir1 ( $\Phi_{\Delta} = 0.47$ ) [4, 42, 43].

As already established, the phosphorescence of complexes **Ir1** – **Ir3** (from a triplet state) is effectively quenched in the presence of molecular triplet oxygen (<sup>3</sup>O<sub>2</sub>) [44]. For example, for **Ir3**, the one with most intense emission among the three, the quantum yield drops from 77% in N<sub>2</sub>-saturated solution ( $[\text{}^3\text{O}_2] = 0 \text{ mol L}^{-1}$ ) to only 14% in O<sub>2</sub>-saturated solution ( $[\text{}^3\text{O}_2] = 1.22 \times 10^{-3} \text{ mol L}^{-1}$ ). The quenching rate constant ( $k_q$ ) of the three complexes – obtained from Stern-Volmer plots (Figure SI2) – are very similar, in the order of  $4 \times 10^9 \text{ L mol}^{-1} \text{ s}^{-1}$  (Table 1). The magnitude is the same to other previously reported similar Ir(III) complexes [4, 30]. These emission quenching processes caused by molecular oxygen can occur by a non-radiative energy transfer from the complex's T<sub>1</sub> state to oxygen's singlet excited state, <sup>1</sup>Δ<sub>g</sub>, resulting in the formation of singlet oxygen species (<sup>1</sup>O<sub>2</sub>) in the process known as photosensitization [4, 44,



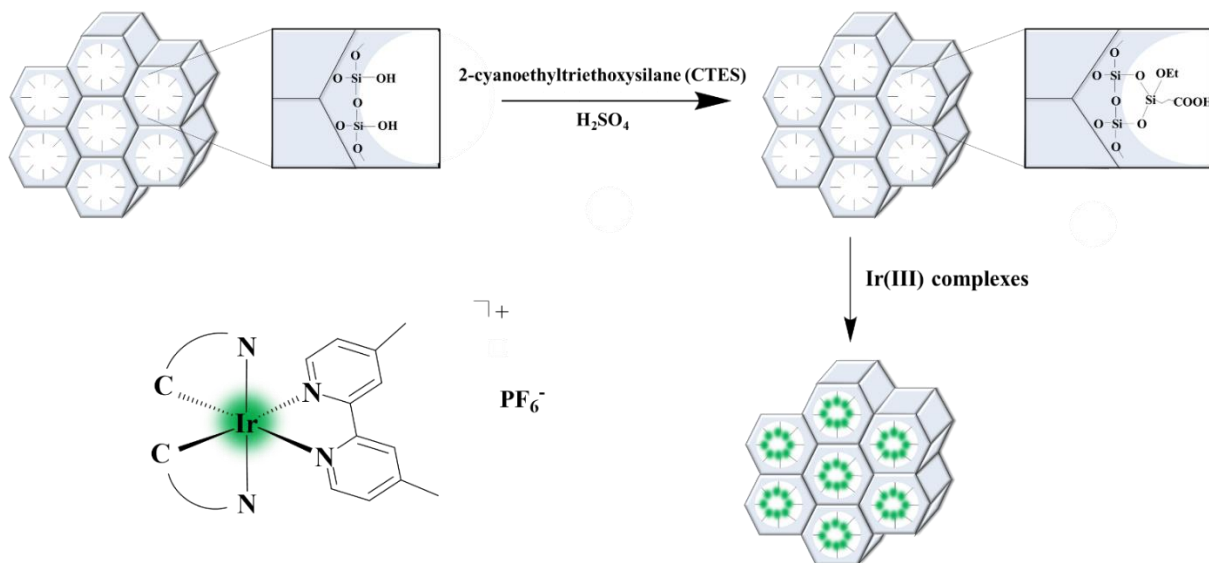
45]. The deactivation from oxygen's  $^1\Delta_g$  to its ground state,  $^3\Sigma_g$ , leads to a very characteristic narrow emission band around 1270 nm (Figure SI3) whose intensity can be used (via Equation SI5) for the quantification of the produced singlet oxygen by determination of the quantum yield ( $\Phi_\Delta$ ). The  $\Phi_\Delta$  values for the investigated complexes are high, in the order of 50% (Table 1), similar to the values for other published Ir(III) complexes [4, 30].

*Synthesis and characterization of the complex@MCM41-COOH nanoparticles*

Although the investigated Ir(III) complexes have suitable photophysical properties and are good candidates for efficient singlet oxygen photosensitizers in biological applications, their use in cellular environment is limited because  $[\text{Ir}(\text{NC})_2(\text{dmb})]^+$  complexes present high toxicity, as previously mentioned [30]. In summary, in the absence of light irradiation, the cellular viability decreases to less than 20% in the presence of  $8 \mu\text{mol L}^{-1}$  of the complexes; the complex **Ir1**, for example, leads to more than 90% decrease in cell viability in concentrations as small as  $2 \mu\text{mol L}^{-1}$  [30].

Therefore, the investigated complexes were encapsulated in the mesopores of MCM-41 silica nanoparticles, well known to be an inert nanocarrier in the cellular medium. The MCM-41 type material was obtained by sol-gel methodology and subjected to a post-synthetic route to attain surface-modification with carboxylic acid, Figure 2, to form MCM41-COOH nanoparticles. Then the cationic Ir(III) complexes were adsorbed on the surface of their mesoporous channels, to which the COOH groups play a major role. The covalent coupling between the carboxylic acid and the MCM-41 starting material were confirmed by FTIR spectral analysis (Figure SI4). Since  $\text{Cl}^-$  salts are very soluble in water while  $\text{PF}_6^-$  salts are not, the  $\text{Cl}^-$  counterion of the investigated  $[\text{Ir}(\text{NC})_2(\text{dmb})]^+$  series was substituted by  $\text{PF}_6^-$  before encapsulation to prevent the leakage of complexes from the nanoplatforms. For the sake of clarity and convenience, the MCM41-COOH samples incorporated with Ir(III) complexes **Ir1** – **Ir3** are named hereafter as complex@MCM41-COOH.

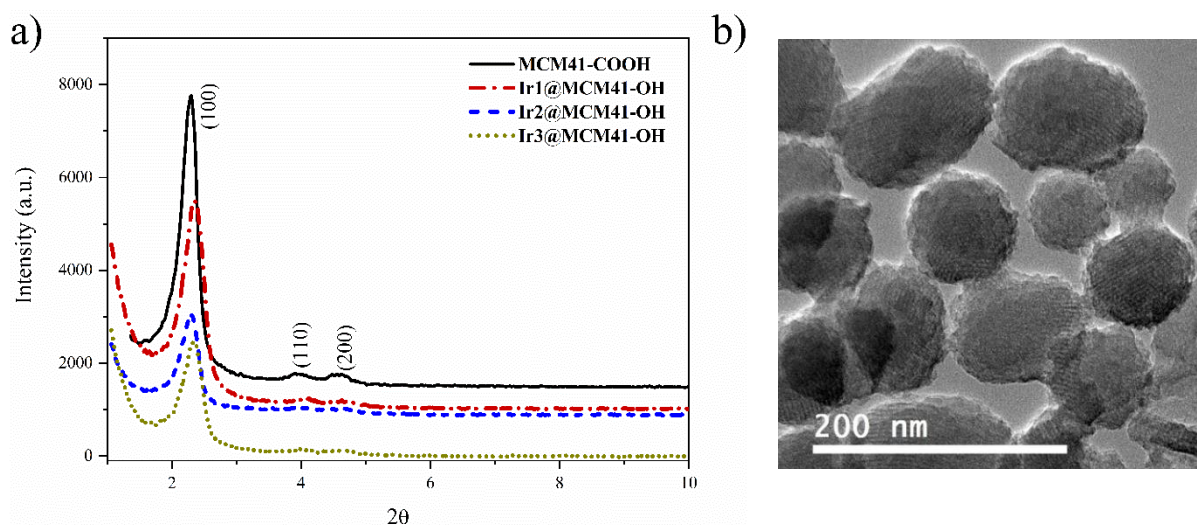
**Figure 2.** Schematic illustration of the MCM41-COOH obtained by post-synthetic route, incorporated with Ir(III) complexes.



The XRD patterns (Figure 3a) for both pristine MCM41-COOH nanoparticles and those incorporated with **Ir1** – **Ir3** displays three characteristic diffraction peaks around 2.3, 3.9 and 4.6, attributed to the [100], [110] and [200] lattice planes, typical of silica MCM-41 with hexagonally ordered mesopores (space group  $\text{P6mm}$ ) [46–48]. Comparing with the XRD pattern of the starting MCM-41 material, no significant changes in position of diffraction peaks for the hybrid nanoparticles were observed, which indicates that the synthetic procedures did not affect the structural integrity of the host [33]. Nevertheless, the (100) peak for Ir(III)-containing samples slightly shifts to higher angles, which suggests a slight increase in the pore size due to the insertion of the complex. In addition, the decrease in peak intensity brings evidence that Ir(III) complexes incorporation occurred mainly inside the mesoporous channels [35, 49].

Morphological studies of MCM41-COOH silica nanoparticles via transmission electron microscopy (TEM) revealed that the nanostructured mesopores have a highly ordered long-range hexagonal arrangement, Figure 3b, an observation that corroborates the results obtained by XRD. The average particle size is 150 nm, which was also confirmed by the DLS analysis (Table SII).

**Figure 3.** a) XRD patterns of unmodified MCM41-OH nanoparticles and those incorporated with Ir(III) complexes; and b) TEM images of MCM41-COOH nanoparticles.



The immobilization of Ir(III) complexes in the mesoporous channel of MCM41-COOH nanoparticles was also confirmed by zeta potential measurements (Table S11). Whereas the non-encapsulated nanoparticles present larger negative zeta potential ( $\sim -35$  mV) because of the carboxylic acids coordinated to  $\text{SiO}_2$  surface, the shift towards positive zeta potentials of complex@MCM41-COOH nanoparticles (between  $-25$  and  $-31$  mV) is ascribed to the incorporation of the positively-charged Ir(III) complexes on the mesoporous surface.

#### *Photophysical properties of complex@MCM41-COOH nanoparticles*

The UV irradiation of a dispersion of complex@MCM41-COOH nanoparticles in  $\text{H}_2\text{O}$  at 298 K leads to emissions in different colors that depend on the incorporated complex. The emission spectra of the samples are shown in Figure 4 and the photophysical parameters are summarized in Table 2.

The emission spectra of complexes **Ir2** and **Ir3** encapsulated in MCM41-COOH is shifted to higher energies when compared to their emission in solution ( $\Delta\lambda_{\text{max}} \sim 20$  nm), as a consequence of the rigidochromic effect that is observed only for transitions with a high dipole moment (i.e. charge transfer transitions, such as MLCT) [5, 39, 46, 51]. The dipoles reorientation of the solvent/medium molecules in response to the new dipole configuration of the MLCT states (that differs from the original in the ground state) occurs promptly in fluid solutions, however it is restrained in rigid media, destabilizing the MLCT state [5]. Therefore, the observation of a strong rigidochromism for the emission of MCM41-COOH nanoparticles incorporated with complexes **Ir2** and **Ir3** evidences even more that the nature of  $T_1$  state of

these complexes in solution is mostly  ${}^3\text{MLCT}_{\text{Ir}(\text{NC})\rightarrow\text{dmb}}$ . On the other hand, LC excited states (which show zero variation in the dipole moment in relation to the ground state) is environmentally-independent [5]. The non-observation of rigidochromism for complex **Ir1** reinforces its  ${}^3\text{LC}_{\text{pqi}\rightarrow\text{pqi}}$  nature.

**Figure 4.** Emission spectra of MCM41-COOH nanoparticles incorporated with Ir(III) complexes dispersed in  $\text{H}_2\text{O}$  ( $1 \text{ mg mL}^{-1}$ , approximately  $0.6 \times 10^{-5} \text{ mol mL}^{-1}$  of complex) at 298 K ( $\lambda_{\text{exc}} = 365 \text{ nm}$ ).

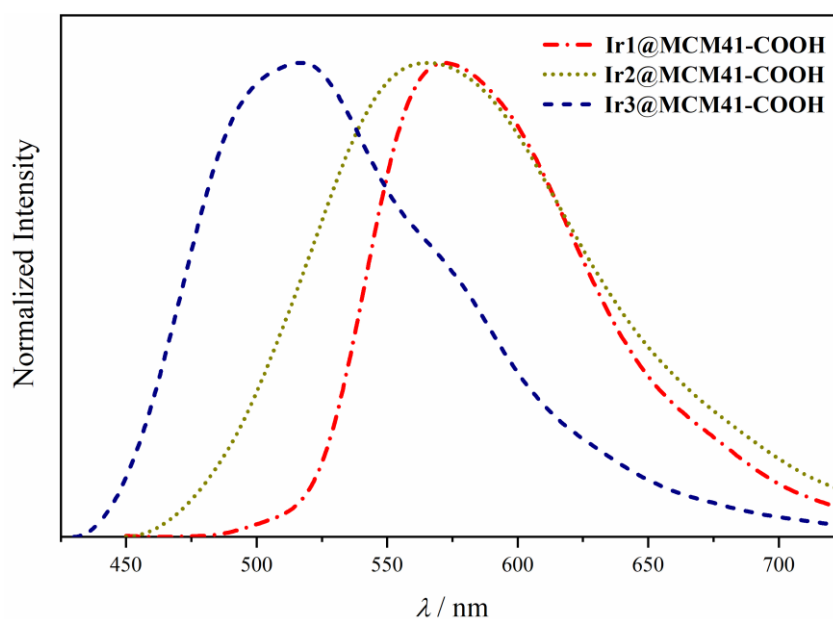


**Table 2.** Photophysical parameters of the nanoparticles incorporated with Ir(III) complexes dispersed in  $\text{H}_2\text{O}$  at 298 K.

Sample	$\lambda_{\text{max}}$ (FWHM)/ nm <sup>a</sup>	$\phi / \%$ <sup>b</sup>			$\tau_0 / \mu\text{s}$ <sup>c</sup>		$k_q /$ $10^9 \text{ L}$ $\text{mol}^{-1} \text{ s}^{-1d}$	$\Phi_{\Delta} / \%$ <sup>e</sup>
		$\text{N}_2$ - saturated ( $\phi$ )	Air- equilibrated	$\text{O}_2$ - saturated	$\tau_1$	$\tau_2$		
<b>Ir1@MCM41</b> <b>-COOH</b>	570 (90)	4.8	3.9	2.2	0.6	2.5	0.39	$50 \pm 1$
<b>Ir2@MCM41</b> <b>-COOH</b>	563 (126)	2.6	2.4	1.9	0.4	3.1	0.09	$41 \pm 3$
<b>Ir3@MCM41</b> <b>-COOH</b>	516 (110)	8.5	6.0	4.2	0.7	1.6	0.55	$52 \pm 1$

<sup>a</sup> Emission maximum and full-width at half maximum; <sup>b</sup> Absolute emission quantum yield, measured using an integrating sphere; <sup>c</sup> Emission lifetime in  $\text{N}_2$ -saturated solution; <sup>d</sup> Estimated quenching rate constant [50]; <sup>e</sup> Singlet oxygen quantum yield measured in air-equilibrated  $\text{CD}_3\text{CN}$  solution against complex Ir1 in the same solvent ( $\Phi_{\Delta} = 0.47$ ) [4, 42, 43].

The rigidification process in bulky systems also leads to an increase in the radiative decay [52], which would result in an increase of  $\phi_0$ . However, in the investigated porous system, the values of  $\phi_0$  for the incorporated complexes (Table 2) are much lower than in H<sub>2</sub>O. One hypothesis is that, although the measurements were made in deaerated solutions, such decrease is due to the effects of quenching by oxygen molecules that were retained in the pores along with the complexes.

The kinetic curves of emission decays monitored at  $\lambda_{\max}$  are composed of several exponential components. The faster components are possibly attributed to the radiative deactivation of the Ir(III) complexes confined in mesopores with greater oxygen retention, while the slower components are assigned to a more protected encapsulation in mesopores with less oxygen retention. For a quantitative estimation, such exponentials were simply adjusted to a second-order exponential with two lifetimes according to Equation 1, where  $\tau_1$  and  $\tau_2$  represent the average emission lifetimes of the Ir(III) complexes in mesopores with more or less retained oxygen content, respectively. The obtained values are summarized in Table 2. As expected, these values, in particular  $\tau_2$ , are longer in the MCM41-COOH mesopores than in solutions [52].

$$I = A_1 e^{(-t/\tau_1)} + A_2 e^{(-t/\tau_2)} \quad (1)$$

The  $k_q$  values obtained from Stern-Volmer graphs (Figure SI5) for nanoparticles dispersed in H<sub>2</sub>O were calculated using the slowest lifetime component,  $\tau_2$ . The  $k_q$  magnitudes calculated for the hybrid nanoparticles (Table 2) are smaller than those for the aqueous solution of Ir(III) complexes (Table 1), which indicates that there is a certain degree of impediment for O<sub>2</sub> to reach the complex inside the nanoparticle (without considering possible oxygen molecules already retained in the pores). Even though the  $k_q$  are slower for the nanoparticle than for the dissolved complexes, the suppression is still fast enough to guarantee a very efficient production of singlet oxygen (Figure SI6). When comparing among the three hybrid nanoparticles, **Ir1**@MCM41-COOH and **Ir3**@MCM41-COOH exhibit  $k_q$  of the same magnitude, while **Ir2**@MCM41-COOH exhibits lower value. These facts may indicate that complex **Ir2**, as the smallest and least susceptible to steric impediments, can reach smaller and more internal pores in the MCM41-COOH and, therefore, be more protected from O<sub>2</sub> quenching. Also, the much smaller  $k_q$  value for **Ir2**@MCM41-COOH is reflected in the lower  $\Phi_\Delta$  value among the three nanoparticles. For example, complex **Ir2** goes from the most efficient when solubilized (i.e. 53%) to the least efficient in nanoparticles (i.e. 41%).

*Toxicity of complex@MCM41-COOH, Photodynamic Therapy and Cellular uptake*

The toxicity of the MCM41-COOH nanoparticles with and without the complexes was investigated through cell viability experiments, using the healthy Hepa-RG cell line and the cancerous Hep-G2 cell line, both liver cells. Considering the 100% survival rate of those untreated cells, survival rates for cells in the absence and presence of irradiation were calculated.

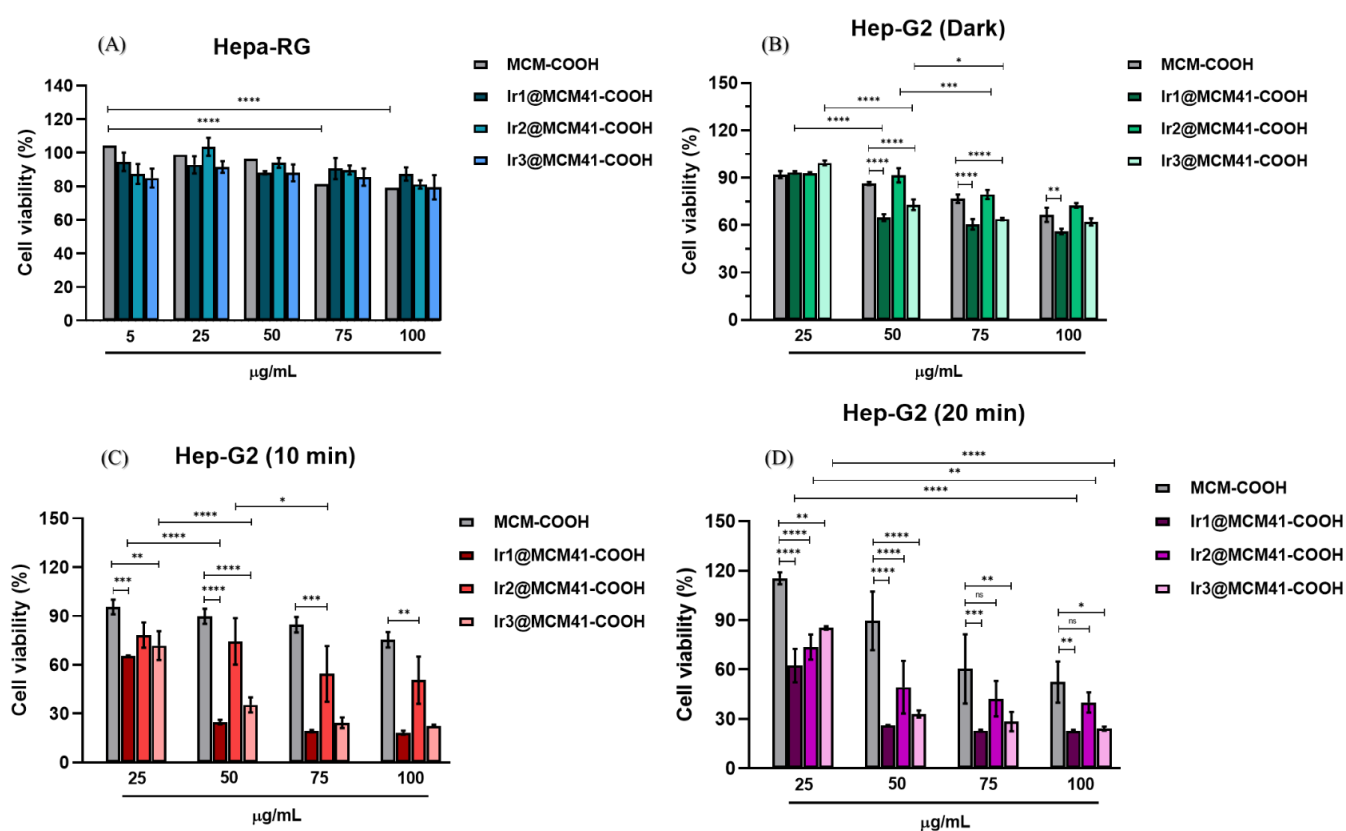
Cell viability performed in healthy cells (Figure 5A) showed that, statistically, the pristine nanoparticles (without encapsulated complexes) exhibit toxicity only at the highest concentrations, with cell viability of around 80%. Addition of Ir(III) complexes in the complex@MCM41-COOH nanoparticles do not lead to any changes in their statistical analysis, with similar cell viability to the pristine sample. These results indicate a good retention of the complexes inside the silica, without leakage to the cell media, otherwise a drop in cell viability would be expected [30]; it also indicates that the low cytotoxicity of the studied nanoparticles in the absence of irradiation can potentially lead to less side effects than traditional chemotherapy [53].

In the presence of cancer cell Hep-G2 (incubated for 24 h) in dark, the investigated nanoparticles present dose-dependent toxicity, with the lowest cell viabilities at 100  $\mu\text{g/mL}$ . Ir2@MCM41-COOH present statistical resemblance to pristine MCM41-COOH nanoparticles at any dosages, while the other complex@MCM41-COOH nanoparticles with **Ir1** and **Ir3** showed intrinsic toxicity that decrease their viabilities as compared to pristine. The results revealed that the nanoparticles imparted a higher toxicity against cancer cells, even in the dark, which was probably related to the greater internalization of nanoparticles.

The Hep-G2 cells incubated with the investigated nanoparticles were then irradiated with a 405 nm LED for 10 min and 20 min (Figure 5 C and D, respectively). For the pristine MCM41-COOH nanoparticles, the cell viability after 10 minutes of irradiation is similar to that observed in the dark, suggesting the lower cell viability for higher dosages of pristine sample is not resulted from the light itself, but rather the presence of the nanoparticles. In fact, a previous study has shown that Hep-G2 cells undergo apoptosis in the presence of silica nanoparticles through the generation of reactive oxygen species [54]. As for the complex@MCM41-COOH nanoparticles, even though Ir2@MCM41-COOH at low concentrations (25 and 50  $\mu\text{g/mL}$ ) present similar results to the pristine nanoparticle, the other nanoparticles with **Ir1** and **Ir3** show an excellent photodynamic effect already at 25  $\mu\text{g/mL}$ , decreasing cell viability to around 30% with only 10 min of irradiation, with similar trends at 20 min irradiation as well. These results are similar to the ones observed by Sun et al [27] for

which the cellular viabilities decreased to 20% for irradiated samples incubated with PPF-Ir-g-(POEGMA-b-PGal) at a concentration of 50  $\mu\text{g/mL}$ .

**Figure 5.** In vitro studies of MCM41-COOH and complex@MCM41-COOH nanoparticles for cancer therapy. Cell viability of (A) Hepa-RG and (B) Hep-G2 cells after 24 h of incubation in the dark; cell viability of Hep-G2 cell line after 24 h of incubation and irradiated for (C) 10 min ( $24 \text{ J}\cdot\text{cm}^{-2}$ ) and (D) 20 min ( $48 \text{ J}\cdot\text{cm}^{-2}$ ) using a 405 nm LED biotable. All experiments assessed by MTT. Statistical analysis was performed by two-way ANOVA with Tukey's comparison. The measurements are represented by average  $\pm$  standard error, \* $p < 0.05$ , \*\* $p < 0.01$ , \*\*\* $p < 0.001$  and \*\*\*\*  $p$ -value  $< 0.0001$ ).

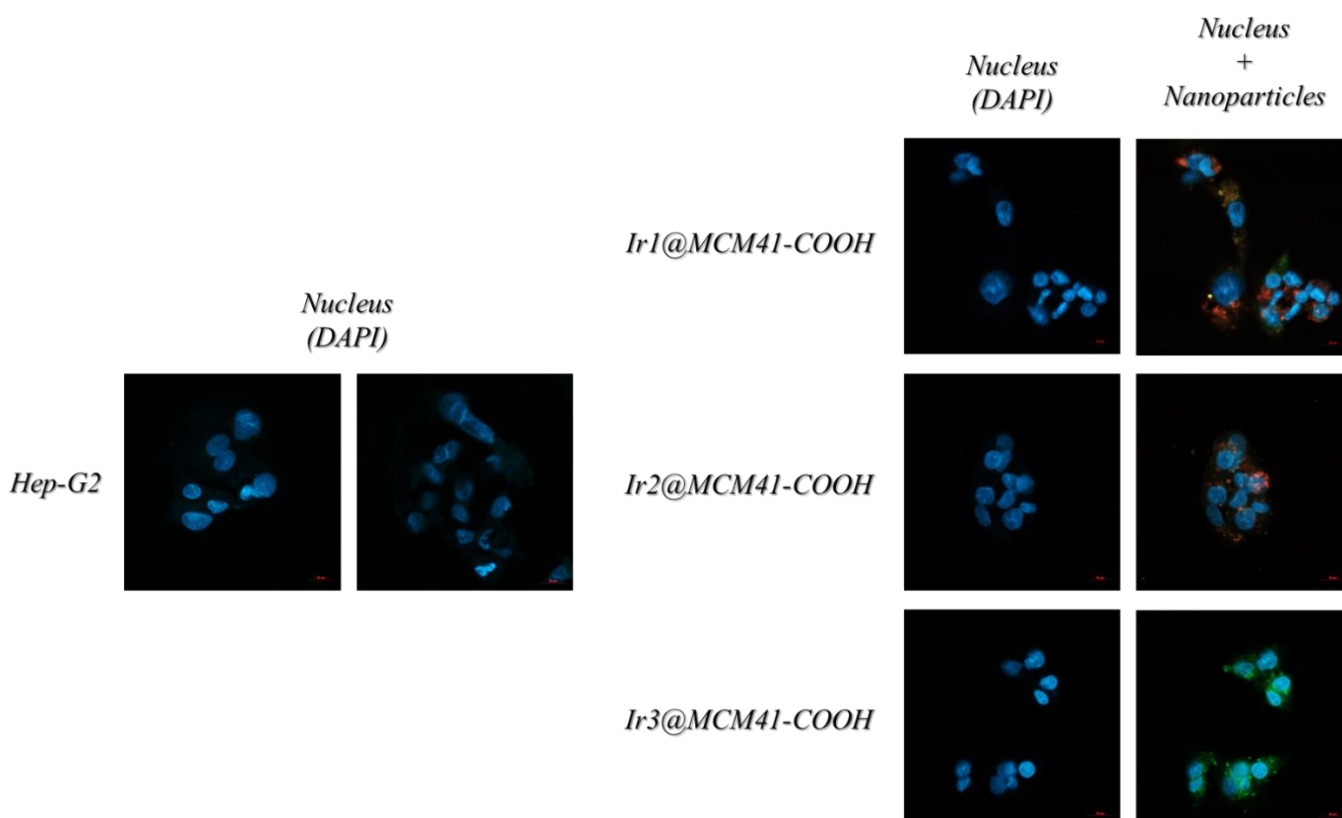


At higher doses, all nanoparticles lead to further decreases in cell viability, reaching around 15-20% of cell viability when a dosage of 100  $\mu\text{g/mL}$  of Ir1@MCM41-COOH and Ir3@MCM41-COOH is applied; even the Ir2@MCM41-COOH sample presents a statistically satisfactory result, bringing cell viability to around 45-50% for a dosage of 100  $\mu\text{g/mL}$ . Nevertheless, continuing the irradiations up to 20 min, a larger drop in viability of cells with nanoparticles Ir2@MCM41-COOH is observed, reaching 35-40% viability for the 100  $\mu\text{g/mL}$  dose. In this sense, the photodynamic effects of Ir2@MCM41-COOH against Hep-G2 are dose and time-dependent, while Ir1@MCM41-COOH and Ir3@MCM41-COOH nanoparticles

occur more quickly and are only dose dependent. These results of PDT corroborate the results of singlet oxygen quantum yield, which shows lower yields for **Ir2** inside MCM41-COOH.

To investigate how the cells interact with the nanoparticles in the biological culture, confocal microscopy experiments were performed with the complex@MCM41-COOH nanoparticles incubated for 24 h with posterior fixation and coloration of the nucleus with DAPI. The obtained results (Figure 6) indicate uptake of the nanoparticles by the cells cytoplasm, probably by phagocytosis, not being detected in the cell nucleus. It was also noticed that all the nanoparticles behave the same, besides the fact of presenting a small aggregation, evidenced by larger colourful dots in the micrographs.

**Figure 6.** Confocal microscopy of the cellular uptake behavior of complex@MCM41-COOH in Hep-G2 cell line. Green and red fluorescence, nanoparticles; blue fluorescence, nuclei stained with Hoechst 33258 (DAPI). Scale bars represent 20  $\mu\text{m}$ .



## Conclusions

Ir complexes@MCM41-COOH hybrid nanoparticles were successfully prepared and applied for photodynamic therapy of cancerous liver cells. The functionalized nanoparticles produced high amounts of singlet oxygen after light irradiation, being superior to the results in



water for Ir1@MCM41-COOH and Ir3@MCM41-COOH. Cellular assays showed low toxicity in healthy and cancerous strains, in the absence of light, presenting a high photodynamic action in the presence of light, in a short time of illumination and low concentration of nanoparticle. It is noteworthy that Ir complexes are highly toxic when free in solution, and the nanoparticulate approach has led to a safe use of these organic/inorganic photosensitizers with a much higher response than traditional organic PS. The results presented are very promising, as MCM41 is very versatile for theranostic applications and the development of new Ir-MCM41 hybrid nanomaterials through the association of molecules on the surface, as well as therapies combined with PDT, may open up new possibilities for *in vitro* and *in vivo* investigations in the field of cancer treatment research.

### Experimental procedures

All chemicals and solvents employed in the syntheses were purchased from Sigma-Aldrich or Synth and used without further purification. The complexes of the series  $[\text{Ir}(\text{NC})_2(\text{dmb})]^+$  were synthesized in previous contributions [4, 39] and used as available in the laboratory. Here, the preparation of the hybrid complex@MCM41-COOH nanoparticles are described.

#### *Syntheses of MCM-41 and surface modification with -COOH groups*

A previously established method was used for the synthesis of MCM-41 type mesoporous silica nanoparticles, using n-Cetyltrimethylammoniumbromide (CTAB) as a structure-directing agent [55]. CTAB (0.70 g, 1.9 mmol) was firstly dissolved in distilled water (336.0 mL) and aqueous NaOH (2.0 M, 2.45 mL) was added to this solution, followed by subsequent thermostabilization of the system to 353 K. Tetraethoxysilane (TEOS, 3.5 mL, 18.1 mmol) was added dropwise to the resulted solution under magnetic stirring and kept for 2 hours to produce a white precipitate that was filtered and washed with a mixture of deionized water/ethanol. The obtained MCM-41 silica nanoparticles were dried in oven at 313 K for 24 hours. For the removal of the surfactant template, calcination was carried out at 823 K for 5 hours in air. Modifications to carboxylic acids were carried out indirectly [56]. MCM-41 (1.0 g) was dispersed in toluene and 2-cyanoethyltriethoxysilane (CTES, 0.48 mL) was added dropwise, the reaction mixture was kept at reflux for 8 hours. The product was centrifuged and washed several times with water and ethanol, with subsequent drying in an oven. The product containing -CN groups was hydrolyzed in an acid medium. Thus, 1 g of the nanoparticle was dispersed in 120 mL of a 48%  $\text{H}_2\text{SO}_4$  solution, and the mixture heated to 373 K for 24 hours.

Finally, the product was collected by centrifugation and washed several times with water until the pH reaches neutrality. The obtained MCM-41-COOH was dried in oven at 317 K.

*Immobilization of  $[Ir(NC)_2(dmb)]^+$  complexes in MCM41-COOH nanoparticles*

MCM41-COOH was first dispersed in 15 mL of ethanol and then sonicated for 15 minutes. For the adsorption of Ir(III) complexes into the mesopores, stock ethanolic solutions of the complexes were made and added to MCM41-COOH dispersions, being vigorously stirred for 24 h at room temperature and protected from light. The hybrid solids were then filtered and dried under vacuum. The obtained complex@MCM41-COOH solids were centrifuged to remove the non-encapsulated molecules and the actual loadings of the complexes calculated from the UV-Vis spectrum of the eluates after the centrifugation procedure, using the Lambert-Beer law. The encapsulation yield of the complexes inside the pores are shown in Table 3.

**Table 3.** Encapsulation yield of Ir complexes inside MCM41-COOH

<b>Samples</b>	<b>Nominal mass (mg/100mg NP)</b>	<b>Real mass (mg/100mg NP)</b>	<b>Efficiency (%)</b>
<b>Ir1@MCM41-COOH</b>	1.0	0.30	30%
<b>Ir2@MCM41-COOH</b>	1.0	0.48	48%
<b>Ir3@MCM41-COOH</b>	1.0	0.59	59%

**References**

- [1] J.P. Paris, W.W. Brandt, Charge Transfer Luminescence of A Ruthenium(II) Chelate, *J. Am. Chem. Soc.* 81 (1959) 5001–5002.
- [2] K. Kalyanasundaram, M. Grätzel, Applications of functionalized transition metal complexes in photonic and optoelectronic devices, *Commun. Chem. Rev.* 177 (1998) 347–414.
- [3] Y. You, S.Y. Park, Phosphorescent Iridium(III) complexes: Toward high phosphorescence quantum efficiency through ligand control, *J. Chem. Soc. Dalt. Trans.* 9226 (2008) 1267–1282.

- [4] K.P.S. Zanoni, A. Ito, M. Grüner, N.Y. Murakami Iha, A.S.S. De Camargo, Photophysical dynamics of the efficient emission and photosensitization of  $[\text{Ir}(\text{Pqi})_2(\text{NN})]^+$  complexes, *Dalt. Trans.* 47 (2018) 1179–1188.
- [5] K.P.S. Zanoni, R.L. Coppo, R.C. Amaral, N.Y. Murakami Iha, Ir(III) complexes designed for light-emitting devices: Beyond the luminescence color array, *Dalt. Trans.* 44 (2015) 14559–14573.
- [6] S.A. Moore, D.L. Davies, M.M. Karim, J.K. Nagle, M.O. Wolf, B.O. Patrick, Photophysical behaviour of cyclometalated Iridium(III) complexes with phosphino(terthiophene) ligands, *Dalt. Trans.* 42 (2013) 12354–12363.
- [7] D.L. Ma, C. Wu, W. Tang, A.R. Gupta, F.W. Lee, G. Li, C.H. Leung, Recent advances in Iridium(III) complex-assisted nanomaterials for biological applications, *J. Mater. Chem. B.* 6 (2018) 537–544.
- [8] K.K.-S. Tso, K.K.-W. Lo, Strategic Applications of Luminescent Iridium(III) Complexes as Biomolecular Probes, Cellular Imaging Reagents, and Photodynamic Therapeutics, in: *Iridium(III) Optoelectron. Photonics Appl.*, 2017: pp. 415–477.
- [9] R.D. Costa, E. Ortí, H.J. Bolink, F. Monti, G. Accorsi, N. Armaroli, Luminescent ionic transition-metal complexes for light-emitting electrochemical cells, *Angew. Chemie - Int. Ed.* 51 (2012) 8178–8211.
- [10] J.I. Goldsmith, W.R. Hudson, M.S. Lowry, T.H. Anderson, S. Bernhard, Discovery and high-throughput screening of heteroleptic iridium complexes for photoinduced hydrogen production, *J. Am. Chem. Soc.* 127 (2005) 7502–7510.
- [11] J.H. Alstrum-Acevedo, M.K. Brennaman, T.J. Meyer, Chemical approaches to artificial photosynthesis, *Inorg. Chem.* 44 (2005) 6802–6827.
- [12] M.E. Köse, B.F. Carroll, K.S. Schanze, Preparation and spectroscopic properties of multiluminophore luminescent oxygen and temperature sensor films, *Langmuir.* 21 (2005) 9121–9129.
- [13] F. Shao, B. Elias, W. Lu, J.K. Barton, Synthesis and characterization of Iridium(III) cyclometalated complexes with oligonucleotides: Insights into redox reactions with DNA, *Inorg. Chem.* 46 (2007) 10187–10199.
- [14] Y. Yamazaki, H. Takeda, O. Ishitani, Photocatalytic reduction of  $\text{CO}_2$  using metal complexes, *J. Photochem. Photobiol.* 25 (2015) 106–137.
- [15] N.D. Silavwe, A.S. Goldman, R. Ritter, D.R. Tyler, Reduction of  $\text{CO}_2$  and Other Substrates Using Photochemical Reactions of The  $\text{W}_2(\text{CO})_{10}^{2-}$  Complex, *Inorg. Chem.* 28 (1989) 1231–1236.

- [16] C. Yang, F. Mehmood, T.L. Lam, S.L.F. Chan, Y. Wu, C.S. Yeung, X. Guan, K. Li, C.Y.S. Chung, C.Y. Zhou, T. Zou, C.M. Che, Stable luminescent Iridium(III) complexes with bis(N-heterocyclic carbene) ligands: Photo-stability, excited state properties, visible-light-driven radical cyclization and CO<sub>2</sub> reduction, and cellular imaging, *Chem. Sci.* 7 (2016) 3123–3136.
- [17] S.P.Y. Li, C.T.S. Lau, M.W. Louie, Y.W. Lam, S.H. Cheng, K.K.W. Lo, Mitochondria-targeting cyclometalated Iridium(III)-PEG complexes with tunable photodynamic activity, *Biomaterials.* 34 (2013) 7519–7532.
- [18] B. Liu, S. Monro, Z. Li, M.A. Javed, D. Ramirez, C.G. Cameron, K. Colón, J. Roque, S. Kilina, J. Tian, S.A. Mcfarland, W. Sun, New Class of Homoleptic and Heteroleptic Bis(terpyridine) Iridium(III) Complexes with Strong Photodynamic Therapy Effects, *ACS Appl. Bio Mater.* 2 (2019) 2964–2977.
- [19] J.S. Nam, M.G. Kang, J. Kang, S.Y. Park, S.J.C. Lee, H.T. Kim, J.K. Seo, O.H. Kwon, M.H. Lim, H.W. Rhee, T.H. Kwon, Endoplasmic Reticulum-Localized Iridium(III) Complexes as Efficient Photodynamic Therapy Agents via Protein Modifications, *J. Am. Chem. Soc.* 138 (2016) 10968–10977.
- [20] H. Huang, S. Banerjee, P.J. Sadler, Recent Advances in the Design of Targeted Iridium(III) Photosensitizers for Photodynamic Therapy, *ChemBioChem.* 19 (2018) 1574–1589.
- [21] E. Gianotti, B. Martins Estevão, F. Cucinotta, N. Hioka, M. Rizzi, F. Renò, L. Marchese, An efficient rose bengal based nanoplatforM for photodynamic therapy, *Chem. - A Eur. J.* 20 (2014) 10921–10925.
- [22] J. Zhang, C. Jiang, J.P. Figueiró Longo, R.B. Azevedo, H. Zhang, L.A. Muehlmann, An updated overview on the development of new photosensitizers for anticancer photodynamic therapy, *Acta Pharm. Sin. B.* 8 (2018) 137–146.
- [23] M.Q. Mesquita, C.J. Dias, S. Gamelas, M. Fardilha, M.G.P.M.S. Neves, M.A.F. Faustino, An insight on the role of photosensitizer nanocarriers for photodynamic therapy, *An. Acad. Bras. Cienc.* 90 (2018) 1101–1130.
- [24] C.K. Lim, J. Heo, S. Shin, K. Jeong, Y.H. Seo, W.D. Jang, C.R. Park, S.Y. Park, S. Kim, I.C. Kwon, Nanophotosensitizers toward advanced photodynamic therapy of Cancer, *Cancer Lett.* 334 (2013) 176–187.
- [25] M. Aioub, L.A. Austin, M.A. El-Sayed, Gold nanoparticles for cancer diagnostics, spectroscopic imaging, drug delivery, and plasmonic photothermal therapy, Elsevier Inc., 2018.

- [26] J. Zhao, X. Zhang, L. Fang, C. Gao, C. Xu, S. Gou, Iridium(III) Complex–Derived Polymeric Micelles with Low Dark Toxicity and Strong NIR Excitation for Phototherapy and Chemotherapy, *Small*. 16 (2020) 1–9.
- [27] P. Sun, G. Wang, H. Hou, P. Yuan, W. Deng, C. Wang, X. Lu, Q. Fan, W. Huang, A water-soluble phosphorescent conjugated polymer brush for tumor-targeted photodynamic therapy, *Polym. Chem.* 8 (2017) 5836–5844.
- [28] Z. Feng, P. Tao, L. Zou, P. Gao, Y. Liu, X. Liu, H. Wang, S. Liu, Q. Dong, J. Li, B. Xu, W. Huang, W. Wong, Q. Zhao, Hyperbranched Phosphorescent Conjugated Polymer Dots with Iridium ( III ) Complex as the Core for Hypoxia Imaging and Photodynamic Therapy, *ACS Appl. Mater. Interfaces* 2017. (2017) 28319–28330.
- [29] Y. Zhang, H. Fu, S. Chen, B. Liu, W. Sun, H. Gao, Construction of an Iridium(III)-complex-loaded MOF nanoplatfom mediated with a dual-responsive polycationic polymer for photodynamic therapy and cell imaging, *Chem. Commun.* 56 (2020) 762–765.
- [30] M.C. Grüner, K.P.S. Zanoni, C.F. Borgognoni, C.C. Melo, V. Zucolotto, A.S.S. De Camargo, Reaching Biocompatibility with Nanoclays: Eliminating the Cytotoxicity of Ir(III) Complexes, *ACS Appl. Mater. Interfaces*. 10 (2018) 26830–26834.
- [31] A.C.P. da Silva, P.H.Y. Cordeiro, B.M. Estevão, W. Caetano, H. Eckert, S.M.O. Santin, M.P. Moisés, N. Hioka, A.L. Tessaro, Synthesis of highly ordered mesoporous MCM-41: Selective external functionalization by time control, *J. Braz. Chem. Soc.* 30 (2019) 1599–1607.
- [32] B. Martins Estevão, I. Miletto, L. Marchese, E. Gianotti, Optimized Rhodamine B labeled mesoporous silica nanoparticles as fluorescent scaffolds for the immobilization of photosensitizers: A theranostic platform for optical imaging and photodynamic therapy, *Phys. Chem. Chem. Phys.* 18 (2016) 9042–9052.
- [33] B. Martins Estevão, F. Cucinotta, N. Hioka, M. Cossi, M. Argeri, G. Paul, L. Marchese, E. Gianotti, Rose Bengal incorporated in mesostructured silica nanoparticles: structural characterization, theoretical modeling and singlet oxygen delivery, *Phys. Chem. Chem. Phys.* 17 (2015) 26804–26812.
- [34] J. Karges, D. Díaz-García, S. Prashar, S. Gómez-Ruiz, G. Gasser, Ru(II) Polypyridine Complex-Functionalized Mesoporous Silica Nanoparticles as Photosensitizers for Cancer Targeted Photodynamic Therapy, *ACS Appl. Bio Mater.* 4 (2021) 4394–4405.
- [35] Y. Ellahioui, M. Patra, C. Mari, R. Kaabi, J. Karges, G. Gasser, S. Gómez-Ruiz, Mesoporous silica nanoparticles functionalised with a photoactive Ruthenium(II)

- complex: Exploring the formulation of a metal-based photodynamic therapy photosensitizer, *Dalt. Trans.* 48 (2019) 5940–5951.
- [36] D.O. Oluwole, I. Uddin, E. Prinsloo, T. Nyokong, The effects of silica based nanoparticles on the photophysicochemical properties, in vitro dark viability and photodynamic therapy study of zinc monocarboxyphenoxy phthalocyanine, *Journal Photochem. Photobiol. A Chem.* 329 (2016) 221–231.
- [37] M.C. Gonçalves, Sol-gel silica nanoparticles in medicine: A natural choice. design, synthesis and products, *Molecules.* 23 (2018) 1–26.
- [38] A. Liberman, N. Mendez, W.C. Trogler, A.C. Kummel, Synthesis and surface functionalization of silica nanoparticles for nanomedicine, *Surf. Sci. Rep.* 69 (2014) 132–158.
- [39] K.P.S. Zanoni, B.K. Kariyazaki, A. Ito, M.K. Brennaman, T.J. Meyer, N.Y. Murakami Iha, Blue-green iridium(III) emitter and comprehensive photophysical elucidation of heteroleptic cyclometalated Iridium(III) complexes, *Inorg. Chem.* 53 (2014) 4089–4099.
- [40] A.R.G. Smith, P.L. Burn, B.J. Powell, Spin-orbit coupling in phosphorescent Iridium(III) complexes, *ChemPhysChem.* 12 (2011) 2429–2438.
- [41] T.H. and T.F. H. Yersin, A. F. Rausch, R. Czerwieniec, Charge-Transfer Excited States in Phosphorescent Organo-Transition Metal Compounds: A Difficult Case for Time Dependent Density Functional Theory?, *Coord. Chem. Rev.* 255 (2011) 2622–2652.
- [42] J.C. de Mello, H.F. Wittmann, R.H. Friend, An improved experimental determination of external photoluminescence quantum efficiency, *Adv. Mater.* 9 (1997) 230–232.
- [43] W. Xing, M. Yin, Q. Lv, Y. Hu, C. Liu, J. Zhang, *Rotating Electrode Methods and Oxygen Reduction Electrocatalysts*, Elsevier, 2014.
- [44] M.C. DeRosa, R.J. Crutchley, Photosensitized singlet oxygen and its applications, *Coord. Chem. Rev.* 233–234 (2002) 351–371.
- [45] C. Schweitzer, R. Schmidt, Physical Mechanisms of Generation and Deactivation of Singlet Oxygen, *Chem. Rev.* 103 (2003) 1685–1758.
- [46] Zanoni, K. P.S. Vilela, R. R. C., Silva, D. A. I., Murakami Iha, N. Y., Eckert, H., de Camargo, A.S.S. Photophysical Properties of Ir(III) Complexes Immobilized in MCM-41 via Templated Synthesis, *Inorg. Chem.* 28 (2019) 4962–4971.
- [47] J.S. Beck, J.C. Vartuli, W.J. Roth, M.E. Leonowicz, C.T. Kresge, K.D. Schmitt, C.T.W. Chu, D.H. Olson, E.W. Sheppard, S.B. McCullen, J.B. Higgins, J.L. Schlenker, A New

- Family of Mesoporous Molecular Sieves Prepared with Liquid Crystal Templates, *J. Am. Chem. Soc.* 114 (1992) 10834–10843.
- [48] C. Huo, J. Ouyang, H. Yang, CuO nanoparticles encapsulated inside Al-MCM-41 mesoporous materials via direct synthetic route, *Sci. Rep.* 4 (2015) 1–9.
- [49] F. Havasia, A. Ghorbani-Choghamaranib, F. Nikpoura, Pd-Grafted Functionalized Mesoporous MCM-41: A Novel, Green and Heterogeneous NanoCatalyst for the Selective Synthesis of Phenols and Anilines from Aryl Halides in Water, *New J. Chem.* (2015) 6504–6512.
- [50] W. Xing, M. Yin, Q. Lv, Y. Hu, C. Liu, J. Zhang, *Oxygen Solubility, Diffusion Coefficient, and Solution Viscosity*, Elsevier B.V., 2014.
- [51] K.P.S. Zanoni, A. Ito, N.Y. Murakami Iha, Molecular-engineered [Ir(Fppy)<sub>2</sub>(Mepic)] towards efficient blue-emission, *New J. Chem.* 39 (2015) 6367–6376.
- [52] M. Baroncini, G. Bergamini, P. Ceroni, Rigidification or interaction-induced phosphorescence of organic molecules, *Chem. Commun.* 53 (2017) 2081–2093.
- [53] J.J. Hu, Q. Lei, X.Z. Zhang, Recent advances in photonanomedicines for enhanced cancer photodynamic therapy, *Prog. Mater. Sci.* 114 (2020) 100685.
- [54] J. Ahmad, M. Ahamed, M.J. Akhtar, S.A. Alrokayan, M.A. Siddiqui, J. Musarrat, A.A. Al-Khedhairi, Apoptosis induction by silica nanoparticles mediated through reactive oxygen species in human liver cell line HepG2, *Toxicol. Appl. Pharmacol.* 259 (2012) 160–168.
- [55] A. Wada, S.I. Tamaru, M. Ikeda, I. Hamachi, MCM-enzyme-supramolecular hydrogel hybrid as a fluorescence sensing material for polyanions of biological significance, *J. Am. Chem. Soc.* 131 (2009) 5321–5330.
- [56] S. Shen, P.S. Chow, S. Kim, K. Zhu, R.B.H. Tan, Synthesis of carboxyl-modified rod-like SBA-15 by rapid co-condensation, *J. Colloid Interface Sci.* 321 (2008) 365–372.

## 6. Conclusions

The two series of  $[\text{Ir}(\text{C}^{\wedge}\text{N})_2(\text{N}^{\wedge}\text{N})]^+$  complexes explored in this work exhibit intense emission when in solutions but their efficiency becomes strongly compromised by the interaction with molecular oxygen. In order to overcome this problem, in this work, the guest complex molecules were dispersed in solid hosts resulting in versatile materials with improved photophysical characteristics. Among the employed strategies  $[\text{Ir}(\text{C}^{\wedge}\text{N})_2(\text{dmb})]^+$  complexes were immobilized in hybrid organosilicate monoliths of the type GPTS:TEOS and adsorbed into pre-functionalized mesoporous MCM-41 nanoparticles, and  $[\text{Ir}(\text{C}^{\wedge}\text{N})_2(\text{dnbp})]^+$  complexes were encapsulated into the MCM-41 mesostructure through a self-templated method.

The GPTS:TEOS-derived organosilicate hybrid material prepared via hydrolysis and polycondensation of the GPTS and TEOS precursors were successfully developed. Due to the high concentration of the epoxy groups of the GPTS precursor in the matrix, that attains some extent of flexibility to the host, the resulting monoliths were free from cracks and showed very good optical quality. The hybrid monolithic xerogels loaded with  $[\text{Ir}(\text{Fppy})_2(\text{dmb})]^+$  complex exhibit higher absolute quantum yield and excited state lifetime values as compared to the complex in solution, which is attributed to the protection of the complex molecules from exposure to environmental  $\text{O}_2$ , provided by the rigid organosilicate host. Comparing the spectra of Ir-doped GPTS:TEOS xerogels with the pristine one, no significant changes in the energy of the peaks are observed, which indicates that the incorporation of Ir(III) complex did not affect the structural and chemical integrity of the host matrix.

The  $[\text{Ir}(\text{C}^{\wedge}\text{N})_2(\text{dnbp})]^+@$ MCM-41 materials were obtained in a simple, one-step route by incorporating the amphiphilic complexes into CTAB micelles, which act as templates for the highly organized mesopore formation of MCM-41. As in the above-mentioned case, the restricted diffusion of  $^3\text{O}_2$  into the mesopores remarkably prevents the triplet emission quenching even in pure  $\text{O}_2$  atmosphere. In addition, dual complex@MCM-41 systems were obtained by mixing the  $\text{FlrDbp}@$ MCM-41 and  $\text{pqiIrbp}@$ MCM-41 nanoparticles in different proportions, and we observed that the energy transfer between MCM-41 optical solids is weakened as compared to Ir(III) complexes in solutions, a remarkable characteristic that may be exploited for designing white-light emitting systems. These are important perspectives for the development of more-stable and more-efficient light-emitting systems (e.g. optoelectronic devices, optical rigidity sensors and biological markers) in assorted colors, even in  $\text{O}_2$ -rich environments.

Despite their promising applications, such systems can, in general, not be directly applied to biological systems due to the cytotoxicity of CTAB and the complex which remain inside



the pores. In this case, the possible leakage of these species could result in the apoptosis of healthy cells. In order to circumvent this drawback and amplify the range of applications in biophotonics, a post-synthetic strategy was employed. MCM-41 nanoparticles were functionalized with acid carboxylate groups and subsequently conjugated with Ir(III) complex molecules. The complex@MCM41-COOH nanoparticles exhibited high efficiency in the photoproduction and delivery of  $^1\text{O}_2$ . *In vitro* experiments showed that Hep-G2 liver cancer cell proliferation was reduced in the presence of the functional nanoparticles and after 10 min of blue-light irradiation. Thus, the obtained hybrid materials represent a step in the design of multifunctional platforms for cancer theranostic.

Altogether, the experimental strategies used in this work stands as an advance in the design of photo-functional materials with promising applications in optical sensors, luminescent devices and photodynamic therapy. The experimental strategy used in this work can be explored in the production of emitting materials in other regions of the spectrum through the exchange of the organometallic compound. In fact, although emphasis was given to the study of complexes of the  $[\text{Ir}(\text{Xppy})_2(\text{Rbpy})]^+$  series, the development of the project also included a 6-month internship in Germany (Capes/ Print funding) in the group of Prof. Cristian Strassert, at the University of Münster (WWU). During that period, phosphorescent Pt(II) complexes were included in the research by exploring the use of host-guest approach for the encapsulation of two Pt(II) complexes bearing dianionic tridentate  $\text{N}^-\text{N}^-\text{N}^-$  luminophoric ligands. These moieties included tert-butyl ( $^t\text{Bu}$ ) substitution pattern, while a variable monodentate coligand was employed. The results are under compilation to be soon submitted to publication.

## Appendix

### Supporting information: Structural and photophysical characterization of highly luminescent organosilicate xerogel doped with Ir(III) complex

#### General supporting results

**Fig. S1** FTIR spectra of pure FIrDmb complex

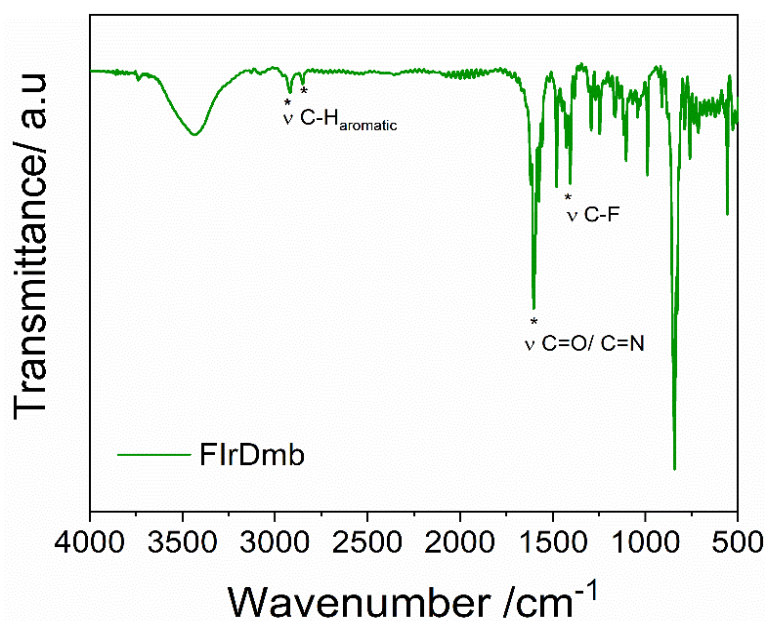


**Fig. S2** <sup>13</sup>C normalized signal intensity as a function of the contact time in <sup>13</sup>C{<sup>1</sup>H} CPMAS for the CH species in GPTS epoxy ring for samples GPTS:TEOS and GPTS:TEOS:FIrDmb.

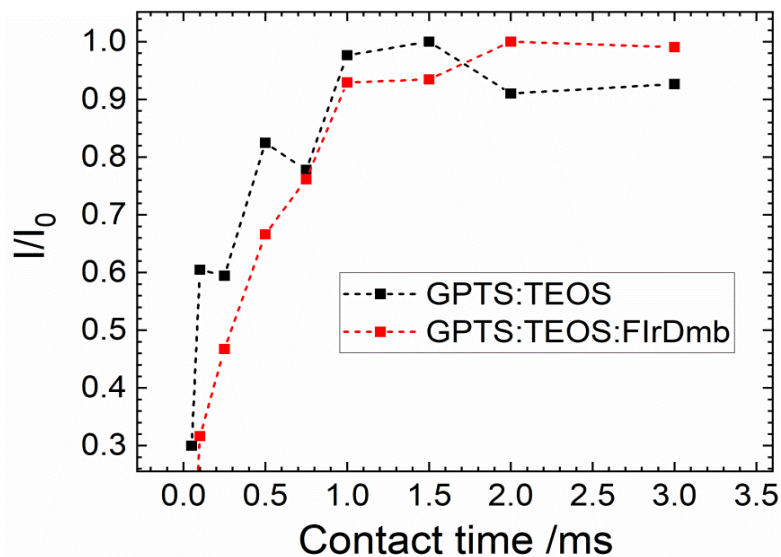


**Fig. S3**  $^{19}\text{F}$  MAS NMR spectrum for the GPTS:TEOS:FlrDmb xerogel. The is centered at -107 ppm. This chemical shift value is in the range expected for the pure Ir(III) complex [1], indicating that the interaction of the complex with the host matrix do not occur through fluorinated groups.

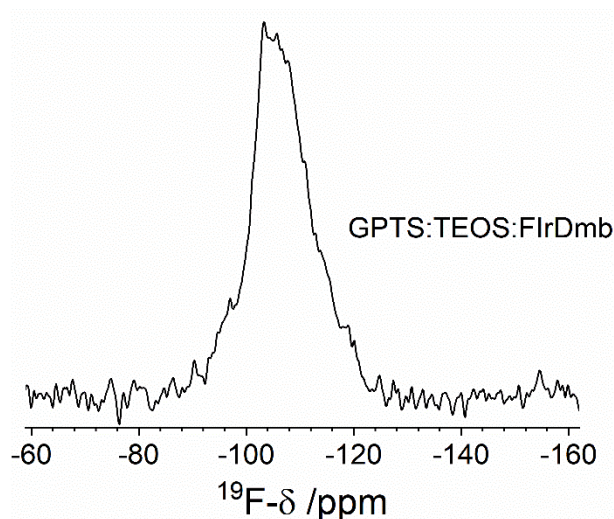


**Fig. S4** Possible products of the GPTS epoxy ring opening reaction. Letters are related to the  $^{13}\text{C}$  peak attributions in Figure 5b. Adapted from Ref. [2]

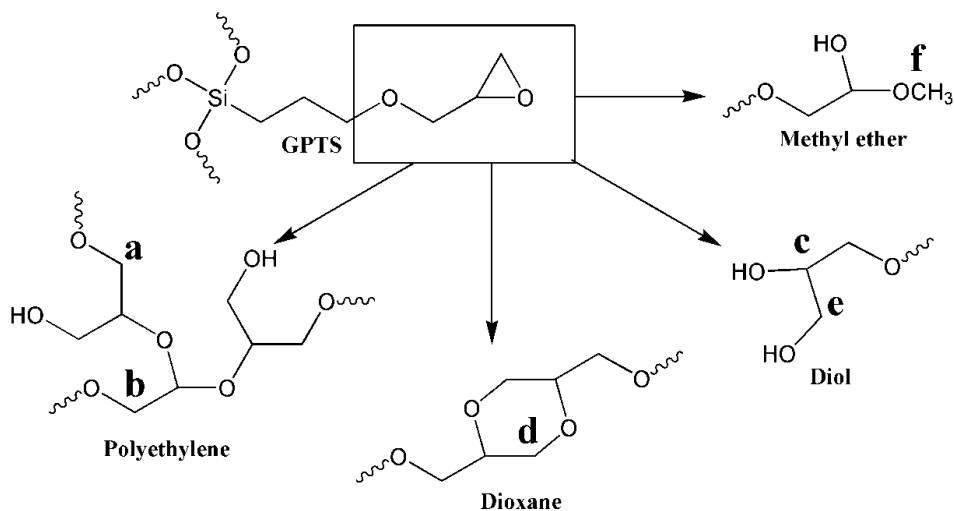
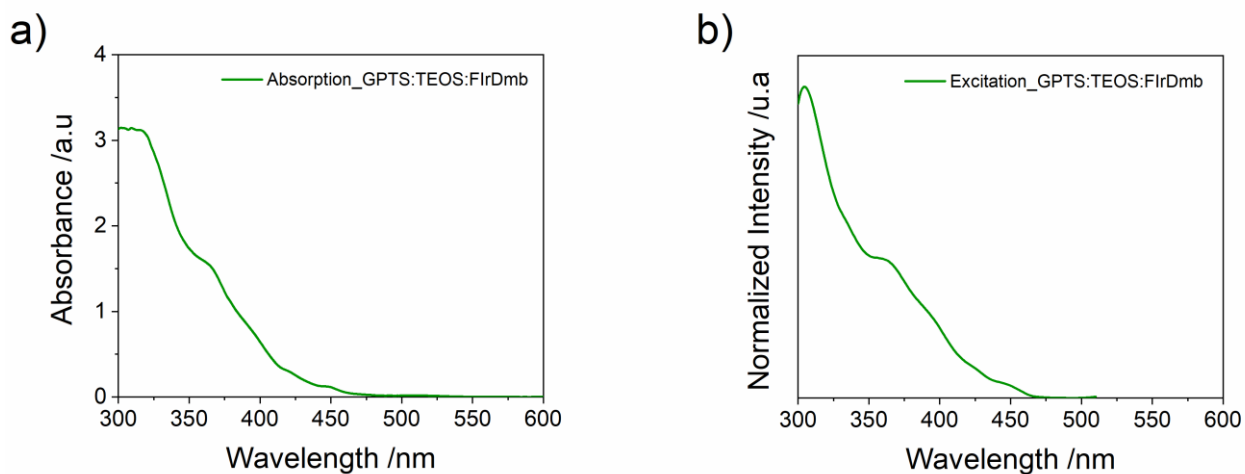


**Fig. S5** Absorption (a) and excitation (b) spectra ( $\lambda_{\text{emis}} = 508 \text{ nm}$ ) of GPTS:TEOS:FlrDmb xerogel. The absorption at high energy bands is obscured due to the high concentration of the complex in the matrix ( $3.18 \text{ mmol.L}^{-1}$ ) and the intense absorption of the hybrid matrix in UV region. Although these effects make interpretation of the absorption spectrum complicated, the excitation spectrum emphasizes that the low-energy bands in the region from 300 to 500 nm are largely preserved in the solid material



## References

- [1] K.P.S. Zanoni, R.R.C. Vilela, I.D.A. Silva, N.Y. Murakami Iha, H. Eckert, A.S.S. De Camargo, Photophysical Properties of Ir(III) Complexes Immobilized in MCM-41 via Templated Synthesis, *Inorg. Chem.* 58 (2019) 4962–4971.
- [2] P. Innocenzi, C. Figus, T. Kidchob, M. Valentini, B. Alonso, M. Takahashi, Sol-gel reactions of 3-glycidoxypropyltrimethoxysilane in a highly basic aqueous solution, *Dalt. Trans.* (2009) 9146–9152.

## Supporting information: Photophysical properties of Ir(III) complexes immobilized in MCM-41 via templated synthesis

### General experimental methods

All chemicals and solvents used for the syntheses were purchased from Sigma-Aldrich, Synth, or Dyesol and used as supplied.

#### *Syntheses of [Ir(C<sup>N</sup>)<sub>2</sub>(dnbp)]<sup>+</sup> complexes*

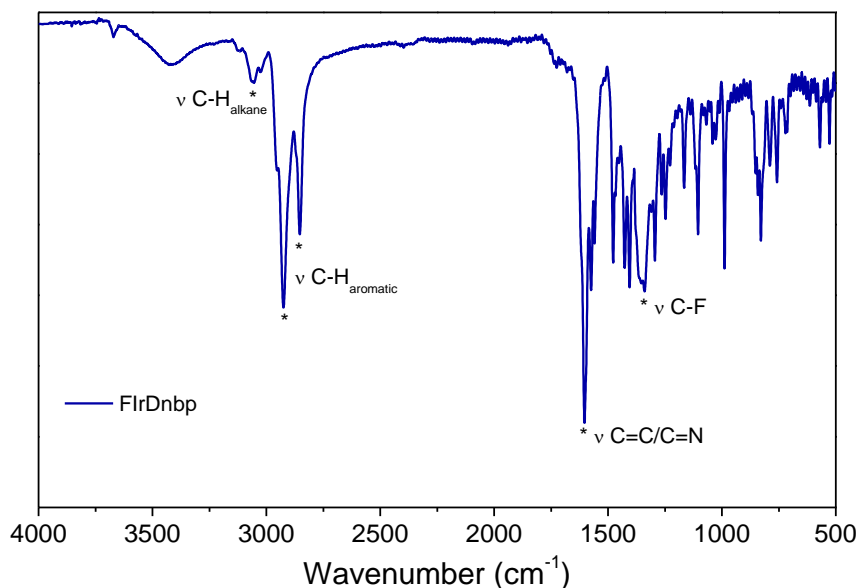
#### ***mer*-bis[2-(4,6-difluorophenyl)pyridinato-C<sup>2</sup>,N](4,4'-dinonyl-2,2'-bipyridine)**

**iridium(III) chloride - [Ir(*Fppy*)<sub>2</sub>(*dnbp*)]Cl (F<sub>Ir</sub>Dnbp).** Iridium chloride hydrate (IrCl<sub>3</sub>·H<sub>2</sub>O, 0.51 g, 1.7 mmol, Sigma-Aldrich) and 2-(2,4-difluorophenyl)pyridine (*Fppy*H, 0.57 mL, 3.6 mmol, Sigma-Aldrich) were dissolved in a 5/3 (v/v) solution of 2-ethoxyethanol/water (8 mL) and heated at reflux with stirring for 24 h. After cooling to room temperature, the greenish-yellow powder was collected by filtration to yield 0.88 g of [Ir(*Fppy*)<sub>2</sub>(μ-Cl)]<sub>2</sub>, employed in the following steps without further purification. 4,4'-dinonyl-2,2'-bipyridine (*dnbp*, 0.20 g, 0.50 mmol, Dyesol) and [Ir(*Fppy*)<sub>2</sub>(μ-Cl)]<sub>2</sub> (0.30 g, approx. 0.25 mmol) were mixed in 2-ethoxyethanol (10 mL) and heated at reflux with stirring for 18 to 20 h to produce [Ir(*Fppy*)<sub>2</sub>(*dnbp*)]Cl. Upon cooling, the resultant solution was roto-evaporated until an oil was formed, which was redissolved in a 70/1 (v/v) solution of dichloromethane/methanol (5 mL). The final product was purified through column chromatography using a silica gel (200-400 mesh Sigma-Aldrich) stationary phase and dichloromethane/methanol eluent solutions with increasing extents of methanol over time. Finally, the solvent was roto-evaporated to isolate the [Ir(*Fppy*)<sub>2</sub>(*dnbp*)]Cl as a brownish-yellow powder which was dried under vacuum to obtain 0.33 g (0.32 mmol, 67 % yield) of pure product.

<sup>1</sup>H NMR (300 MHz, CD<sub>3</sub>OD), δ/ppm: 8.60 (s; 2H), 8.32 (d; *J* = 7 Hz; 2H), 7.90 (t; *J* = 7 Hz; 2H), 7.82 (d; *J* = 6 Hz; 2H), 7.63 (d; *J* = 6 Hz; 2H), 7.42 (d; *J* = 7 Hz; 2H), 7.10 (t; *J* = 6 Hz; 2H), 6.65 (dt; *J* = 9, 3 Hz; 2H), 5.67 (dd; *J* = 9, 3 Hz; 2H), 1.5–0.7 (m; 38H).

MS (CH<sub>2</sub>Cl<sub>2</sub>:CH<sub>3</sub>OH): molecular weight calculated for [M – Cl]<sup>+</sup> (IrC<sub>50</sub>H<sub>56</sub>F<sub>4</sub>N<sub>4</sub>) = 981.22; *m/z* found = 981.41 (39%), 979.40 (23%), 982.40 (20%), 980.41 (13%), 983.41 (5%).

FTIR (KBr):

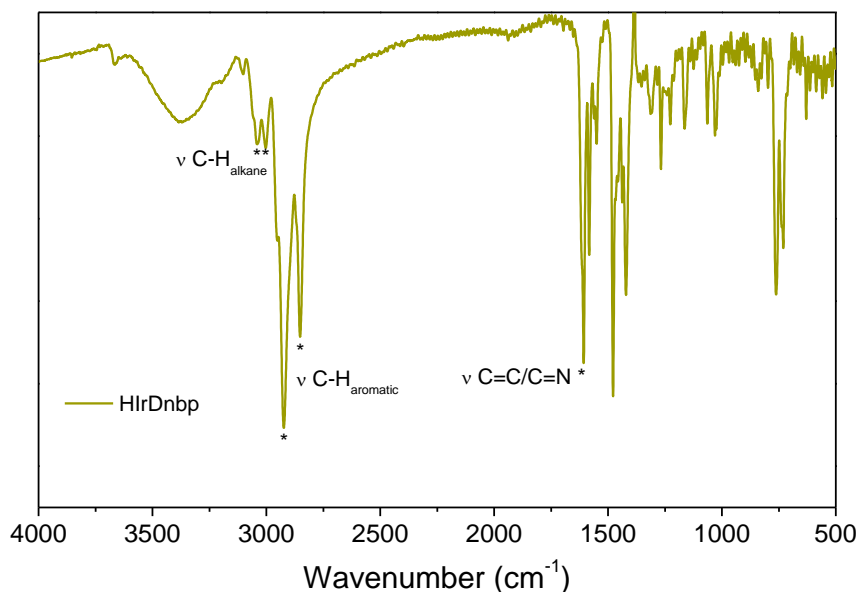


***mer*-bis[2-phenylpyridinato-C<sup>2</sup>,N](4,4'-dinonyl-2,2'-bipyridine)iridium(III) chloride - [Ir(*ppy*)<sub>2</sub>(*dnbp*)]Cl (**HlrDnbp**). The compound was synthesized following the same procedure to [Ir(*Fppy*)<sub>2</sub>(*dnbp*)]Cl, starting from 2-phenylpyridine (*ppy*H, 0.57 mL, 3.9 mmol) and IrCl<sub>3</sub>·H<sub>2</sub>O (0.56 g, 1.9 mmol) to produce 0.89 g of [Ir(*ppy*)<sub>2</sub>(μ-Cl)]<sub>2</sub> in the first step, then from *dnbp* (0.23 g, 0.58 mmol) and [Ir(*ppy*)<sub>2</sub>(μ-Cl)]<sub>2</sub> (0.30 g, approx. 0.28 mmol) to produce 0.27 g (0.29 mmol, 51 % yield) of pure [Ir(*ppy*)<sub>2</sub>(*dnbp*)]Cl in the second step.**

<sup>1</sup>H NMR (300 MHz, CD<sub>3</sub>OD), δ/ppm: 8.56 (s; 2H), 8.08 (d; *J* = 8 Hz; 2H), 7.80 (m; 6H), 7.57 (d; *J* = 6 Hz; 2H), 7.35 (d; *J* = 6 Hz; 2H), 6.99 (m; 4H), 6.83 (t; *J* = 7 Hz; 2H), 6.23 (d; *J* = 8 Hz; 2H), 1.5–0.7 (m; 38H).

MS (CH<sub>2</sub>Cl<sub>2</sub>:CH<sub>3</sub>OH): molecular weight calculated for [M – Cl]<sup>+</sup> (IrC<sub>50</sub>H<sub>60</sub>N<sub>4</sub>) = 909.26; *m/z* found = 909.44 (39%), 907.44 (22%), 910.45 (21%), 908.44 (12%), 911.45 (5%), 912.45 (1%).

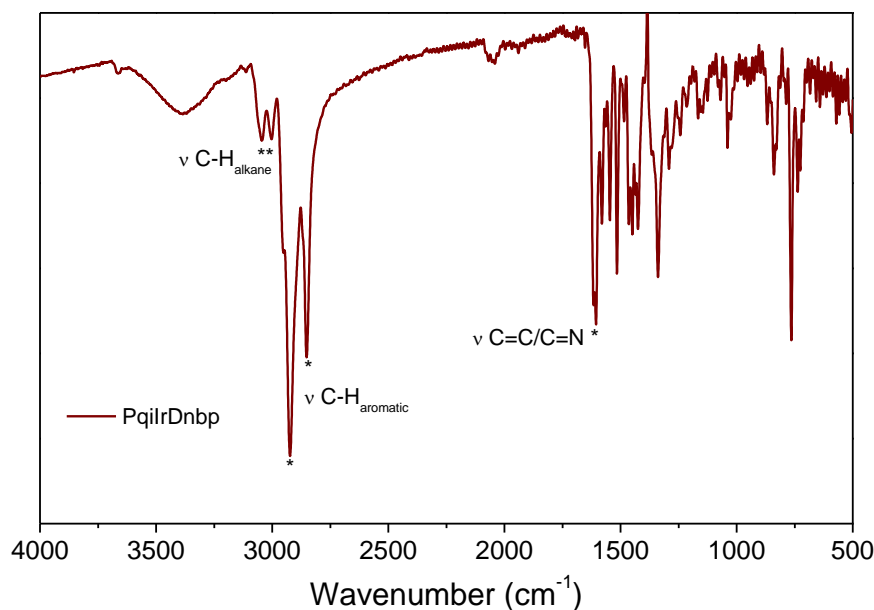
FTIR (KBr):



***mer*-bis[2-phenylquinolinato-C<sup>2</sup>,N](4,4'-dinonyl-2,2'-bipyridine)iridium(III) chloride - [Ir(*pqi*)<sub>2</sub>(*dnp*)]Cl (**pqiIrDnbp**). The compound was synthesized following the same procedure to [Ir(*Fppy*)<sub>2</sub>(*dnp*)]Cl and [Ir(*ppy*)<sub>2</sub>(*dnp*)]Cl, starting from 2-phenylquinoline (*pqi*, 0.76 g, 3.7 mmol) and IrCl<sub>3</sub>·H<sub>2</sub>O (0.56 g, 1.9 mmol) to produce 0.90 g of [Ir(*pqi*)<sub>2</sub>(μ-Cl)]<sub>2</sub> in the first step, then from *dnp* (0.20 g, 0.49 mmol) and [Ir(*pqi*)<sub>2</sub>(μ-Cl)]<sub>2</sub> (0.30 g, approx. 0.25 mmol) to produce 0.31 g (0.30 mmol, 60 % yield) of pure [Ir(*pqi*)<sub>2</sub>(*dnp*)]Cl in the second step. <sup>1</sup>H NMR (500 MHz, CD<sub>3</sub>OD), δ/ppm: 8.38 (m; 4H), 8.16 (m; 4H), 8.08 (d; *J* = 5 Hz; 2H), 7.80 (d; *J* = 8 Hz; 2H), 7.38 (m; 6H), 7.15 (t; *J* = 5 Hz; 2H), 6.99 (t; *J* = 6 Hz; 2H), 6.79 (t; *J* = 6 Hz; 2H), 6.51 (d; *J* = 8 Hz; 2H), 1.4–0.8 (m; 38H).**

MS (CH<sub>2</sub>Cl<sub>2</sub>:CH<sub>3</sub>OH): molecular weight calculated for [M – Cl]<sup>+</sup> (IrC<sub>58</sub>H<sub>64</sub>N<sub>4</sub>) = 1009.37; *m/z* found = 1009.47 (33%), 1010.47 (23%), 1007.47 (22%), 1008.47 (14%), 1011.48 (7%), 1012.48 (1%).

FTIR (KBr):



#### *Preparation of PMMA films with Ir(III) complexes*

The Ir(III) compounds (5 mg) were mixed with PMMA (250 mg) in dichloromethane (7 mL) and left to dry in petri dishes overnight, protected from humidity and light.

#### *<sup>1</sup>H NMR in solution*

<sup>1</sup>H NMR spectra of CD<sub>3</sub>OD solutions of the complexes were recorded using a Bruker AIII 500 (500 MHz) or an INOVA 300 (300 MHz) spectrometer. The residual solvent signals were employed as internal standards.

#### *Solid State <sup>19</sup>F NMR*

Solid State <sup>19</sup>F MAS NMR experiments were performed on an Agilent DD2 600 MHz spectrometer interfaced with a 5.64 T magnet using a 3.2 mm probe and spinning speeds of 25.0 kHz for pure [Ir(C<sup>N</sup>)<sub>2</sub>(dnbp)]Cl complex, [Ir(C<sup>N</sup>)<sub>2</sub>(dnbp)]@MCM-41, and four physical mixtures containing 1 mg of [Ir(C<sup>N</sup>)<sub>2</sub>(dnbp)]Cl and variable amounts (24.5 mg, 49.0 mg, 73.5 mg, and 98 mg) of MCM-41 ground together in a mortar. A Hahn Echo sequence with π/2 pulse length of 2.5 μs, π pulse length of 5 μs, and inter-pulse delay of 160 μs (4 rotor periods) was used in all experiments. This was necessary to remove the intense probe background caused by the signal of the spinner caps and other F-containing probe components. <sup>19</sup>F chemical shifts are reported relative to CFCl<sub>3</sub> using powdered AlF<sub>3</sub> (-172 ppm) as a secondary standard. To check for potential systematic quantification errors, we conducted Hahn spin echo intensity measurements as a function of the number of rotor cycles. These results indicate that the spin-



spin relaxation times of the complex in the solid state and of the complex incorporated into MCM-41 are essentially identical, confirming that the use of the Hahn spin echo sequence does not cause any systematic quantification errors in the present case.

#### *FTIR spectra*

FTIR measurements were performed using a Thermo Scientific™ Nicolet™ iS50 IR Spectrometer under room temperature. Prior to measurements, samples were diluted in KBr (1 mg complex : 80 mg KBr) using an agate mortar and pressed under high pressures to produce IR transparent pastille discs.

#### *Mass spectra*

Mass spectroscopy was performed using a Bruker Daltonics MAXIS HD.

#### *Photophysical characterization*

UV-Vis absorption spectra were recorded on a Hewlett-Packard diode array spectrophotometer model 8453. Steady-state and time-resolved emission spectra were recorded using a Horiba Fluorolog time-correlated single photon-counting. A xenon lamp ( $\lambda_{\text{exc}} = 365$  nm, 1 nm bandwidth, 400 nm long pass filter) or a Horiba Delta Diode ( $\lambda_{\text{exc}} = 370$  nm, frequency = 20 kHz) were employed as excitation sources for steady-state or time-resolved measurements, respectively. Emission intensities (photon counting) of steady-state spectra were corrected for the system spectral response. For measurements of solutions at room temperature, the absorbance of sample solutions was set between 0.1 and 0.3 in a quartz cuvette with 1.000 cm optical path length. Solutions were bubbled with N<sub>2</sub> for at least 20 minutes prior to standard measurements. For MCM-41 powders, samples were placed in a sealed quartz cuvette with 1.000 cm optical path length and the emission was detected using a front-face apparatus.

The oxygen quenching experiments in the MCM-41 samples were performed by using a Schlenk line to alternate (3 times) vacuum evacuation for 2 min and insertion of gas (air, N<sub>2</sub> or O<sub>2</sub>) for another 2 min inside the sealed cuvette.

Absolute emission quantum yields ( $\phi_0$ ) were measured using a BaSO<sub>4</sub> coated integrating sphere, model Horiba Quanta- $\phi$ . For degassed solutions at room temperature,  $\phi_0$  were measured applying the methodology described by de Mello *et al.* [1], with samples positioned in the center of the sphere. For MCM-41 powders, the standard equation was applied, Equation S1, with samples positioned at the bottom of the sphere,

$$\phi_0 = \frac{P_s - P_b}{L_b - L_s} \quad (\text{S1})$$

in which P and L are respectively the integral of the phosphorescence and the area under the lamp signal, while subscripts s and b indicate the sample or the blank. The blank sample consisted of an MCM-41 sample produced with no complexes inside the CTAB micelles and the emission spectra were recorded with 375 nm excitation to avoid influence from the silica emission as much as possible (at higher wavelengths, however, the absorption of the complex inside the mesopores becomes too low to result in detectable emission intensities).

The radiative ( $k_r$ ) and nonradiative decay ( $k_{nr}$ ) rates were calculated by

$$k_r = \frac{\phi_0}{\tau_0} \quad (S2)$$

$$k_{nr} = \frac{1 - \phi_0}{\tau_0} \quad (S3)$$

where  $\tau_0$  is the emission lifetime.

The quenching rate constant ( $k_q$ ) was obtained by Stern–Volmer analyses using

$$\frac{\phi_0}{\phi} = k_q \tau_0 [{}^3\text{O}_2] + 1 \quad (S4)$$

in which  $\phi_0$  is the emission quantum yield of the complex in a sample solution with a known  $[{}^3\text{O}_2]$  concentration.

The  $x$  and  $y$  CIE coordinates were calculated by Equations S5a and S5b from their  $X$ ,  $Y$  and  $Z$  tristimulus, Equations S6a to S6c, using photoluminescence spectral data,  $I(\lambda)$ . The numerical values of the CIE  $\bar{x}(\lambda)$ ,  $\bar{y}(\lambda)$  and  $\bar{z}(\lambda)$  standards, are available as online free-access tables.

$$x = \frac{X}{X + Y + Z} \quad (S5a)$$

$$y = \frac{Y}{X + Y + Z} \quad (S5b)$$

$$X = \int_{380}^{780} I(\lambda) \bar{x}(\lambda) d\lambda \quad (S6a)$$

$$Y = \int_{380}^{780} I(\lambda) \bar{y}(\lambda) d\lambda \quad (S6b)$$

$$Z = \int_{380}^{780} I(\lambda) \bar{z}(\lambda) d\lambda \quad (S6c)$$

### Morphological characterization

X-ray powder diffraction (XRD) was performed in a Rigaku Miniflex diffractometer with a Cu-K $\alpha$  radiation ( $\lambda = 0.15418$  nm, 30 kV, 15 mA). The  $d_{[hkl]}$  spacings were calculated by Equation S7, in which  $\theta_{[hkl]}$  is the scattering angle and  $\lambda$  is the wavelength of the incident irradiation (equal to 1.5418 Å in the employed equipment).

$$d_{[hkl]} = \frac{\lambda}{2 \sin \theta_{[hkl]}} \quad (S7)$$

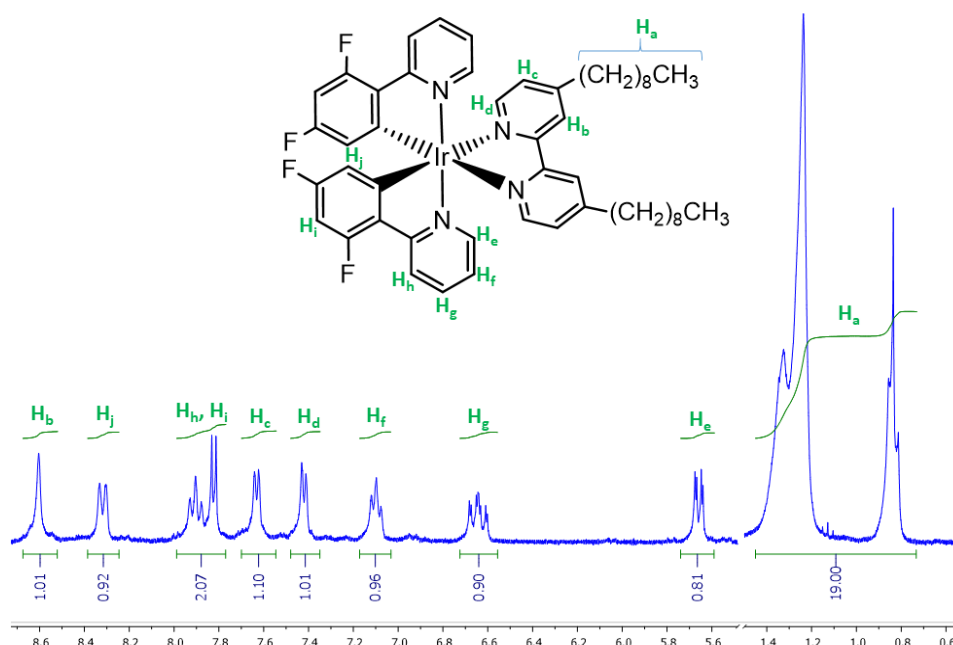
The average lattice constant ( $a_0$ ) was calculated by Equation S8.

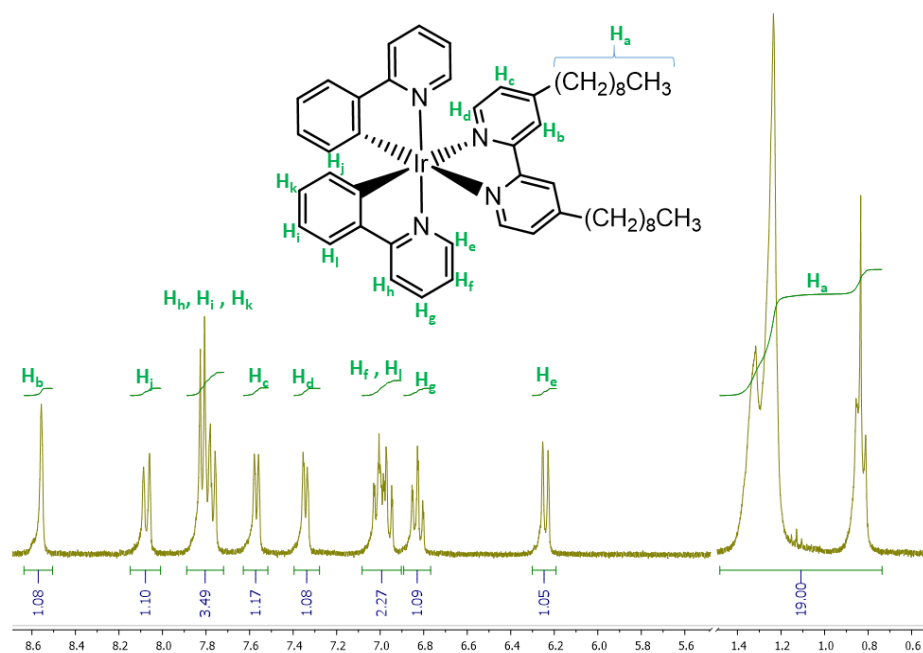
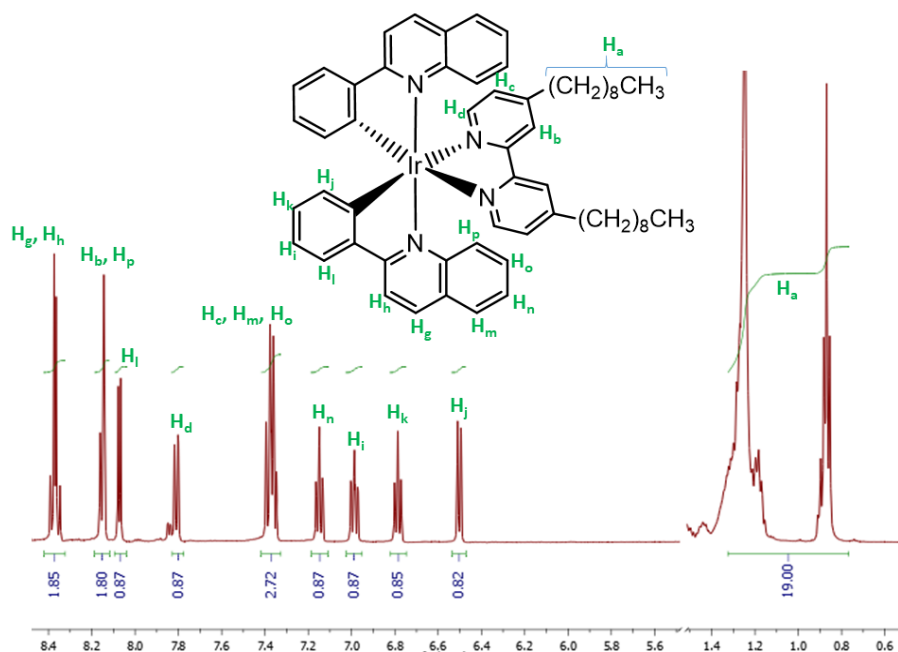
$$a_0 = \frac{2}{\sqrt{3}} d_{[100]} \quad (S8)$$

Transmission electron microscopy was performed in a JEOL JEM-2100 Microscope. The volume and size of pores were evaluated by N<sub>2</sub> adsorption/desorption isotherms registered at 77 K using a Micromeritics ASAP 2020 instrument. Prior to sorption studies, samples were degassed at 200 °C for 2h. The  $S_{\text{BET}}$  parameter was calculated through the BET method using the results from relative pressures between 0.05 to 0.2. The pore size distributions were calculated by the KJS method [2].

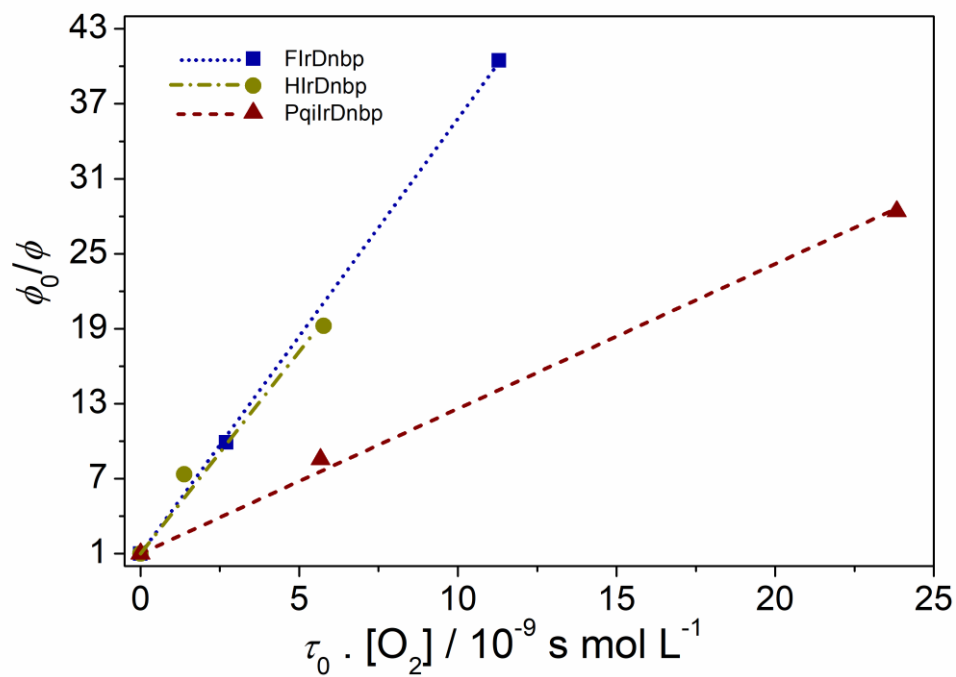
### General supporting results

**Figure S1.** <sup>1</sup>H NMR spectrum (300 MHz) of FIrDnbp in CD<sub>3</sub>OD.

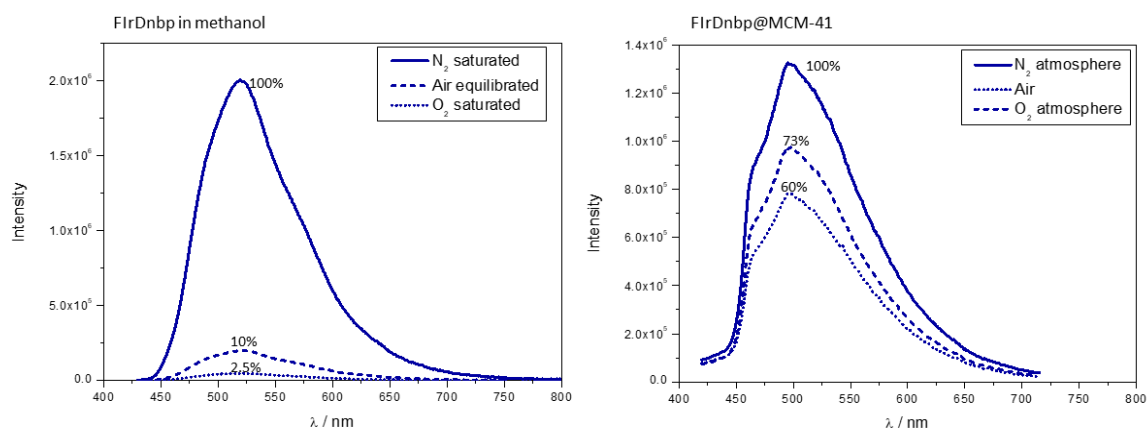


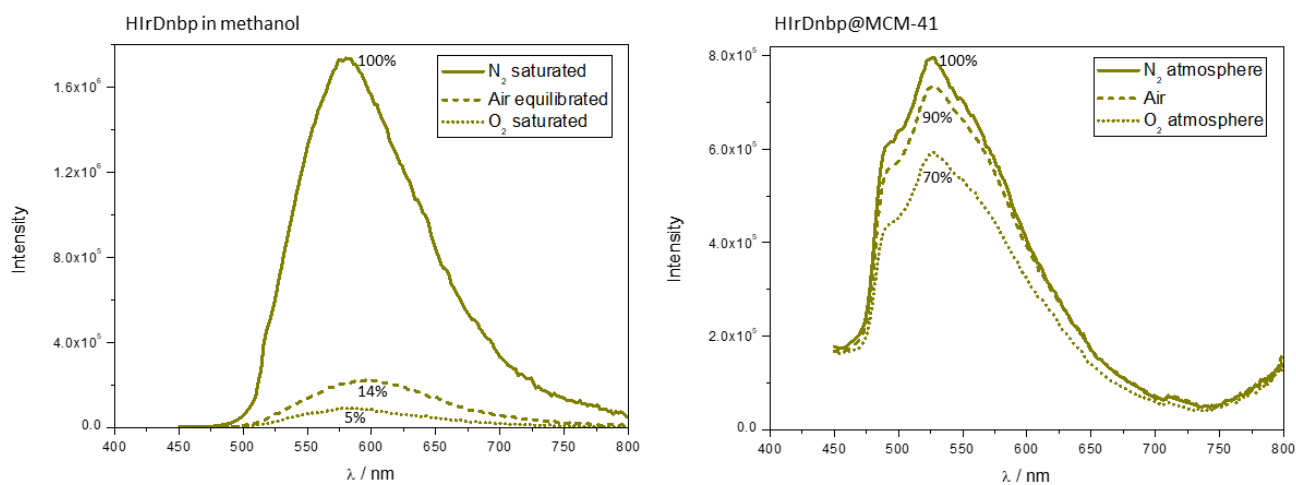
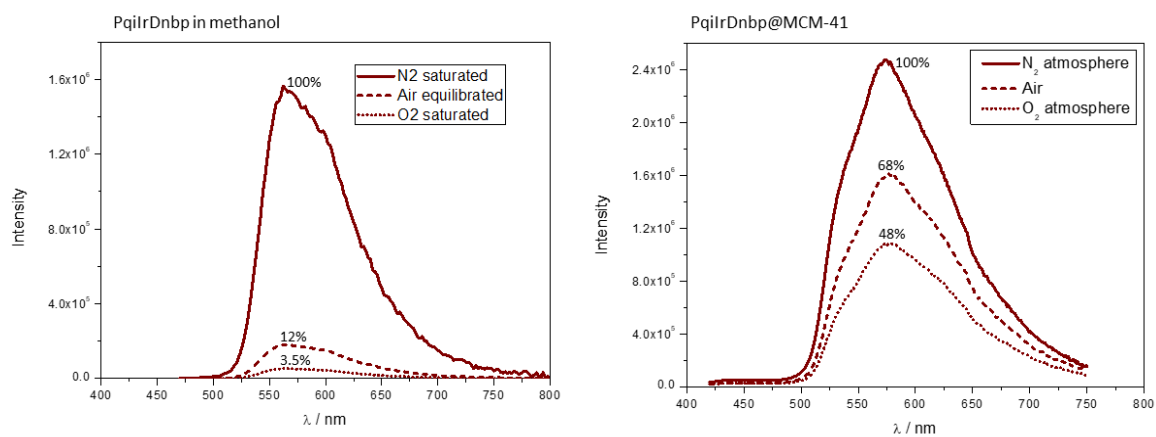
**Figure S2.**  $^1\text{H}$  NMR spectrum (300 MHz) of  $\text{HIrDnbp}$  in  $\text{CD}_3\text{OD}$ .**Figure S3.**  $^1\text{H}$  NMR spectrum (500 MHz) of  $\text{PqIrDnbp}$  in  $\text{CD}_3\text{OD}$ .

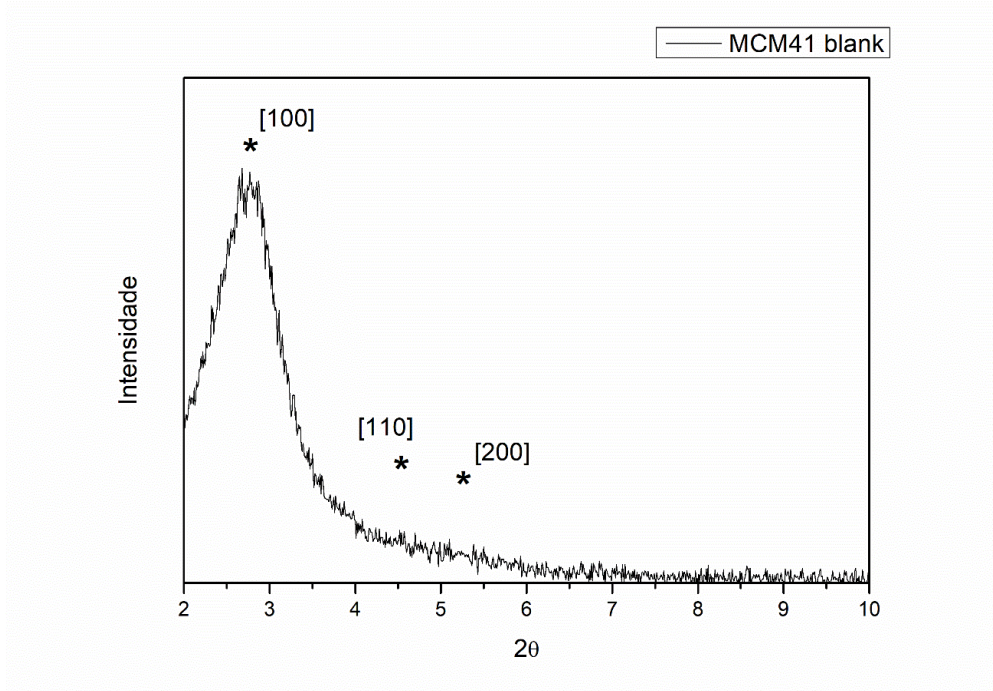
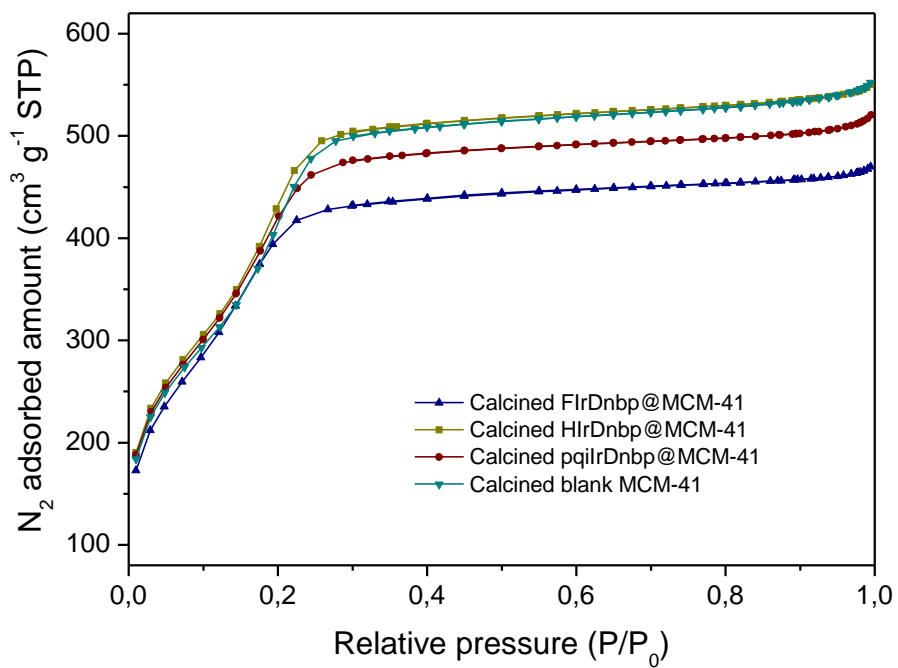
**Figure S4.** Stern-Volmer plots for the emission of the investigated complexes in methanol.



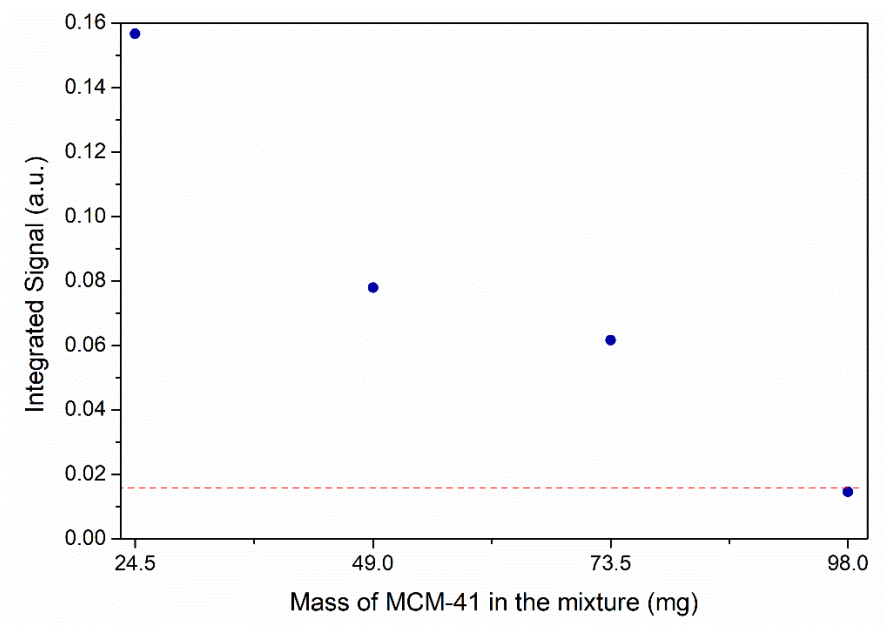
**Figure S5.** Emission spectra in different  $O_2$  concentrations for FlrDnbp in methanol or encapsulated in MCM-41.



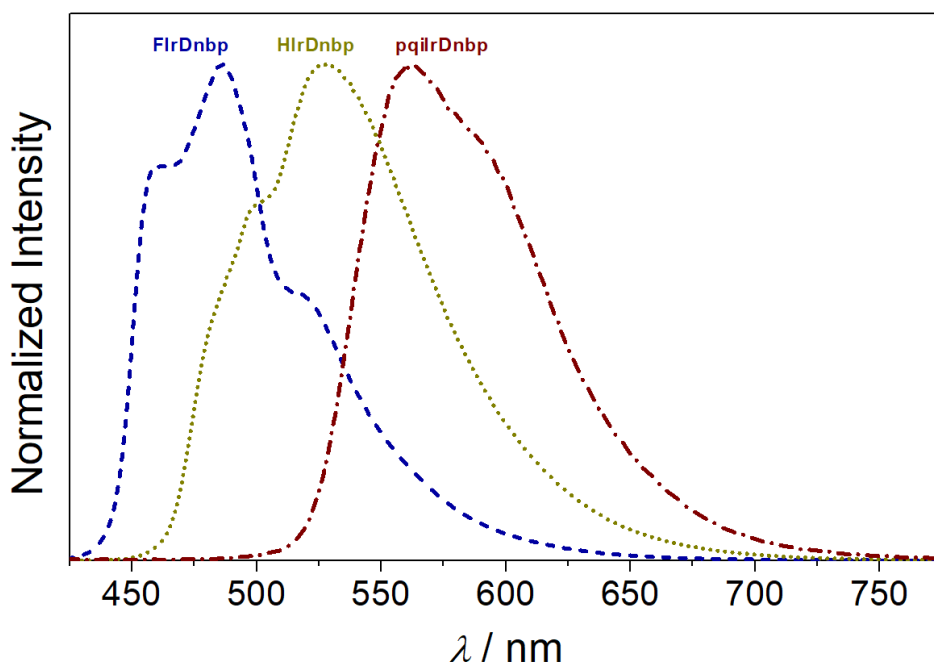
**Figure S6.** Emission spectra in different O<sub>2</sub> concentrations for HIrDnbp in methanol or encapsulated in MCM-41.**Figure S7.** Emission spectra in different O<sub>2</sub> concentrations for PqiIrDnbp in methanol or encapsulated in MCM-41.

**Figure S8.** XRD pattern of blank MCM-41 nanoparticles (without complex; non-calcined).**Figure S9.**  $N_2$  sorption isotherms of the developed MCM-41 nanoparticles (type IV without hysteresis).

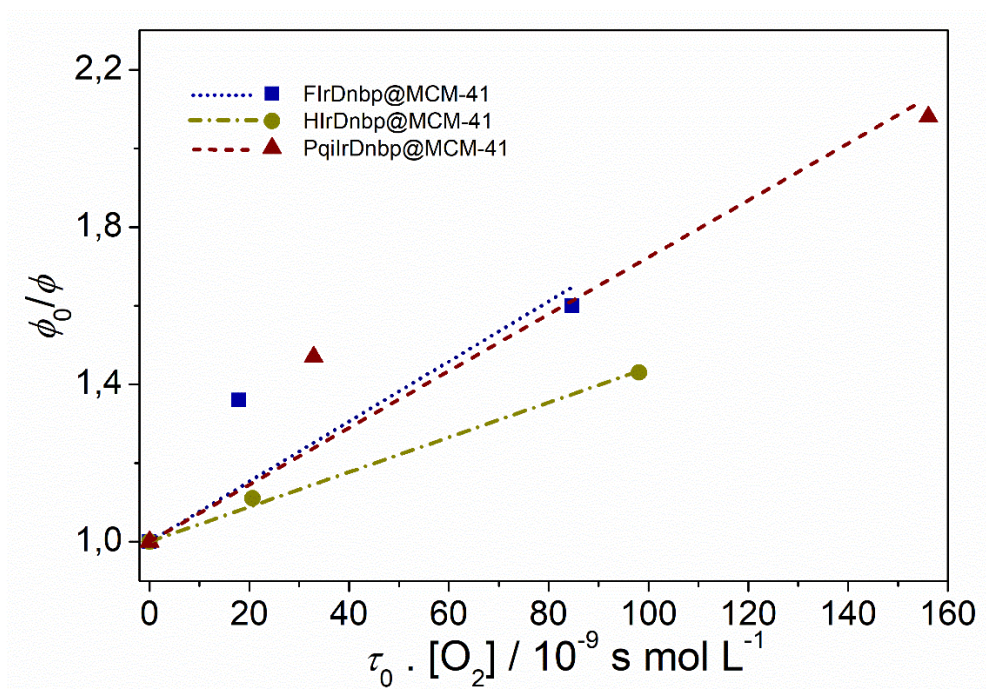
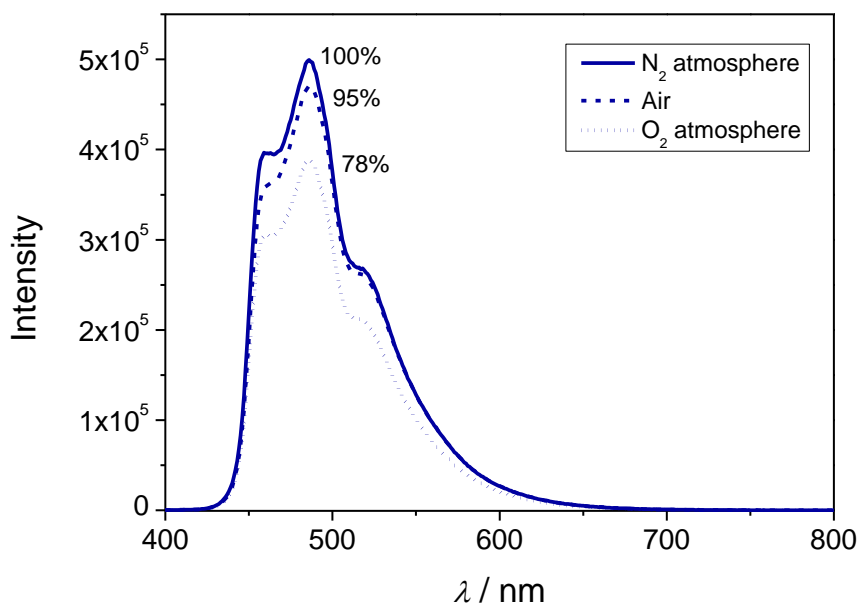
**Figure S10.** Signal area found by integration of the NMR spectrum for four different FirDnbp: MCM-41(blank, non-calcined) physical mixtures. All mixtures have 1 mg of FirDnbp complex. Notice that the mixture where the FirDnbp complex was diluted in 98 mg of MCM-41 reproduces well the signal area found for FirDnbp@MCM-41 (marked in dashed red line).

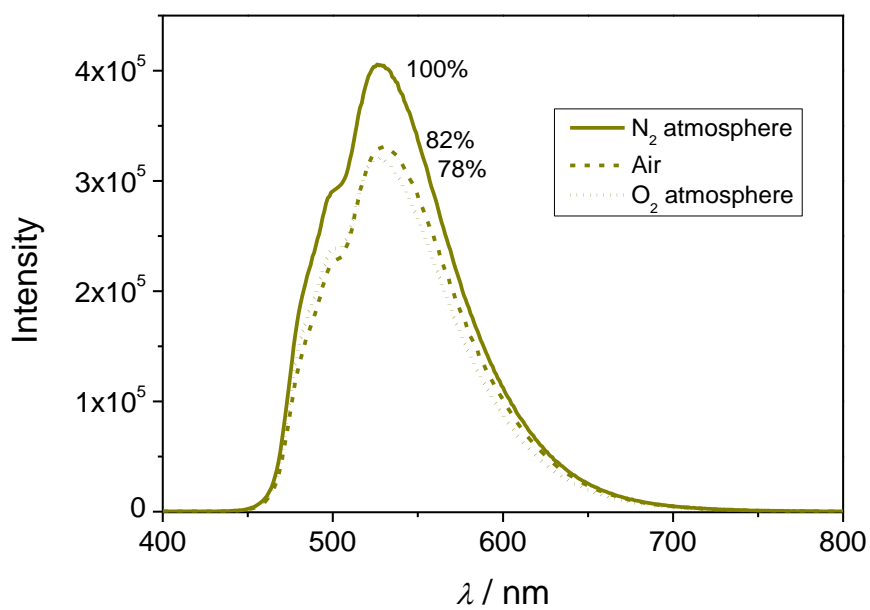
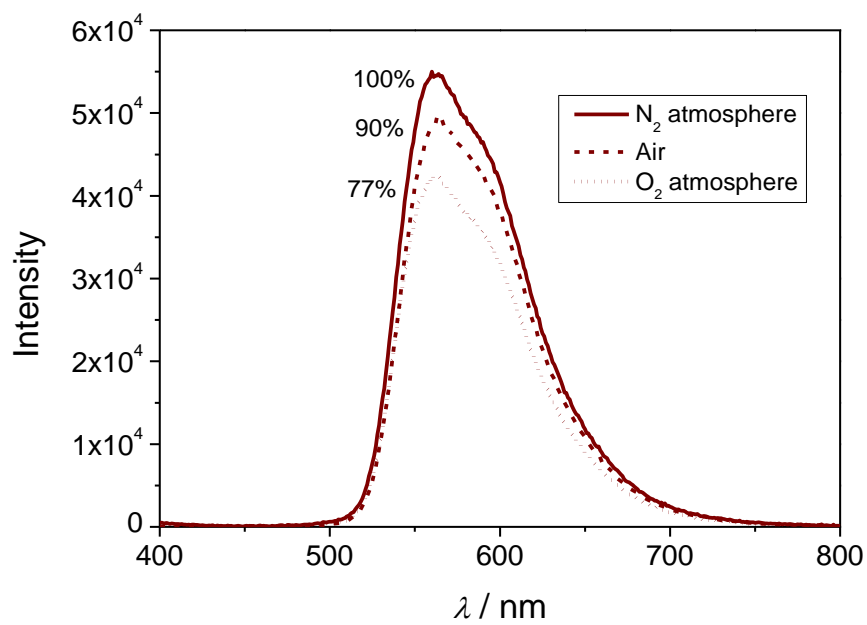


**Figure S11.** Emission spectra of  $[\text{Ir}(\text{C}^{\wedge}\text{N})_2(\text{dnbp})]^+$  complexes in PMMA films at 298 K ( $\lambda_{\text{exc}} = 360$  nm).

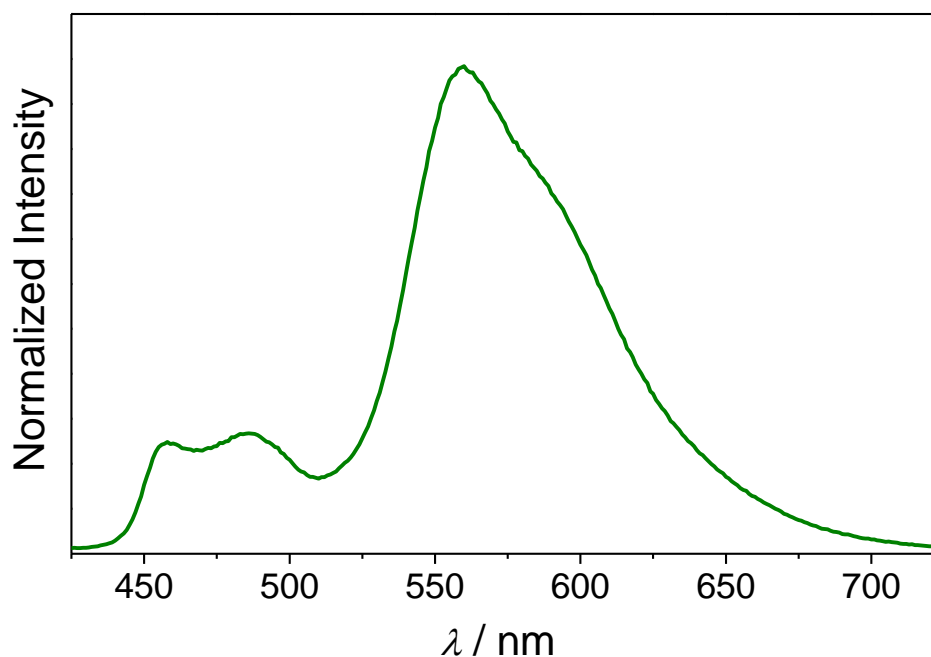




**Figure S12.** Stern-Volmer plots for the emission of the investigated complexes encapsulated in MCM-41.**Figure S13.** Emission spectra in different  $\text{O}_2$  concentrations of FIrDnbp in PMMA film.

**Figure S14.** Emission spectra in different O<sub>2</sub> concentrations of HIrDnbp in PMMA film.**Figure S15.** Emission spectra in different O<sub>2</sub> concentrations of pqiIrDnbp in PMMA film.

**Figure S16.** Emission spectra ( $\lambda_{\text{exc}} = 365$  nm) of a PMMA film doped with a 5:1 FIrDnbp:pqiIrDnbp mixture.



## References

- [1] J.C. De Mello, H.F. Wittmann, R.H. Friend, An improved experimental determination of external photoluminescence quantum efficiency, *Adv. Mater.* 9 (1997) 230–232.
- [2] A.A.S. Gonçalves, M.J.F. Costa, L. Zhang, F. Ciesielczyk, M. Jaroniec, One-Pot Synthesis of  $\text{MeAl}_2\text{O}_4$  (Me = Ni, Co, or Cu) Supported on  $\gamma\text{-Al}_2\text{O}_3$  with Ultralarge Mesopores: Enhancing Interfacial Defects in  $\gamma\text{-Al}_2\text{O}_3$  To Facilitate the Formation of Spinel Structures at Lower Temperatures, *Chem. Mater.* 30 (2018) 436–446.

## Supporting information: Mesoporous silica nanoparticles incorporated with Ir(III) complexes: From photophysics to photodynamic therapy

### Experimental procedures

#### *Photophysical characterization*

The electronic absorption spectra were recorded on a Perkin Elmer Lambda 1050 UV/Vis/NIR spectrometer. Quartz cuvettes with a 1.000 cm optical path length were used in the measurement of fluid solutions. The experiments were always preceded by measurements of a blank using the same cuvette and solvent. Steady-state and time-resolved emission spectra were recorded using a Horiba Fluorolog time-correlated single photon-counting. A xenon lamp ( $\lambda_{\text{exc}} = 365$  nm) or a Horiba Delta Diode ( $\lambda_{\text{exc}} = 370$  nm, frequency = 20 kHz) were employed as excitation sources for steady-state or time-resolved measurements, respectively. For measurements, the concentration of Ir(III) complexes in aqueous solutions was set to be  $\sim 10^{-5}$  mol mL<sup>-1</sup>, whereas 1 mg mL<sup>-1</sup> of the powder samples were used (approximately  $0.6 \times 10^{-5}$  mol mL<sup>-1</sup> of complex). The solutions were bubbled with N<sub>2</sub> for at least 15 minutes prior to standard measurements and the oxygen quenching experiments were performed by insertion of gas (air, N<sub>2</sub> or O<sub>2</sub>) for another 10 minutes each, inside the sealed cuvette. Absolute emission quantum yields ( $\phi_0$ ) were measured using a BaSO<sub>4</sub> coated integrating sphere, model Horiba Quanta- $\phi$  and all spectra were automatically corrected by the spectral response and sensitivity curves of the equipment detector.

#### *Determination of emission quantum yield:*

Absolute emission quantum yields ( $\phi_0$ ) were measured applying the methodology described by de Mello *et al.* [1], with samples positioned in the center of the sphere.

$$\phi_0 = \frac{P_s - P_b}{L_b - L_s} \quad (SI1)$$

in which P and L are the integral of the phosphorescence and the area under the lamp signal, respectively. The subscripts s and b indicate the sample or the blank. The blank sample consisted of an MCM41-COOH sample produced with no complexes encapsulated.

#### *Radiative and non-radiative constants:*

The radiative ( $k_r$ ) and nonradiative decay ( $k_{nr}$ ) rates were calculated by

$$k_r = \frac{\phi_0}{\tau_0} \quad (SI2)$$

$$k_{nr} = \frac{1 - \phi_0}{\tau_0} \quad (SI3)$$

where  $\tau_0$  is the emission lifetime of the sample in degassed solvent.

*Quenching rate constant:*

The quenching rate constant ( $k_q$ ) was obtained by Stern–Volmer analyses using

$$\frac{\phi_0}{\phi} = k_q \tau_0 [{}^3\text{O}_2] + 1 \quad (SI4)$$

in which  $\phi$  is the emission quantum yield of the complex in a sample solution with a known  $[{}^3\text{O}_2]$  concentration ( $[{}^3\text{O}_2] = 1.22 \times 10^{-3} \text{ mol L}^{-1}$  for saturated  $\text{O}_2$  solution and  $0.26 \times 10^{-3} \text{ mol L}^{-1}$  in saturated air solution [2]), while  $\phi_0$  and  $\tau_0$  are the emission quantum yield and the emission lifetime of the complexes in saturated  $\text{N}_2$  solutions ( $[{}^3\text{O}_2] = 0 \text{ mol L}^{-1}$ ).

*Singlet oxygen quantum yield ( $\Phi_\Delta$ ):*

Singlet oxygen quantum yields ( $\Phi_\Delta$ ) in deuterated acetonitrile were obtained from Equation SI5 [3] using  $[\text{Ir}(\text{pqi})_2(\text{dmb})]$  as hexafluorophosphate ( $\text{PF}_6^-$ ) salts in the same solvent as a reference ( $\Phi_\Delta = 0.47$  [3]).

$$\Phi_\Delta^S = \Phi_\Delta^{\text{Ref}} \frac{I^S}{I^{\text{Ref}}} \frac{1 - 10^{-A^{\text{Ref}}}}{1 - 10^{-A^S}} \quad (SI5)$$

in which  $\Phi_\Delta^S$  is the singlet oxygen quantum yield of the sample  $\Phi_\Delta^{\text{ref}}$  is the singlet oxygen quantum yield of the reference,  $A^S$  and  $A^{\text{ref}}$  are the absorbances at the excitation wavelength of sample and reference solutions;  $I^S$  and  $I^{\text{ref}}$  and are the integrals of the oxygen's emission spectrum at 1270 nm for sample and reference solutions.

*Morphological characterization*

X-ray powder diffraction (XRD) was performed in a Rigaku Miniflex diffractometer with a Cu-K $\alpha$  radiation ( $\lambda = 0.15418 \text{ nm}$ , 30 kV, 15 mA). Transmission electron microscopy was performed in a JEOL JEM-2100 Microscope.

### *Dynamic light scattering (DLS) size distribution and Zeta Potentials*

The hydrodynamic diameter of the nanoparticles was analyzed by dynamic light scattering (DLS) in the Malvern Zetasizer, which was also used for zeta potential measurements.

### *Fourier Transform Infrared Spectroscopy (FTIR)*

FTIR measurements were performed at room temperature using a Thermo Scientific™ Nicolet™ iS50 IR Spectrometer equipment. Prior to measurements, samples were diluted in KBr (1 mg:80 mg KBr) using an agate mortar and pressed under high pressures to produce IR transparent pastille discs.

### *Cell viability and Photodynamic Therapy*

The cell lines were maintained in Dulbecco's modified Eagle's medium (DMEM) (Vitrocell) and Minimum Essential Medium Earle (MEM - Earle) supplemented with 10% of fetal bovine serum (Vitrocell) and 1% L-glutamine (Vitrocell) at 37 °C and in 5% CO<sub>2</sub>. Human hepatoma (HepaRG) cells were provided by Dra. Natalia Inada from Physics Institute of São Carlos, University of São Paulo, Brazil and human hepatocarcinoma (Hep-G2) were purchased from Rio de Janeiro Cell Bank (BCRJ). The cell viability was assed indirectly by mitochondrial activity using MTT assay of Hepa-RG and Hep-G2. 24-well culture plates containing 5x10<sup>4</sup> cells mL<sup>-1</sup> were prepared 24 h before the experiments, for an efficient adhesion of the cells in the wells. After that, the cells were treated with a dispersion of MCM41-COOH and complex@MCM41-COOH (all nanoparticles are stored in powder form) from 5 to 100 µg/mL prepared directly in DMEM (Hepa-RG) and MEM-Earle (Hep-G2), and incubated with the cells for 24 hours. After 24 h of incubation in the dark, the wells were washed with PBS (to remove non-internalized nanoparticles) and phenol-red-free medium were added, not to interfere with radiation. The cells were then irradiated at 405 nm for 10 and 20 min, applying a dose of 24 and 48 J cm<sup>-2</sup>, respectively. At the same time, experiments without lighting were performed to investigate possible toxicity in the dark, therefore, the viability test was performed 24 hours after the application of the nanoparticles. The cells were then taken to the incubator for 24 hours and in the following day the cell viability test was performed. For the cell viability test, after 24 hours the culture medium without phenol was removed from the wells and a new medium was added in the presence of the MTT reagent. After 3 hours, the medium was removed and 400 µL of DMSO was added to each well. The MTT absorbance was measured at 580 nm in a

microplate reader (Spectramax M3, Molecular Devices). The viable cells were calculated based on the following equation:

$$\text{Cell viability} = \frac{\text{Mean absorbance of treated wells} * 100}{\text{Mean absorbance of control well}}$$

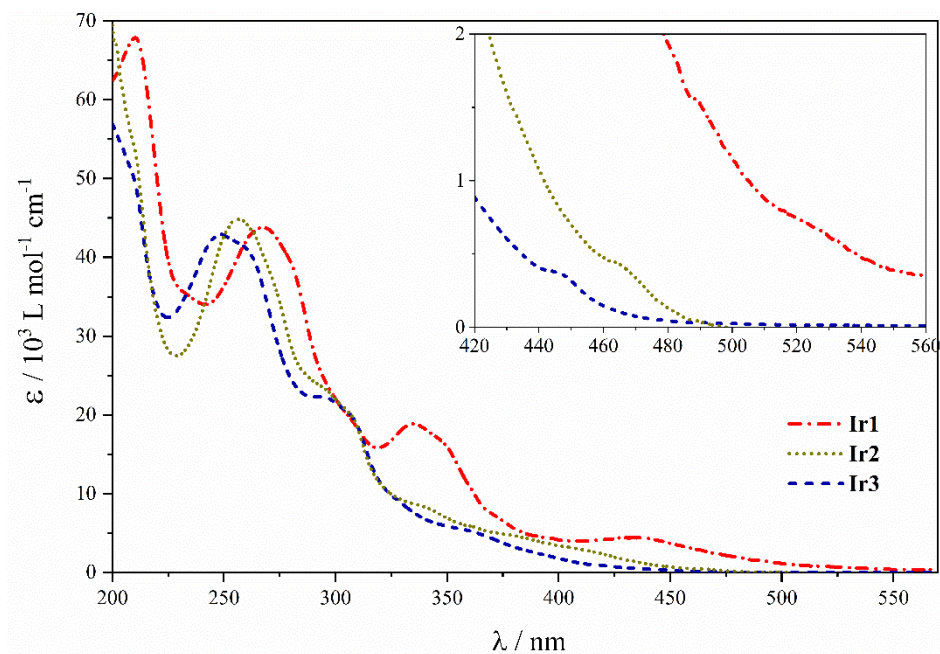
The results represent the mean  $\pm$  SD of data normalized to untreated controls from three independent experiments in triplicate. Statistical analysis was performed using two-way ANOVA with Tukey's comparisons.

#### *Cellular uptake*

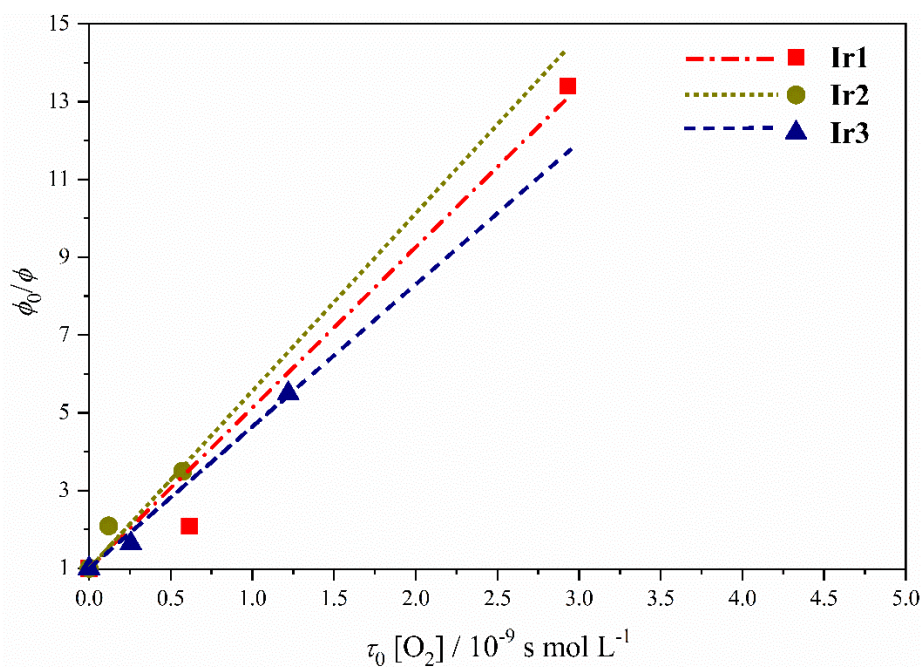
Cells were seeded on round glass slide in 12-well plates at the concentration of  $10^5$  cell/well and left to adhere for 24 hours. The internalization was carried out incubating complex@MCM41-COOH at the concentration of 50  $\mu\text{g/ml}$ . After incubation (24 h), cells were washed two times with Phosphate-Buffered Saline (PBS 1x, Gibco), fixed with 4% paraformaldehyde (PAF) in PBS 1x for 20 minutes. Nuclei was stained with Hoechst 33342 (DAPI - 4  $\mu\text{g/ml}$ ). Images were acquired with a Zeiss LSM 900 confocal microscope equipped with specific laser  $\lambda_{\text{exc}} = 405$  nm. The images were collected and the colors represented are: blue (nucleus), green (Ir3@MCM41-COOH), red (Ir1@MCM41-COOH and Ir2@MCM41-COOH).

## General supporting results

**Figure S11.** Absorption spectra of Ir(III) complexes as water-soluble chloride ( $\text{Cl}^-$ ) at 298 K.

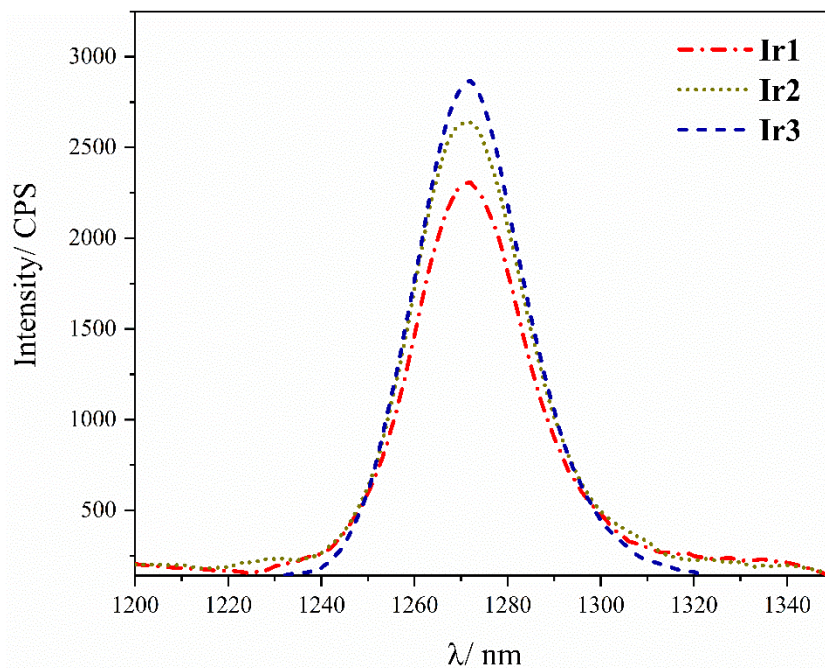


**Figure S12.** Stern-Volmer plots for the emission quenching of the investigated Ir(III) complexes in aqueous solutions ( $\sim 10^{-5} \text{ mol mL}^{-1}$ ) at 298 K.

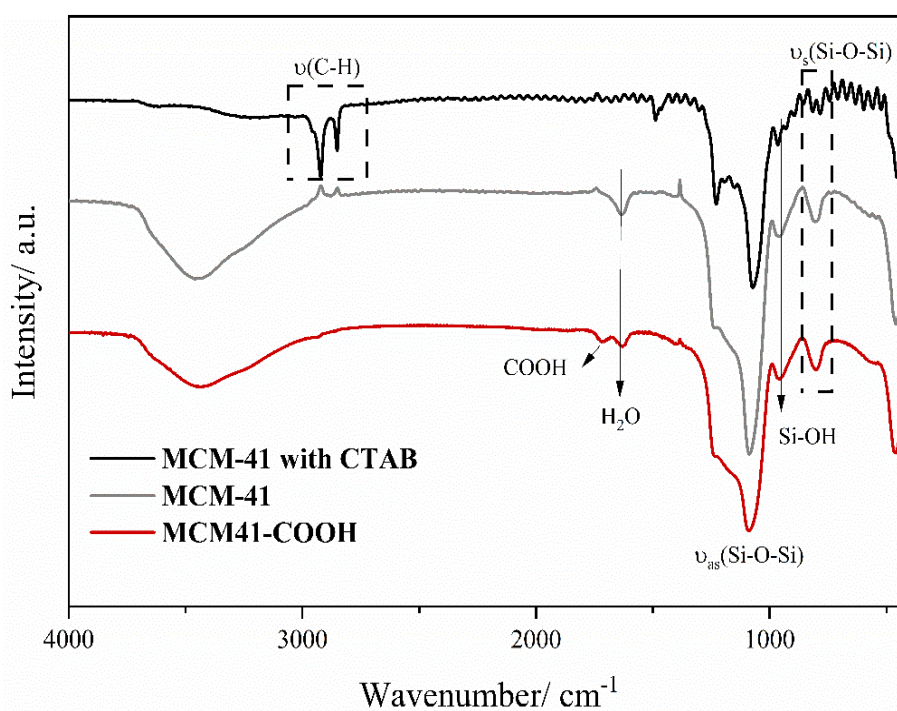




**Figure SI3.** Emission spectra of singlet oxygen's 1270 nm emission in deuterated acetonitrile solutions of complexes of Ir(III) complexes as water-soluble chloride ( $\text{Cl}^-$ ) at 298 K ( $\lambda_{\text{exc}} = 365 \text{ nm}$ ).

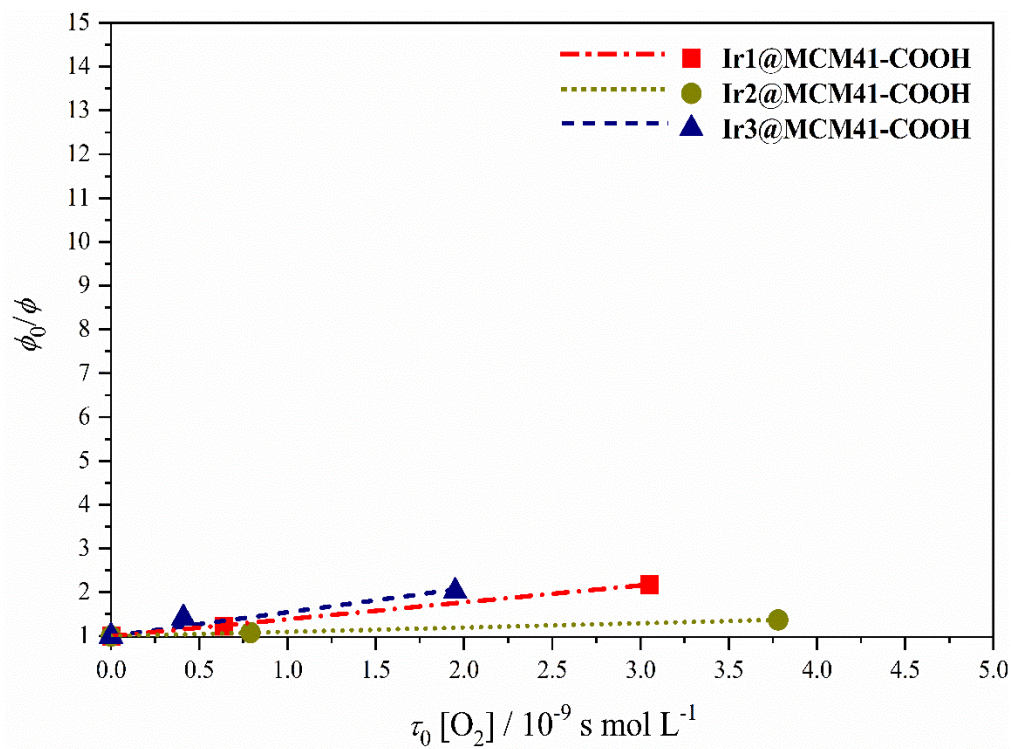


**Figure SI4.** The FTIR spectra of MCM41 with CTAB, calcined MCM41 and MCM41-COOH materials showed typical bands between 1300 and 500  $\text{cm}^{-1}$ , which are mostly ascribed to the mesoporous silica framework:  $\nu_{\text{as}}(\text{O-Si-O})$  at 1078 and 1221  $\text{cm}^{-1}$ ,  $\nu_{\text{s}}(\text{O-Si-O})$  at 807  $\text{cm}^{-1}$  and  $\nu(\text{Si-OH})$  at 970  $\text{cm}^{-1}$ . The band in the region between 2980 and 2880  $\text{cm}^{-1}$  of the MCM41 spectrum with CTAB are assigned to the C-H stretching of the methyl and methylene groups of the surfactant. The absence of this vibration bands in the subsequent MCM41 and MCM41-COOH materials highlight that the template was successfully removed. The C=O stretching vibration mode at 1719  $\text{cm}^{-1}$ , only observed for MCM41-COOH, confirm the presence of carboxylic acid groups. For all spectra, the bending mode vibration of water is observed at 1628  $\text{cm}^{-1}$ .

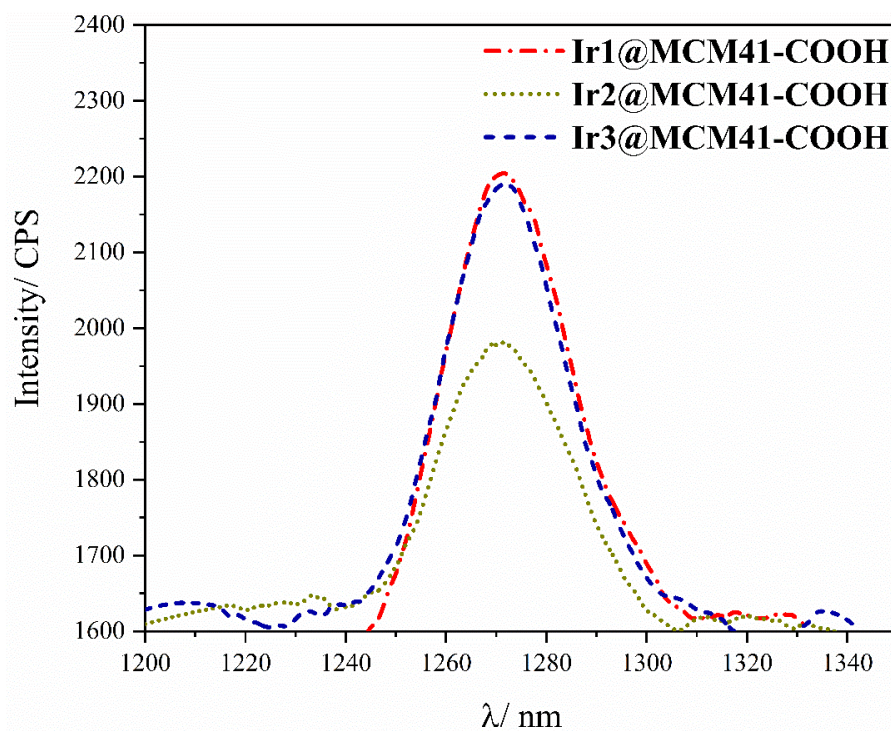


**Table SI3.** Characteristics of the acid-functionalized nanoparticles incorporated with Ir(III) complexes.

Sample	Zeta Potential/ mV	Size/ nm
MCM41-COOH	$-34,6 \pm 5,4$	$200,6 \pm 46,4$
Ir1@MCM41-COOH	$-31,3 \pm 8,5$	$299,1 \pm 61,6$
Ir2@MCM41-COOH	$-25,6 \pm 4,9$	$422,8 \pm 159,0$
Ir3@MCM41-COOH	$-25,4 \pm 4,6$	$302,4 \pm 99,3$

**Figure SI5.** Stern-Volmer plots for the emission quenching of aqueous dispersions of Ir(III) complex incorporated in MCM41-COOH nanoparticles ( $1 \text{ mg}\cdot\text{mL}^{-1}$ , that is, approximately  $0.6 \times 10^{-5} \text{ mol mL}^{-1}$  of complex) at 298 K in the presence of oxygen for  $\tau_2$ . For comparison, the results were plotted with the same scale as in Figure SI2.

**Figure S6.** Emission spectra of singlet oxygen's 1270 nm emission in deuterated acetonitrile solutions of MCM41-COOH nanoparticles incorporated with Ir(III) complexes at 298 K ( $\lambda_{\text{exc}} = 365$  nm).



## References

- [1] J.C. de Mello, H.F. Wittmann, R.H. Friend, An improved experimental determination of external photoluminescence quantum efficiency, *Adv. Mater.* 9 (1997) 230–232.
- [2] W. Xing, M. Yin, Q. Lv, Y. Hu, C. Liu, J. Zhang, *Rotating Electrode Methods and Oxygen Reduction Electrocatalysts*, Elsevier, 2014.
- [3] K.P.S. Zanoni, A. Ito, M. Grüner, N.Y. Murakami Iha, A.S.S. De Camargo, Photophysical dynamics of the efficient emission and photosensitization of  $[\text{Ir}(\text{Pqi})_2(\text{NN})]^+$  complexes, *Dalt. Trans.* 47 (2018) 1179–1188.